Simulation of the TRIUMF Proton Therapy Facility for Applications to 3D Printing in Radiotherapy

Clayton Daniel Lindsay

A Dissertation Submitted in Partial Fulfillment of the Requirements for the Degree of

DOCTOR OF PHILOSOPHY

in the Department of Physics and Astronomy

University of Victoria

We acknowledge with respect the Lekwungen peoples on whose traditional territory the university stands and the Songhees, Esquimalt and W̱SÁNEĆ peoples whose historical relationships with the land continue to this day.

Simulation of the TRIUMF Proton Therapy Facility for Applications to 3D Printing in Radiotherapy

by

Clayton Daniel Lindsay
B.Sc., University of Victoria, 2007
M.Sc., University of Victoria, 2009

Supervisory Committee

Dr. Cornelia Hoehr, Co-Supervisor
(Department of Physics and Astronomy)

Dr. Andrew Jirasek, Co-Supervisor
(Department of Physics and Astronomy)

Dr. Wayne Beckham, Departmental Member
(Department of Physics and Astronomy)

Dr. Irina Paci, Outside Member
(Department of Chemistry)

Dr. Thomas Ruth, Departmental Member
(TRIUMF)

Abstract

Proton therapy, a relatively young modality in radiation therapy, has proven useful in cases where a sharp dose gradient or low secondary irradiation is required. In Canada proton therapy it was performed at the TRIUMF Proton Therapy Facility in the treatment of large or difficultly positioned ocular melanomas. This rare primary malignant cancer of the eye has a poor prognosis if untreated. Patient vision sparing is critical for quality of life and is strongly affected by the accuracy of the chosen treatment. Reduction in irradiation of critical structures is a proven strength of proton therapy due to the high dose-gradient and finite range in tissue. But, with the advantage of steep dose gradients, comes the requirement of precision target positioning and planning.

Monte Carlo particle transport software is a valuable tool for understanding treatment doses in cases where measurement is time consuming or difficult. Accurate simulation of primary proton dose to water aids in the evaluation of beam characteristics and allows for study into improving dose application for patient treatment. In this work, a full Monte Carlo model of the TRIUMF proton therapy facility was developed. Measurements were taken in water to validate simulated results within 2% over the treatment depth for a wide range of beam modulations.

The second advantage of proton therapy lies in its reduced dose bath to healthy tissue. This is especially important in pediatric cases where extraneous dose comes with a high risk of secondary carcinogenesis. Whereas multi-angle photon treatments necessarily irradiate large volumes of healthy tissue to produce a flat target dose, proton treatments may irradiate a target with a single beam. With this advantage comes a trade-off - protons produce a large number of neutrons as they are prepared for patient treatment. These neutrons are the largest contributor to secondary dose in proton therapy and must be well modeled and shielded to ensure patient safety. The second part of this work involves the measurement of secondary neutron doses in the TRIUMF treatment room. Measurements were validated within 20% of simulated

values with uncertainties dominated by calibration of the detector. Neutron doses to an anatomic human model showed that calibrated secondary doses were in line with similar treatment facilities reporting globally. Simulations indicated that the source of neutrons was primarily in the unshieldable region of the beamline opening. Thus the total treatment time was the determining factor in secondary dose to the patient.

With primary proton dose well modeled, it became possible to study the precision of treatment and possible avenues for improvement. The beam modulation wheels and optimization scheme was developed in the late 90's when computational and manufacturing technologies were less developed. Updated optimization methods indicated that moving to a smooth scheme of energy modulation, as opposed to a stepped modulation wheel, could improve distal dose sharpness. This was contrary to the long-held belief that there was an optimal number of steps for modulation. The third portion of this work explored the use of 3D printers to enable the fabrication of smoothly transitioning modulator wheels. Materials and printer methods were studied, indicating a strong candidate in the PolyJet$^{\text{TM}}$ method for beam modulation. Both stepped and newly-optimized smooth modulator wheels were printed and validated. Total turnaround time for modulator production was under 24 hours - proving the feasibility of patient-specific beam modulation.

The last portion of this work explored the use of positron emitting isotopes for dose validation. Protons traversing tissue or plastic generate β^+ emitting isotopes via nuclear interactions. The resulting back-to-back annihilation photons can be reconstructed into the isotope distribution produced by the beam. This can potentially provide information about beam position in the target and hence position of a phantom or patient. An anatomic 3D printed eye phantom was designed and irradiated to test the feasibility of this method. While a strong isotope signal was reconstructed, the test did not yield a viable technique due to the low resolution of the phantom scan. The phantom position was poorly reconstructed using the transmission scan. Despite this, it could be possible to improve this method by using other methods for phantom position registration.

Table of Contents

Supervisory Committee ii

Abstract iv

Table of Contents vi

List of Figures x

List of Tables xv

Abbreviations xvi

Acknowledgements xvii

Dedication xviii

1 Introduction 1

1.1 Beam Modulation and 3D Printing 2

1.2 Secondary Neutron Dose 3

1.3 Positron Emission Tomography Dosimetry 4

1.4 Thesis Scope 5

2 Background 6

2.1 Physics of Radiotherapy 6

2.1.1 Photon Interactions 8

2.1.2 Electron Interactions 10

2.1.3 Protons Interactions 11

2.1.4 Nuclear Interactions and Activation 12

2.2 Proton Therapy 13

2.2.1 Basic Definitions in Radiotherapy 15

2.2.2 The Bragg Peak . . . 18
2.2.3 Beam Modulation . . . 20
2.2.4 Proton Beam Generation . . . 22
2.2.5 Proton Dosimetry . . . 23
2.2.6 Treatment of Ocular Melanomas . . . 24
2.3 The TRIUMF Proton Therapy Facility . . . 25
2.3.1 *TRIUMF Accelerator* . . . 25
2.3.2 *Beamline 2C* . . . 28
2.3.3 *Dose Delivery System* . . . 28
2.4 Monte Carlo Simulation . . . 30
2.5 Positron Emission Tomography . . . 31

3 Simulation of the TRIUMF Proton Therapy Facility 32
3.1 FLUKA Monte Carlo Transport Package . . . 32
3.1.1 Transport Parameters . . . 33
3.1.2 Combinatorial and Voxel Geometries . . . 33
3.1.3 Units and Scoring Quantities . . . 35
3.2 Geometry . . . 36
3.2.1 Overview and Coordinate System . . . 37
3.2.2 Scatterer . . . 37
3.2.3 Collimators . . . 39
3.2.4 Detectors . . . 40
3.2.5 Range Shifter . . . 44
3.2.6 Modulator Wheels . . . 45
3.2.7 Target Geometries . . . 47
3.3 Beam Model . . . 51
3.3.1 Energy Calibration . . . 51
3.3.2 Beam Profile . . . 51
3.4 Summary . . . 52

4 Measurements and Model Validation 53
4.1 Primary Dose Measurements . . . 53
4.1.1 Methods and Hardware . . . 53
4.1.2 Uncertainties . . . 57
4.1.3 Pristine Depth Dose . . . 57

4.1.4 Range-Shifted Bragg Peak . . . 62
4.1.5 Spread Out Bragg Peak . . . 63
4.1.6 Waterbox Profiles . . . 69
4.1.7 Beam Measurements . . . 72
4.2 Simulated Primary Dose . . . 76
4.2.1 Uncertainties . . . 77
4.2.2 Beam Calibration . . . 79
4.2.3 Pristine Depth Dose . . . 79
4.2.4 Range-Shifted Bragg Peak . . . 81
4.2.5 Spread out Bragg Peak . . . 82
4.2.6 Profiles . . . 85
4.3 Neutron Measurements . . . 86
4.3.1 Methods and Hardware . . . 86
4.3.2 Uncertainties . . . 89
4.3.3 Neutron Measurements . . . 90
4.4 Simulated Neutron Dose Rate . . . 91
4.4.1 Uncertainties . . . 92
4.4.2 Beam Angle and Size Simulation . . . 94
4.4.3 Neutron Survey Simulation . . . 97
4.5 Summary . . . 102

5 Simulated Dose to Anatomy 103
5.1 Primary Dose to Eye Anatomy . . . 103
5.1.1 Anatomic Eye Model . . . 104
5.1.2 Tumour Volume Definition . . . 105
5.1.3 Beam Planning . . . 108
5.1.4 Primary Dose Estimation . . . 112
5.1.5 Primary Dose to Eye Anatomy . . . 114
5.2 Secondary Dose to Anatomy . . . 121
5.2.1 Simulation Methods and Uncertainties . . . 122
5.2.2 Neutron Sources . . . 124
5.2.3 Neutron Dose to VIPMAN Model . . . 133
5.3 Summary . . . 134

6 3D Printed Plastics for PT 142

6.1 Introduction . . . 142
6.2 3D Printed Plastics for Beam Modulation in Proton Therapy . . . 143
6.2.1 Introduction . . . 144
6.2.2 Materials and Methods . . . 145
6.2.3 Results and Discussion . . . 149
6.2.4 Conclusions . . . 155
6.2.5 Acknowledgements . . . 156
6.3 Supplementary Data . . . 156

7 Stepless Beam Modulators for PT 160
7.1 Introduction . . . 160
7.2 Design and Application of 3D-printed Stepless Beam Modulators in Proton Therapy . . . 161
7.2.1 Introduction . . . 161
7.2.2 Materials and Methods . . . 164
7.2.3 Results and Discussion . . . 170
7.2.4 Conclusions . . . 174

8 Activated Printed Eye Phantom 178
8.1 Introduction . . . 178
8.2 Materials and Methods . . . 180
8.2.1 Lucite Cylinder Experiment . . . 180
8.2.2 Plastic Eye Phantom Experiment . . . 182
8.3 Results and Discussion . . . 187
8.3.1 Lucite Cylinder . . . 187
8.3.2 Anatomic Eye Phantom . . . 187
8.4 Conclusions . . . 191

9 Summary and Conclusions 194
9.1 Dissertation Summary . . . 194
9.1.1 Outlook . . . 196

Bibliography 197

List of Figures

Figure 2.1	Various modality depth-dose distributions and cell survival curves	7
Figure 2.2	Photon interactions in water	8
Figure 2.3	Electron mass stopping powers	10
Figure 2.4	Proton interactions in water	11
Figure 2.5	Target volume definitions	14
Figure 2.6	Sample dose-volume histogram and isodose contours	17
Figure 2.7	Proton depth-dose in water - $74MeV$ beam	18
Figure 2.8	Proton ranges and water equivalent ratios	19
Figure 2.9	Spread out Bragg Peak depth-dose distributions	21
Figure 2.10	Diagram of eye anatomy	25
Figure 2.11	TRIUMF cyclotron and beamline 2C-1 schematics	26
Figure 2.12	TRIUMF cyclotron stripping foil diagram	26
Figure 2.13	TRIUMF dose delivery system (treatment head).	27
Figure 3.1	FLUKA combinatorial geometry diagram	34
Figure 3.2	Sample FLUKA output types - USRBIN and USRTRK	36
Figure 3.3	Treatment head geometry 3D FLUKA rendering	37
Figure 3.4	FLUKA schematic of geometry materials	38
Figure 3.5	Scatterer schematic and rendering	39
Figure 3.6	Secondary collimator schematic and rendering	40
Figure 3.7	Nozzle schematic and rendering	41
Figure 3.8	Profile monitor schematic and rendering	42
Figure 3.9	Diagnostic ion chamber schematic and rendering	43
Figure 3.10	Quadrant chamber schematic and rendering	43
Figure 3.11	Range shifter schematic and rendering	44
Figure 3.12	Modulator wheel photos	46
Figure 3.13	Stepped wheel schematic and rendering	47

Figure 3.14	Smooth wheel profile and FLUKA renderings	48
Figure 3.15	Waterbox schematic and rendering	49
Figure 3.16	VIPMAN phantom schematic and rendering	50
Figure 3.17	Anatomic eye model rendered in SolidWorks and FLUKA VOXEL model	50
Figure 4.1	Photo of waterbox setup	55
Figure 4.2	Diagram of Bragg peak characteristics and definitions	58
Figure 4.3	Peak finding algorithm	59
Figure 4.4	Bragg peak raw data for Markus chamber and diode probes	60
Figure 4.5	Raw BP - comparison of Markus chamber and diode measurements	61
Figure 4.6	Markus chamber data for range shifted Bragg peaks	63
Figure 4.7	Range shifter depth shifts and peak widths	64
Figure 4.8	Diagram of SOBP characteristics and definitions	65
Figure 4.9	Plateau finding algorithm	66
Figure 4.10	$8mm$ SOBP data for Markus chamber and diode probes	67
Figure 4.11	$14mm$ SOBP data for Markus chamber and diode probes	67
Figure 4.12	$23mm$ SOBP data for Markus chamber and diode probes	68
Figure 4.13	$14mm$ SOBP Markus/diode normalized comparison	70
Figure 4.14	Diagram of profile plot definitions	70
Figure 4.15	Beam profiles - raw data in veritcal and horizontal direction	71
Figure 4.16	Beam profile raw data	72
Figure 4.17	Profile monitor output with fitted FLUKA input beam	73
Figure 4.18	Diagram of transmission curve characteristics and definitions	74
Figure 4.19	Transmission curve fitting algorithm	75
Figure 4.20	TRIUMF transmission curve data	76
Figure 4.21	Simulated BP statistical uncertainties	77
Figure 4.22	FLUKA dose uncertainties	78
Figure 4.23	Fitted calibration curves for range shifter peak and width	80
Figure 4.24	Transmission scan - comparison of measurement and FLUKA simulation	80
Figure 4.25	$74MeV$ Bragg peak - comparison of Markus data to FLUKA simulation	81

Figure 4.26	Range shifted BP - comparison between Markus data and FLUKA simulation	82
Figure 4.27	$8mm$ SOBP - comparison between Markus data and FLUKA simulation	83
Figure 4.28	$14mm$ SOBP - comparison between Markus data and FLUKA simulation	83
Figure 4.29	$23mm$ SOBP - comparison between Markus data and FLUKA simulation	84
Figure 4.30	Beam profile - comparison of simulation and measurement	85
Figure 4.31	Sample neutron spectrum and BF3 conversion factors	88
Figure 4.32	TRIUMF DDS schematic showing neutron survey meter placement	89
Figure 4.33	Neutron survey BF3 doserate measurements	91
Figure 4.34	AmBe correction factor	93
Figure 4.35	Neutron survey simulation uncertainty	95
Figure 4.36	Quadrant chamber beam deflection	96
Figure 4.37	Proton beam current - small beamspot	98
Figure 4.38	Proton beam current - large beamspot	98
Figure 4.39	Simulated neutron dose rate - large and small beamspots	99
Figure 4.40	Neutron dose rate - simulation and measurement comparison	101
Figure 4.41	Averaged simulated dose rate for large and small beamspots	101
Figure 5.1	Anatomic eye sphere model and VOXEL FLUKA slice	106
Figure 5.2	Tumour target definitions for $8mm$ modulation	109
Figure 5.3	Tumour target definitions for $14mm$ modulation	110
Figure 5.4	SOBP dose distributions for shifted and unshifted plans	113
Figure 5.5	Interpolated approximate dose in eye anatomy with isodose contours	115
Figure 5.6	Dose volume histograms for dose approximation on eye tumour targets	116
Figure 5.7	Simulated dose to eye anatomy generated using MC with isodose contours	118
Figure 5.8	SOBP calculated using interpolated dose method compared to MC simulated	119
Figure 5.9	Dose volume histograms for MC simulated dose	120

Figure 5.10	Mean dose at target volume centers - primary normalization factors	121
Figure 5.11	Absorbed dose uncertainty by organ	123
Figure 5.12	Equivalent dose uncertainty by organ	123
Figure 5.13	Neutron fluences along DDS beamline by source region	126
Figure 5.14	Neutron fluence generated by DDS components	127
Figure 5.15	Simulated neutron energy spectra at VIPMAN by neutron source	127
Figure 5.16	Ambient dose equivalent by organ	128
Figure 5.17	Equivalent dose generated by non-planned components	130
Figure 5.18	Equivalent dose generated by patient collimator	130
Figure 5.19	Equivalent dose generated by modulator wheel	131
Figure 5.20	Equivalent dose generated by range shifter	131
Figure 5.21	Equivalent dose by tissue generated neutrons	132
Figure 6.1	Photos of 3D-printed modulator wheels	148
Figure 6.2	Laser profilometer scans of test cubes	153
Figure 6.3	Measured SOBP's for 3D-printed wheels	154
Figure 6.4	Caliper measured print errors	157
Figure 6.5	CT scan profiles for test cubes	158
Figure 6.6	Measured beam dose profile for 3D-printed wheels	159
Figure 7.1	10-step Koehler optimized SOBP	162
Figure 7.2	20-step Koehler optimized SOBP	162
Figure 7.3	Stepless modulator wheel 3D rendering	165
Figure 7.4	Stepless modulator wheel thickness profile	165
Figure 7.5	Simulated Koehler and Gardey SOBP's	172
Figure 7.6	Simulated SOBP's for stepless wheel	172
Figure 7.7	Simulated bio-equivalent dose for flat and stepless optimized SOBP's	173
Figure 7.8	Measured SOBP's for stepped and stepless $8mm$ wheels	175
Figure 7.9	Measured SOBP's for stepped and stepless $14mm$ wheels	175
Figure 7.10	Measured SOBP's for stepped and stepless $23mm$ wheels	176
Figure 8.1	Photo of Lucite cylinder experiment	180
Figure 8.2	Photo of uPET machine	181

Figure 8.3 Anatomic eye model - CAD, raycast and VOXEL renderings 183
Figure 8.4 Render of plastic eye phantom and gimbal 184
Figure 8.5 Photos of laser and field-light alignment of plastic eye phantom 185
Figure 8.6 Measured and simulated images of PET activity in Lucite cylinder 188
Figure 8.7 Lucite cylinder simulated and measured PET signal . . . 189
Figure 8.8 Eye central-slices of simulated dose, measured PET signal, isotope distribution and simulated PET signal 190
Figure 8.9 Eye phantom angle and translational optimizations 192

List of Tables

Table 2.1 Isotopes generated in tissue during proton therapy 14

Table 3.1 FLUKA MC parameters 52

Table 4.1 Table of measured SOBP output factors for the Markus chamber and diode. 69

Table 5.1 Table of tumour volume definitions with anatomical characteristics. 107

Table 5.2 Table of calculated tumour depths, range shifts and collimator sizes required to position SOBP over the CTV. . . 112

Table 5.3 Absorbed dose, weighting and equivalent dose for plan A . 135

Table 5.4 Absorbed dose, weighting and equivalent dose for plan B . 136

Table 5.5 Absorbed dose, weighting and equivalent dose for plan C . 137

Table 5.6 Absorbed dose, weighting and equivalent dose for plan D . 138

Table 5.7 Absorbed dose, weighting and equivalent dose for plan E . 139

Table 5.8 Absorbed dose, weighting and equivalent dose for plan F . 140

Table 6.1 Caliper measured print dimensions and errors 149

Table 6.2 Printed densities and stopping powers for test objects . . 151

Table 7.1 Koehler and Gardey SOBP characteristics 172

Table 7.2 Stepless wheel characteristics 172

Abbreviations

BCCA - British Columbia Cancer Agency
BF3 - boron trifluoride
BP - Bragg peak
CAD - computer aided design
CPT - charged particle therapy
CTV - clinical target volume
(C)DVH - (cumulative) dose volume histogram
DDS - dose delivery system
DNA - deoxyribonucleic acid
GTV - gross tumour volume
IC - ion chamber
ICRU - International Commision on Radiation Units
LET - linear energy transfer
MC - Monte Carlo
MCS - multiple Coulomb scattering
MU - monitor unit
MV - megavoltage (X-rays)
OAR - organ at risk
PET - positron emission tomography
PMMA - Poly(methyl methacrylate)
PT - proton therapy
PTV - planning target volume
QA - quality assurance
RBE - relative biological effectiveness
RS - range shifter
SOBP - spread out Bragg peak
WC - wire chamber

Acknowledgements

First and foremost I want to thank my primary supervisor Dr. Conny Hoehr. But for her guidance, patience and endlessly supportive attitude, this project would have never been possible. She was always willing to indulge me in whatever direction I may have gone, encouraged exploration, celebrated successes and supported me in failures. I am forever grateful to her. I also would like to thank my co-supervisor Andrew Jirasek who has been so patient and helpful in navigating academia.

This project has had a great many collaborators I'd thank: Mike Trinczek for his countless hours helping with experiments; Richard Lee for help with CT scans; Greg Stortz and Vesna Sossi at the UBC PET suite; Cheryl Duzenli for clinical context and planning; and many others. Probably more than anyone, the students taught me the most in this work. I spent many hours picking the brains of Joel Kumlin and Nick Unick about inane little engineering questions. Of course Chelsea Dunning was always there to lighten the mood. I learned so much about myself mentoring her and I'm so proud to see her succeed.

I wouldn't have been even able to start this project without the BC Cancer Victoria center and all of the generous and knowledgeable physicists led by Wayne Beckham. Classes pointed me in the right direction and internship work there kept me afloat when I badly needed the support.

Last I'd thank my Dad. If anyone has been on my side from the beginning and always offered help it's him. Sometimes I might be reluctant, but he was always interested in what I was doing. He was always asking questions and offering help in any way he could give it. I couldn't have done this without him.

Dedicated to Crystal Brasseur

"We all are in the gutter,
but some of us are looking at the stars"
- Oscar Wilde

Chapter 1

Introduction

Uveal melanomas are a primary malignant cancer affecting the iris, ciliary body or choroid layer of the eye. Relatively rare, at a yearly rate of 4.3 per million in the United States[1], this site is the most common form of ocular cancer with the choroid consisting of 80% of cases[2]. The primary tumour, depending on size and location, can cause visual blurring or flashing. Metastatic spread is fatal and untreatable with a 92% death rate at 2 years[3]. Common sites of metastasis include liver, lung and bone occurring in 93%, 24% and 15% of metastatic cases respectively[3].

Before the widespread acceptance of radiation therapy, classic treatment for this disease has been removal of the eye (enucleation). Modern eye-sparing techniques such as charged particle therapy (CPT), eye-plaque brachytherapy and stereotactic radiosurgery can allow for acceptable disease control while potentially sparing patient vision. In Canada this disease is treated primarily with ^{125}I or ^{198}Au eye-plaque brachytherapy. In cases of large tumours, especially those that grow into the eye, dose coverage by plaque can be problematic due to falloff towards the centre of the eye. Increasing total activity to compensate for this effect also increases risk of adverse effects due to higher dose exposure to healthy tissue. Additionally, should a tumour grow close to the optic disk, brachytherapy can significantly increase risk of side effects including neuropathy and blindness[4].

In such cases of large tumour base size or proximity to the optic disk, charged particle therapy can offer an improved dose distribution with tighter falloff and better uniformity throughout the tumour volume. Comprising $\sim 90\%$ of all CPT treatments, proton therapy (PT) is the most common modality. Monoenergetic protons apply dose in a sharp peak at depth with a steep falloff and relatively high peak-to-entrance dose ratio when compared to standard radiotherapy techniques. This peak, known

as the Bragg Peak (BP), is too narrow in depth to uniformly treat a realistic tumour target. A monoenergtic proton beam must be degraded in steps to form a series of peaks whose cumulative dose distribution can cover a tumour volume. This method of 'painting' the BP into a spread out Bragg Peak (SOBP), known as beam modulation, allows positioning uniform dose at depth and simple, accurate profile shaping.

In Canada PT was offered at the TRIUMF cyclotron through a partnership with the British Columbia Cancer Agency (BCCA) and the University of British Columbia (UBC) department of opthamology, until February of 2019. To date 205 patients have been treated yielding 91% 5-year local control rate, 80% globe preservation and 82% metastasis free survival[5]. PT at TRIUMF has proven to be a highly successful modality, but has recently concluded due to economic pressures.

Monte Carlo (MC) simulations are a powerful tool used in medical physics to predict treatment dose in a patient and secondary dose for radiation safety purposes. A full MC model of the TRIUMF treatment room and dose delivery system (DDS) geometry would allow for simulating detailed proton dose to the eye as well as extraneous dose produced by the neutrons produced in the treatment apparatus itself. This information enables three subjects to be studied: the primary dose deposition profile and potential for improvement; the scale of neutron dose to patient anatomy and efficacy of shielding; and the viability of using positron emission tomography for *in vivo* dose validation.

1.1 Beam Modulation and 3D Printing

TRIUMF was an early adopter of proton therapy for eye treatments. Initial design and commissioning occurred in the 1990's[6, 7]. At the time the site was developed for a $70MeV$ beam - with all of the beam-modulating wheels optimized for this energy. Later it was found that a $74MeV$ beam was required for more flexible and efficient treatment plans. The wheels were developed with a custom TRIUMF FORTRAN code[8] and required precision machining on site out of Lucite (PMMA) discs. The dose distribution, resulting from the $74MeV$ beam on the $70MeV$ design wheels, presented a sloped target region which was not planned. This was due to the strong dependence of wheel optimization on proton beam spread and energy. Significant resources in design and machining work went into the production of the wheels and it was determined that the ones designed for $70MeV$ still met the required standards for treatment with the $74MeV$.

The methods developed for beam modulation optimization[8] used basic input data such as range, peak width and output factor to estimate dose deposition. The optimization was a simple matrix inversion on a small number of wheel steps due to computational constraints of the time. With a well-validated primary dose deposition profile from MC simulations, a much more detailed set of data could be used as input to a more complex optimization. Potentially improved wheel designs could be calculated with an increased number of steps - or even remove the requirement of steps altogether. However, production of such complex wheel geometries could prove slow and expensive since specialized knowledge in machining is required.

Three dimensional (3D) printing is a burgeoning technology which allows for the additive manufacturing of objects. Objects are iteratively constructed in layers from constituent components such as plastic, metal or living tissue. This process allows for complex geometries to be constructed in a single piece without specialized knowledge or expertise in machining. All that is required is a geometry file compatible with the printer. This technology has started to appear in radiotherapy applications including PT range compensation [9] and patient-specific phantom dosimetry [10]. However, few studies have been done in the suitability of different 3D printing methods or materials. The combination of new optimized wheel geometries and the ease of 3D printing for manufacture may make it simple to develop $74MeV$ optimized wheels. Additionally, a short window for design and manufacture window could allow custom wheels to be produced for each patient.

1.2 Secondary Neutron Dose

At the time of commissioning, measurements of secondary neutron dose were performed[11] to ensure patient safety during treatment. The methods of measurement involved neutron bubble dosimeters and bulky Boron Trifluoride (BF3) detectors. A rough picture of secondary dose was developed - enough to know that a patient would not receive dangerous levels of secondary dose. The DDS shielding was designed with neutron dose in mind. Shielding was placed around components thought to produce the largest neutron flux. However, a detailed analysis of neutron production in the DDS components or in patient anatomy was not possible due to detector limitations.

MC simulations have improved massively and computational constraints have been lifted since the original design of the DDS. The FLUKA particle transport MC software package[12] is now a standard tool used in radiation protection at TRIUMF

and by the Canadian Nuclear Safety Commission. This software allows for the detailed simulation of neutron production in the DDS geometry and energy deposition in simulated patient anatomy. However, simulation of neutron secondary doses requires a massive amount of compute power due to their relatively low production and interaction cross-sections. WestGrid and Compute Canada[13] offer educational institutions access to the scale of computational resources required to do such simulations. Implementation of a FLUKA MC simulation on at this scale would give a detailed understanding of the origin of secondary neutrons, as well as how those neutrons affect patient anatomy - potentially giving valuable information on DDS design and treatment planning.

1.3 Positron Emission Tomography Dosimetry

The sharp and precise nature of the proton Bragg peak demands a detailed understanding of both patient positioning and beam characteristics. Study of the deposition of dose, known as dosimetry, can be achieved via external measurements - utilizing waterboxes or film. However, measuring how a proton beam deposits dose in external media only infers how a patient will be affected. Measurement of dose in the actual anatomy of the patient, known as *in vivo* dosimetry, is difficult to accomplish in a non-invasive manner. Detectors placed in the patient could be harmful, especially near delicate anatomy like the eye, and would only offer single points of references for dose. There are several successful techniques for 3D dosimetry such as diode arrays[14] or polymer gels[15]; but, none provide *in vivo* dose verification. Proton therapy could allow for true *in vivo* dosimetry via the use of positron emitting isotopes or other secondary emissions[16, 17].

When treatment-energy protons, or heavy ions, traverse tissue they undergo nuclear interactions which generate positron emitting isotopes. Having half-lives between two and twenty minutes, the signal from decaying positrons may be reconstructed into a 3D volume. The reconstructed volume of produced isotopes may then be used to garner information on the dose deposited in tissue. This process, known as positron emission tomography (PET) for *in vivo* dosimetry, has been studied including systems with built-in PET detection[18, 19] and offline PET detection post-treatment[20, 21]. PET activation was measured on phantoms and in a post-treatment patient at TRIUMF using UBC hospital scanners[22, 23]. Signal was successfully measured. However, the study was inconclusive with regard to treatment

accuracy due to limited resolution and time required to transport the patient to the scanner.

While signal from the patient PET scan was low, phantoms were able to be transported via a pneumatic transport line to the scanner within minutes. Reconstruction and evaluation of dose to a plastic phantom is feasible at the facility. To date, only plastic cylinders and one patient have been irradiated to test for signal. 3D printing would allow the production of an anatomically-accurate eye phantom. A tumour volume could be defined, a beam planned, and the phantom positioned in a similar way to a patient's gaze angle. This is a more realistic phantom setup, allowing for studying eye positioning and resulting PET signal. Additionally, a well developed MC simulation of isotope production would greatly aid in the evaluation of the PET scan signal.

1.4 Thesis Scope

This thesis project has four main parts. The first, and most fundamental to the work, is the simulation and validation of the TRIUMF DDS. Chapters 3-4 involve the definition of the DDS geometry, measurement of primary proton dose and validation of simulated data to measurement in water. The second, covered in chapter 4-5, was the measurement of secondary neutron dose and simulation in an anatomical phantom. The third study, the exploration of 3D printed materials and design of stepless beam modulator wheels, are covered in two published works presented in chapters 6-7. Last, covered in chapter 8, an anatomical eye PET phantom was tested for feasibility.

Chapter 2

Background

2.1 Physics of Radiotherapy

Within three years of its discovery in 1895, ionizing radiation was being used therapeutically in the treatment of cancer[24]. Early applications involved the placement of radioactive sources in close proximity to treatment sites (Brachytherapy). By the early 1930's, external beams in the kilovoltage (kV) to low megavoltage (MV) range were seeing success as a minimally invasive treatment modality. Through the ensuing years, a great many more modalities have been developed involving the external application of photons, neutrons, electrons, protons or heavy ions. All of these rely on the principle of differential cell-kill (killing of cancer cells while sparing healthy tissue) for their therapeutic benefits.

Upon traversing a medium, ionizing radiation may undergo interactions that deposit energy. The type of interaction and magnitude/profile of energy deposition depends on both the type of radiation and qualities of the medium. In tissue, cells in close proximity to an ionization event may be directly damaged by the incoming particle, or indirectly damaged via chemical interactions with reactive oxygen species formed as a result of the ionization. Should a cell be unable to repair damage to its deoxyribonucleic acid (DNA), its fate will be that of immediate programmed death (apoptosis), disorderly destruction over the course of subsequent cell divisions (mitotic death), or reproductive deactivation (senescence). Cells which do not die, but suffer DNA damage, can potentially become cancerous[25].

The probability of tissue cell death on the larger scale is dependent on many factors such as: the total amount of energy deposited; the nature of the ionizing

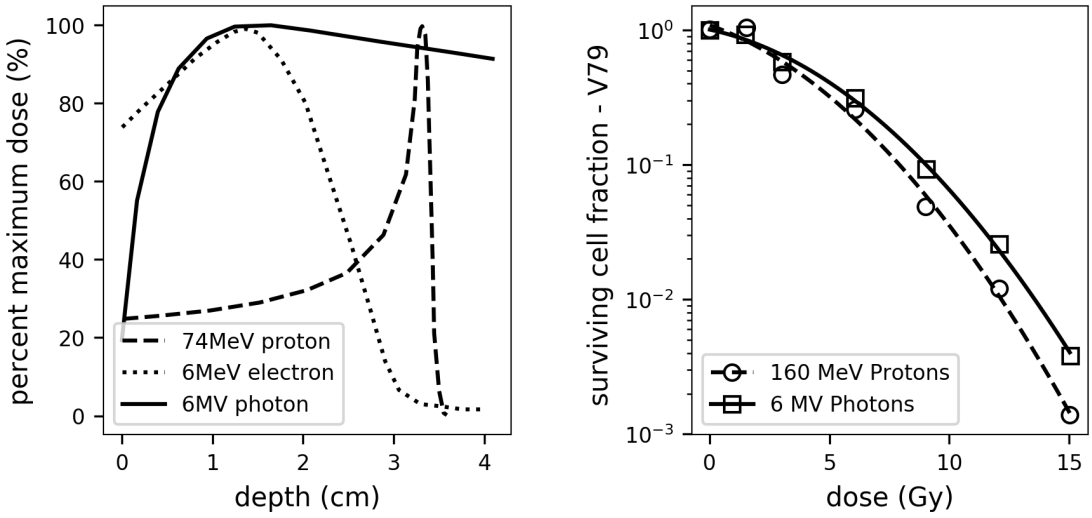

Figure 2.1: (left) Depth vs dose in water distributions, scaled to maximum dose, for $74MeV$ protons, $6MeV$ electrons and $6MV$ photons. (right) *In vitro* cell survival as a function of absorbed dose due to 160MeV protons and 6MV photons for V79 chinese hamster cell line (adapted from [26]).

particle; radio-resistive properties of the cell; or timing of the therapy. The most important factor in cell-kill is intuitively the amount of energy deposited - known as the absorbed dose which is measured in joules per kilogram or Gray ($1Gy = 1J/kg$). For the sake of brevity, in this document the term 'dose' will refer to absorbed dose unless otherwise qualified.

Figure 2.1(left) shows the dose deposition profile (known as a depth-dose curve) for three types of treatment beam - $6MeV$ electrons, $6MV$[1] and $74MeV$ protons. The energy and type of particle results in a drastically different depth profile. Electrons peak shallow ($1.45cm$), drop off quickly, and have high surface dose. Photons peak shallow ($1.5cm$), drop off slowly and have lower surface dose. Protons have a sharp peak and drop-off at $3.5cm$ depth with low surface dose. Thus to achieve equivalent doses to the same target, the delivery of these three modalities are necessarily very different.

For the same delivered dose, Figure 2.1(right) shows the fraction of surviving cells (V79 hamster cell line) after exposure to two kinds of ionizing radiation - $6MV$ photons generated using a clinical linear accelerator and $160MeV$ generated using

[1]the quantity $6MV$ refers to photons generated in a linear accelerator with electrons of peak energy $6MeV$

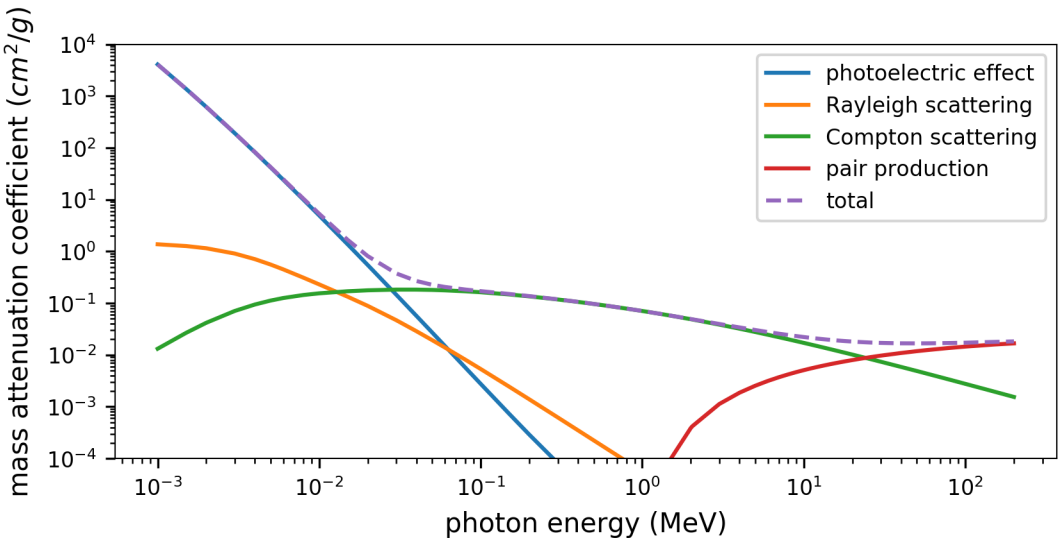

Figure 2.2: Photon mass attenuation broken down by interaction in water. Taken from NIST XCOM photon cross section database[27]

a clinical cyclotron. Here, for most levels of absorbed dose, protons are measurably more effective at killing cells *in vitro* than the photons[26]. This ratio of effectiveness is known as relative biological effectiveness (RBE):

$$RBE_R = \frac{D_X}{D_R} = \frac{\text{dose of reference radiation X for a biological endpoint}}{\text{dose of radiation type R for a biological endpoint}} \tag{2.1}$$

This quantity is always defined for a specific biological endpoint (cell kill, tumour control, negative tissue effects, etc) and for a reference radiation (often Co60 photons or $6MV$ photons). The efficacy of cell-kill, and hence tumour control, depends strongly on the type of radiation. Of particular importance are the physical processes which result in energy deposition which are covered in the following sections.

2.1.1 Photon Interactions

By far the most common modality in cancer treatment, therapeutic energy photons (typically 6-20MV) can be produced by a relatively inexpensive and compact linear accelerator. The photon depth-dose of $6MV$ distribution of Figure 2.1(left) has a steep rise to a maximum at $1.5cm$ depth, followed by an exponential falloff characterized by the composition of the medium being traversed. Photons remaining in the

beam at depth x which have not undergone any interaction can be expressed as[28]

$$N(x) = N_0 \cdot e^{-\mu x} \cdot B(x, E, A, L) \tag{2.2}$$

Where: N_0 is the initial number of photons in the beam; μ is defined as the linear attenuation coefficient[2]; B is an experimentally measured buildup factor depending on depth (x), particle energy (E), beam area (A) and off-axis distance (L). This exponential behavior is due to the probabilistic nature of photon interactions with the medium. Photons may pass completely through a medium - imparting no energy at all. Should they interact, one of four processes can occur: the photoelectric process, Compton incoherent scattering, pair production and Rayleigh coherent scattering. Figure 2.2 shows the individual mass attenuation[3] for each process in water[27].

- *Photoelectric process* - interaction of incoming photon with a bound electron. The photon is absorbed and the ejected electron has an energy of the incoming photon, less the atomic binding energy. This process is dominant below $\sim 30keV$.

- *Compton Scattering* - scattering of incoming photons off a bound electron. The photon scatters, losing energy to the binding energy of the atom plus the outgoing kinetic energy of the electron. This is the most important process in the therapeutic energy range for photons - dominating interactions from $\sim 30keV$-$25MeV$.

- *Pair Production* - production of a electron/positron pair in the presence of atomic nucleus. The photon converts into a pair above $1.02MeV$ having total kinetic energy of the original photon minus twice the electron mass. These interactions dominate over $\sim 25MeV$.

- *Rayleigh Scattering* - coherent scattering of incoming photon without energy loss. No energy is imparted to the medium. Mainly occurring at low energies and dominated by the photoelectric process.

The first three of these processes produce energetic electrons which go on to impart energy to the medium. The mechanism by which they deposit energy is discussed in the next section.

[2] fraction of photons that interact per unit thickness of attenuator

[3] 'mass attenuation' is defined as attenuation divided by medium density

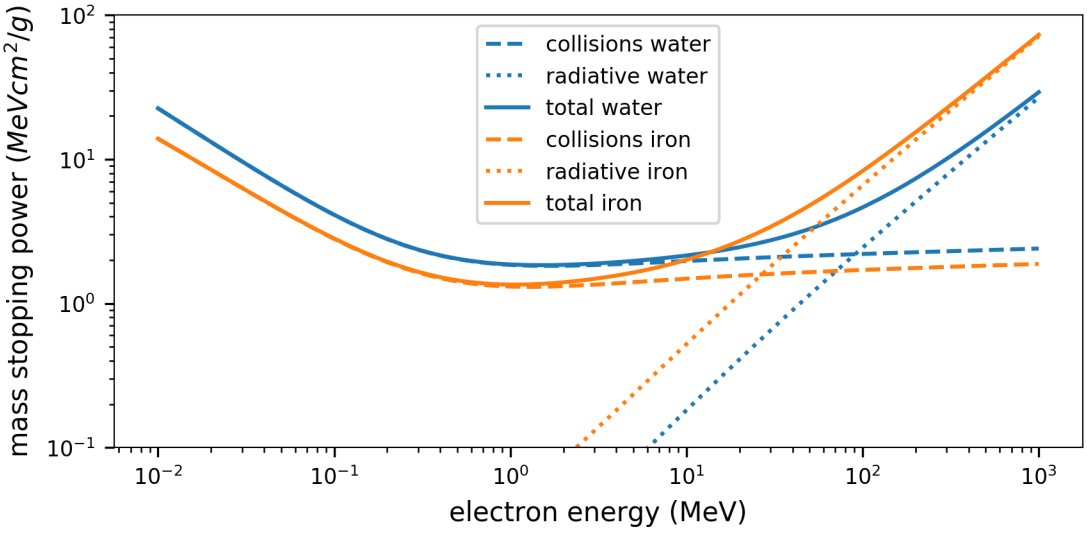

Figure 2.3: Electron mass stopping powers for water and iron broken down by radiative and collisional components. Taken from NIST ESTAR database[29]

2.1.2 Electron Interactions

As opposed to photons, charged electrons will undergo many interactions in a medium. On average, a small fraction of the electron's kinetic energy will be imparted to almost every atomic nuclei in the vicinity of the electron's trajectory [30]. The result is reasonably approximated by a continuous loss of energy in the medium[31], with the electrons coming to a stop at a range dependent on its initial energy. The $6MV$ electron depth-dose of Figure 2.1(left) shows electron dose peaking at $\sim 1.5cm$ depth and dropping to zero at a $\sim 3cm$ depth within the water. This loss of energy is expressed as mass stopping power S/ρ:

$$\frac{S}{\rho} = \frac{1}{\rho}(S_{col} + S_{rad}) \equiv -\frac{1}{\rho}\left\langle \frac{dE}{dx} \right\rangle \tag{2.3}$$

Where ρ is the local density of the medium and $< dE/dx >$ is the expectation value of the rate at which electrons loses energy. This quantity may be expressed as the sum of contributions from collisional (S_{col}) and radiative (S_{rad}) processes:

- *Collisional interactions* - Coulomb interactions resulting in a portion of the electron's energy being imparted to atoms in the medium (soft collisions at large distance), in the production of more high energy electrons known as delta rays (hard collisions at short distances). Energy may be also be carried away

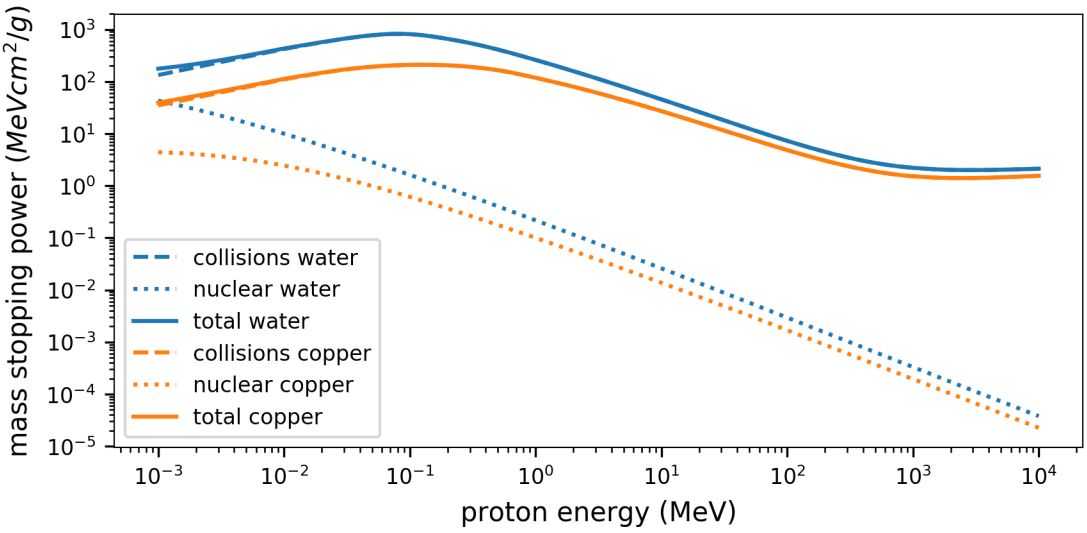

Figure 2.4: Proton mass attenuation broken down by interaction in water and copper. Taken from NIST PSTAR proton cross section database[29].

in the form of transition photons resulting from inner vacated atomic orbitals.

- *Inelastic radiative interactions* - inelastic Coulomb process with the atomic nucleus. The electron is deflected and a significant portion of its energy converted to a Bremsstrahlung photon[4] . This photon may go on to produce more ionizations or carry energy away from local area.

Figure 2.3 shows the electron mass stopping power including radiative and collisional contributions. Collisions are important at low energies whereas radiative dominate at higher energies. Bremsstrahlung production scales with Z^2 and is insignificant in tissue below $10MeV$.

2.1.3 Protons Interactions

Similar to electrons, protons deposit primarily energy via collisions/ionizations of atomic electrons in the medium[32, 33]. With the same magnitude of charge and a mass ∼2000 times larger than the electron, protons experience substantially less angular deflection when traversing a medium. In addition, due to the $1/m^2$ scaling for a given velocity, in the production of Bremsstrahlung photons[30], proton radiative

[4]known as 'breaking radiation' - Bremsstrahlung photons are produced due to deceleration of charged particles

losses at therapeutic energies are negligible. However, protons may deposit energy via inelastic collisions with an atomic nuclei via strong interactions. Similar to equation 2.4, Proton stopping power is expressed as a sum of two components:

$$\frac{S}{\rho} = \frac{1}{\rho}(S_{col} + S_{nuc}) \tag{2.4}$$

Where ρ is the local density of the medium, S_{col} and S_{nuc} are contributions from collisional and nuclear processes respectively.

- *Collisional interactions* - Coulomb interactions resulting in a portion of the proton's energy being imparted to electrons or atoms in the medium. This may result in the production of δ rays and transition photons which carry energy away from the local area.

- *Nuclear interactions* - separated into three categories defined by the International Commission on Radiation Units (ICRU) Report 62[34]

  - *elastic* - scattering of the proton off an atomic nucleus with kinetic energy conserved (eg. scattering of a proton off ^{12}C nucleus: ^{12}C(p,p)^{12}C)
  - *non-elastic* - nuclear interactions where kinetic energy is not conserved (eg. ejection of a neutron from ^{12}C : ^{12}C(p,pn)^{11}C)
  - *inelastic* - non-elastic collisions in which the kinetic energy is not conserved, but the resulting bombarded nucleus has the same constituents (eg. excitation of ^{12}C neutron by proton: ^{12}C(p,p)^{12}C*)

All of these processes can impart energy to the medium. Figure 2.4 shows mass stopping powers for proton interactions in water and copper. Nuclear interactions are rare, occurring at the 2-3% level, but much more catastrophic - resulting in significant energy loss[32]. Proton interactions can produce secondary gammas, electrons, neutrons and nuclear fragments - thus to simulate proton dose in a medium, all of these particles must be considered.

2.1.4 Nuclear Interactions and Activation

Neutrons

Due to their lack of charge, neutrons traverse media with the same characteristic exponential falloff as photons. They only interact with nuclei in the medium via the

strong interaction in one of five ways: elastic, non-elastic, inelastic, neutron capture or spallation[35]. The former three are describe in §2.1.3. Neutron capture involves the absorbtion of an neutron by a nucleus (eg: $^1\mathrm{H}(n,\gamma)^2\mathrm{H}$). Spallation involves the breakup of C, N and O in tissue and occurs at energies higher than $20MeV$. By far the most common processes in tissue are elastic ($> 2MeV$), non-elastic ($< 5MeV$) and capture. Neutron interaction cross sections typically increase with hydrogen density and neutron energy. In general, dose deposited by neutrons is a complicated function of the neutron energy spectrum which requires the concept of equivalent dose which is discussed later in § 2.2.1.

β^+ Isotope Activation by Proton Bombardment

Protons traversing a medium have a probability to undergo inelastic collisions producing unstable nuclei. Neutron deficient nuclei produced in this way may undergo β^+ decay:

$$ {}^{X}_{Y}A \rightarrow {}^{X}_{Y-1}A + \beta^+ + \nu_e \tag{2.5} $$

The decay of such a nucleus occurs with a half-life τ and produces a positron (β^+). The positron goes on the annihilate in the medium yielding two characteristic γ-rays. These may deposit additional energy in the medium or exit the volume. Common β^+ emitting isotopes produced in tissue from proton bombardment are shown in Table 2.1[36, 37]. At up to a half-life of 20 minutes, escaping γ-rays can be used to reconstruct the distribution of isotopes produced in tissue. This process is known as positron emission tomography (PET) and is a common modality in diagnostic imaging[38].

2.2 Proton Therapy

Protons were first considered for therapeutic use in 1946 by Wilson[39]. At that time, it was possible to generate $125MeV$ proton beams which could penetrate $12cm$ in tissue. Several advantages over photons were noted as shown in Figure2.1 (left). Protons have a relatively low entrance dose, sharp dose-peak at depth (selectable by beam energy) and finite range with little exit dose In addition, protons are easily collimated compared to photons (due to their electric charge) and scatter very little in tissue (due to their mass). The main disadvantages to this modality included cost[40]

Process	Production Threshold (MeV)	Half-life (m)
$^{16}O(p,pn)^{15}O$	16.79	2.037
$^{16}O(p,\alpha)^{13}N$	5.66	9.965
$^{14}N(p,pn)^{13}N$	11.44	9.965
$^{12}C(p,pn)^{11}C$	20.61	20.390
$^{14}N(p,\alpha)^{11}C$	3.22	20.390
$^{16}O(p,pn)^{11}C$	59.64	20.390

Table 2.1: Table of common β emitting isotopes produced in tissue during proton therapy irradiation.[37, 36]

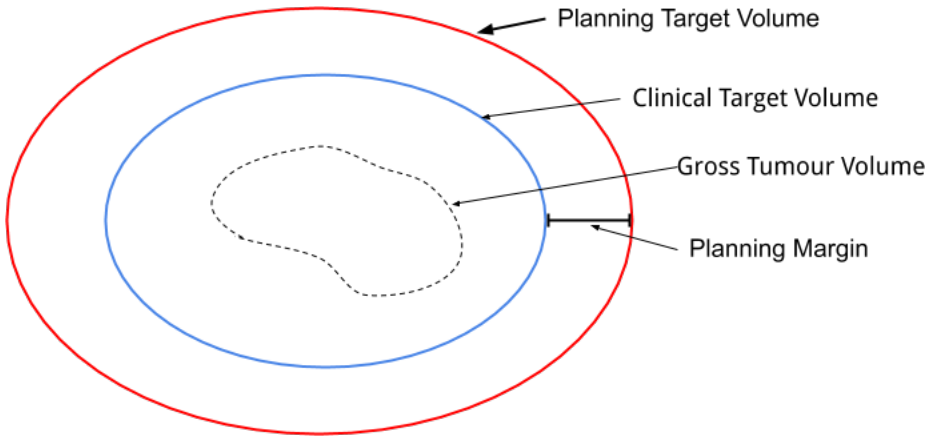

Figure 2.5: Diagram depicting volumes in radiotherapy target delineation.

and less clinical data on the efficacy and biological effect of protons as compared to photons.

Early implementation of proton therapy were in laboratory-like environments treating intra-cranial tumours[41], prostate[42], and ocular melanomas[43]. Today, proton therapy is used for a multitude of tumour sites, showing specific benefit where high dose gradients and low secondary dose is desirable[44]. Two such cases in particular benefit strongly from the use of proton therapy - pediatric central nervous system (CNS) sites to avoid secondary carcinogenesis [45] and ocular tumours which benefit greatly from highly localized delivery to avoid damage to the eye[46].

In this section the basics of radiotherapy, proton beam generation, dose distributions and treatment of ocular melanomas are discussed.

2.2.1 Basic Definitions in Radiotherapy

The primary goal of external beam radiotherapy is to control the growth of cancerous tumours. While ionizing radiation is effective in killing cancer cells, it also poses a risk to healthy tissues. Complications from healthy tissue exposure can range from skin irritation, to tissue necrosis to long-term secondary carcinogenesis[25]. Ideally, a uniform-dose of radiation is applied to a well-delineated tumour volume with minimal extraneous dose to healthy tissue. The quantity of dose prescribed, target to be irradiated, and dose limits to organs at risk (OAR) and are determined by the clinical knowledge of a physician. Some basic definitions and terms are required to properly define the problem.

Target Volumes

The volume to be irradiated is known as the planning target volume (PTV). This encompasses the identified tumour mass - gross tumour volume (GTV); the surrounding tissue requiring treatment - clinical target volume (CTV); and a surrounding margin allowing for uncertainty in patient positioning, imaging and mechanical limitations. Figure 2.5 shows a diagram of these three volumes. These definitions are an international standard as reported by the International Commission on Radiological Protection (ICRP)[47].

Proton Biological Dose

There is a vast amount of experience and study into dose required for tumour control in photon radiotherapy[48]. Treatments are highly site dependent but may typically range from 40-60Gy administered in 20-30 fractions. This knowledge however does not directly translate to proton therapy. As in Figure 2.1(right), protons are more effective in cell-kill than photons. From cell-kill experiments, this enhancement on average ranges from 1.05 to 1.15 [49, 50]. While clinical outcomes are not necessarily well-informed by cell-kill studies, they are used to inform clinical practice. Thus clinically the proton RBE is generally accepted as a value of $RBE = 1.1$; however, proton RBE may reach as high as 2.05 at the end of the Bragg peak [51]. This is due to the linear energy transfer (LET) or restricted stopping power defined as:

$$LET_{\Delta} = \frac{1}{\rho}\left(\frac{dE}{dl}\right) = -\frac{1}{\rho}\left(\frac{dE}{dx}\right)\Bigg|_{E=0}^{E=\Delta} \tag{2.6}$$

Where ρ and dE/dx are as in stopping power (equation 2.4) and Δ is a cutoff energy for energetic δ-rays. LET is the local energy deposited in the medium by a particle - normally expressed in $keV/\mu m$. For protons, dE/dx increases as they slow down (due to increased time for Coulomb interactions). Thus LET increases as the proton reaches the end of its track - increasing its RBE. Studies are ongoing into the implementation of this effect in treatment planning[52]. That is, uniformity of 'biological dose' is optimized[53]:

$$D_{Biological} = RBE \cdot D_{absorbed} \tag{2.7}$$

This quantity is used as an analog to photon dose, such that clinical knowledge can be translated to the newer modality of proton therapy.

Equivalent Dose

This notion of endpoint-based dose scaling can be extended to other particles and modalities. Equivalent dose measured in Sieverts (Sv) is a commonly used metric defined as:

$$H[Sv] = w_R \cdot D[Gy] \tag{2.8}$$

Where D is the average absorbed dose in an organ or tissue and w_R is a weighting

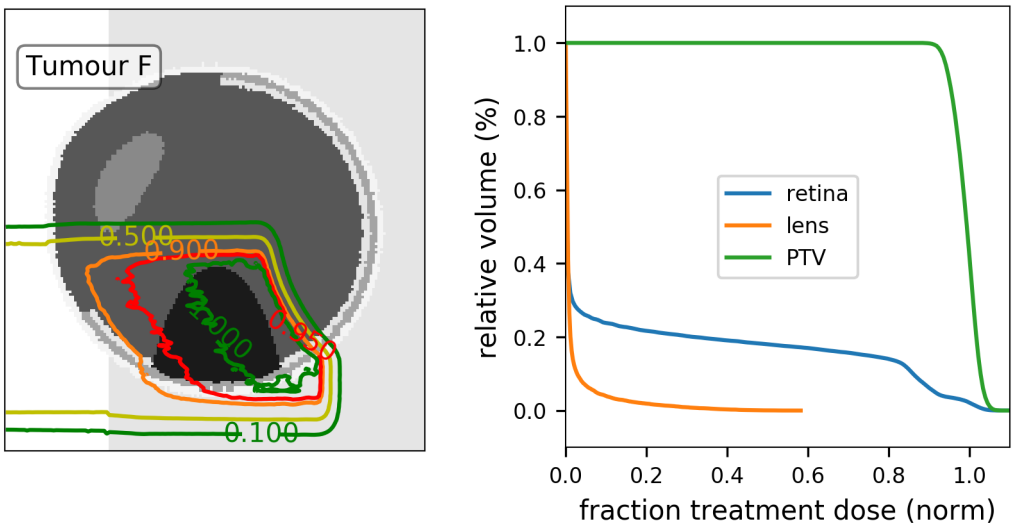

Figure 2.6: (left) Sample isodose curves with tumour target shown in black. (right) Sample cumulative dose-volume histogram showing dose to PTV, retina and lens for isodose curves on (left).

factor dependent on the type and energy of radiation[54]. For photons and electrons $w_R = 1$; for protons $w_R = 2$; for neutrons w_R is energy dependent, ranging from 5-20. Endpoint probability, such as carcinogenisis or acute radiation effects, are then assessed against this metric.

Isodose Contours and Dose Volume Histograms

For a given configuration of patient, setup of external beam delivery and dose (known as a treatment plan) evaluation of dose uniformity and OAR avoidance is critical. Two tools used in evaluation are shown in Figure 2.6 - isodose curves (left) and cumulative dose volume histograms (DVH) (right). Isodose curves are shown overlaid on patient anatomy depicting contours of dose. These aid in understanding the geometric distribution of dose. Here the 100% line represents 100% of the prescribed treatment dose. Cumulative DVH quantify the fraction of a specified volume receiving at least a certain fraction of treatment dose. In the the DVH of Figure 2.6(right) 91% of the target volume is receives at least 95% of the prescription dose, 4% of the lens receives 10% and 23% of the retina receives 10%. These metrics are used in treatment planning optimization.

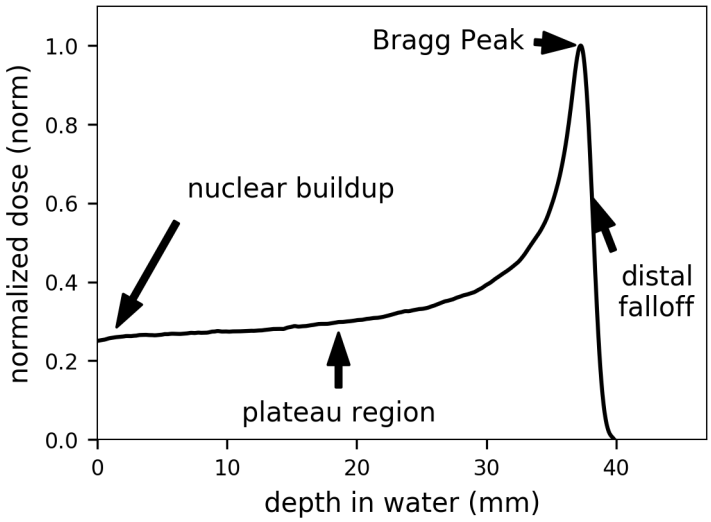

Figure 2.7: Proton depth-dose distribution in water for a $74MeV$ beam.

2.2.2 The Bragg Peak

The principle advantage to proton therapy is in the depth-dose distribution. Shown in Figure 2.7, a mono-energetic beam of protons has a depth-dose distribution which is distinct from that of photons or electrons. A mono-energetic proton beam produces a peak at depth, known as the Bragg Peak (BP), followed by a rapid distal falloff. The area of dose increase from entrance to the peak is known as the 'plateau region'. At the entrance, there is a small dip in dose deposition which deviates from the expected stopping power. Protons entering the waterbox produced far fewer secondary particles, thus there is no dose equilibrium until a characteristic depth is met. Once the beam has traversed a few millimeters, knock-on protons reach equilibrium. This part of the distribution is known as the 'nuclear buildup' region.

The overall shape of the distribution is owing the proton stopping power (equation 2.4). The majority of energy is deposited by a myriad of collisions, each deflecting the proton's trajectory. This process is known as multiple Coulomb scattering (MCS). MCS increases with the Z of the medium and decreases with proton velocity. The sharpness of this peak is defined by the sharpness of the proton energy distribution and amount of MCS occurring in the medium[32].

The range (R_0) of the BP is defined as the depth at which half of the protons that undergo only EM collisions have stopped. This can be directly measured using a Faraday cup, but is also well approximated by the distal 80% dropoff point in water

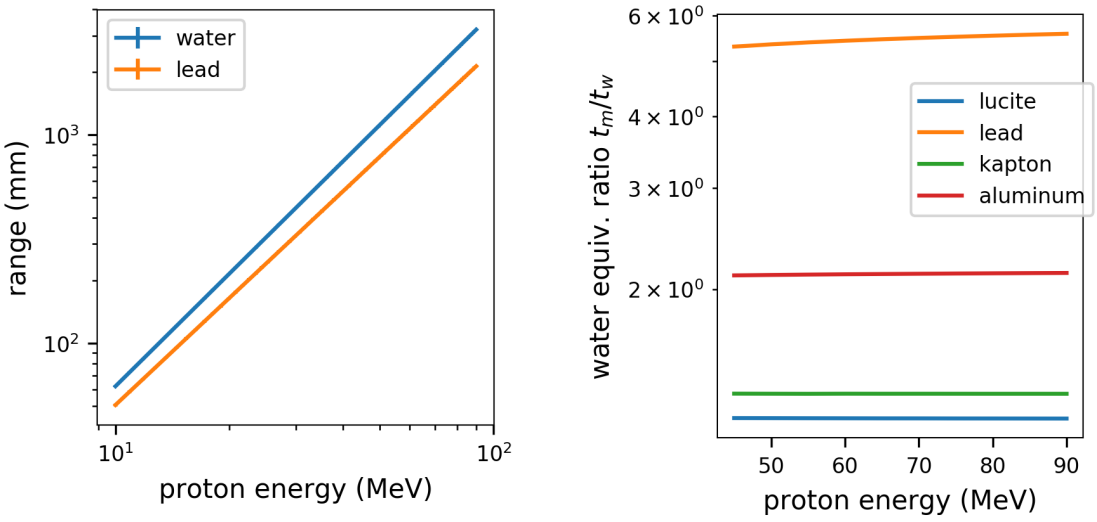

Figure 2.8: (left) Proton range in water and lead as a function of energy. (right) Water equivalent ratio for various materials used in proton therapy.

[55]. Figure 4.7(left) shows R_0 of protons in water and lead over a therapeutic range of proton energies. Notable is the straight line in a log-log plot - indicating a power law relationship[56]. This quantity is valuable in proton therapy planning to determine beam energy required to reach the target. Note that this quantity is determined largely experimentally. The stopping power could be integrated to determine this value; but, multiple coulomb scattering leads to a reduction in range known as 'range straggling'. Integrating the stopping power yields the mean free path of the proton, not range as defined by R_0.

Also useful in proton therapy is the notion of water equivalent thickness of a material - the thickness of a material m required to produce an equivalent range reduction in water[57]:

$$t_w = t_m \frac{\rho_m}{\rho_w} \frac{\bar{S_m}}{\bar{S_w}} \tag{2.9}$$

Where ρ_s is the material density, rho_w is water density and $\bar{S}$ is the mean proton mass stopping power for each material. This value is energy dependent and also determined experimentally either by direct measurement or by measuring stopping power. Figure 4.7(right) shows calculated[58] water equivalent thicknesses of materials in the TRIUMF beamline for the pertinent energy range.

While the addition of beam degrading material can widen the BP, and change its range, a BP resulting from a mono-energetic beam is not appropriate for treatment. For example, the $74MeV$ BP of Figure 2.7 has a 90%-90% peak width of $\sim 1mm$. If a tumour was to be treated with this beam, only $1mm$ in depth of the volume would receive at leats 90% of peak dose. To be therapeutically useful, a uniform dose distribution over the target volume is required. Photon treatments achieve this by application of multiple beams. In proton therapy this is possible with beam modulation (beam blocking or degradation) that varies in time.

2.2.3 Beam Modulation

A uniform depth-dose distribution may be achieved with a single proton beam by adding together BP's corresponding to an optimized combination of proton energies. This technique is known as 'beam modulation' and is commonly implemented by varying the incoming proton beam energy in time. Figure 2.9 (left) shows a series of BP's - each colour having a different beam energy determined by a degrader thickness. The sum of these peaks produces the blue line which should ideally be uniform

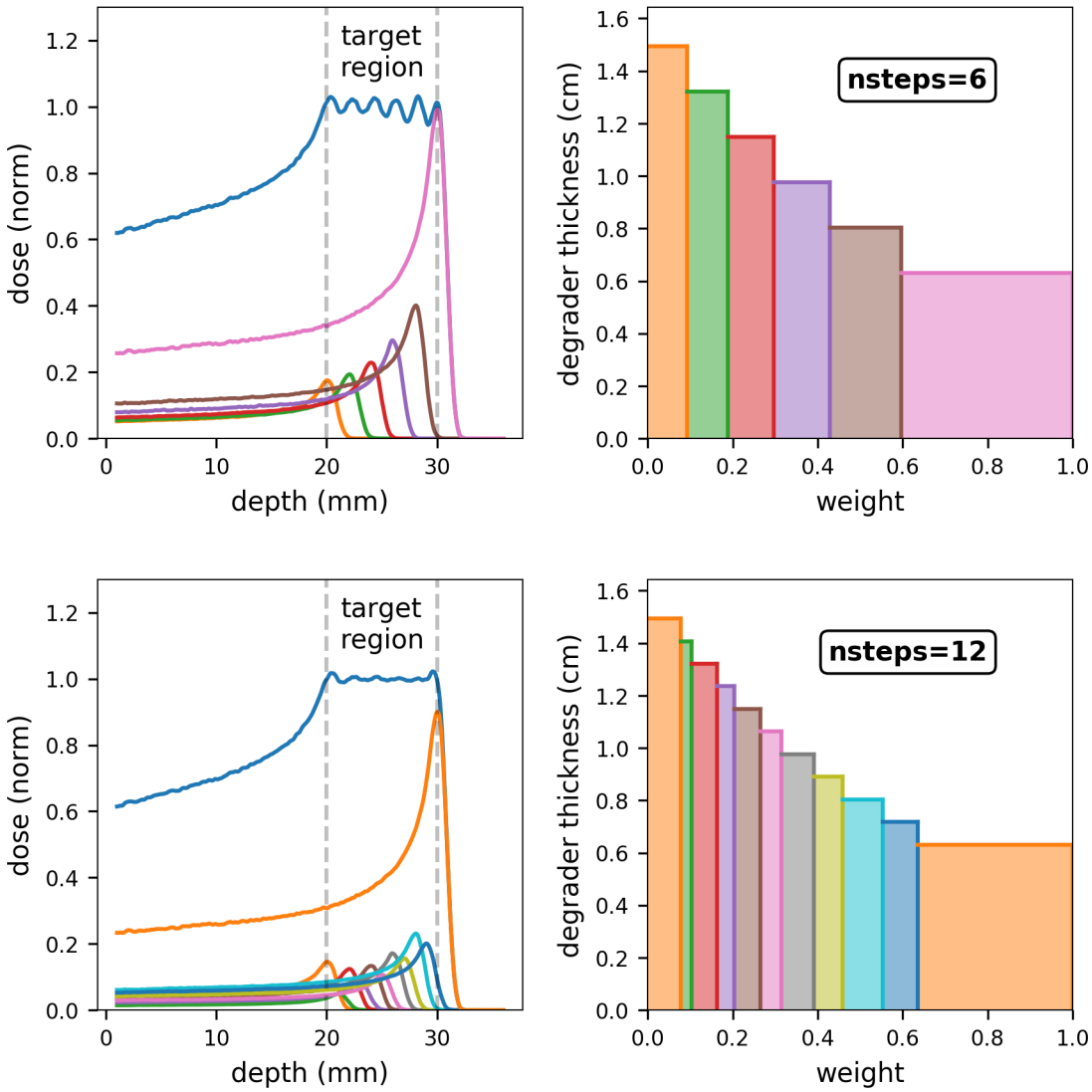

Figure 2.9: (left) Simulated SOBP distributions in water for an optimized 6-step (top) and 12-step (bottom) weighting. (right) Degrader thickness weightings for 6 and 12 step weightings.

throughout the defined target region (20-30mm depth in this case). Figure 2.9 (right) shows the 8 step thicknesses and weights which produce this distribution. Addition of more steps as in the lower portion of the figure shows an improved uniformity in the resultant dose distribution by the addition of 4 steps. The details of optimization of thickness and weights, as well as the details of optimization metrics, are discussed in detail in Chapter 7.

2.2.4 Proton Beam Generation

To be of use therapeutically, protons must be accelerated to 70-250MeV such that they penetrate tissue to a tumour site. Due to their mass, it is much more costly to accelerate protons to these energies than electrons. However, also due to their mass, protons do not radiate significant Bremsstrahlung radiation (§2.1.3), so their direction may be changed during acceleration without severe loss of energy. This allows for the use of cyclotrons in producing energetic protons for treatment purposes.

Cyclotrons, invented by Ernest O. Lawrence in 1930, are circular particle accelerators which makes use of a perpendicular magnetic field to steer protons in a spiral trajectory as they gain energy. Energy is imparted to the protons using an accelerating gap, across which an alternating current is applied. A cyclotron consists of four key components:

- *proton source* - at the center of the cyclotron. Hydrogen gas is ionized and protons are extracted for acceleration.
- *magnetic confinement* - electromagnets (or superconducting magnets) produced a perpendicular magnetic field which steers protons in a circular trajectory.
- *radio frequency system* - applies alternating current across the dee gaps to accelerate protons.
- *extraction system* - system to kick protons out of the magnetic field for extraction. This can be done via a kicker, or, if negative hydrogen ions are accelerated, via an extraction foils as is being done at TRIUMF.
- *vacuum system* - system to provide vacuum inside the cyclotron structure to minimizes scattering ans beam loss.

Modern superconducting medical accelerators the size of a car can accelerate protons to $\sim 250 MeV$ at currents suitable for efficient patient treatment. Proton energy on extraction is fixed, but a beam degrading system can be used for fast energy selection. More detail on the TRIUMF cyclotron is given in §2.3.1.

2.2.5 Proton Dosimetry

Measurement of dose output in treatment is crucial to ensure the application of the prescribed dose. Since direct measurement of dose deposition in a patient is not possible, the next best practice is to calibrate the output of a machine to a known standard and model dose in a patient with these data. The practice of measuring dose is known as dosimetry and is separated into two categories - absolute and relative.

Proton Absolute Dosimetry

Absolute dosimetry involves directly measuring ionization or absorbed energy under standard conditions. This is not practical in the clinic as it requires specialized instruments and careful attention to beam conditions. For protons, two standard methods are employed:

Calorimetry - The only direct method of measuring dose involving the precise measurement of temperature increase, ΔT, in an irradiated medium. Dose deposited in a known quantity of a medium with heat capacity c is:

$$D = c \cdot \Delta T \cdot \frac{1}{1-h} \cdot \Pi k_i \tag{2.10}$$

Where h is the physicochemical heat defect (fractional energy lost to physical change of medium) and k_i are corrections for heat transport (determined experimentally), field non-uniformity, and non-medium equivalent materials. This process requires an extreme amount of precision in temperature measurement. It is commonly performed at national level laboratories such as Canada's NRC.

Faraday Cup - This method relies on the collection of protons directly in air. Charge is collected and recorded via a current measurement. Dose in water at depth x can be calculated as:

$$D_{water}(x) = \phi \cdot \frac{S_w(z)}{\rho_w} \cdot \Pi k_i \tag{2.11}$$

Where S_w is the stopping power of water, ρ_w the density of water, k_i a set of correction factors and ϕ the particle fluence defined as:

$$\phi = \frac{dN}{dA} \tag{2.12}$$

The number of protons, during a given exposure or treatment, crossing an infinitesimal element of area dA normal to x. The Faraday cup records the number of protons from which fluence and dose at a depth in water can be calculated.

Proton Relative Dosimetry

Relative dosimetry used for the majority of clinical purposes. Commonly, each clinic will have a set of reference measurement devices which are calibrated at a larger laboratory capable of doing absolute dose measurements. Treatment machine outputs, often measured as monitor units (MU) by a built-in ion chamber, are calibrated to these reference devices. Measurement devices for clinical dosimetry include ion chambers (measuring ionization of air), diodes (measuring ionization in solid medium like silicon) and radiographic film (chemical changes due to ionization). This work is concerned only with relative dosimetry and specifics of equipment used are described in the methods section (§4.1).

2.2.6 Treatment of Ocular Melanomas

Ocular melanomas, specifically of the choroid and ciliary body, are the most common malignant tumours of the eye occurring at a rate of 6 per million in the US [59]. Most common metastases occur in the liver and lung[60] with poor prognosis for survival. The most common treatment is eye-plaque brachytherapy - with larger tumours or those located close to the optic nerve or macula prescribed external beam therapy. Major OAR's are the lens, optic nerve and macula.

Typically appearing as a 'mushroom' shaped masses in the eye, the disease is characterized by two metrics - apical height and basal width. Figure 2.10 shows the anatomy of the eye with a tumour mass overlaid. The basal width is the maximum width of the mass on the globe of the eye. The apical height is the depth to which the mass protrudes into the eye. The tumour is categorized into four tiers ranging

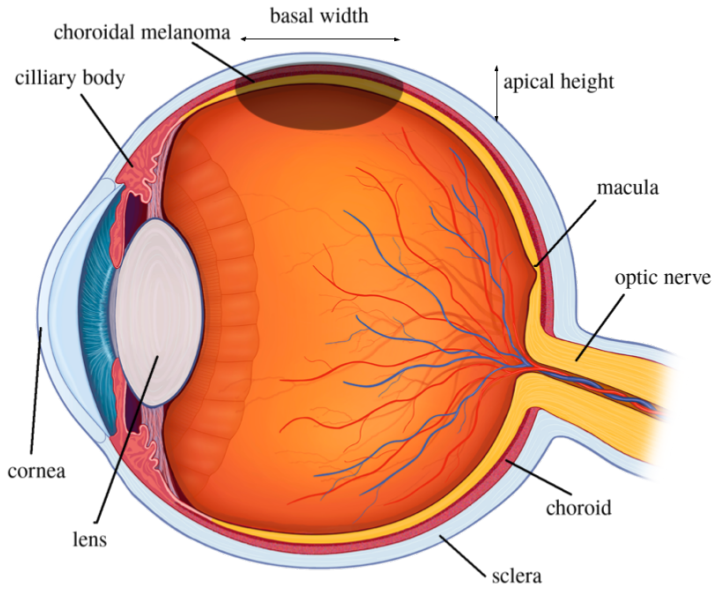

Figure 2.10: Diagram of eye anatomy showing choroidal melanoma and OARs macula, lens, optic nerve.

from <12-18+mm basal width and 3-15mm apical height.

In Canada, patients prescribed proton therapy for treatment of ocular melanomas used to be treated at the TRIUMF proton therapy facility. Treatment was implemented as a single field uniform dose (SFUD). One mono-energetic beam of $74MeV$ is modulated and range shifted to treat a tumour which is localized by radiographic imaging of targeting clips surgically inserted into the eye close to the tumour. Details of the facility and delivery components are covered in detail in the following sections and in Chapter 3.

2.3 The TRIUMF Proton Therapy Facility

2.3.1 *TRIUMF Accelerator*

The TRIUMF facility on the southern end of the UBC campus is home to the world's largest cyclotron. At 18 meters in diameter, it is capable of accelerating H^- ions to a maximum energy of 520 MeV at a peak current of $220\mu A$. Designed as a multi-user system, it is capable of simultaneous beam extraction at various energies and currents to its three beamlines as shown in figure 2.11.

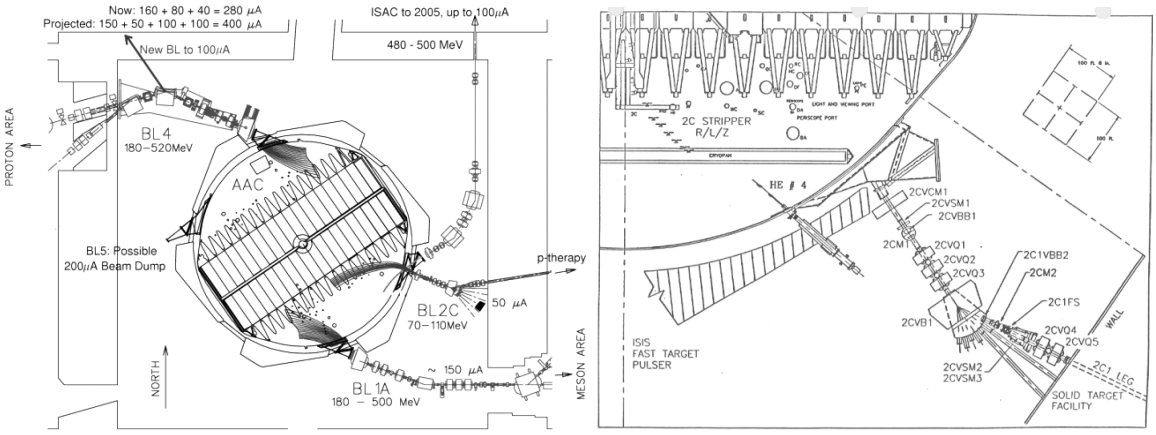

Figure 2.11: (left) Schematic of the TRIUMF cyclotron. (right) Schematic of beamline 2C-1.[61]

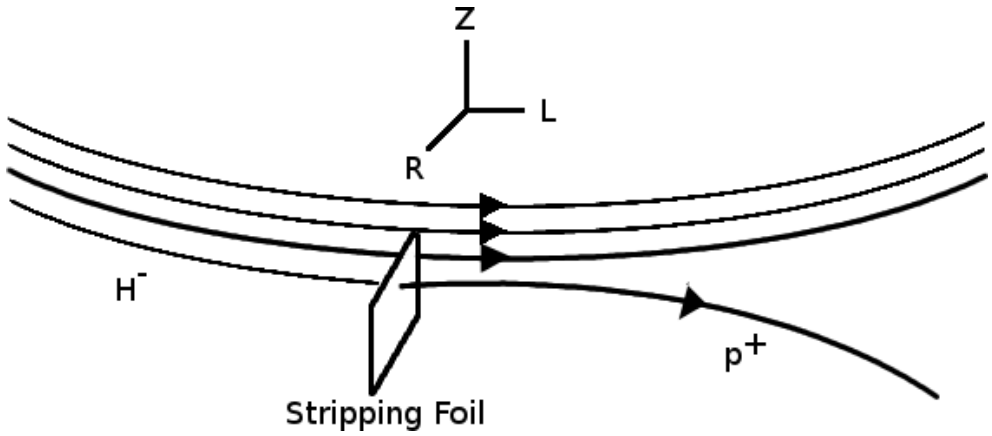

Figure 2.12: Cartoon depicting stripping of H^- ions in a cyclotron. Energy, current and beam extraction selected by R,Z and L stripping foil coordinates respectively.

Extraction is achieved by insertion of a thin stripping foil into the cyclotron. Various foil compositions, shapes and locations are available via a foil carousel attached to a robotic probe. H^- ions passing through a foil are stripped of their electrons, resulting in positively charged protons which are then bent away from the direction of acceleration as shown in figure 2.12. Here the three coordinates of the foil, R,L, and Z, respectively determine the energy, exit point and current of the extracted beam. A standard 0.001" carbon wire is capable of extracting up to 0.5% of the maximum intensity.

In addition to current selection through stripping foil, the cyclotron output may be limited, prior to injection, in the 300keV Ion Source Injection System (ISIS). A beam stop, known as a pepper-pot, consisting of a solid metal stopper drilled with

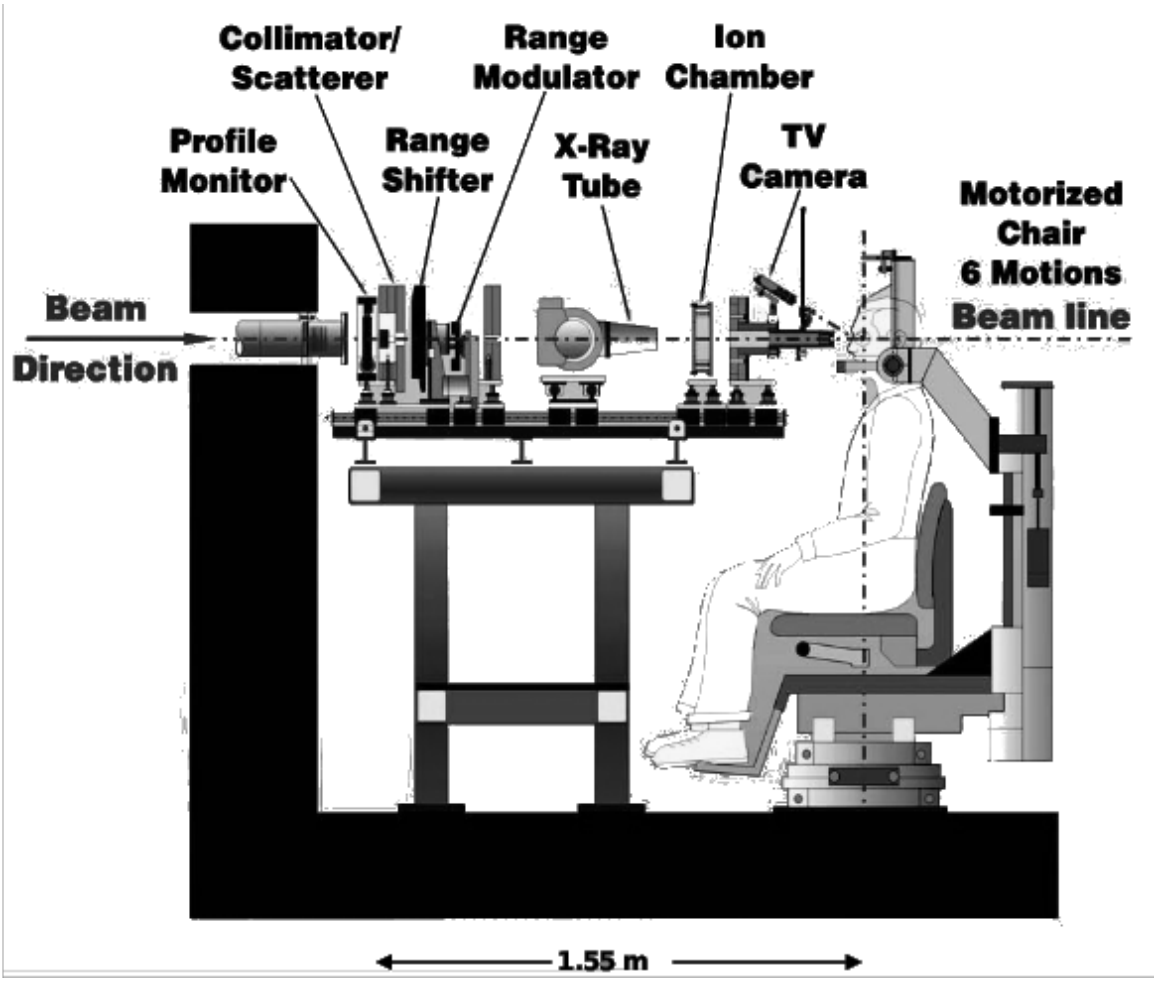

Figure 2.13: TRIUMF dose delivery system (treatment head).

a series of holes, is capable of reducing the injection input by a factor of 30-40. Running at limited $10\mu A$ circulating current and using a standard carbon extraction wire, therapeutically acceptable currents of 3-10nA can be routinely extracted to a beamline for delivery.

2.3.2 *Beamline 2C*

One of the four beamlines from the TRIUMF accelerator, BL2C is designed to carry protons of energies between 65-120MeV. Shown in figure 2.11(right), the line is equipped with five quadrupole and two dipole magnets for focussing as well as three dipoles for steering. BL2C selectively supplies protons to either the proton therapy facility (PTF) or a solid target for radioisotope production through the use of a switcher dipole magnet. Beam current to the PTF is controlled by a combination of this switcher, two beam blockers, extraction foil position and finally by a fast shutter (FS) blocker. The FS is a pneumatic blocker with a closing time on the order of 100ms and is used as the primary control during patient treatment. Backup blockers have response times of less than one second[6]. Control of this system is available manually to the PTF control room as well as the automated treatment control system. Lastly, the line is equipped with two multi-wire profile monitors to measure beam position and a non-saturating secondary emission monitor (SEM) to count beam current at the beam's steel exit window. The SEM output is used in the interlock system in dose delivery.

Characteristics of beam exiting BL2C are determined by the beamline tune and the cyclotron conditions – both of which vary in time and require real time monitoring. During treatment, an operator in the main cyclotron control room is in communication with the PTF control room at all times to adjust beam parameters such as spot size, angle and current. Beam energy is determined in a daily calibration before any treatments.

2.3.3 *Dose Delivery System*

The proton therapy dose delivery apparatus, shown in figure 2.13, is comprised of components designed to degrade the beam to provide a therapeutically useful dose distribution in the patient. Beam entering the PTF traverses several components before depositing dose in the patient:

Beam profile monitor: 16 wire ionization chamber located at BL2C exit window used to monitor centering and beam profile. The cyclotron operator will use feedback from this monitor prior to treatment to centre and shape the beam entering the PTF.

Scatterer / First Collimator: Lead disc of 0.8mm thickness mounted on a copper collimator of aperture size $12mm$, surrounded by polyethylene shielding. The scatterer is designed to spread out the incoming beam to a therapeutically useful size while shielding secondary neutron dose produced in the lead. The above scatterer specifications are capable of reaching a depth of $32mm$ in eye tissue at an extracted energy of $74MeV$.

Diagnostic Ion Chamber: Ionization chamber attached to an integrating circuit used to measure ionizations over time (beam current) emerging from the first collimator.

Range Shifter: Adjustable thickness Lucite degrader used to shift the position of the SOBP within the patient. Range shifter (RS) thickness is controlled by the operator in the PTF control room.

Range Modulator: Rotating Lucite wheel of variable thickness used to modulate the incoming proton beam energy resulting in a spread out the final dose distribution. The wheel rotates at 240 RPM with four modulations per rotation. Transverse size of the final dose distribution is determined by this wheel. A library of wheels is available with a range from 5-25mm.

Second Collimator: Copper/brass collimator purposed with removing protons scattered by the scatterer / first collimator. This collimator is also surrounded with polyethylene to control secondary neutron dose produced in the copper.

Transmission Ion Chamber: Composite air filled ion chamber positioned directly upstream of the nozzle. This device's two independently instrumented ion chambers (primary and backup) are purposed with monitoring dose to the patient, measured in monitor counts (MC). Additionally this device contains four quadrant collection plates to provide information on beam centring.

Nozzle / Patient Collimator: Final collimation before treatment. A patient-specific brass collimator is mounted on the end of a stainless steel nozzle apparatus to shape the lateral profile of the beam.

2.4 Monte Carlo Simulation

Simulation is an invaluable tool in treatment planning, facility design and dosimetry. It's often impractical or impossible to measure primary or secondary dose distributions. This is especially the case for dose deposition in tissue, where there are few ways to make non-invasive *in vivo* measurements. The most accurate method of simulating dose deposition is using Monte Carlo (MC) particle transport software.

The Monte Carlo method involves the repeated random sampling for the purpose of simulating a probability distribution which does not necessarily have an analytical representation. This process allows the reproduction of complicated distributions, such as particle interaction cross-sections, from a flat pseudo-random number generator. Particle transport software makes use of the MC method to simulate the transport of particles through a medium in a step-wise fashion:

1. begin with a particle type, energy, and momentum and geometry
2. transport the particle a set distance, time or energy decrement in space
3. use the MC method to determine a set of probabilistic interactions which the particle undergoes in that time-step
4. simulate particle interactions (scattering, ionization, etc) further using the MC method to determine probabilistic physics outcomes (scattering angle, ionized photon energy, etc)
5. begin tracking any other particles produced
6. record desired metrics such as energy deposition or particle fluence
7. repeat from step 2 until the primary particle is reduced to some energy threshold

Critical to the accuracy of MC particle transport is the step-size and the number of particles transported. Increasing the number of particles interacting in a volume reduces the uncertainty in recorded metrics as a Poisson distribution - counting of events occurring. Decreasing the step size improves the minimum resolution over which quantities can be measured. For uncharged particles it is possible to simulate each individual physics interaction. For charged particles, not all Coulomb interactions can be simulated. Instead an average scattering angle, energy deposition, and secondary production is used for the step size. Both of these necessitate increased

computation time. Also critical to accuracy is the material compositions, geometries and accuracy of physics measurements input (eg. cross-sections). Important to note also is that there is no time-evolution between particle tracks. Any delayed emissions, such as those from secondary isotopes generated, are typically not simulated.

Further details on the specific transport software, geometry and input parameters are discussed in detail in Chapter 3.

2.5 Positron Emission Tomography

As discussed in §2.1.4, protons traversing tissue may produce positron emitting isotopes including $^{11}C, ^{13}N, ^{15}O$. With half-lives ranging from 2-20 minutes, a positron is emitted which goes on to encounter an electron in the medium. Annihilation occurs and two (nearly) back-to-back $511keV$ photons are produced. Detection of coincident photons can then be used to reconstruct the distribution of isotopes via filtered back-projection or maximum likelihood estimation[62]. Positron emission tomography for *in vivo* dose verification has shown promising success in proton therapy. This topic is discussed in further detail in Chapter 8.

Chapter 3

Simulation of the TRIUMF Proton Therapy Facility

The goal of the first portion of this work is to simulate primary proton dose in water. An accurate simulation of primary dose allows for studies into optimization of beam modulation and gives confidence in studying secondary neutron doses to patients. This chapter covers aspects of the simulation software and parameters used to model the TRIUMF DDS. Section 3.1 describes the MC transport software FLUKA: geometry definitions, transport parameters and physical quantities scored. Section 3.2 describes the components simulated and how their geometries are defined in the software. This section serves as documentation of the simulation software, hence it forms the bulk of the chapter. Lastly, section 3.3 rounds out the chapter describing the parameters and justification of the input beam.

3.1 FLUKA Monte Carlo Transport Package

FLUKA is a Monte Carlo particle transport software package which can accurately simulate nuclear and electromagnetic interactions up to 1TeV[12]. Originally intended for high energy physics simulations, FLUKA has developed into more general uses in a wide array of fields from radiation protection to aerospace engineering. FLUKA is written in FORTRAN with its inputs defined by a series of user instructions known as 'cards'. The software is intended to run generically on card input alone; but, more sophisticated usage requires writing custom FORTRAN callback routines. In addition to physics settings, FLUKA cards define the particle source, geometry and

physical quantities to be measured.

While FLUKA encapsulates all of the physics simulation, the Flair [63] software package serves as a graphical user interface. This allows for graphical geometry definition and 3D rendering of components. Flair also provides a basic plotting package, but in this work all plotting is done externally using the 'matplotlib' python package [64].

3.1.1 Transport Parameters

FLUKA has a variety of physics models available depending on physical regime, computing resources and accuracy requirements. The 'DEFAULTS' card defines the overall physics behaviour of the simulation. Specifically, the 'HADROTHErapy' setting is designed for calculation in charged particle therapy. While this setting is sufficient for simulating primary proton doses, for neutron,photon and activation the more accurate 'PRECISIOn' setting is recommended [12]. Some key features of the 'PRECISIOn' model include[12]:

- Low energy neutron transport (including thermal)
- 100keV transport threshold
- 100keV delta ray production threshold
- Maximum 5% proton kinetic energy loss per step

These settings produce FLUKA's best agreement in nuclear activation [12] and allow for accurate proton dose calculation with a low delta ray threshold and kinetic energy loss per step. Low energy neutron ($< 20\ MeV$) transport is necessary to accurately gauge secondary neutron dose.

For the purpose of this work, any simulation run requiring only primary dose readout is performed using the 'HADROTHErapy' setting. This is to be consistent with the literature and greatly increases the speed of the simulation. Any neutron dose or PET isotope activation runs use the 'PRECISIOn' setting.

3.1.2 Combinatorial and Voxel Geometries

Geometries of objects in FLUKA can be defined using two input methods: combinatorial and voxel.

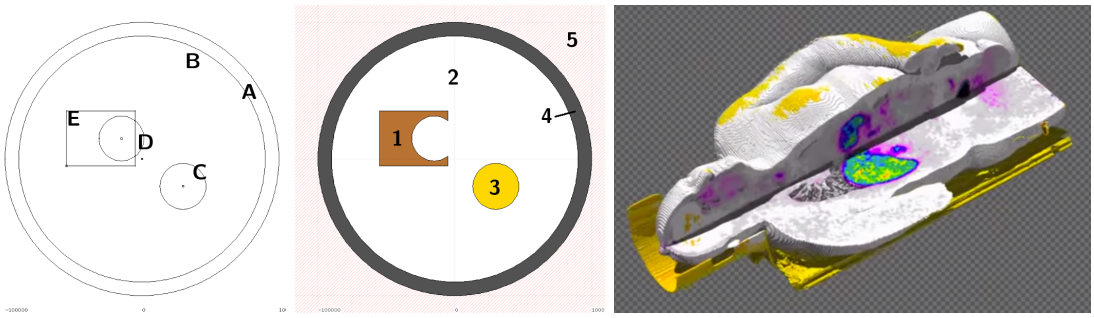

Figure 3.1: Example combinatorial bodies (left) and regions (middle) as defined in FLUKA. Voxelized CT-scan rendered in Flair (right).

Combinatorial geometries consist of exact shapes - spheres, parallelepipeds, cylinders, etc. These shapes are known as 'bodies' and are combined using a boolean expression to describe physical volumes known as regions. Figure 3.1 (left) shows some example bodies forming the boundaries defined in a geometry combining to form regions in Figure 3.1 (middle). Here the region labelled '1' is defined as:

$$REG(1) = BODY(E) - BODY(D)$$

In this way the irregular shape of Region 1 can be well-defined and given an appropriate material type. Region 4 is a special region defined in any FLUKA simulation - a black hole. Any particle crossing into this region is deleted, ending its transport. Region 5, the outer void, is never reached and has no material definition.

Voxel geometries consist of a set of parallelepipeds all of equal size forming a regular grid. This definition allows for detail of a geometry of arbitrary complexity via increasing the resolution of the grid. FLUKA allows any given simulation to have one contiguous section of any model to be comprised of voxels (defined with the VOXELS card). While the entire DDS could be described in this way, it is extremely expensive computationally to do so. Instead only irregularly shaped or dynamic components (such as CT scans, patient-specific collimators, etc.) are described using this method. Figure 3.1 (right) shows a CT scan rendered using the FLUKA voxel geometry format. In this work, voxel geometries are used to model human anatomy (§ 3.2.7) and smooth modulation components (§ 3.2.6)

3.1.3 Units and Scoring Quantities

Physical quantities are recorded or 'scored' in a FLUKA via a set of instructions known as scoring cards. Scoring requires a write to disk, so a minimalistic approach is best when deciding quantities to score. Physical quantities can be read on a by-region or geometric basis. For example - proton dose deposited in a patient may be read out as total dose for the whole patient region, or a grid may be defined over the patient region to read out dose in three dimensions.

Three dimensional quantities (energy deposition, PET isotope activation, etc) may be read out using a 'USRBIN' card. This defines the region and resolution of readout and also offers particle filtering. Figure 3.2 (left) shows such a quantity - proton energy deposition in water in two dimensions (lateral and depth coordinates). The USRBIN output reports energy deposition in a regular grid.

If more information on particles in a region is desired (momentum, energy distribution, particle origin) this may only be determined on a region basis. For this a 'USRTRK' card describing the fluence of particles through a volume may be used. This returns an estimate of the energy / solid angle distribution of particles passing through a volume. This requires particle interactions to read out, so works poorly in cases of low statistics or low interaction cross section (air measurements). Alternatively a 'USRBDX' card records particle properties when they cross a region boundary. The advantage to this is all particles are accounted for, even those not interacting. Figure 3.2 (right) shows 'USRBDX' readout of the energy spectrum of beam protons at various positions in the beamline. Fluence is output as a double differential in energy and solid angle, but collapsed to only show the energy distribution.

In this work the quantities output from the simulation include:

Dose Equivalent: particle weighted equivalent dose calculated from particle fluence[65]. This scoring method is used in determining organ dose in the human water phantom and proton primary dose in the waterbox. Scored as a 'USRBIN' quantity most often in units of $Gy/\ cm^3$.

Neutron Fluence: particle path length in a volume as a function of energy. Used in dose and BF3 detector response calculations. Scored using 'USRTRACK' or 'USRBDX' in units of cm^{-2}.

Ion Chamber Energy Deposition: energy deposition in air inside of beamline ionization chambers. Requires large number of primary particles to achieve

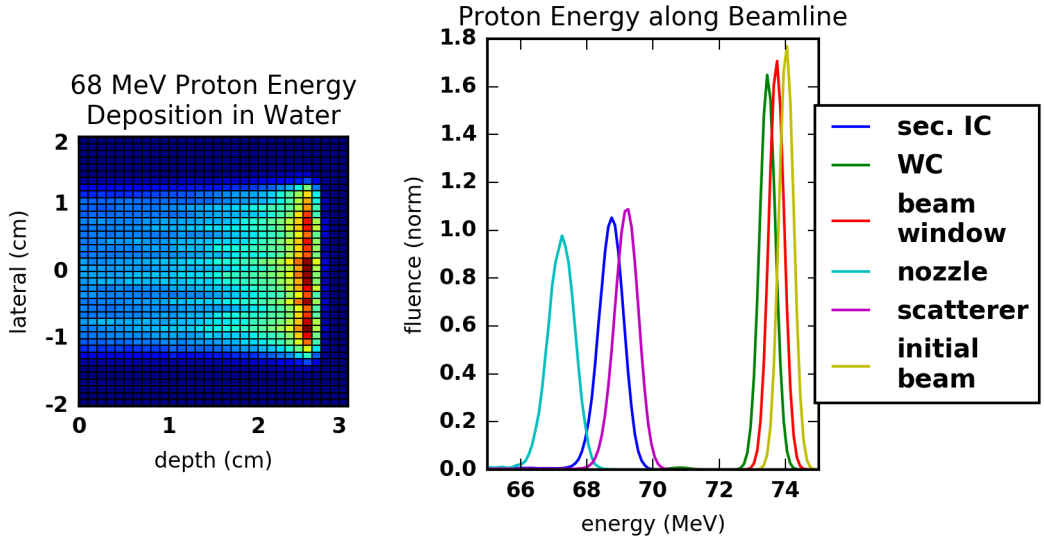

Figure 3.2: Proton energy deposition in water as example USRBIN FLUKA output (left) and beam energy USRTRK FLUKA output (right).

reasonable statistics due to low density gas. This quantity is primary used to score the transmission curve for optimization and beam energy estimation[66]. Read out as a region 'USRBIN' in units of $GeV/\ cm^3$

PET Isotope Activation: number of PET activated nuclei produced in a volume. FLUKA lacks a 'USRBIN' readout for isotopes. To preserve spatial information this is scored using a custom FORTRAN routine which tracks exact position and isotope type. This is stored as x,y,z,isotope format in binary.

3.2 Geometry

The FLUKA geometry was built with a focus on components which make a significant contribution to the desired readout quantities - primary and secondary dose. These include all treatment head components which directly interact with the proton beam as well as volumes which could provide significant neutron shielding (table, X-Ray tube). This section will elaborate on components briefly described in §2.3.3.

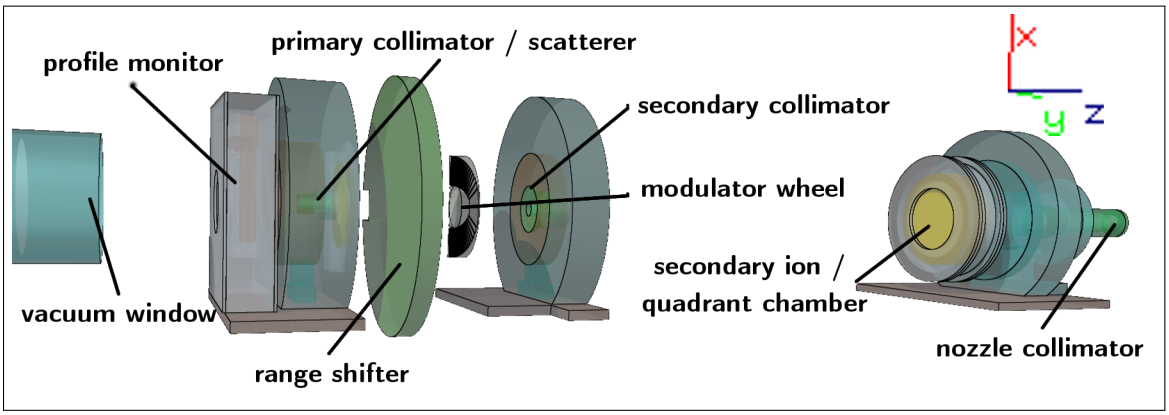

Figure 3.3: Full treatment head geometry rendered in FLUKA including all beam shaping and monitoring devices. Total distance traversed in air is $\sim 1.7\,m$ with water equivalent thickness W_{eq}= 1.7 mm.

3.2.1 Overview and Coordinate System

The DDS is supplied protons by the TRIUMF accelerator via the 2C1 beamline modelled as a vacuum window on the left side of Figure 3.3. In this Flair 3D-render the beam proceeds left to right through the beam monitors, degraders and collimators required to applied a clinical SFUD passive scatter plan. Overall the system is approximately $2m$ long from the vacuum window to the patient isocenter located $10cm$from the nozzle.

Figure 3.3 shows a schematic of the input geometry along the beam line with the important regions as defined in FLUKA. Materials listed are the default material components provided by the FLUKA database. The simulation employs a Cartesian coordinate system with the origin at the beam scatterer. The x axis extends in the vertical direction (down-up); the y axis in the horizontal direction (left-right); the z axis is positive with the direction of the beam going from left to right in the figure.

3.2.2 Scatterer

Key to the SFUD method of planning is good uniformity in the lateral direction. Scattering is an effective method for producing a Gaussian beam distribution given small angles to due MCS[32]. Combining a near-Gaussian profile with lateral collimation allows for a dose clinically acceptable dose profile at the cost of beam current. Loss of this current is not an issue with the TRIUMF accelerator, only a tiny portion of the total current is applied during treatment ($6nA$ vs 200 μA). However, collimating

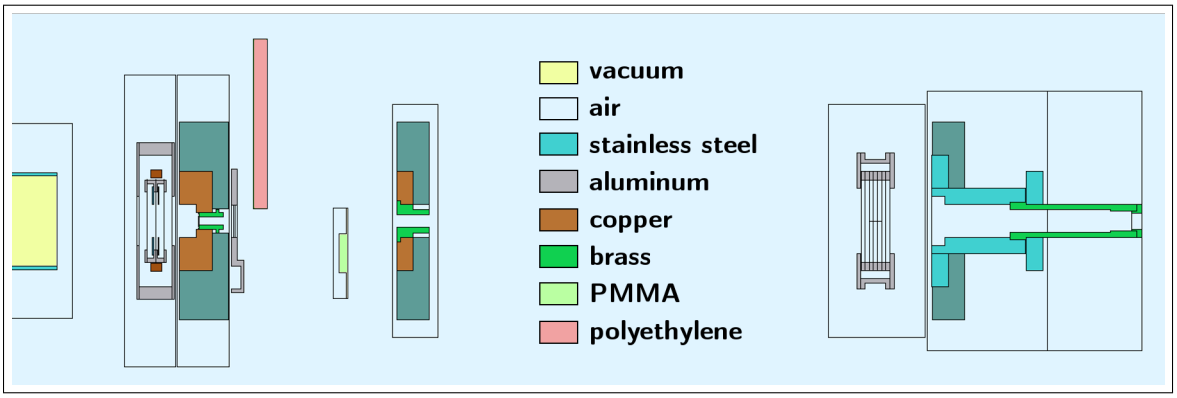

Figure 3.4: Schematic of central-axis cross-section of FLUKA treatment head geometry shown with predominant materials.

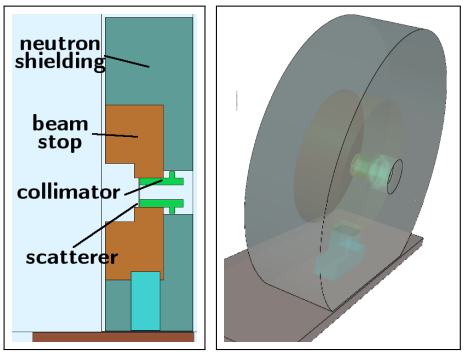

beam degraders		
scatterer (lead)	0.91 g/cm^2	W_{eq}= 5.0 mm
collimators		
beam stop (copper)	44.8 g/cm^2	E_{max}= 214 MeV
primary col. (brass)	34.1 g/cm^2	E_{max}= 184 MeV

Figure 3.5: Lead scatterer and primary collimator assembly with polyethylene neutron shielding (left). Table of beam degraders with water-equivalent thicknesses (W_{eq}) and collimators with maximum stoppable proton energy (E_{max}).

the proton beam produces unwanted secondary neutron dose to the patient. Thus a beam scatterer must be appropriately shielded.

The scatterer assembly of the DDS, shown in schematic and 3D render in Figure 3.5, consists of a lead disc of 0.8mm thickness mounted on a copper collimator of aperture size $12mm$, surrounded by polyethylene shielding. The above scatterer specifications are capable of reaching a depth of 32mm in eye tissue at an extracted energy of $74MeV$[6]. Being a high-Z material directly in the beamline, the scatterer has the largest impact on proton range of all the DDS assemblies at $\sim 5mm$.

The modelled FLUKA geometry closely matches the design drawings with no approximations necessary for simulation.

3.2.3 Collimators

In addition to the primary collimator located in the scatterer assembly, two other collimators serve to shape the beam laterally - the secondary and patient collimators.

The secondary collimator, shown in Figure 3.6 is located $30cm$ downstream of the scatterer and consists of a $2cm$ brass aperture surrounded by copper and polyethylene shielding. Here the copper stops any high-energy protons scattered at a large angle and the polyethylene provides neutron shielding. The primary purpose of this collimator is to remove protons scattered when traversing the range shifter and / or modulator wheel which sit just upstream of the assembly.

Lastly the nozzle collimator, shown in Figure 3.7, is located $10cm$ from the patient isocenter. There the final lateral shaping is done on a patient-specific basis. Each nozzle collimator is milled to produce a field with a lateral profile of the tumour

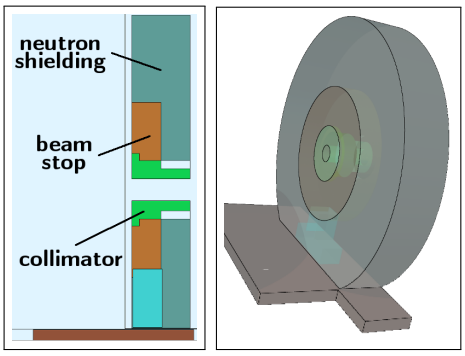

collimators		
beam stop (copper)	22.8 g/cm^2	E_{max}= 146 MeV
secondary col. (brass)	43.7 g/cm^2	E_{max}= 215 MeV

Figure 3.6: Secondary collimator assembly with polyethylene neutron shielding (left). Collimator thickness and maximum stoppable proton energy (E_{max}) (right).

target plus safety margins. Each brass collimator is $\sim$1.5cm thick, capable of stopping protons of up to 110MeV. Ideally the majority of collimation is performed further upstream of the patient to reduce secondary neutron dose.

No major approximations are made to simulate the geometry of the secondary or nozzle collimators. To properly model a patient-specific collimator it would be necessary to build a voxel structure; while that method was explored it is not documented in this work.

3.2.4 Detectors

To ensure beam conditions are within tolerance throughout patient treatment, the DDS is equipped with three banks of detectors - a profile monitor, upstream (diagnostic) and downstream (primary) ion chambers.

The beam profile monitor, shown in Figure 3.8, is positioned $\sim$12cm downstream of the vacuum window. When treating a patient or performing quality assurance, BL2C1 and the cyclotron parameters must be tuned to center and shape the incoming beam within treatment tolerances [6]. The main tool for accomplishing this is the beam profile monitor. This device houses two air-ionization chambers, one horizontal and one vertical, both having 16 copper wires (2mm spacing) for readout. Beam degradation through aluminum and Mylar foils in this assembly is minimal ($< 0.5mm$ total). The modelled geometry is accurate, missing only the copper wires which are excluded as they have minimal impact on the beam and increase computational complexity.

The diagnostic ion chamber, shown in Figure 3.9 is an air-ionization chamber located between the scatterer and range shifter. Readout is achieved via copper

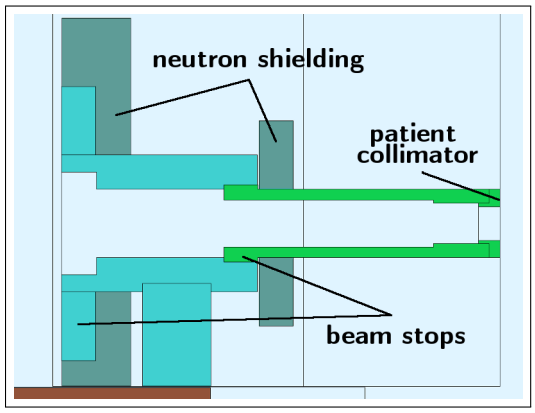

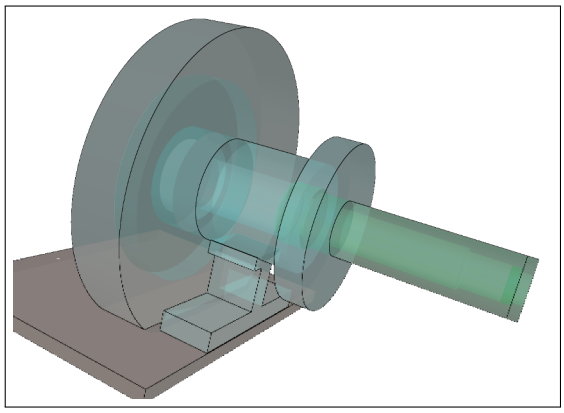

collimators		
beam stop (stainless)	19.6 g/cm^2	E_{max}= 139 MeV
patient col. (brass)	18.8 g/cm^2	E_{max}= 111 MeV

Figure 3.7: Nozzle assembly with nozzle collimators, custom patient collimator and neutron shielding (upper). Collimator thickness and maximum stoppable proton energy (E_{max}) (lower).

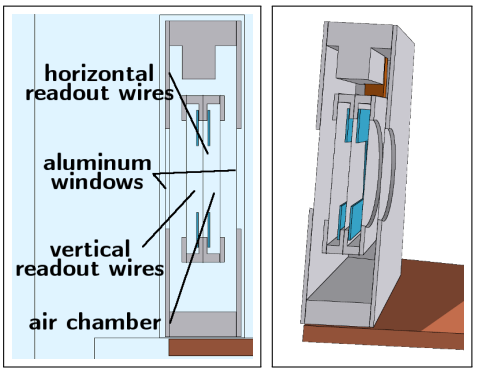

beam degraders		
foils (Kapton)	0.02 g/cm^2	W_{eq}= 0.2 mm
readout (copper)	<0.005 g/cm^2	W_{eq}= <0.05 mm

Figure 3.8: Profile monitor wire chamber schematic and 3D cut-out rendering (left). Table of beam degraders with water-equivalent thicknesses (W_{eq}) (right).

coating on an inner Mylar foil. The primary purpose of this chamber is for energy calibration via transmission scan as described in §3.3.1. Again beam through the Mylar foils of this housing are modelled and negligible. Readout of this chamber in the MC is taken as energy deposited in the air adjacent the readout foil. Here deposited energy is proportional to counts on the IC as discussed in §2.3.3.

The final detector assembly, shown in Figure 3.10, is located $\sim$100cm downstream of the detector and just upstream of the nozzle. Three independent ion chambers are housed in this aluminum frame - primary / backup chambers for dose calibration and a four-quadrant ion chamber for beam centring.

The primary ion chamber is an air-ionization chamber with copper readout, similar to the diagnostic chamber. This chamber's readout is known as monitor units (MU) and is calibrated to a reference ion chamber. Patient dose during treatment is recorded using this IC. Should it fail during treatment, an identical IC is located downstream known as the backup chamber.

Sandwiched between these two chambers is a quad-readout chamber for beam centering. Four isolated copper foils provide readout. During treatment, ideally readout on these chambers are all within 10% to provide idea beam centering. There is an automatic interlock should any of these values exceed 50% of the average readout. At this point, beam uniformity is unacceptable for patient treatment with a $>$ 5% variation over the treatment field [7].

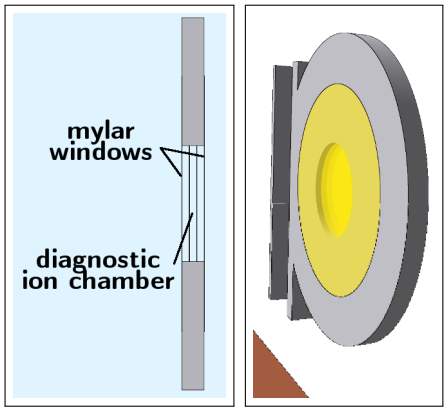

beam degraders		
foils (Kapton)	0.01 g/cm^2	W_{eq}= 0.1 mm
readout (copper)	<0.005 g/cm^2	W_{eq}= <0.05 mm

Figure 3.9: Diagnostic ion chamber (left). Table of beam degraders with water-equivalent thicknesses (W_{eq}) and collimators with maximum stoppable proton energy (E_{max}) (right).

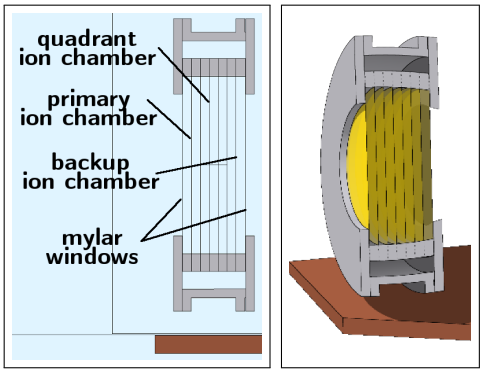

beam degraders		
foils (Kapton)	0.03 g/cm^2	W_{eq}= 0.3 mm
readout (copper)	<0.005 g/cm^2	W_{eq}= <0.05 mm

Figure 3.10: Combined quadrant ion chamber and primary / secondary ion chambers (left). Table of beam degraders with water-equivalent thicknesses (W_{eq}) (right).

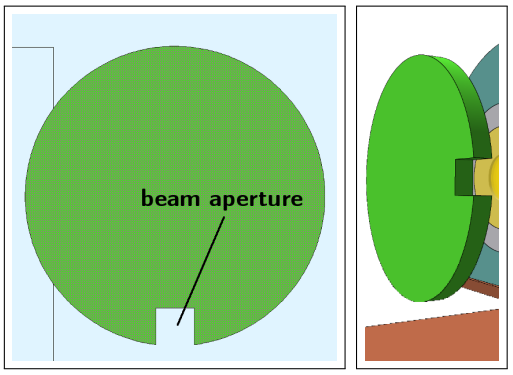

beam degraders		
range shifter (polyethylene)	1.7-28.6 g/cm^2 [a]	W_{eq}= 2-34 mm

[a] range shifter has a range of degrading thicknesses

Figure 3.11: Range shifter wheel (left). Table of beam degraders with water-equivalent thicknesses (W_{eq}) (right).

3.2.5 Range Shifter

The Lucite range shifter, shown in Figure 3.11, is positioned $8cm$ downstream of the scatterer. Discussed in §2.2.6, target positioning is achieved by means of a static beam degrading range shifter. The physical range shifter (RS) is a graded Lucite slab on a stepper motor which may be rotated through a thickness range of 2-34mm in thickness. To compensate for the grade, a small wedge is positioned downstream of the shifter. Range shifter beam-degrading thickness (T_{RS}) is defined in terms of the stepper motor setting (R) as:

$$T_{RS} = (1.97 + 0.010075 * R)/10.0(mm) \tag{3.1}$$

FLUKA is not able to model a graded wedge shape in 3D. There is no simple body or way to smoothly grade a region through a finite combination of the available bodies. Due to this limitation, the RS is modelled as a solid cylinder with a small beam aperture. This beam aperture is filled with the appropriate thickness of Lucite for a given range shifter motor setting. This neglects the small air-gap between the physical compensating wedge and the graded plastic. Fortunately this air gap has only a small impact on lateral scatter profile and a negligible impact on proton range. The range shifter is not simply replaced by a small plastic degrader in the simulation, however, to better model neutron shielding provided by the Lucite volume.

3.2.6 Modulator Wheels

The PMMA modulator wheel, shown in Figure 3.12 (upper), is positioned $\sim 20cm$ downstream of the scatterer between the range shifter and secondary collimator. Discussed in §2.2.6, modulation of the beam is necessary to produce a clinically useful target width. This is achieved by the modulator wheel which spins at 240RPM (4 modulations per rotation). Each thickness of the modulator wheel produces a different proton energy and therefore specific BP depth in the target. The resulting dose distribution is ideally flat over the desired target width. Modulator wheels are categorized into standard target sizes ranging from 8-23mm. The design and fabrication of these wheels forms a significant portion of this thesis and is discussed in detail in chapters 6 and 7.

Modelling a spinning wheel in MC necessitates some approximations. Several simulations representing different time intervals of rotation must be performed and combined. This requires much more computational power (in excess of $10\times$) than a standard pristine simulation.

Weighted Slabs

The simplest method for approximating the dose distribution from a modulator wheel involves running a single simulation step for each thickness of the wheel. The actual wheel geometry is replaces by a static slab of PMMA of the appropriate thickness. The 'USRBIN' dose distributions can then be combined with a weighting corresponding to the angle-share of each thickness of the wheel. This is computationally cheap, requiring only one simulation per step, but it ignores the effect of the beam which is typically covering multiple steps simultaneously. This effect is small but measurable[32]

Rotating Wedges

Through the use of 'WED' wedge bodies, the exact geometry of a stepped modulator may be represented in FLUKA. Each step is defined by a wedge originating from the origin of the wheel. The entire wheel region may then be rotated through a series of translation and rotation operations via 'ROT-DEFI' cards. A python script was written to build custom wedge and rotation cards for any arbitrary wheel definition. Figure 3.13 shows a beam-eye-view of the wedge geometry along with a Flair 3D render well-resembling the real geometry in Figure 3.12. Rotations in increments of

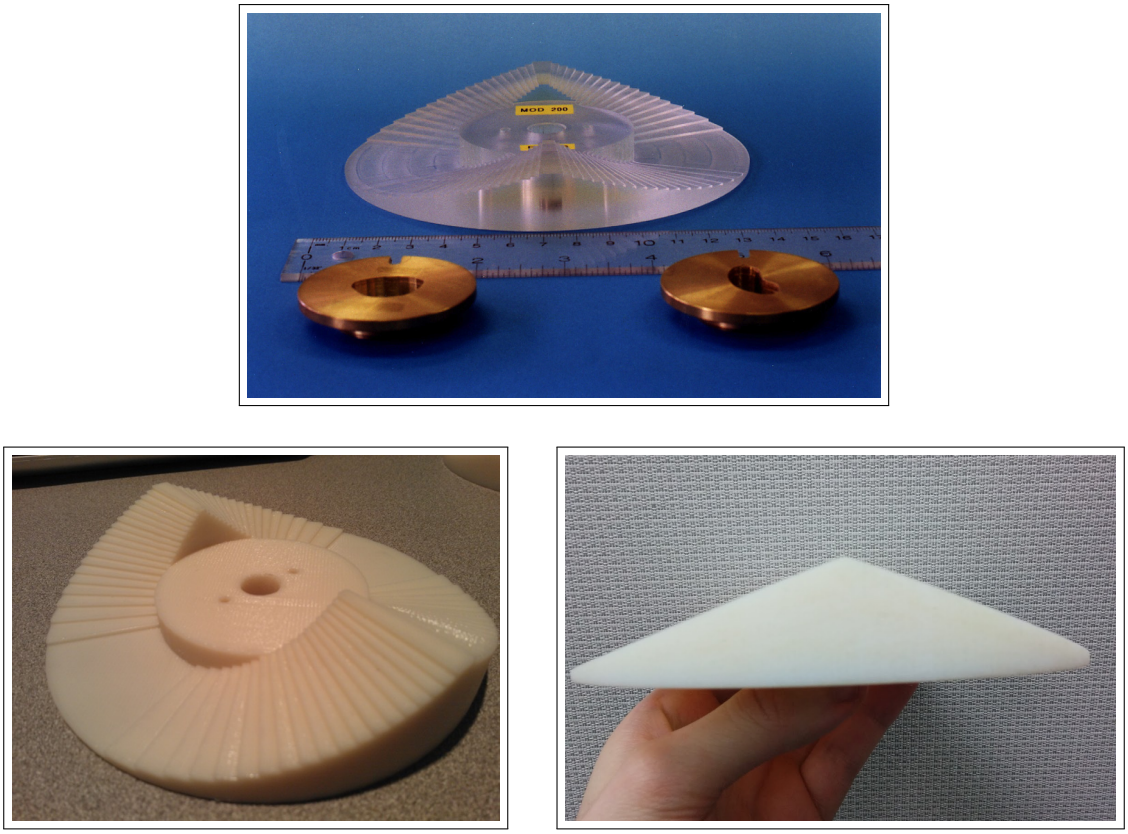

Figure 3.12: Standard Lucite modulator wheel shown with brass patient collimators (top), 3D printed (Fused Filament Fabrication) replica wheel (bottom left) and profile of 3D printed smooth modulator (PolyJet) (bottom right).

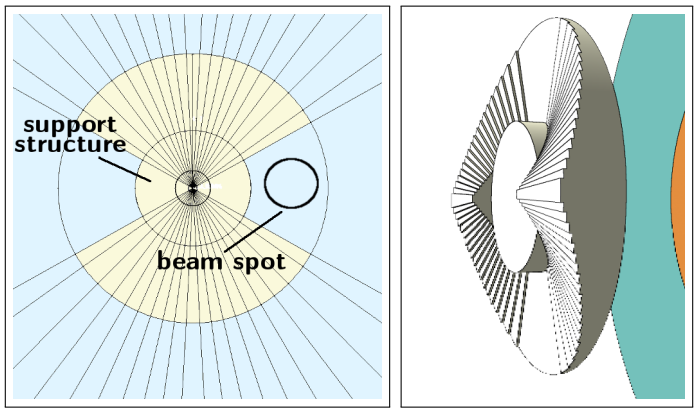

Figure 3.13: Stepped wheel FLUKA wedge geometry (left) and 3D rendering (right).

0.7^o[32] in a 180^o arc (258 total) are simulated and their resulting outputs summed. Only 180^o are required instead of 360^o due to the symmetry of the wheel.

Smooth Voxel Modulators

Lastly, this work explores the development and fabrication of 'continuous' or 'stepless' modulator wheels. Details on design and implementation are found in chapter 7. Figure 3.14 (left) and (middle) show portions of a smooth wheel modelled with the FLUKA voxel geometry. Here the voxel geometry is sampled at a resolution of $0.2mm$, the limit lateral resolution of the 3D printer used to construct the wheel. Only the portion of the wheel intersecting the beam is modelled (with $5cm$ margin for scatter). This is a FLUKA computational limit on the number of voxels. As with stepped wheels, the smooth model is summed in increments of 0.7^o. A custom voxel volume must be generated for each wheel step. This is done by an external Python script which takes the wheel angular profile and inserts the new geometry into the FLUKA input file automatically. Figure 3.14 (right) shows a down-sampled ($1mm$ voxel size) full-wheel inserted into a FLUKA simulation.

3.2.7 Target Geometries

Waterbox

The waterbox, a PMMA walled box filled with water, is the primary target used in calibration, quality assurance and validation of the simulation in this work. The waterbox is shown in Figure 3.15 positioned $\sim 8cm$ downstream of the nozzle collimator. Only the PMMA entrance window is simulated having a water-equivalent thickness

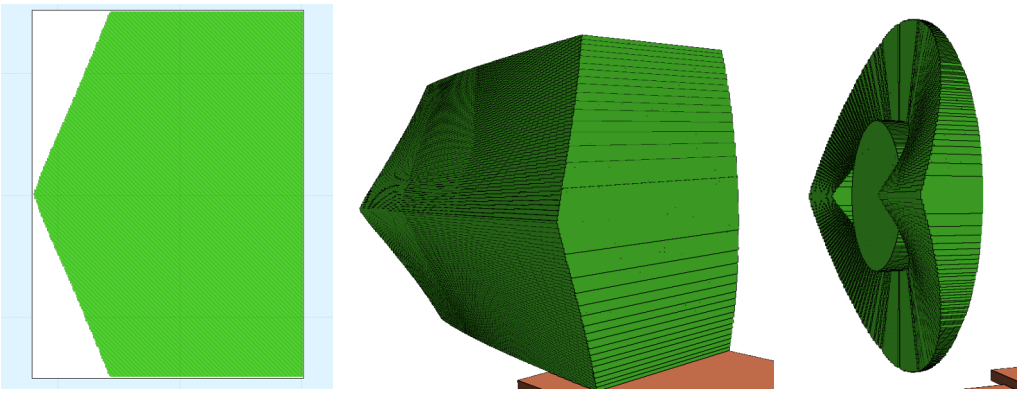

Figure 3.14: Smooth wheel section profile at a resolution of $0.2mm$(left), 3D rendered section (middle) and 1 mmresolution full-wheel rendering (right).

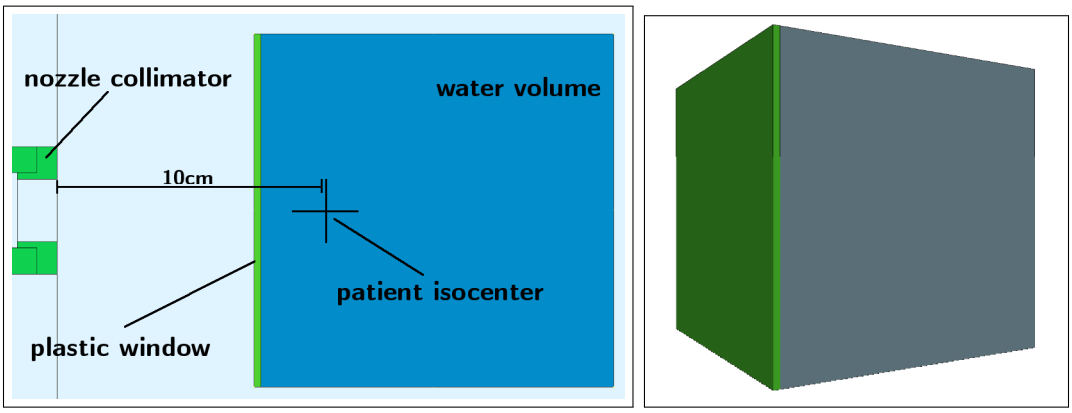

beam degraders

box window (polyethylene)	0.32 g/cm^2	W_{eq}= 3.3 mm

Figure 3.15: FLUKA region schematic of the waterbox target with labelled patient isocenter (left) and Flair 3D rendering of the box (right).

of $3.3mm$ at $62MeV$, the average energy of the beam at that position. Measurements are done in the waterbox using various detectors detailed in §4.1.1. Readout in simulation was achieved by various configurations of 'USRBIN' detectors.

VIP-Man

VIP-Man is an anthropomorphic phantom[67] developed in 2000 as a result of the Visible Human Project[68]. At $0.33 \times 0.33 \times 1mm$ resolution with all major types of tissue contoured and labeled, this phantom provides exquisite detail for dose calculations. Figure 3.16 shows a down-sampled $4 \times 4 \times 4mm$ VIP-Man phantom imported into FLUKA as a voxel geometry. Due to a limitation in the maximum number of voxels, a finer resolution was not possible for whole-body simulation. While dose to larger organs will not be heavily affected by the poor resolution, small organs such as those at risk in the eye (macula, optic nerve, optic disc) are very poorly modelled. Each tissue type is represented by a FLUKA region and readout is done via dose and energy fluence 'USRTRK' detectors.

Voxelized Eye Model

To achieve finer resolution for small organs of the eye, an anatomic[69] computer aided design (CAD) model was converted to FLUKA format. Shown in Figure 3.17, the original CAD model was simplified and a positionable tumour model was added.

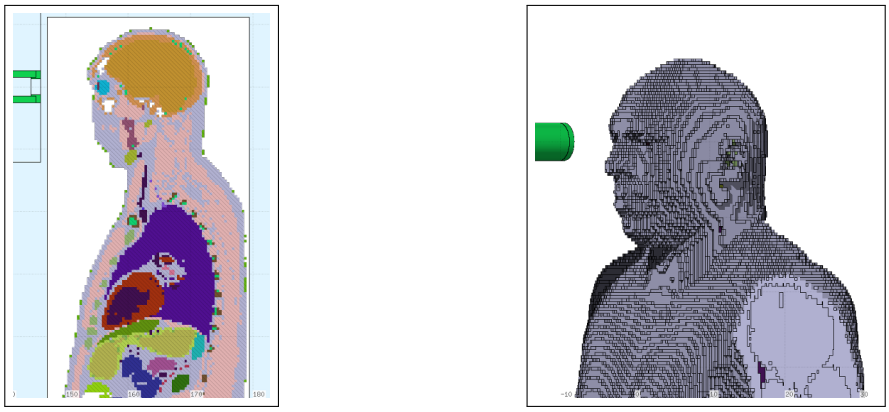

Figure 3.16: VIPMAN anatomical phantom shown with cross section in FLUKA voxels (left) and 3D rendering (right).

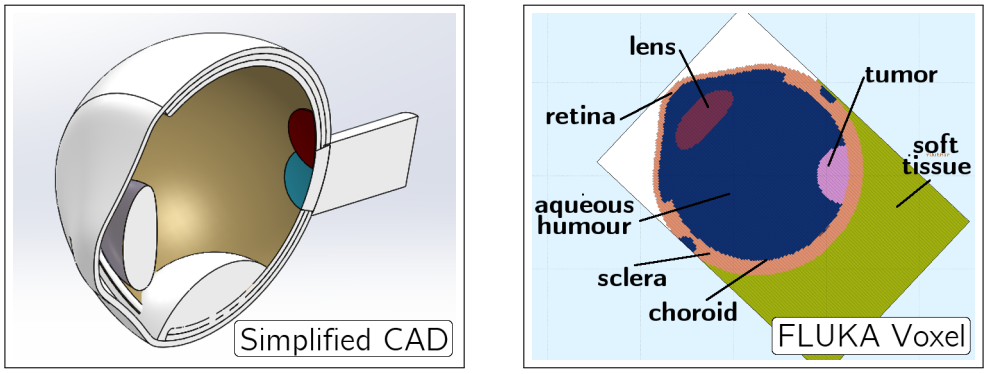

Figure 3.17: CAD Eye Model rendered in SolidWorks (left), FLUKA VOXEL representation (right).

The model was then ray-traced at a $0.2mm$ resolution using the FreeCAD python library[70]. This was imported into FLUKA as a voxel geometry. All eye tissues were modelled[71] as individual regions and dose readout was performed using both 'USRBIN' and 'USRTRK' detectors in the case of neutron dose.

3.3 Beam Model

FLUKA allows definition of beams via the 'BEAM' and 'BEAMPOS' cards. Here flat, circular or Gaussian shaped beams may be defined with flat or Gaussian energy spectra. While the TRIUMF beam is not perfectly Gaussian, to first approximation it can be modelled as a $74.0 \pm 0.25 MeV$ beam[6] with a Gaussian spatial distribution measured by the profile monitor. The width and centering of the beam are highly operator dependent while the energy selection is very consistent between beam tunes.

3.3.1 Energy Calibration

While the suggested beam energy is a reasonable approximation, a calibration measurement known as a 'transmission scan' is performed before measurements or patient treatment. This scan involves taking a ratio of IC measurements over a range of RS thicknesses to ensure the beam energy is within the expected range. It also provides a very precise measurement of beam energy and spread. The calibration of the FLUKA simulation to transmission scan data is discussed in detail in the following chapter.

3.3.2 Beam Profile

Spatial beam profiles vary widely between beam tunes. For the highest precision measurements such as output factors it is necessary to obtain profile monitor readouts and customize a simulation to a beam tune. However, the majority of measurements are agnostic to beam tune centering and spread as long as quadrant chamber tolerances are observed[7]. Thus the majority of simulations used a centered beam with x,y FWHM of $1.0cm$ and $2.0cm$ respectively. While this effect is important in MC beam modelling, ultimately it has no effect on treatment quality due to scatterer beam washout[72].

TG-268 Index	Item Name	Description
2, 3	Code Version	FLUKA, 2011.2c-5, 15/10/2016 [65] [12]
4	Validation	[74]
5	Timing	pristine proton - 1200 core-hour neutron - 12000 core-hour
8	Source Description	74.1 $\pm$ 0.15MeV, 1.0x2.1cm FWHM [6]
9,10	Physics Settings	HADROTHE, LOWNEUT defaults [65] [12]
11	Variance Reduction	modulated runs 5x phase space repeat upstream of wheel
12	Scoring	proton - DOSE-EQ ; neutron - DOSE-EQ USRTRK energy spectrum
13	Histories	proton pristine - 10^8; neutron - 10^9
14	Uncertainties	pristine $< 2\%$, neutron $< 16\%$ / organ standard FLUKA batch method [12]
15	Post-processing	protons - binned 1x1x0.5mm (x,y,z) neutrons - spectrum converted to H*(10) [75] [76]

Table 3.1: Table of Monte Carlo parameters as recommended in RECORDS TG-268.

3.4 Summary

To close this chapter, extra parameters of the simulation are presented in a standard form conforming to the suggestions of AAPM TG-268 report[73]. Outlines of run times, uncertainty limits, score binning, and variance reduction are shown in Table 3.1.

Chapter 4

Measurements and Model Validation

The focus of this chapter is the validation of the FLUKA MC model by comparison of measured data to simulated results. Measurements of primary proton dose and secondary neutron dose rate for the TRIUMF DDS are described in detail. Sections 4.1 and 4.3 cover the experimental setup, data display and analysis for primary proton and secondary neutron dose rates respectively. Simulation methods, results and comparison to measured data are detailed in sections 4.2 and 4.4.

4.1 Primary Dose Measurements

The bulk of this chapter involves the measurement of dose deposition in water due to beam (primary) protons. This section contains experimental methods, estimated uncertainties and recorded data for measuring beam characteristics and proton dose in water.

4.1.1 Methods and Hardware

The general measurement procedure in a proton dose measurement was as follows:

1. setup of waterbox and device stage / probe
2. requesting beam from the TRIUMF control room
3. controlling beam on/off using the fast shutter at the PT control room

4. ensuring proper beam centering/width on the profile monitor
5. calibrating daily energy using the range shifter transmission method
6. performing probe beam centering
7. acquiring data for a pre-determined number of monitor counts on the primary ion chamber
8. recording data in the PT control via printout (beam characteristics) or digital recording (protons)

Beam Setup

The beam provided to the DDS was determined by the TRIUMF control room operator at the request of the PT operator. Beamline 2C1 can receive an extracted beam between 65-115MeV at a maximum 10 nA current. This is achieved by operator-positioning of the stripper foil within the cyclotron. Treatment is typically performed at 74MeV, 6 nA; this was the case for the majority of measurements in this work.

After beam of the requested parameters is provided to the PT room, the TRIUMF operator observed the beam profile on the PT profile monitor to ensure appropriate beam shaping and centering. The primary effect of beam size/centering is in beam output. With an off-center or spread out beam, the output rate of the beam is low resulting in a longer patient treatment time [7].

With a centered and well-shaped beam, steering was adjusted by the TRIUMF operator to ensure that the down-stream beam was centered. The TRIUMF operator adjusted steering magnets such that the quadrant chamber, as described in sections 2.3.3 and 3.2.4, registered counts not varying by more than 10% between the quadrants. This ensures appropriately reproducible dose distributions for treatment [6].

Once beam was provided, control is handed over to the PT operator by operation of the fast shutter blocker as described in section 2.3.2. Before proceeding with measurements or treatment, the beam energy must be precisely determined via ion chamber transmission scan.

Waterbox Measurements

Once the beam is well characterized using the DDS ion chambers, reproducible waterbox measurements can be performed. Waterbox hardware setup is shown in Figure

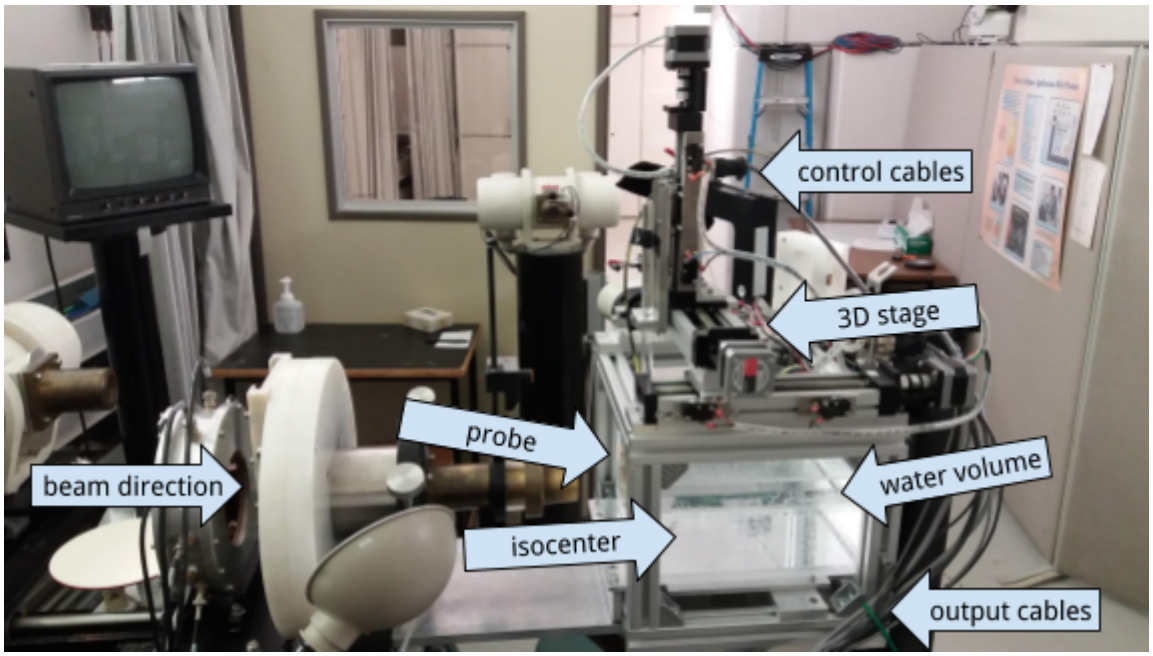

Figure 4.1: Photo of the waterbox setup at the end of the TRIUMF DDS.

4.1 and the MC geometry is described in section 3.2.7. The waterbox consists of a 3D stage, detector and lucite box containing water (in thermal equilibrium with the PT room). Two probes were used in these studies - both requiring laser alignment to the patient isocenter and zeroing to the waterbox front window.

Reproducing the zeroing and laser alignment process yielded a $0.5mm$ setup error. The main source of this error was in aligning the probe front with the window (beam-line direction). Setup positioning uncertainty is taken into account in data processing by applying an uncertainty to all data-points equal to this $0.5mm$ error multiplied by the gradient of the cubic-spline interpolated data at this point. This is most notable in the distal falloff region of the BP where the gradient is highest.

Two probes were used in waterbox measurements: a Markus type ion chamber and a Si PIN diode. The standard in PT is to use the Markus chamber for axial and diode for lateral relative measurements as discussed in 2.2.5. Note that while counts representing absolute dose are measured, only relative dose is reported. For comparison to simulation, the data are normalized to pristine peak dose or SOBP mid-point. Absolute dose is measured during annual QA using a pinpoint ion chamber taking into account temperature and pressure corrections. This is unnecessary for relative measurements taken within a short time window. Calibration to absolute dose is beyond the scope of this work.

Markus Chamber

The standard in proton dosimetry in the axial direction, a Markus type ion chamber provides the most accurate relative dose distribution for a wide range of proton energies [32] [77]. This is a small parallel-plate ion chamber commonly uses for precision radiation field measurements. A PTW Markus chamber (model N23343 [78]) was used to measure axial and profile data for centering. The most important dimensions of this chamber are the $88mm^2$ circular active area and the $1.06mm$ effective depth of measurement.

The probe was mounted on the waterbox 3D-stage affixed to a vendor-provided acrylic rod. The probe was covered by the waterproof cap ($2mm$ acrylic) for all measurements. Initial setup requires zeroing of the cap to the front of the waterbox. Adjustment of waterbox position was required to ensure the cap is flush with the box and that there is no force bending the acrylic rod. Once zeroed, the whole apparatus was adjusted to laser-center to the patient isocenter.

Diode

While not as accurate in relative dose measurement, diodes have been found to be within 1% for ocular energies [79]. Use of a diode in addition to ion chambers allows for a cross-check measurement with the added benefit of a smaller active area for precise measurement of beam profiles. A Siemens diode (model BPW34 [80]) was used to measure axial dose and profile data for simulation comparison. The diode was face was oriented to face the incoming beam. The most important dimensions of this chamber are the 2.65x2.65mm square active area and the 0.4-0.6mm effective depth of measurement. In addition, the heat shrink wrap adds a 0.3-0.6mm water equivalent depth of measurement for a combined depth of measurement of $0.9\pm0.4mm$.

The diode was mounted on the waterbox 3D-stage affixed to a custom steel rod. Initial setup required zeroing of the heat wrap to the front of the waterbox and aligning the diode face using axial lasers. Once zeroed, the whole apparatus was adjusted to laser-center to the patient isocenter.

A diamond based detector was included in the original PT commissioning, but was found to poorly reconstruct relative dose at all depths without correction [6] [81].

4.1.2 Uncertainties

Measurements of primary dose include three categories of uncertainties (in order of magnitude): probe position accuracy, statistical fluctuations in measurement, and uncertainties introduced in the process of analysis and fitting. All dose measurements were recorded at minimum three times and standard deviation on those measurements were included in reported uncertainty calculated as:

$$\Delta D_{meas} = \sqrt{(\Delta x \nabla D)^2 + (\sigma_{meas})^2 + (\sigma_{fit})^2} \tag{4.1}$$

Where D_{meas} is the average measured dose, σ_{meas} is the standard deviation of measured dose, ∇D is the gradient of dose distribution calculated using a cubic spline interpolation [82] [83], Δx is the uncertainty on probe positioning as discussed in §4.1.1, and σ_{fit} is uncertainty introduced in the process of fitting or analysis. Note that σ_{meas} is smaller by a factor of ~ 10 when compared to the gradient term in this calculation. By far the uncertainty is dominated by probe positioning and is most noticeable in high dose gradient regions.

All reported measurements include uncertainties as calculated in equation 4.1 and estimation of terms in this equation are discussed on a per-measurement basis in the following sections.

4.1.3 Pristine Depth Dose

Pristine depth-dose curves form the basis measurement of this study and are a benchmark for the accuracy of the simulation. There are three primary quantities of interest in a pristine BP - peak depth (R_{peak}), peak to entrance ratio Ratio_{pe}, and distal 80-20 falloff width W_{80-20}. Calculation of these quantities, defined in Figure 4.2, is simple and require the measured entrance, peak, 80% distal and 20% distal dose values denoted D_{ent}, D_{peak}, D_{80}, D_{20} respectively. These quantities are calculated from the cubic spline interpolated data with peak finding described as in Figure 4.3.

Axial dose measurements were performed in $0.5mm$ step size extending from the entrance window to $\sim 5mm$ beyond the distal falloff. A further measurement at $0.25mm$ (lower limit step size in software) was taken in order to resolve the $\sim 3mm$ distal falloff region. These data were spliced together, averaged and analyzed in increments of $0.25mm$.

Raw data of sample pristine peaks recorded by the diode and Markus are shown

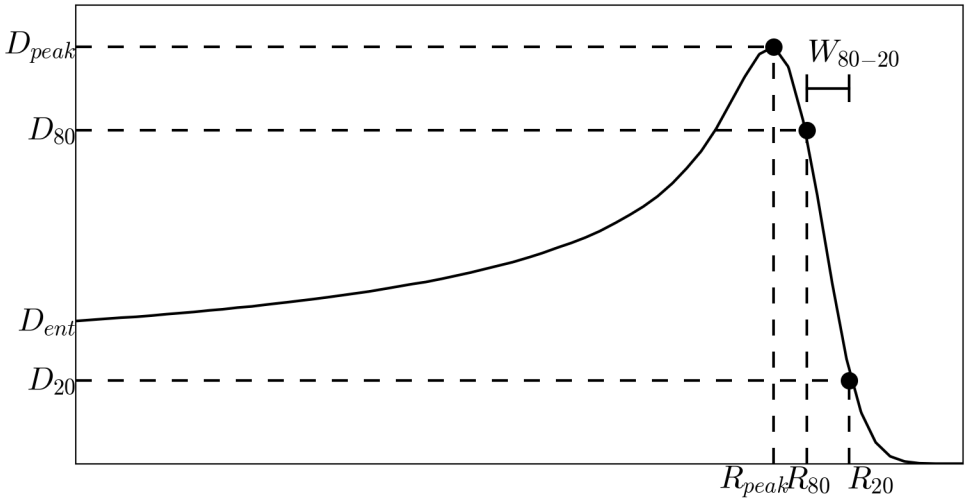

Figure 4.2: Pristine Bragg peak plot illustrating important analysis metrics including peak dose D_{peak}, peak range/depth R_{peak}, entrance dose D_{ent}, 80% distal dose D_{80} and range R_{80}, 20% distal dose D_{20} and range R_{20}, and distal falloff width W_{80-20}.

Algorithm - Pristine Peak Finding

It's impossible for a discreet measurement of a pristine BP to yield a data point exactly coincident with the peak of the dose distribution. The peak position, R_{peak}, must be estimated by interpolating the measured distribution. Piece-wise cubic polynomial fitting is used to determine a more accurate peak position [82] [83] [84]. The fitting procedure is as follows:

1. isolate highest data point as peak approximation
2. apply cubic-spline fitting to surrounding 10 points to acquire interpolating function
3. sample interpolating function at $0.2mm$ accuracy to determine best guess at maxima
4. find true function maxima using least-squares optimization and maxima guess

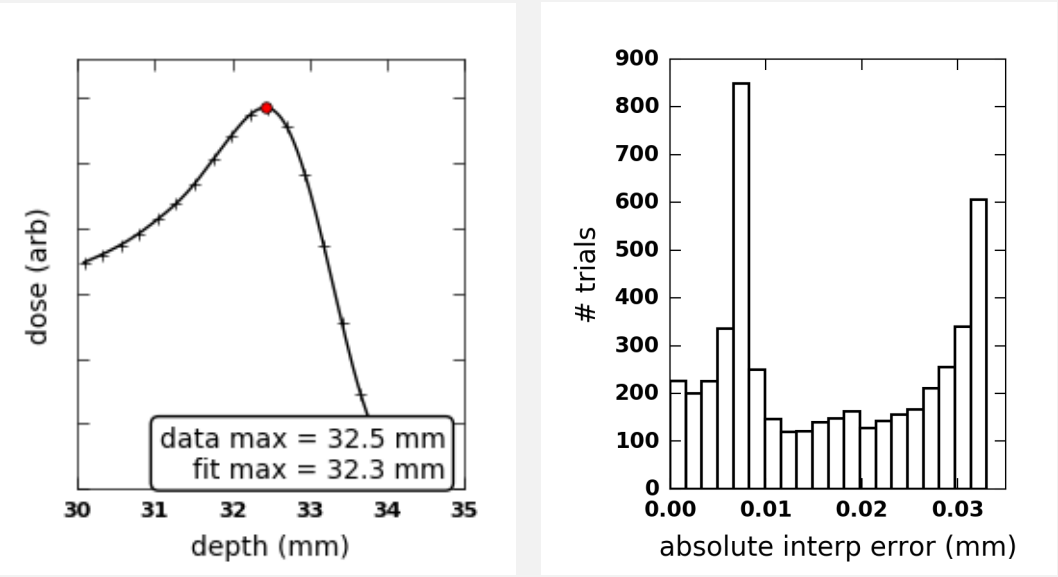

The left image shows a cubic-spline fit to data measured at $0.5mm$ increments. Here the fitted peak differs from the maxima by $0.2mm$. Due to the discreet nature of the points, the peak fitting itself adds uncertainty to the reported result. The right image shows 5000 trials of peak fitting with an offset sampled from a normal distribution of $\sigma = 0.25mm$ (the step size of measured data). The distribution is bi-modal likely due to the discrete nature of the cubic-spline sampling. The resulting error from the entire peak fitting is at most $0.035mm$, negligible compared to the measurement error of $0.5mm$.

Figure 4.3: Description of peak finding algorithm and estimated uncertainties associated with BP analysis.

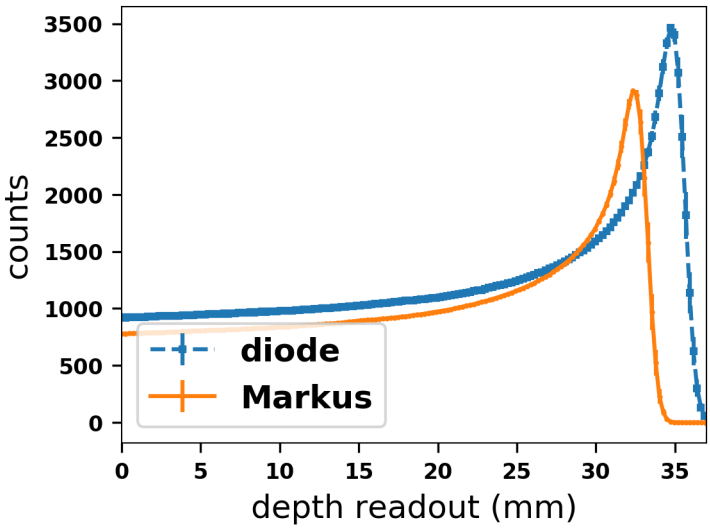

	diode	Markus
R_{peak}	34.8	32.4
D_{peak}	3473	2922
R_{80}	35.3	33.0
R_{20}	36.1	33.7
W_{80-20} $(\pm 0.3mm)$	0.8	0.7
$Ratio_{PE}$ (± 0.02)	3.77	3.75

Figure 4.4: Raw data measured for a $74MeV$ pristine BP for the diode and Markus chamber probes.

together in Figure 4.4. As expected, the two are not coincident due to the differing geometries of the probes as described in §4.1.1. On average, range differences between these two measurements are $2.4 \pm 0.4mm$ which is consistent with the presence of the $2mm$ waterproof cap and the total positioning error of $0.5mm$. Additionally the absolute output differs between the two measurements. This is largely arbitrary due the choice of signal gain on readout. This effect is account for in normalization of measured quantities. What may be compared is the peak to dose ratio - which, within accuracy of the measurement, does not differ between the two probes.

Figure 4.5 shows a pristine $74MeV$ peaks measured with the Markus and diode. Here the depth offsets were matched to the dose peak and doses normalized to one. Within measurement accuracy there is no discernible difference in peak width or normalization. A greater than 3% difference occurs at the distal falloff due to position error and width difference. Note that these distributions should not be identical due to the difference in active area and probe readout width in the axial direction. These measurements, however, are not precise enough to note the difference. For this reason, the remainder of this work will compare only Markus chamber axial dose data to simulated results.

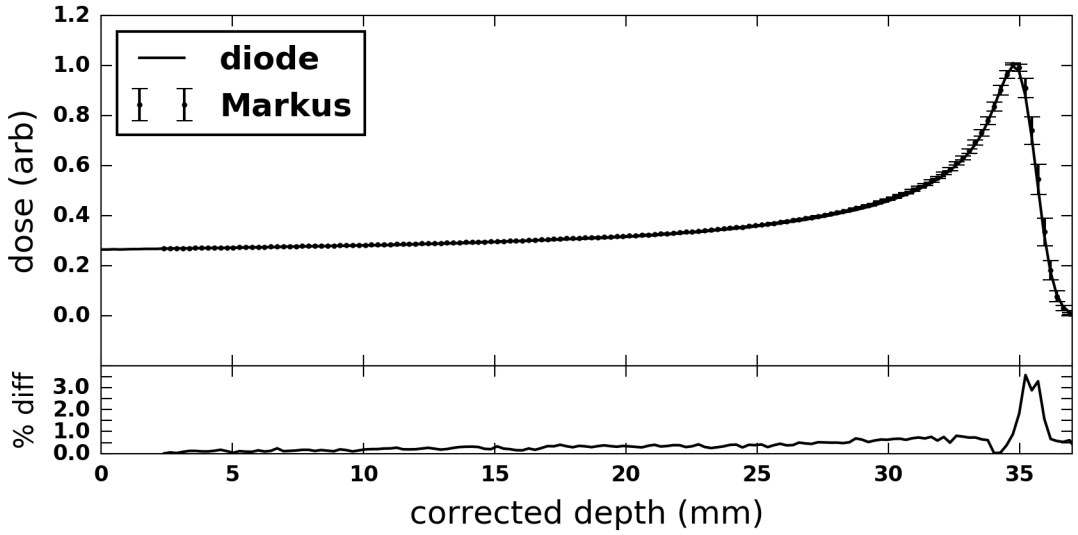

Figure 4.5: Comparison of Markus and diode probe outputs for $74MeV$ beam with Markus depth and dose normalized to diode output. Greater than 3% difference occurs at the distal falloff owing to positioning uncertainty and difference in peak width.

4.1.4 Range-Shifted Bragg Peak

The range shifter is used in every patient treatment for positioning the depth of the dose distribution. As described in sec 3.2.5, it is modelled as a solid cylinder of Lucite (PMMA). Measurement of dose distributions degraded by this device are necessary to validate the Monte Carlo geometry model. The thickness degrading the beam is selected using an integer value known as range shifter units which correspond to turns on the stepper motor controlling the rotation of the lucite wedge. This setting may range from ∼200 (for back of eye choroid) to ∼1800 (iris tumors). Via equation 3.1 this is a Lucite thickness ranging from $4mm$ to $20mm$.

Figure 4.6 shows axial dose measurements of range-shifted BP for settings spanning the clinical regime. Tabulated in this figure are the shifted peak depths and output factors (OF_{RS}) defined as as the ratio of D^{RS}_{peak} of the shifted BP to $D^{pristine}_{peak}$:

$$OF_{RS} = D^{RS}_{peak}/D^{pristine}_{peak} \tag{4.2}$$

There is a consistent drop in OF_{RS} of $\sim 10\%$ per $5mm$ of PMMA blocking the beam. This is owing to the scattering of protons out of the beam and into the primary/secondary collimators.

Figure 4.7 (left) shows a plot of the shift of proton peak depth against range shifter thickness. The slope of this plot is the measured water-equivalent thickness (W_{eq}) [85, 57, 58, 86] of the blocking material:

$$W_{eq} = \frac{\text{range shift in water}}{\text{thickness blocking material}} \tag{4.3}$$

Here the measured value of 1.15 ± 0.01 is consistent with the predicted value of 1.157[58] for PMMA at ocular energies $\sim 75MeV$. This value is dependent on both beam energy and thickness traversed, but is roughly constant over a wide range of energies (1.157-1.158 from 70-180MeV[58]). Thus this measurement is not refined enough to predict beam energy to any useful degree of precision.

Figure 4.7 (right) depicts BP 50%-50% width and distal falloff width (W_{80-20}) as $4.7\pm0.3mm$ and is $0.7\pm0.3mm$ respectively. In theory both of these values should increase with thickness of beam-blocker due to increased energy spread. However, again this effect is not measurable using the 3D-stage system as the increase in energy spread is proportional to the range of stopping powers over the input energy spectrum. The TRIUMF beam will be found to have a spread of ∼2%, which amounts to an

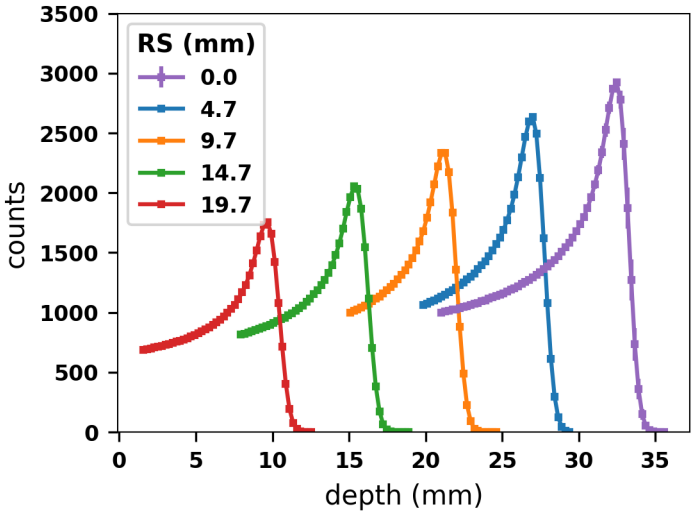

RS (mm)	R_{peak} ($\pm 0.3mm$)	OF_{RS} (± 0.02)
0	32.4	1.00
4.7	26.9	0.90
9.7	21.2	0.80
14.7	15.4	0.71
19.7	9.6	0.60

Figure 4.6: Markus-measured BP for range shifter settings (RS) spanning the clinical regime. Tabulated are dose peak depths R_{peak} and measured range shifter output factors OF_{RS}. Note that these are peak measurements with no entrance dose recorded.

increased energy spread smaller than most accurately measured and simulated values of stopping power ($\sim$3%) [87, 29, 88].

4.1.5 Spread Out Bragg Peak

Patient treatment is always performed with a modulated proton beam as the dose distribution from a pristine beam is too sharp for any size of axial volume. Validation of SOBP distributions, as used in patient treatment, are indicative of accuracy of simulated beam modulation. There are three primary quantities of interest in a SOBP - range (d_{90}), modulation width m_{98}, and distal falloff width W_{80-20}. These clinical metrics used in treatment planning are depicted in Figure 4.8. They rely on identifying several distal and proximal ranges.

The modulation width m_{98}, determined by the axial size of the target region for treatment, is defined by the proximal 98% and distal 90% ranges. These are percentages of the mid-point dose D_{mid}, dose at the mid-point range R_{mid}. This is a cyclic definition - p_{98} and d_{90} determine R_{mid} but also depend on the dose at R_{mid}. To find this quantity it is necessary to take an iterative approach: first guess R_{mid}, determine p_{98} and d_{90}, redefine R_{mid} and repeat until convergence. This algorithm is known as 'plateau fitting' and is detailed in Figure 4.9.

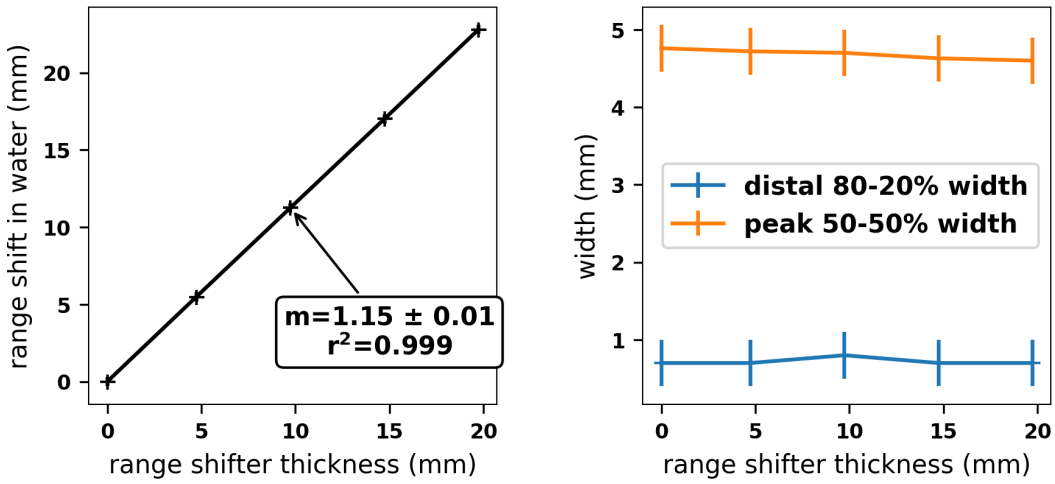

Figure 4.7: Shift of peak range in water (left) and peak 50%-50% and penumbral width W_{80-20} (right) for for varying range shifter thicknesses. Slope of shifted range plot is 1.155. Average peak width is 4.7±0.3mm and mean penumbral width is 0.7±0.3mm.

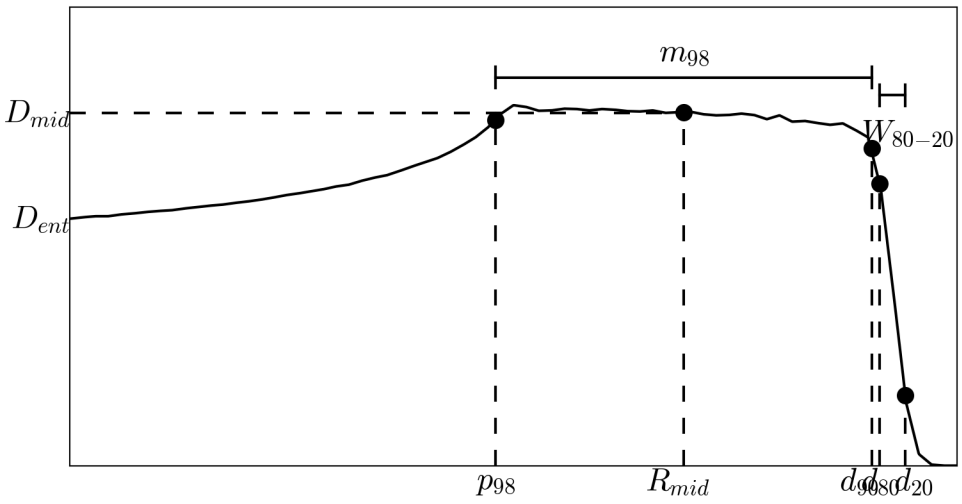

Figure 4.8: Sample SOBP diagram illustrating important analysis metrics including mid-point dose D_{mid}, mid-point range R_{mid}, SOBP range (distal 90% point) d_{90}, distal 80%/20% d_{80}/d_{20}, proximal 98% point p_{98}, distal falloff width W_{80-20}, and 98% modulation width m_{98}.

For consistency it would be expected that the 90% proximal point would be the natural choice for plateau width definition. However, this point is highly unstable with respect to dose measurement/normalization due to the low gradient of the dose distribution [32, 89]. This is a natural consequence of the limitations of beam modulation using cyclotron-generated proton beams. Thus the modulation width is defined by the 98% proximal position.

Modulated Output

Raw data of three beam modulations spanning the clinical regime (8,14 and 23mm) are shown in Figures 4.10, 4.11, 4.12 respectively. As in the pristine BP, Markus and diode ranges differ by $\sim$2.4mm. Plateau and penumbral width measurements are consistent between the two with in the accuracy of the measuring devices for all modulation widths. The measured modulation width is greater from the prescribed widths by 0.1mm-0.5mm. This is because the modulation wheels were designed for a lower treatment energy of 70MeV [6] - yielding a sloped plateau, extending the distance between the proximal 98% and distal 90% points.

Output factors for SOBPs are measured from the center of the plateau region and defined as:

Algorithm - Plateau Fitting

Determining the SOBP plateau limits p_{98} and d_{90} (and therefore modulation width and range) is an iterative process:

1. determine half-area of dose curve by summation as first guess
2. determine p_{98} and d_{90} candidates from dose at guess point using technique from Figure 4.3
3. re-calculate mid-point dose using p_{98} and d_{90}
4. if difference between new mid-point and guess is less than 0.1%, accept midpoint; else repeat from step #2

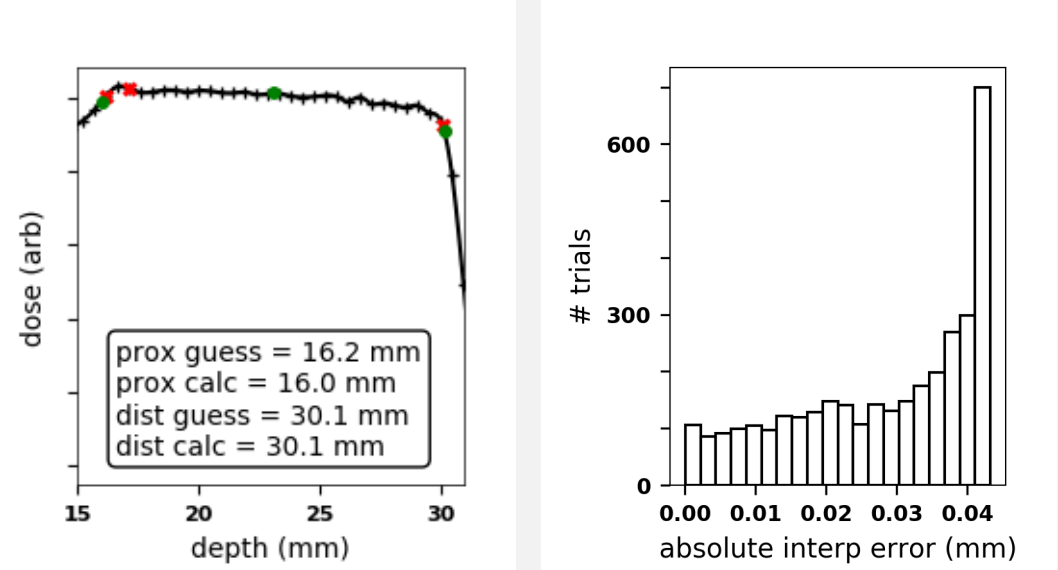

The left image shows a cubic-spline fit to data measured at $0.5mm$ increments - plateau limit guesses are shown in red, fit values in green. Here the fitted proximal limit differs from the guess value by $0.2mm$. This is due to the low gradient of the dose distribution and re-calculation of the normalization point D_{mid} (over use of max value). This is a known effect in plateau fitting which requires a delicate treatment [89, 32].
Due to the discreet nature of the points, the peak fitting itself adds uncertainty to the reported result. The right image shows 5000 trials of peak fitting with an offset sampled from a normal distribution of $\sigma = 0.25mm$ (the step size of measured data). The distribution shows absolute error, resulting in a maximum and most frequent error of $0.045mm$. This worst-case error is included in all quoted measurements requiring plateau-finding.

Figure 4.9: Description of plateau finding algorithm and estimated uncertainties associated with SOBP analysis.

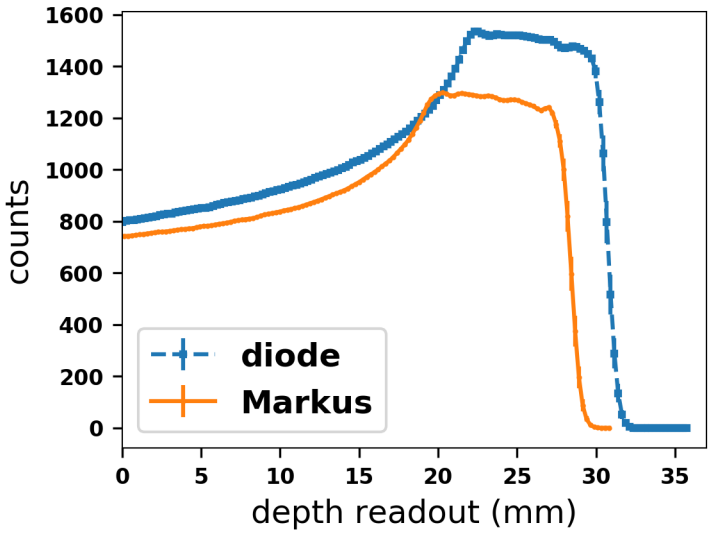

(mm)	diode	Markus
Ratio_{ME}	1.90	1.76
R_{90}	30.0	27.6
W_{80-20}	0.8	0.9
m_{98}	8.3	8.2
D_{mid}	1534	1298

Figure 4.10: Raw data measured using the diode and Markus chamber probes for a $74MeV$ $8mm$ SOBP.

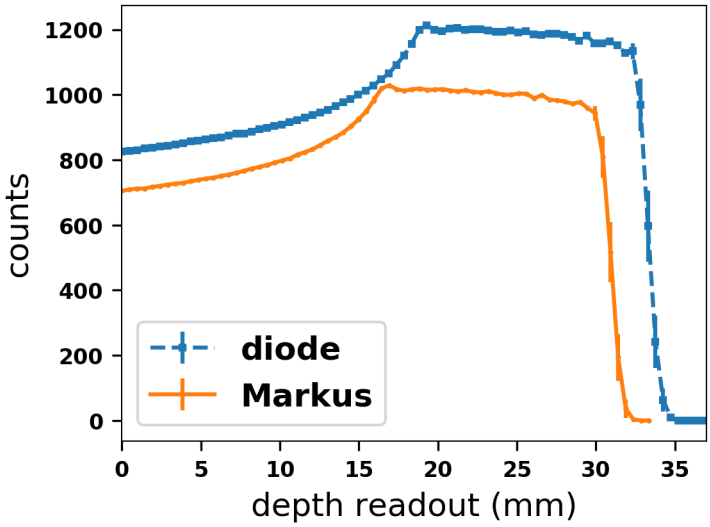

(mm)	diode	Markus
Ratio_{ME}	1.45	1.43
R_{90}	32.6	30.1
W_{80-20}	1.0	1.0
m_{98}	14.1	14.1
D_{mid}	1214	1029

Figure 4.11: Raw data measured using the diode and Markus chamber probes for a $74MeV$ $14mm$ SOBP.

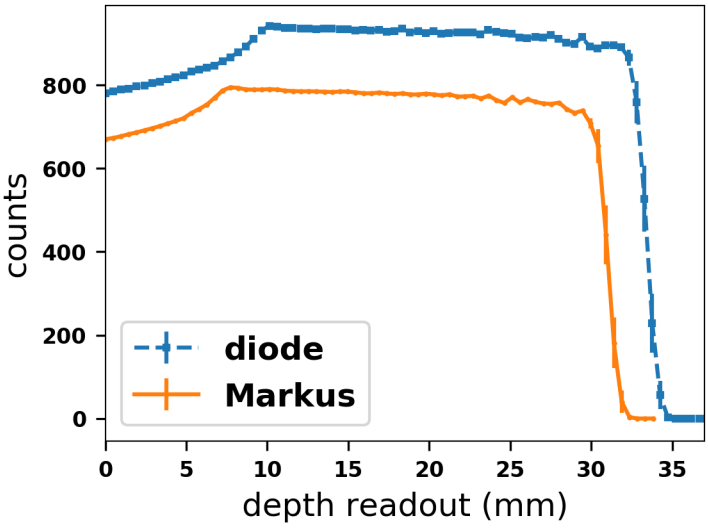

(mm)	diode	Markus
Ratio_{ME}	1.18	1.16
R_{90}	32.5	30.0
W_{80-20}	1.0	1.0
m_{98}	23.5	23.4
D_{mid}	942	794

Figure 4.12: Raw data measured using the diode and Markus chamber probes for a $74MeV$ $23mm$ SOBP.

$$OF_{RS} = D_{mid}/D_{peak}^{pristine} \tag{4.4}$$

Where D_{mid} is the dose at the mid point of the plateau and $D_{peak}^{pristine}$ peak dose from a pristine BP. This definition is for illustrative purposes to compare to simulation. In treatment planning all output factors are relative to the mid-point dose of the $23mm$ calibration wheel. This way, absolute dose to a target can be calculated by multiplying each individual factor[90, 91].

Table 4.1 shows output factors for the measurements above. Again, as in the pristine case, no difference in OF may be seen at the precision of these measurements. The diode/Markus output ratio at the center of the SOBP is consistently 1.18 for all modulation widths.

wheel size (mm)	OF diode (± 0.2)	OF Markus (± 0.2)
23	0.27	0.27
14	0.35	0.35
8	0.44	0.44

Table 4.1: Table of measured SOBP output factors for the Markus chamber and diode.

Figure 4.13 shows the two measurements shifted and normalized to match dose at the midpoint and 90% distal range. The relative difference between the two measurements is below 2% except in the distal falloff region. Here the difference exceeds 3% due to different axial readout sizes between the two devices. This is expected, as was the case with the pristine peak in figure 4.5.

4.1.6 Waterbox Profiles

As described in §2.2.6, the goal for the dose distribution in the lateral dimension is uniformity. This is achieved by scattering an initially small beam into the three collimators of the DDS. Factors heavily affecting this distribution include beam centering, beam size, and scattering components, distance to target, and collimation. Beam centering and size are set by the beam operator according to guidelines for TRIUMF PT[7]. Distance to the target is fixed in the TRIUMF DDS at $10cm$ nozzle-to-isocentre.

Lateral dose measurements were performed using a $0.2mm$ step size. Measurements were performed with pristine peak at $1cm$ water depth and at the center of

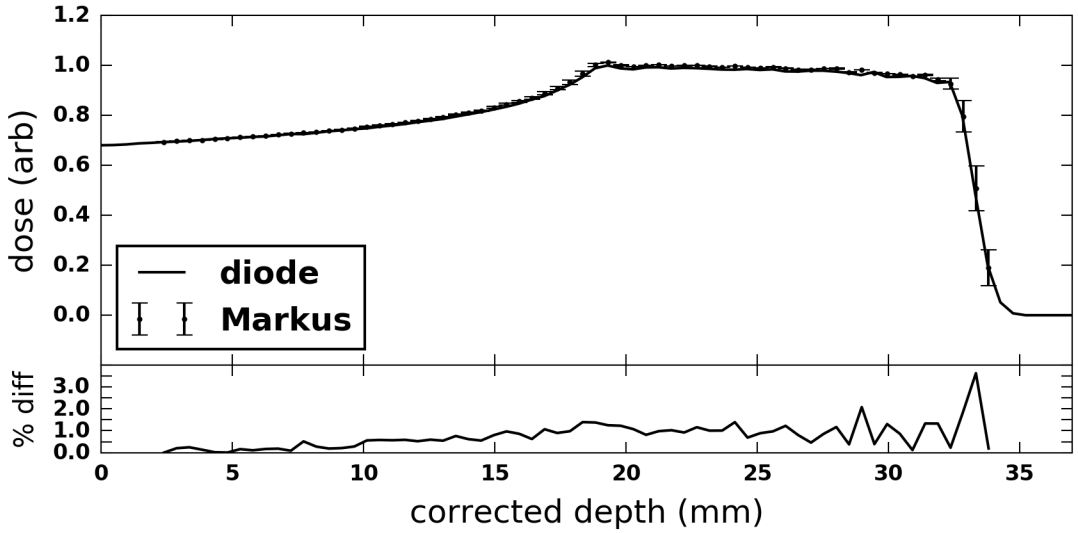

Figure 4.13: Comparison of Markus and diode probe outputs for $74MeV$ $14mm$ SOBP beam with Markus depth and dose normalized to diode output. Greater than 3% difference occurs at the distal falloff owing to positioning uncertainty and difference in peak width.

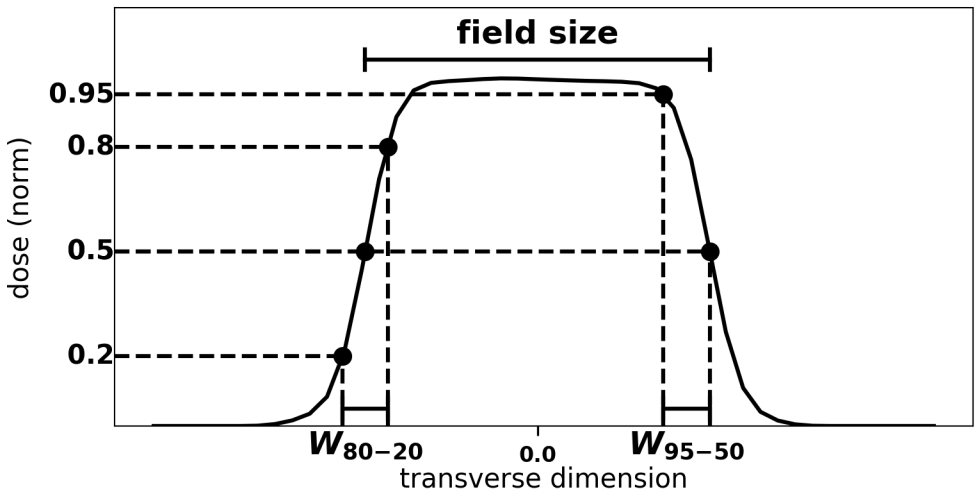

Figure 4.14: Diagram of sample beam profile depicting important analysis quatities: lateral 80-20 penumbral width W_{80-20}, lateral 95-50 penumbral width W_{95-50}, and field size W_{field}.

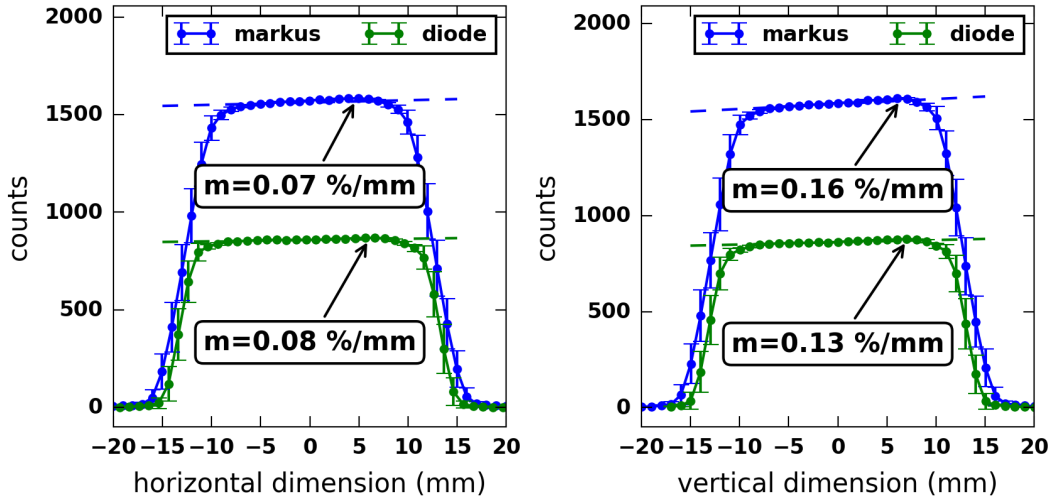

$(\pm 0.3mm)$	diode	Markus
FS	26.3	25.4
W_{80-20}	1.8	2.9

$(\pm 0.2mm)$	diode	Markus
FS	26.0	25.7
W_{80-20}	1.9	2.9

Figure 4.15: Raw profile data measured at $1cm$ depth for the horizontal (left) and vertical (right) lateral dimensions. Measurements performed using a $74MeV$ pristine BP collimated with a $25mm$ nozzle collimator using the diode and Markus chamber probes.

a $23mm$ SOBP ($1.74cm$). These are the two depths used in QA testing - the first for beam centering and the second for SOBP output and absolute dose measurement. This is the configuration used in TRIUMF treatment planning. Figure 4.14 shows the relevant quantities for analysis of a beam profile. Field size is defined as the 50%-50% width of the profile. Lateral penumbral widths are most often assessed 80%-20% and 95%-50%[32].

Figure 4.15 shows lateral profiles for a a $25mm$ collimated pristine beam in the horizontal and vertical directions. This configuration is typically used for initial beam centering. Notable here is the difference between field size and penumbral width as measured by the two devices. This is largely owing to their geometries: the Markus chamber has an electrode diameter of $5.3mm$ whereas the diode a square lateral size of $2.3mm$. As expected the Markus chamber has a poorer lateral resolution due to the increased size of dose sampling in the lateral direction. The result is $\sim$ 0.5-$1mm$ increased penumbral widths and reduced field size. For this reason, diode measurements are recommended for use in QA [77] and will be the measurements used when validating the Monte Carlo model in this work going forward. Also notable are

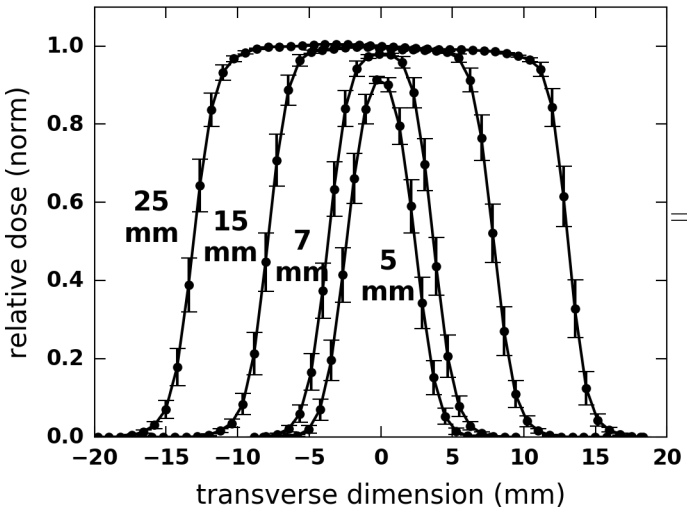

Col. Size (mm)	Field Size ($\pm 0.3mm$)	W_{80-20} ($\pm 0.3mm$)	OF (± 0.01)
5	4.9	2.0	0.91
7	7.4	2.0	0.98
15	15.8	2.1	0.99
25	26.2	2.2	1.0

Figure 4.16: Raw profile data for various collimators measured at SOBP center ($17.4mm$) for a $74MeV$ SOBP of width $23mm$ for the diode.

the field slopes (98%-98%) slopes of Figure 4.15. This value is dependent on beam centering/shape and probe orientation. Here the vertical profile has about twice the slope of the horizontal - this is a known effect associated with the beam supplied by the cyclotron[6] and is within tolerance of 2% max variation per cm. This work includes only the TRIUMF DDS geometry, hence modeling of this effect at the beamline level is out of the intended scope.

Figure 4.16 shows profiles of $23mm$ modulated beams at the midpoint depth ($17.4mm$). This configuration is used for dose calibration and treatment planning. Only the diode is shown here. Lateral penumbra are consistent ($1.5 - 1.9 \pm 0.3mm$) with open field measurements, indicating beam modulation has no effect on the penumbra trend as expected [92, 93]. Note that there is an expected average increase of penumbra size of $\sim 0.5mm$ over the entire proton depth range - undetectable using this apparatus. Overall, lateral penumbral sizes are in the same range (1.5-2.5mm) as other reported measurements for ocular proton therapy [94, 95].

4.1.7 Beam Measurements

Waterbox measurements can be used to validate a Monte Carlo model for dose; however, independent measurements of input beam dimensions and energy are required as model inputs. The DDS has built-in ion chambers which are used to calibrate

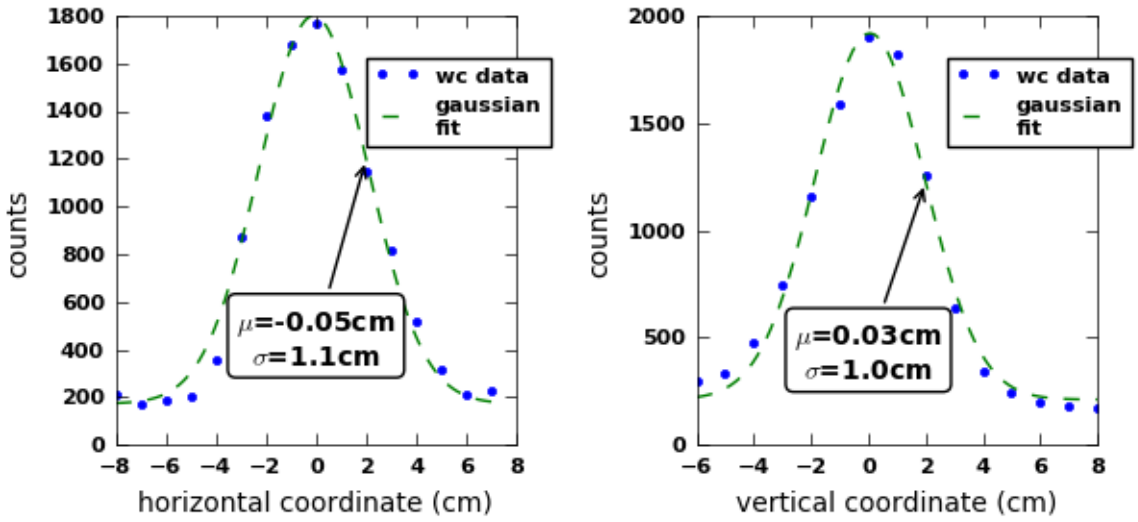

Figure 4.17: Horizontal (left) and vertical (right) beam profiles measured by the wire chamber profile monitor. Gaussian fits to these profiles give a beam centering within $1mm$ and FWHM of $\sim 2.3mm$.

beam shape, centering and energy before every measurement.

Wire Chamber Profile Monitor

The wire chamber profile monitor determines the spatial distribution and positioning of the input beam. This readout is used by the TRIUMF control room operator to tune the beam before waterbox QA measurements or treatment. Figure 4.17 shows a typical wire chamber readout for a tuned beam. The central part of the beam is Gaussian in both directions with a constant term base-line. The periphery of the beam deviates slightly from Gaussian; however, this portion of the beam is collimated out upstream of the scatterer.

Additionally, down stream quadrant chambers are used for beam angle management. Commissioning measurements [6] indicate the beam should not deviate by more than 10% in any quadrant of the downstream chamber. During these measurements the quadrant chamber was monitor and if it deviated by more than 10% the beam was re-turned.

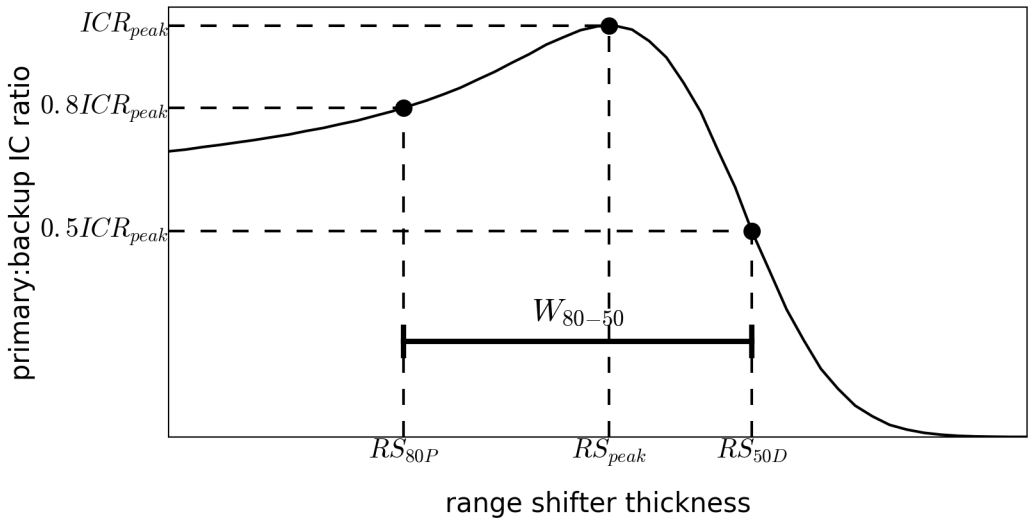

Figure 4.18: Transmission peak diagram showing analysis quantities: peak position RS_{peak} and 80%-50% width W_{80-50}.

Transmission Scan

The final set of measurements in this section is the transmission scan. Both the range and axial distribution of dose in water is dependent on the energy and energy spread of the beam. TRIUMF supplies a beam which is roughly calibrated to the desired energy. However for treatment purposes, it is necessary to confirm the provided beam has a range within clinical expectations. TRIUMF makes use of a proprietary method[6], plotting the ratio of upstream to downstream ion chamber counts as a function of Lucite blocking the beam. This is achieved by measuring counts in these chambers for various range-shifter settings. The resulting plot has a shape similar to a BP as shown in Figure 4.18. To assess the range of the beam, a calibration curve relating range with the peak of the transmission scan is determined in the QA process.

Figure 4.18 shows the two metrics measured from the curve which are used in this study - peak position (RS_{peak}) and 80%-50% peak width (W_{80-50}). As with a BP in water, it is expected that the peak position is correlated to beam energy and peak width correlated to energy spread. Measurement of this curve thereby determines the energy and energy spread to be provided to the Monte Carlo simulation.

There is no closed-form formula for the shape of the transmission curve. Additionally, simulation of the curve is very resource intensive requiring precise estimation

Algorithm - Transmission curve fitting

The peak and width of a given transmission curve data set A_n are determined by fitting a test function $f_{test} : RS \rightarrow ICR$ from range shifter setting (RS) to ion chamber ratio (ICR) to the data. The procedure is as follows:

1. select n measured transmission curves $f_i(RS)$ from a wide range of dates
2. fit f_i to cubic splines to determine peak positions k_i in a similar fashion to Figure 4.3
3. determine test f_{test} by aligning and averaging f_i:

$$f_{test}(RS) = \sum_i f_i(RS - k_i)/n \tag{4.5}$$

4. determine 'stretch' and 'offset' parameters k, b by fitting $f_{test}(k(RS + b))$ to sample data A_n
5. measure RS_{peak} and W_{80-50} from best fit $f_{test}(k(RS + b))$

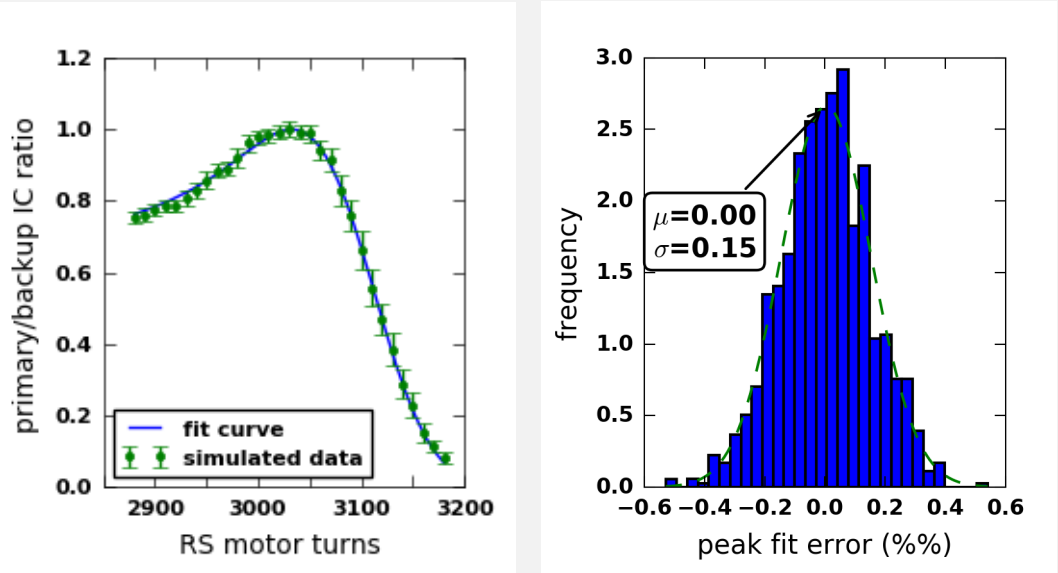

The left image shows the 'fit curve' test function along with simulated transmission curve data. Data sampled at with a maximum 10% uncertainty still allows for a precise fitting of peak and width, despite lack of an analytic model function. The right image shows repetition of this process on synthetic RS curves at 10% uncertainty. The result is a mean peak fitting accuracy of 0.02% (∼6 turns on 3000) with a standard deviation of 0.15% of peak value. Uncertainty on peak fits are taken as this standard deviation and applied to all assessments of RS curve metrics.

Figure 4.19: Description of transmission curve peak/spread fitting and associated uncertainties.

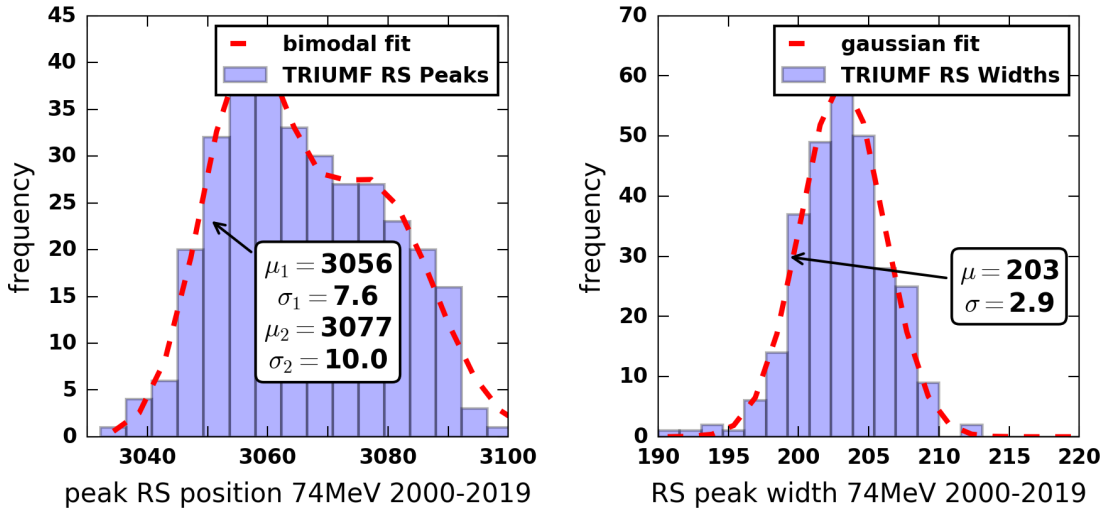

Figure 4.20: Transmission curve peaks (left) and transmission curve 80%-50% spreads (right) for all TRIUMF $74MeV$ beams 2000-2019. Bimodal fit to peak position gives two peaks at 3056 and 3077 corresponding to the two range shifter wheels.

of the peak position at a relatively low sampling rate. Fitting is preformed using an a priori curve shape determined from range scan data. The fitting process is described and associated uncertainties quantified in Figure 4.19.

Transmission scans for all TRIUMF $74MeV$ beams from 2000-2019 were assessed for peak position and spread. Figure 4.20 (left) shows a histogram of RS peak positions. Here the distribution is fit to a bimodal (sum of Gaussians) curve giving two distinct peaks at 3056±8 and 3077±10. These peaks correspond to the two pieces of hardware used during this time-frame, each having a different calibration curve. Figure 4.20 (right) shows a mean energy spread of 203±3, indicating no hardware dependence in the energy spread. The cross correlation between these two quantities was 0.11 - indicating that they may be modeled independently for the purpose of simulation beam energy calibration.

4.2 Simulated Primary Dose

The theory of Monte Carlo simulations is discussed in §2.4 and the details of the model geometry and beam are discussed in §3. This section concerns the validation of measurements of §4.1. The general goal for validation is agreement between the simulation and measurement within 2% of treatment dose in water. To achieve this,

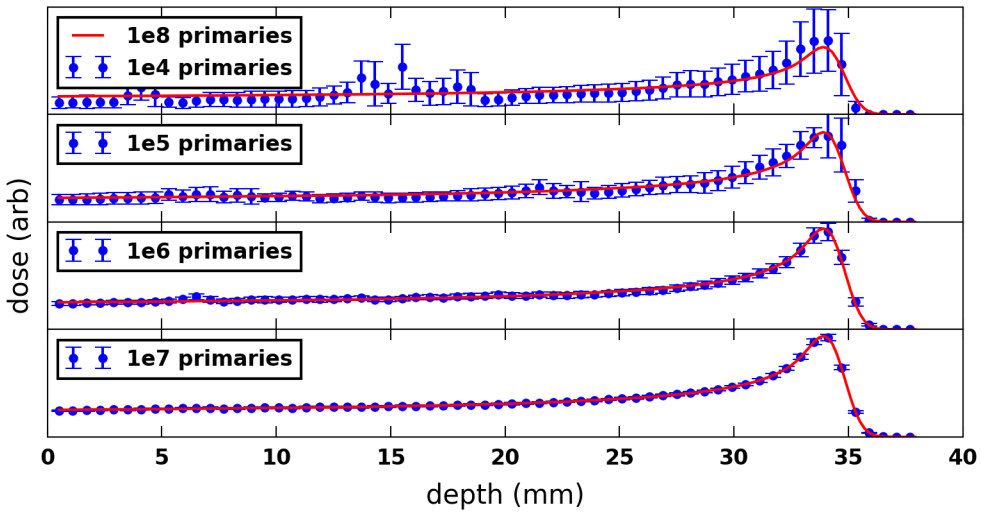

Figure 4.21: Four simulated BP in water corresponding to 10^4,10^5,10^6,10^7 primary particles from top to bottom, compared with $1e8$ primaries shown in red.

an appropriate number of primaries must be selected to simulate dose.

4.2.1 Uncertainties

As discussed in the theory section, physical quantities simulated using Monte Carlo particle transport software are accompanied by statistical uncertainties. The main factor in statistical uncertainty in a measurement is the number of processes of each type recorded. For the case of protons in water or air, this is proportional to the cross section of the interaction (scaling with density to first order), volume over which the quantity is integrated, and number of primary particles.

All simulated quantities in this section are scorings of energy deposition in detector media or water. Each scored volume is ideally identical to the volume of the corresponding measurement device. For example, profiles are measured using the diode as described in §4.1.1. Simulated profiles are scored as dose in water over active volume of the diode. Similarly for the Markus chamber and the primary/secondary ion chambers.

Thus, the only controllable factor in limiting statistical uncertainty is the number of primary particles selected for the simulation. Figure 4.21 shows the effect of increasing the number of input primaries. As the number is increased, the scored quantity of dose converges to the smooth continuous distribution of the BP in water.

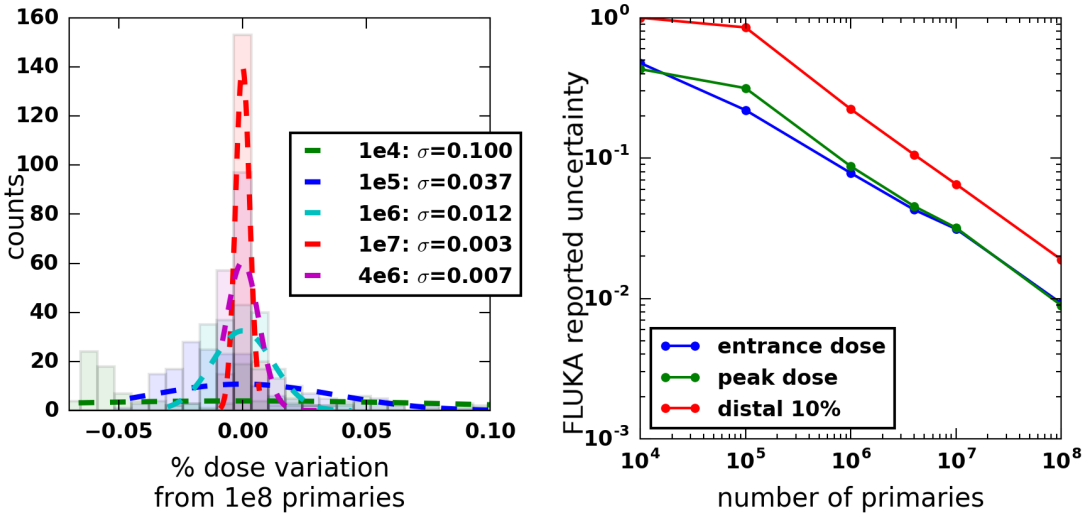

Figure 4.22: Histogram of point-by-point variation in dose for differing input primaries (left) and FLUKA reported statistical uncertainty at entrance, peak and distal 10% points of a pristine BP in water (right).

Figure 4.22 (left) shows histograms of point-by-point variation from the 10^8 primary simulation. Indeed, the variation decreases by roughly a factor of $\sqrt{10} \approx 3.1$ for each factor of ten increase in primaries. This is consistent with a Poisson distributed variable (counting interactions).

Ideally, a measured BP would be compared against simulation in the very large limit - where fluctuations from the convergent value are smaller than fluctuations in measured values. Practically speaking, computational cost increases linearly with number of primaries. Producing only one BP at 10^8 primaries takes 400 core-hours of processing.

Figure 4.22 (right) shows the statistical uncertainty reported by FLUKA over a range of primaries for various measurements on a BP. The reported error is significantly higher at the 10% distal point due to fewer protons interacting with the water at this depth. At 10^8 primaries, the maximum error is 2%. This is the number of primaries used for all quantities measured in waterbox volumes.

For dose in air (primary/secondary ion chambers), the reported error scales with medium density (to first order). Thus uncertainty in air is ∼1000x higher than water. Importance biasing is employed to reduce this by a factor of 10 (FLUKA maximum). With the increased volume of the ion chambers, this reduces maximum uncertainty on readout to 10% for 10^8 primaries.

4.2.2 Beam Calibration

Due to the range/energy relation described in section 2.2.2, the energy of the beam input to a simulation must be calibrated on a beam-tune basis. Before measuring dose in water, beam position, shape, energy, and energy spread for the beam tune must be determined. The beam shape is selected to match the wire chamber profile monitor as in Figure 4.17. It is assumed that this shape remains stable throughout the run [7]. The beam is taken to be centered in the simulation, as this is the goal of beam tuning before measurement and consistent with Figure 4.17.

To calibrate energy, the transmission scan of §4.1.7 is simulated. Each simulated scan consists of thirty points, each being a separate simulation run of 10^8 primaries for a total of 12,000 core-hours. The maximum uncertainty on any point is 10%. Accuracy of fitting transmission scan peak was found to be within 0.15% at a 10% statistical uncertainty per data point (Figure 4.19).

A total of fifteen transmission scans with energies from 69.5-74.5MeV were simulated and their peak positions were plotted to produce Figure 4.23 (left). This calibration curve required 180,000 core-hours of computation. This calibration curve is linear, with uncertainties estimated via the method of Figure 4.19. Additionally, energy spread was independently calibrated with five measurements spanning the range of TRIUMF energy spread values as in Figure 4.20. This yielded an excellent linear fit as shown in Figure 4.23 (right).

Figure 4.24 shows a measured and simulated transmission scan. The percent difference shown below gives a maximum 2.5% variation between the measured and simulated curves. Considering the reported statistical uncertainty on the FLUKA simulated curve was 10%, this difference curve is quite low in magnitude. This is indicative that FLUKA is over-estimating statistical uncertainty in this measurement. Using the calibration curve of Figure 4.23, this beam corresponded to a FLUKA simulation energy of 74.11MeV and spread of 0.15MeV. This is consistent with the target beam energy of 74MeV and Figure 4.20. The following simulation of waterbox dose is calibrated to this energy.

4.2.3 Pristine Depth Dose

With a calibrated beam energy, shape and position, dose simulated in water can be compared to measurement. Here only 74MeV beams are simulated (70MeV beams are validated as a part of a published manuscript in chapter 6).

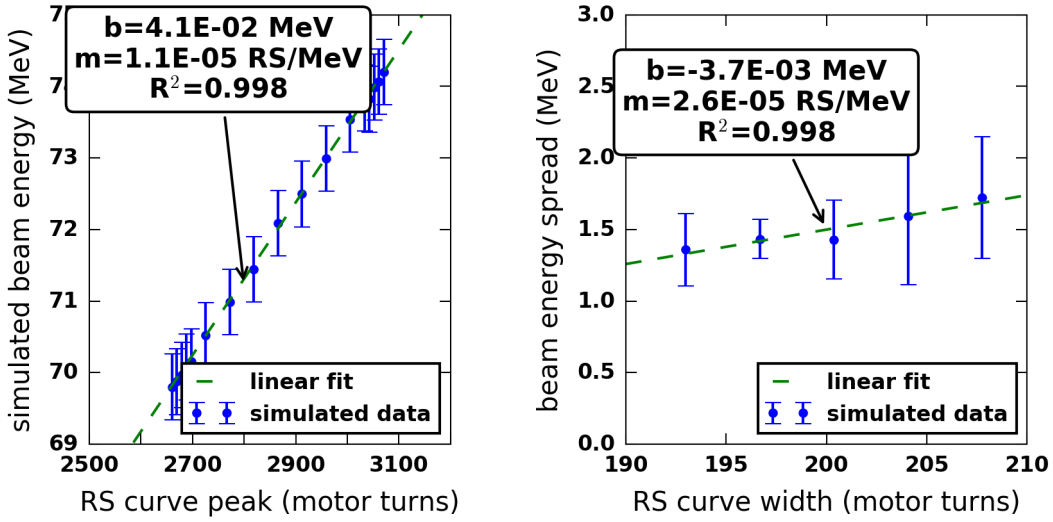

Figure 4.23: (left) plot of peak position as function of energy, peak spread as function of spread at $74MeV$, (right) correlation of spread/energy

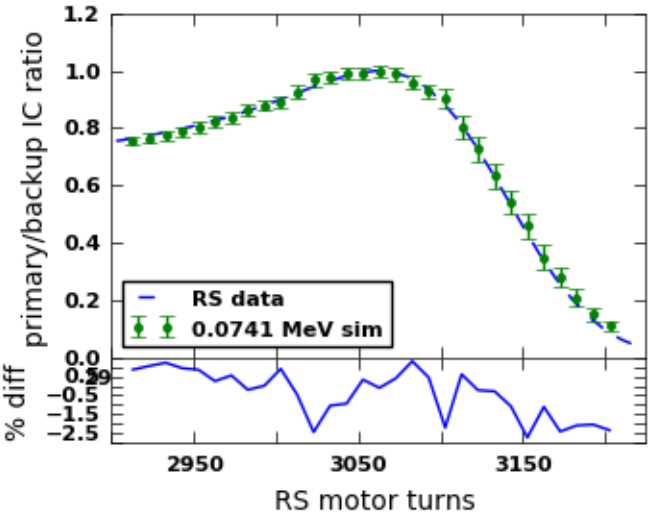

	meas. (±5)	FLUKA sim. (±5)
RS_{peak}	3062	3063
W_{80-50}	201	197

Figure 4.24: Plot of $74MeV$ beam transmission scan and simulated transmission scan, table showing compareable quants.

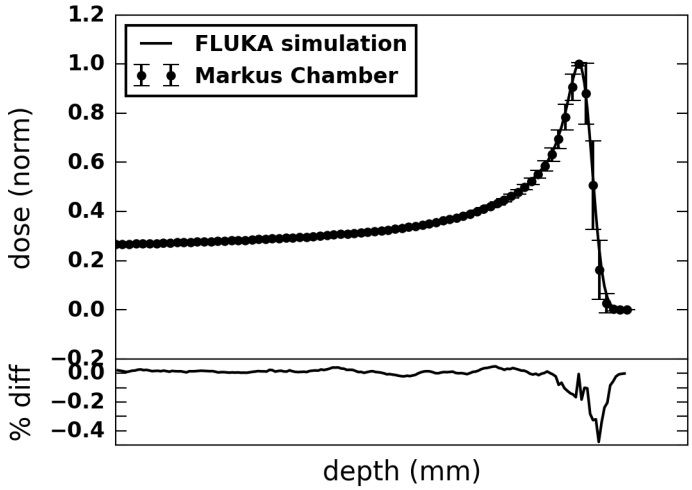

	FLUKA	Markus
R_{peak}	32.4	32.4
$Ratio_{PE}$	3.77	3.75
R_{80}	33.0	33.0
R_{20}	33.9	33.8
W_{80-20}	0.9	0.8

Figure 4.25: Comparison of Markus chamber measured pristine BP to FLUKA simulated pristine BP calibrated to $74.11 \pm 0.15 MeV$.

Figure 4.25 shows a pristine BP as measured by the Markus chamber overlaid with FLUKA simulated pristine BP. Difference plots show a maximum 0.4% of peak dose difference between the two occurring at the distal end of the BP. Discrepancies here are associated with mis-calibrated peak position (energy) or energy spread. The order of the discrepancy is highest here due to the large dose gradient. This difference near the dose gradient is consistent with similar Monte Carlo studies of ocular proton systems [94, 95, 96]. The simulated BP is consistent with measurement throughout the entire depth. All analysis quantities, as tabulated to the right, are consistent between the Markus chamber measurements and FLUKA simulations.

4.2.4 Range-Shifted Bragg Peak

Figure 4.26 shows range-shifted BP measurements overlaid with FLUKA simulated results. As in the case of the pristine peak, the measured data is consistent with simulated results. However, a more pronounced residual associated with the peak of the distribution is notable here. The maximum 1.2% residual is consistent for all range shifts perhaps indicating a systematic inaccuracy in the range shifter calibration (Equation 3.1). This is a very small effect (order 100 microns) and could be accounted for by including uncertainties in the calibration of the range shifter. Variation in beam tune over the course of the run could also produce an effect at this level. This effect

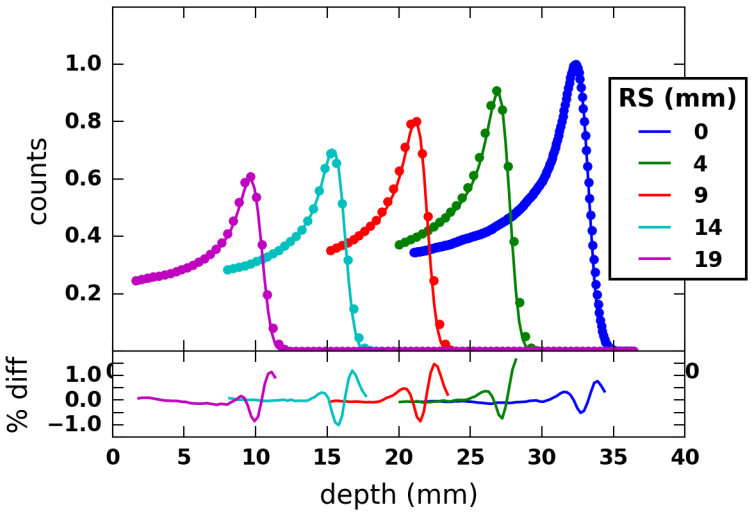

RS (mm)	R_{peak} ($\pm 0.3mm$)	OF_{RS} (± 0.2)
0	32.4	1
4.7	26.8	0.91
9.7	21.1	0.81
14.7	15.3	0.69
19.7	9.5	0.61

Figure 4.26: Comparison of Markus chamber measured range-shifted BP to FLUKA simulated BP calibrated to $74.11 \pm 0.15 MeV$.

is not noticeable when comparing tabulated analysis quantities of Figures 4.26 and 4.6.

4.2.5 Spread out Bragg Peak

Figures 4.27-4.29 show SOBP distributions measured using the Markus chamber for $8mm$,$14mm$ and $23mm$ respectively. All residual plots have a maximum of 0.4% D_{mid} discrepancy. This again most often occurs at the distal end of the distribution as in the pristine case. All plateau metrics, tabulated with the plots, are consistent between measured data and simulated results except for the modulation width of the largest wheel. Here the 90% range is within $0.2mm$, but the modulation width difference is $0.5mm$, exceeding the assigned uncertainty of 0.3mm. Thus the discrepancy occurs due to the assignment of the 98% range point. This point is extremely sensitive to measurement fluctuation and plateau fitting due to the locally low dose gradient for the $23mm$ SOBP. This sensitivity near this point is a well documented effect[89] and likely the cause of the modulation width discrepancy.

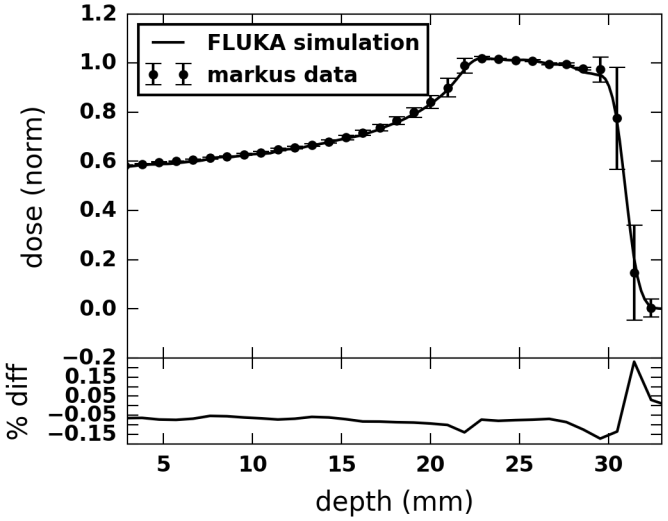

	Markus	FLUKA
R_{90}	30.0	30.0
W_{80-20}	1.1	1.0
m_{98} ($\pm 0.3mm$)	8.2	8.0
$Ratio_{ME}$ (± 0.02)	1.76	1.80

Figure 4.27: FLUKA simulated SOBP overlaid with measured Markus chamber data for a $74.11MeV$ $8mm$ SOBP.

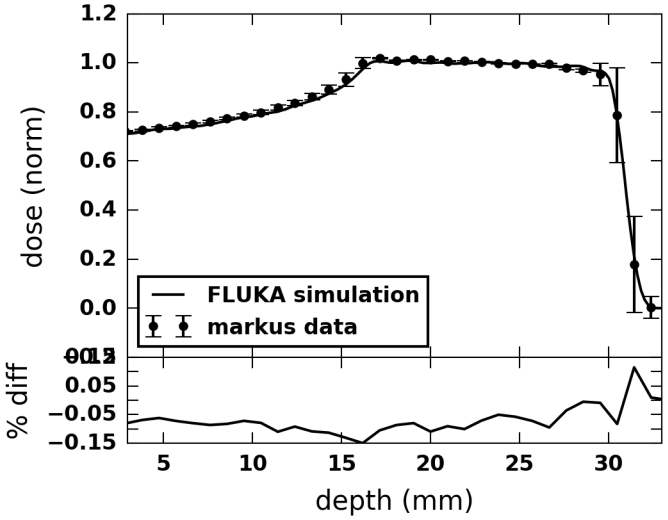

	Markus	FLUKA
R_{90}	30.0	30.2
W_{80-20}	1.0	1.1
m_{98} ($\pm 0.3mm$)	14.1	13.9
$Ratio_{ME}$ (± 0.02)	1.43	1.47

Figure 4.28: FLUKA simulated SOBP overlaid with measured Markus chamber data for a $74.11MeV$ $14mm$ SOBP.

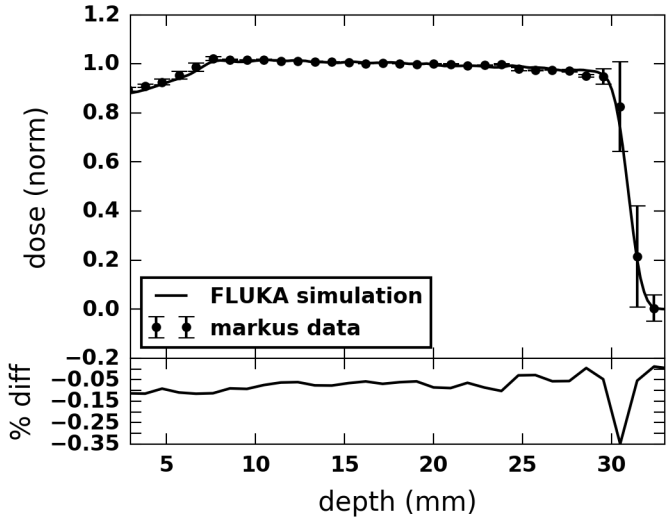

	Markus	FLUKA
R_{90}	30.2	30.0
W_{80-20}	1.0	1.1
m_{98} ($\pm 0.3mm$)	23.6	23.1
$Ratio_{ME}$ (± 0.02)	1.16	1.19

Figure 4.29: FLUKA simulated SOBP overlaid with measured Markus chamber data for a $74.11MeV$ $23mm$ SOBP.

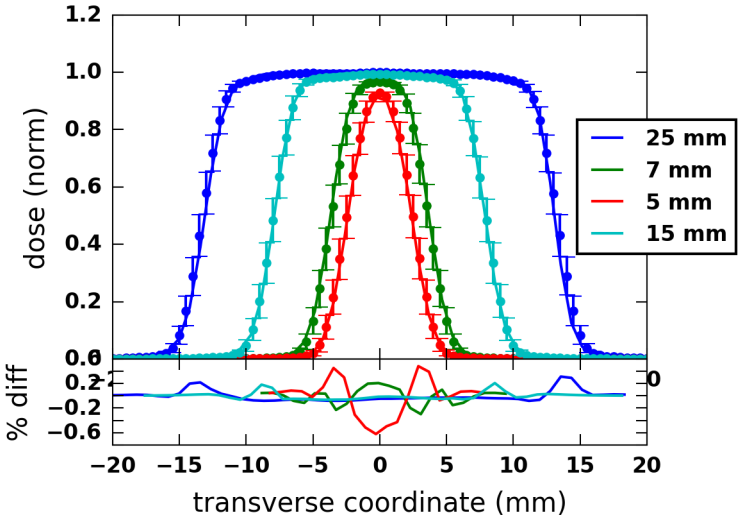

Col. Size (mm)	Field Size (mm)	W_{80-20} (mm)	OF (± 0.01)
5	5.0	2.0	0.93
7	7.4	2.0	0.97
15	15.8	2.1	0.99
25	26.2	2.2	1

Figure 4.30: FLUKA simulated profile overlaid with diode data for various collimators measured at SOBP center (depth) for a $74MeV$ SOBP of width $23mm$.

4.2.6 Profiles

Lastly, Figure 4.30 shows FLUKA simulated profiles corresponding to the diode data of Figure 4.16. Here the simulation yielded a maximum 1% statistical uncertainty in the center of the profile. Residual plots for all collimators except the smallest ($5mm$) are within $\sim$0.2% variation. The most significant discrepancy between simulation and measurement occurs at the lateral penumbra. This effect is not completely accounted for by positioning error alone. There is a real difference in the penumbra which is well documented by other Monte Carlo studies [94, 95]. Despite this, lateral penumbral and field sizes are consistent between FLUKA and diode measurements as tabulated in Figures 4.30 and 4.16. The smallest field size, $5mm$ is discrepant in output factor (0.91 data vs 0.93 FLUKA) due to the $\sim$0.6% difference at the center of the field. Close inspection yields an under-sampling near the peak which causes this effect.

4.3 Neutron Measurements

4.3.1 Methods and Hardware

The general procedure for a neutron survey measurement is as follows:

1. setup of lucite beam stop and neutron detector
2. requesting beam from the TRIUMF control room
3. recording secondary emission monitor counts for requested current
4. controlling beam on/off using the fast shutter at the PT control room
5. ensuring proper beam centering/width on the profile monitor (±5%)
6. calibrating daily energy using the range shifter transmission method
7. recording background counts on neutron detector
8. acquiring data for a pre-determined amount of time (1 minute)
9. recording data in the PT control via manual readout of a counter

Beam Setup

Beam setup was identical to the procedure in sec 4.1.1 with the exception that quadrant chamber deflection was restricted to a maximum deflection of ± 5%. This is because neutron generation is dominated by beam current on the collimators which is highly sensitive to beam centering.

Boron Trifluoride Neutron Detector

Neutron survey measurements were performed using a boron trifluoride (BF3) neutron detector (Centronic REM/N, [97]) colloquially referred to as a 'snoopy' detector. Approximate confirmation of the response of this detector in the PT room is desirable when simulating secondary patient dose. This detector was selected based on availability and ease of use. Other detectors, such as Bonner spheres, offer a better understanding of the neutron spectrum and dose resulting from the beamline; but,

they require significant effort in measurement and simulation. This work which focuses on primary dose characteristics, hence detailed and precise validation of the neutron model was not pursued.

The detector was provided and calibrated, with an Americium Beryllium (AmBe) source, by the TRIUMF radiation protection group. The detector was shielded with a polyethylene moderator and typically suitable for neutrons between $1MeV$ and $20MeV$ [97]. The BF3 response curve (C_{BF3}) is shown in figure 4.31 along with a typical spectrum incident on the detector modeled using FLUKA. Also shown is the fluence to dose conversion factor (C_{AMB74}). Note that this factor is not identical to the BF3 response; hence, measurements using the BF3 detector must be corrected. The experimental spectrum extends out to $\sim 70MeV$, indicating dose rate would be under counted in this case. This effect is small as ∼99% of neutrons produced are below $20MeV$. An more accurate measure of beamline dose rate requires additional detectors suitable for thermal and $> 20MeV$ neutrons. Instead of trying to measure physical dose rate, the goal of this exercise is to simulate the BF3 detector response given a dose calibration to an AmBe source. The reported calibration factor for the detector was $C_{BF3} = 0.049\, uSv/hr/cpm$ with an estimated uncertainty of 20%. The relatively high uncertainty speaks to precision of using this instrument in the context of radiation safety. For reference, neutron dose rates recorded using this factor and instrument are doubled by the radiation safety group in safety measurements [98].

Beam was taken under standard patient conditions. Neutron generation directly scales with beam current; hence, variation in the current and beam angle must be monitored more closely than in proton dose measurements. The beam angle was monitored throughout, and kept within 5% deflection on the quadrant chambers. Beam current was monitored by way of integrated secondary emission monitor (SEM) counts. The TRIUMF operator reported a current of 6 nA and instantaneous SEM count rate ($\dot{N}^{SEM}_{6nA}$) was recorded. This was taken as the approximate count rate corresponding to the requested 6 nA current with an uncertainty of 5% [100].

All measurements were taken over a one minute duration and performed 3 times - recording total SEM count rate ($\dot{N}^{SEM}_i$), primary counts, backup counts, BF3 detector counts (N^{BF3}_i) and quadrant chamber readings. The final reported dose rate ($\dot{D}_{meas}$) was the average of all readings, each scaled by their total integrated SEM counts as:

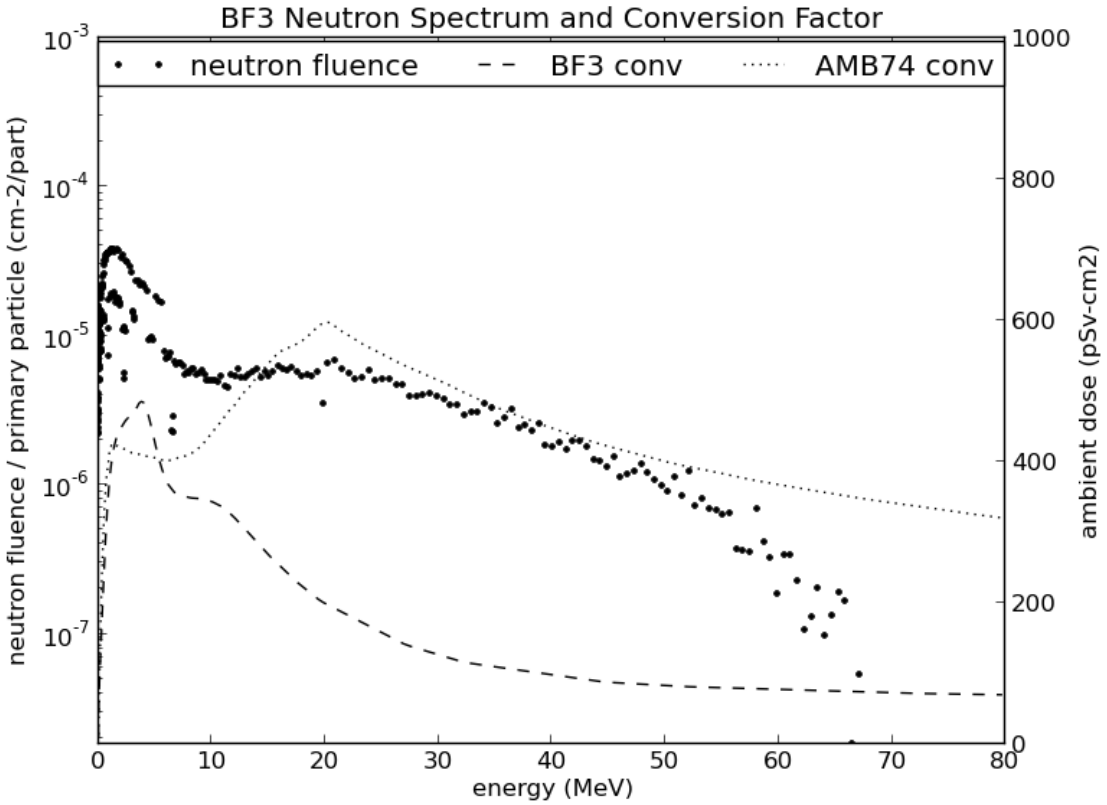

Figure 4.31: Sample FLUKA neutron spectrum (scaled left axis) alongside BF3 to ambient dose [99] and neutron flux to ambient dose [65] conversion factors (scale right axis).

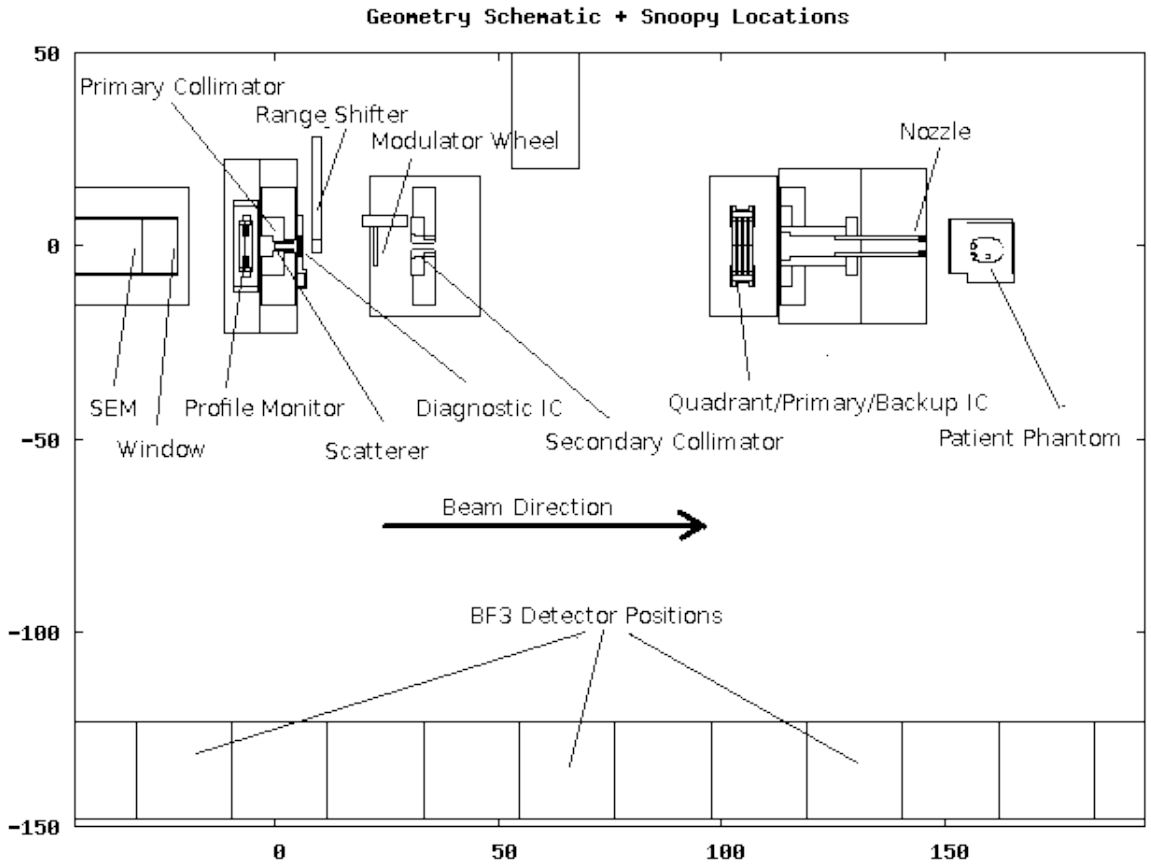

Figure 4.32: FLUKA schematic diagram of detector positions relative to treatment head for neutron survey measurements. Axes are position in *cm*.

$$\dot{D}_{meas} = \sum_i \frac{\dot{N}_i^{SEM}}{\dot{N}_{6nA}^{SEM}} \cdot N_i^{BF3} \cdot C_{BF3} \tag{4.6}$$

4.3.2 Uncertainties

Neutron survey measurements include four categories of uncertainties (in order of magnitude): instrument calibration accuracy, beam centering/size/current fluctuations, detector position accuracy, and statistical fluctuations in measurement. Reported dose rate is calculated via equation 4.6 resulting in an uncertainty ($\Delta\dot{D}_{meas}$) as:

$$\Delta\dot{D}_{meas} = \sqrt{(\frac{\Delta N_{BF3}}{N_{BF3}})^2 + (\epsilon_{cal})^2} \cdot \dot{D}_{meas} \tag{4.7}$$

where ϵ_{cal} is the reported relative error on BF3 calibration of 20%, ΔN_{BF3} is the absolute error on BF3 readout as calculated as in equation 4.1 (without the σ_{fit} term) and $\dot{D}_{meas}$ is as in equation 4.6. Note that the ϵ_{cal} term is larger by a factor of ~ 20 than the ΔN_{BF3} term. By far the uncertainty is dominated by the precision of the detector calibration - limiting the precision of measurements using this detector.

Equation 4.7 does not explicitly include current or beam angle variation. Estimation of these uncertainties are challenging as there is no real-time monitoring of beam angle and current available. However, their effect is small (compared to calibration uncertainty) given the beam angle is restricted to the $\pm$ 5% regime during measurement. While not ideal, confirmation of the smallness of these effects is determined via FLUKA simulation instead of direct measurement.

4.3.3 Neutron Measurements

Beamline Neutron Survey

With calibration conditions measured and monitored as described in sec 4.3, neutron survey measurements were taken in positions as shown in Figure 4.32. The detector was in the horizontal plane of the beam, approximately 1.4 m away, and moved parallel to the beam axis in increments of $20 cm$ down the beamline. The survey was carried out from the scatterer to the nozzle. Measurements were taken as close to the treatment head and beam window as possible given the geography of the room and dose delivery system.

Figure 4.33 shows the measured ambient dose rate using the BF3 detector and provided calibration. These rates were calculated as in equation 4.6. Due to the high uncertainty in calibration, there is an overall high uncertainty in measured dose rate. Normally, this would mean that no information can be gleaned into the shape of the curve since it is consistent with a constant dose rate. However, since the uncertainty is in the magnitude of the rate, the relative magnitudes between the measured points still contain information.

Figure 4.33 shows and overall dose rate decrease down the beamline. This is expected as the bulk of neutrons are generated at the scatterer (position $x = 0$ in the plot) and there is an expected inverse-square drop off in neutron fluence with increasing distance. Generation of neutrons is also reduced downstream due to upstream collimation resulting in decreasing beam current on the downstream collimators. Additionally there is a drop in measured dose rate parallel to the primary collimator -

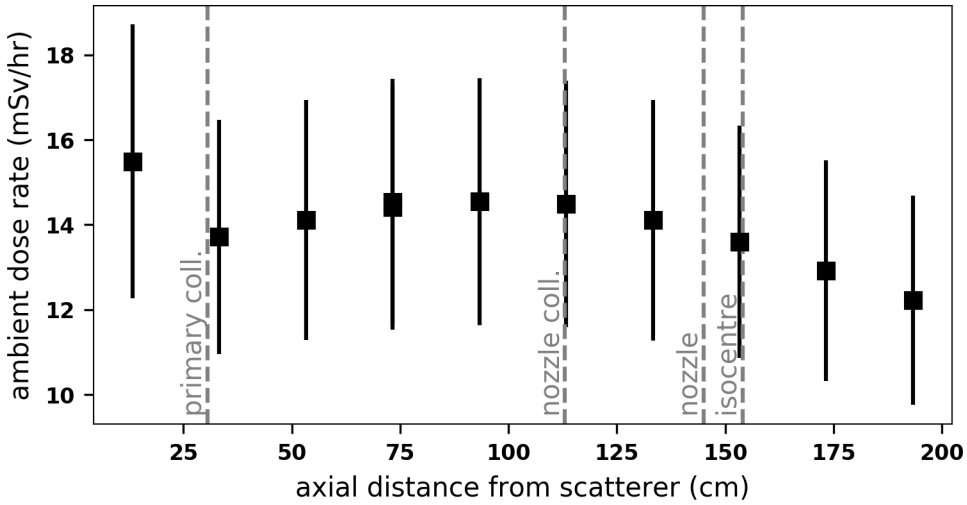

Figure 4.33: Neutron survey measurements using BF3 detector parallel to beamline axis with 1.4 m lateral separation from beam.

this is owing to the polyethylene shielding at this position.

Personal Neutron Dosimeter

During the commissioning of the TRIUMF DDS, a personal neutron dosimeter was placed at the position of a patient's elbow to estimate secondary neutron dose. The measured value was 9.3 mSv/hour. While this measurement was not performed during these studies, it is used as a point of reference for comparison.

4.4 Simulated Neutron Dose Rate

This section concerns the validation of neutron dose measurements of §4.3. The general goal for validation is agreement between the simulation and measurement within the large detector calibration uncertainty of 20% . To achieve this, an appropriate number of primaries must be selected and careful attention must be paid to the beam size and centering.

For the purpose of neutron survey simulation, the ideal quantity to simulate is neutron interactions (and their spectra) within the BF3 gas chamber. Simulation of the BF3 detector and response is beyond the scope of this work. Instead, spectral fluence of neutrons (Ψ_N) through the detector volume are scored and convolved with an

energy-dependent conversion factor (R_{AMB74}) [99] ($R(E)_{BF3}$) to determine ambient dose rate ($\dot{D}_{sim}$) calculated as:

$$\dot{D}_{sim} = \sum_i \Psi_{N_i} \cdot R(E_i)_{AMB74} \equiv \Psi_N \otimes R_{AMB74} \tag{4.8}$$

Where the summation is over the default neutron energy bins recorded by FLUKA. This is the exact dose response of the BF3 detector. However, the provided calibration for the detector, as in §4.3.1, is an approximation. Calibration is performed by measuring BF3 response for an AmBe calibration spectrum (Ψ_{AmBe}) and Equation 4.8 is used to approximate the ambient dose rate for the unknown neutron spectrum (Ψ_N). That is, the calibration factor corrects for the average spectrum of the calibration source:

$$\dot{D}_{meas} = C_{BF3} \cdot \Psi_N \otimes R_{BF3} \sim \frac{\Psi_{AmBe} \otimes R_{AMB74}}{\Psi_{AmBe} \otimes R_{BF3}} \cdot \Psi_N \otimes R_{BF3} \tag{4.9}$$

Where C_{BF3} is the reported calibration factor as in §4.3.1 and $\Psi_N \otimes R_{BF3}$ is the measured BF3 output. Thus given the ambient dose rate output by FLUKA ($\Psi_N \otimes R_{AMB74}$), the best simulated quantity to compare to the measured dose rate of equation 4.8 is:

$$\dot{D}_{cor} = C_{AmBe} \cdot \Psi_N \otimes R_{AMB74} \equiv \left(\frac{\Psi_{AmBe} \otimes R_{AMB74}}{\Psi_{AmBe} \otimes R_{BF3}} \cdot \frac{\Psi_N \otimes R_{BF3}}{\Psi_N \otimes R_{AMB74}} \right) \cdot \Psi_N \otimes R_{AMB74} \tag{4.10}$$

This corrected dose rate accounts for the built-in averaging over the AmBe calibration source and the BF3 detector response. Figure 4.34 shows this AmBe calibration correction factor C_{AmBe} as defined in Equation 4.10. Here the correction factor varies down the beamline due to the variation in neutron spectra. Values range from ∼0.94 to ∼0.84 and contribute an associated uncertainty on the order of 2% as discussed below. All reported dose rates in this section are corrected by this factor.

4.4.1 Uncertainties

As discussed in §4.2.1, quantities scored in FLUKA are subject to statistical uncertainty associated with observation of physical interactions. In the case of neutrons, their modes of production and energy deposition are discussed in §2.1.4.

The main factor in statistical uncertainty in a measurement is the number of pro-

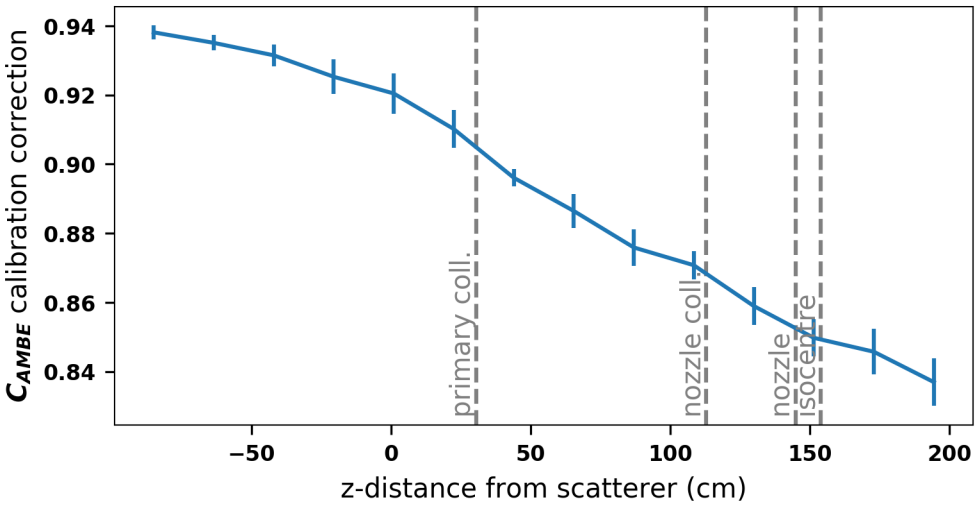

Figure 4.34: Average AmBe dose rate correction factor (C_{AMBE}) as a function of beamline position for the simulated neutron survey. Error bars are one standard deviation amongst all simulated beam angle samples.

cesses of each type recorded. Neutron interaction cross sections (energy deposition) are small compared to protons due to their lack of charge. Hence energy deposition events are more rare, requiring a larger number of neutrons traversing the scoring volume to achieve a low uncertainty in scored dose. However, in recording spectral fluence as described above, no real neutron interaction is required to take place; only traversal through the volume is necessary to be scored. Hence the counts are not suppressed by orders of magnitude by the neutron interaction cross section. With this, a reasonably low statistical uncertainty may be achieved within a tractable computation time.

The reported uncertainty in dose rate ($\Delta\dot{D}_{sim}$) then follows from Equation 4.8 - adding the FLUKA statistical uncertainties (ϵ_{Ψ_i}) per energy bin in quadrature as:

$$\Delta\dot{D}_{sim} = \sqrt{\sum_i \left(\Psi_{N_i} \cdot R(E_i)_{BF3} \cdot \epsilon_{\Psi_i}\right)^2} \tag{4.11}$$

The uncertainty on the final corrected dose rate of Equation 4.10 is then the relative uncertainty of Equation 4.11 added in quadrature with the calculated relative uncertainty for C_{AMBE}.

Figure 4.35 shows the maximum and minimum uncertainty in corrected dose rate. Here the calculated uncertainty is at the $\sim$1% level at $\sim 10^8$ primary protons. We accept this as the target number of primaries for an accurate simulation considering the relatively high measured uncertainty of 20%. Note that on the order of $10^{10} - 10^{11}$ primaries would be required to achieve this same result if absorbed neutron dose was the scored quantity.

4.4.2 Beam Angle and Size Simulation

As discussed in §2.1.4, neutron production is driven by proton beam current on collimators and beam degraders. No degraders were used in the survey so we only examine the effect of beam current on collimators; this is determined by beam shape, angle and input current:

Beam Shape

Beam shape remains stable throughout a run with a target beam FWHM of 1-2cm [100]. This beam size was recorded during the neutron survey and used as input to the simulation as described in 4.1.7.

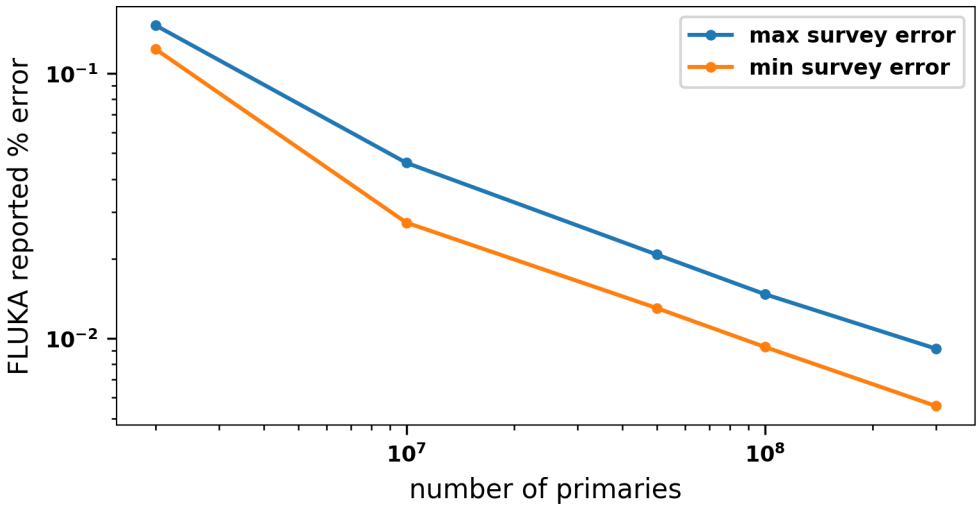

Figure 4.35:]
Maximum and minimum FLUKA relative error for neutron survey simulation, for a range of primaries, as calculated in Equation 4.11.

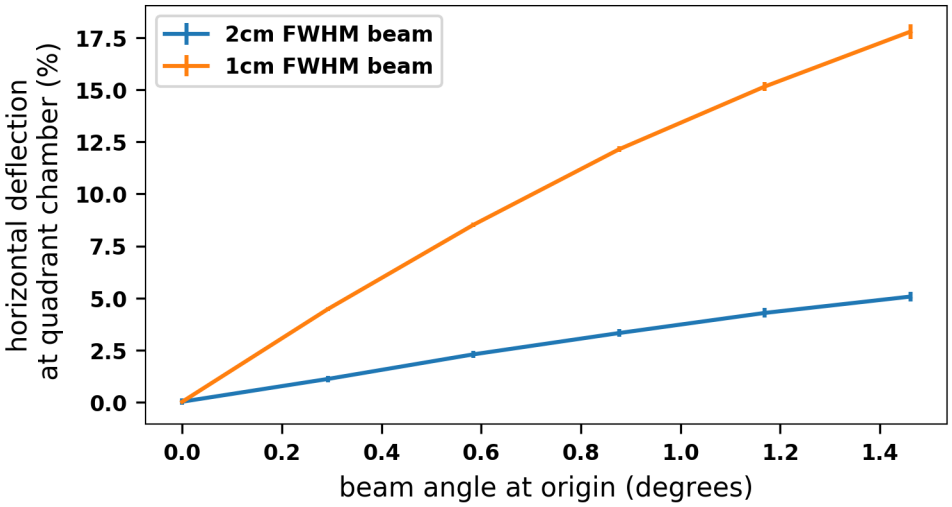

Figure 4.36: Simulated deflection of primary beam at the quadrant chamber for large ($2cm$) and small ($1cm$) beam sizes over a range of initial beam angles. Beam deflection at quadrant chamber is restricted to $\pm$ 5% during patient treatment.

Beam Angle

Beam angle is allowed to vary between $\pm$ 5% deflection at the quadrant chambers. This effect must be simulated and variation in neutron output analyzed for the extrema of allowed beam angles.

The angle information input to FLUKA is the angle of the proton beam at origin. A simulation of various origin angles is necessary to model the resulting beam deflection at the quadrant chamber. Figure 4.36 shows the simulated % deflection recorded by the quadrant chambers for a given beam angle at the origin. Here the extrema of allowed beam angle are 0.33 ± 0.02 and 1.4 ± 0.1 degrees for the $1cm$ and $2cm$ beam sizes respectively. These values are taken as the extrema of simulated beam angle for neutron survey simulation. As expected, quadrant chamber readout is coupled in beam angle and size. This is due to the Gaussian shaped beam profile; a more narrow beam yields a higher readout deflection downstream for a given angle.

Beam Current

Beam current carries an estimated variation through a run at 5%. As discussed in §4.3.3 beam current is monitored via SEM counts and the measured data is corrected to the integrated count rate. Thus, to first order (neglecting coupling between

time-varying current and beam angle), the FLUKA simulation can safely ignore time dependent current variation.

Also of interest in simulating neutron dose is beam current lost at each collimator. Ultimately the FLUKA simulation is useful in modeling secondary dose to a patient. Total secondary patient dose increases as the primary dose rate decreases due to extra time spent in treatment and increased beam current on collimators. Thus it is important to know how beam steering and size affect the current drop across each set of collimators.

Figures 4.37 and 4.38 show the beam current measured down the beamline for $1cm$ and $2cm$ beam sizes respectively. Here plots are shown for the minimum and maximum allowed deflection angles as shown in Figure 4.36. For the $1cm$ beam case about $\sim$40% of the beam current is lost between each of the primary and secondary collimators independent of beam deflection. This differs dramatically from the $2cm$ beam which seems $\sim$80% of the beam lost in the primary collimator. For neutron production this would indicate that the $1cm$ beam would produce higher secondary dose to the patient since more neutrons are generated in the secondary collimator. However, the increased treatment time for the $2cm$ beam dominates neutron dose to a patient as the treatment dose rate is less than half for the $2cm$ compared to the $1cm$ beam. Simulating these effects will be useful in assessing anatomic neutron dose.

4.4.3 Neutron Survey Simulation

Figure 4.32 shows the positions of the detector volumes in the FLUKA simulation. Ambient dose rate was scored and corrected to the AmBe calibration as described in §4.4.

Figure 4.39 shows the simulated survey dose rates for the $1cm$ and $2cm$ beam sizes. Here, five angles spanning the 5% deflection tolerance were simulated. The shape of the curves are similar with most neutron generation occurring at the scatterer/first collimator, followed by a dip in dose in the shielded area around $z = 30cm$, then followed by a rise in dose rate due to roughly isotropic neutron generation around the secondary and nozzle collimators.

The most notable difference between the two beam sizes is the increased ambient dose in the case of the larger beam. This is intuitive as more of the beam is impinging on the upstream collimator. This effect is most noticeable at high beam deflection where the neutron dose rate increases by $\sim$ 20%.

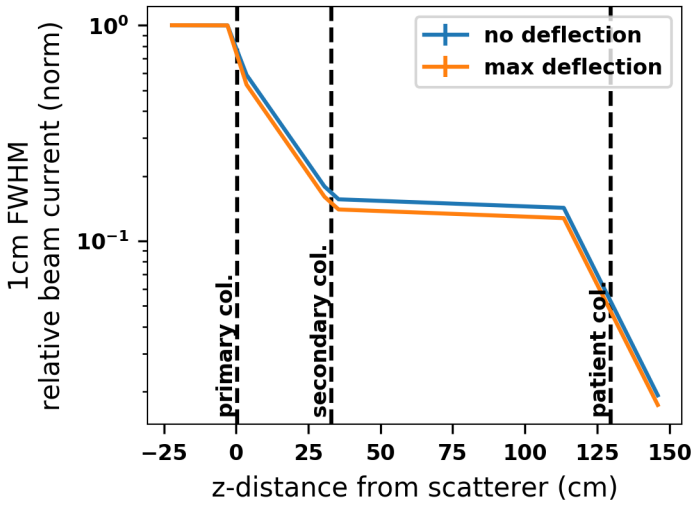

beam deflection	min	max
fractional current lost by col.		
primary	0.41	0.47
secondary	0.43	0.39
patient	0.12	0.11
final current	0.02	0.02

Figure 4.37: (left) Relative proton beam current measured at various positions throughout the DDS for a $1cm$ sized beam at minimum (0 degrees) and maximum (0.33 degrees) allowed beam deflection. Plot is normalized to measured current at the vacuum window. (right) Table showing fraction of beam current lost through each collimator.

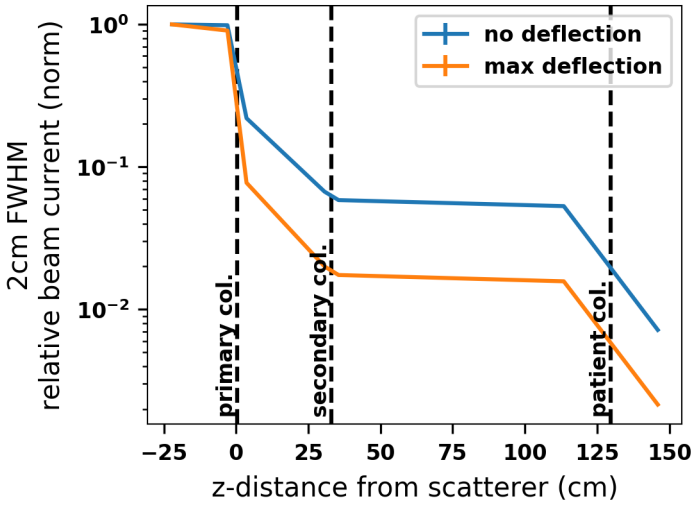

beam deflection	min	max
fractional current lost by col.		
primary	0.77	0.83
secondary	0.16	0.06
patient	0.05	0.01
final current	0.01	0.003

Figure 4.38: (left) Relative proton beam current measured at various positions throughout the DDS for a $2cm$ sized beam at minimum (0 degrees) and maximum (1.45 degrees) allowed beam deflection. Plot is normalized to measured current at the vacuum window. (right) Table showing fraction of beam current lost through each collimator.

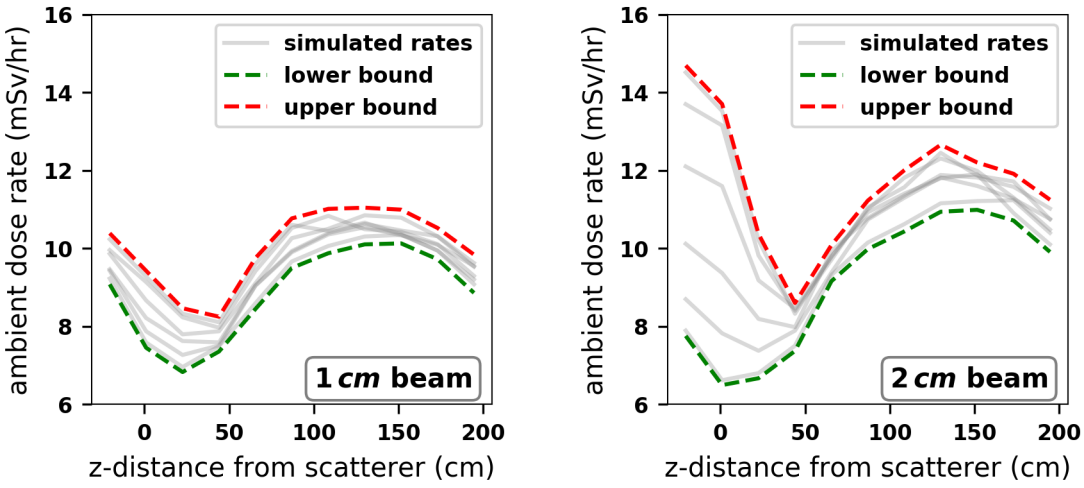

Figure 4.39: FLUKA simulated ambient dose rate as measured by BF3 detector for $1cm$ (left) and $2cm$ (right) beam sizes. Shown are outputs for angles within 5% tolerence range on quadrant chamber along with upper and lower bounds.

Figure 4.41 shows the angle-averaged simulated dose rate for the two beam sizes. This average assumes a flat distribution of beam angles during a measurement. This is unrealistic, but the most reasonable approximation to the average dose rate given no real-time information is available for beam angle distribution. More visible in these plots are the effects of the secondary and nozzle shielding on the dose rate. In the angle-averaged rate, both beam shapes show a notable dip parallel to the nozzle shielding. As expected the $2cm$ beam produces an overall higher neutron dose rate due to more of the beam impinging on the brass collimators throughout the beamline.

Figure 4.40 shows the measured BF3 survey data along with upper and lower angle bounds for a $1.8cm$ beam (the recorded beam size for the measurement). Overall the shape of the measured data matches that of the simulation - a high initial dose rate; a dip corresponding to the shielding; and a gradual dose rate decrease down the beamline.

In magnitude, the data is consistent with simulation except in the region shielded by the primary/secondary collimator shields ($\sim$20-80cm). This could be indicative that the FLUKA simulation over-models the effect of shielding on the resulting neutron flux. Also, the physical neutron shielding may be degraded, reducing its capacity to moderate neutrons produced around the scatterer. Another source of this discrepancy could be the significant difference in neutron energy spectrum as a resulting from moderation in the shielding. The AmBe calibration takes only an average over the calibration spectrum which may not be sufficient to discern differences in dose rate arising from this effect. Compounding this effect is the recording of neutron spectra through the entire detector volume, as opposed to only the active area which has additional un-modeled shielding.

Despite this discrepancy, the FLUKA simulation was able to simulate the magnitude of the ambient dose rate with a reasonable accuracy - especially considering the large uncertainty in detector calibration.

Lastly, Figure 4.41 indicates an average dose rate of 9.5-10.5 mSv/hr at the location of the patient. This is consistent with the personal neutron dosimeter reading of 9.3 mSv/hr taken during the DDS commissioning. Note that the personal dosimeter reading was located below the beamline which could have resulted in a reduced dose rate.

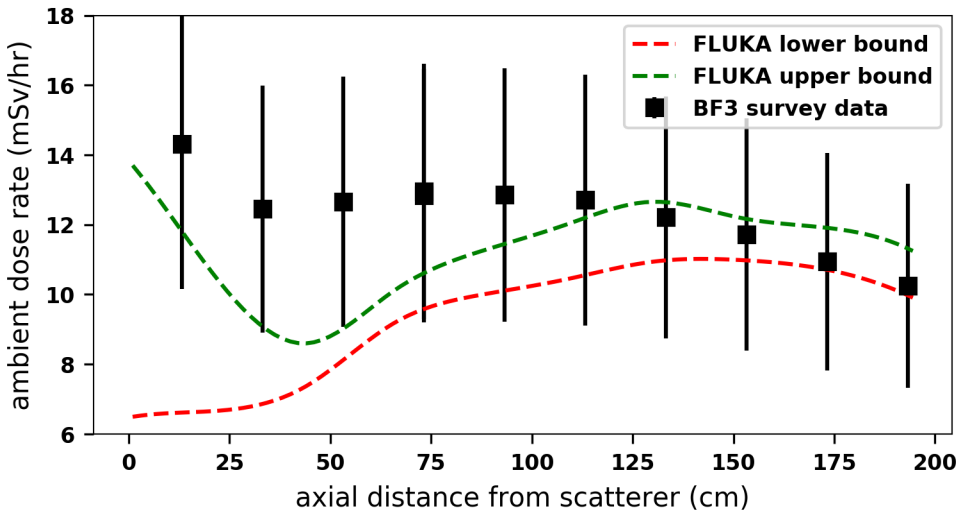

Figure 4.40: FLUKA simulated ambient dose rate for $1.8cm$ beam compared to measured BF3 survey data.

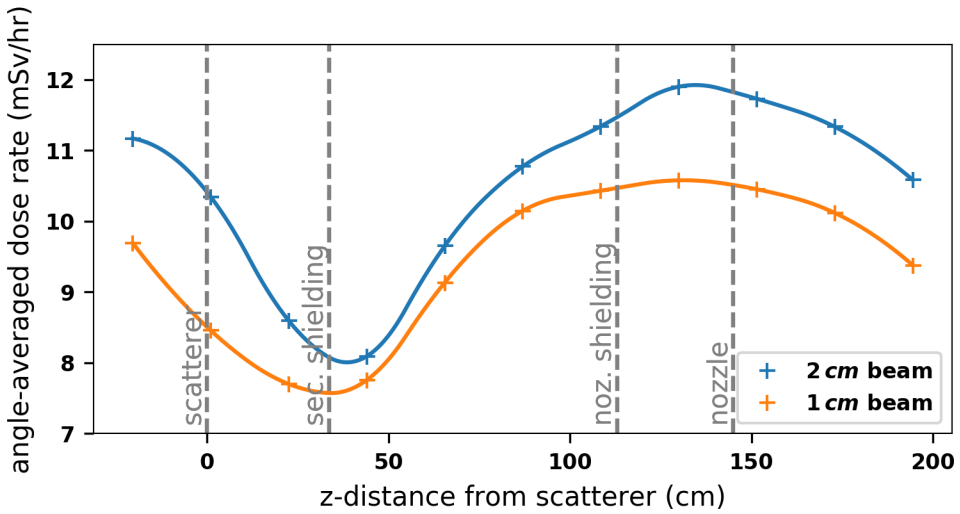

Figure 4.41: FLUKA simulated ambient dose rate averaged over the 5% deflection tolerance range for $1cm$ and $2cm$ beam sizes.

4.5 Summary

Measurements of proton dose distributions in water were taken over the full range of clinically applicable modulation widths, range shifts and patient collimator sizes. The FLUKA beam model was calibrated in energy and shape as measured by the transmission scan and wire chambers respectively. Simulated dose distributions were all within 2% of treatment dose for all such distribution. For the purposes of this work, investigation of beamline component design, the Monte Carlo model was successfully validated.

Neutron survey measurements were performed using a BF3 detector for a typical clinical beam configuration. Careful attention was paid to beam shape and angle - simulating the effects of both on neutron production. The effect of the BF3 AmBe source calibration was approximated and simulated dose rates were accordingly corrected. The resulting simulated dose rates were consistent, within the 20% calibration uncertainty, with the measured values of $\sim$10 mSv/hr. Additionally these results agree with previously measured neutron dose rates of 9.3 mSv/hr. These results do not comprise a precise model validation; but, they lend credibility to further simulated dose rates for anatomical models.

Chapter 5

Simulated Dose to Anatomy

With FLUKA secondary neutron dose rates validated in chapter 4, it is possible to estimate doses to patient anatomy. For this we establish six different tumour geometries on which we will study the effect of beam delivery parameters on the neutron dose. First, we create a 'treatment plan' to cover six different tumour geometries. Then we simulate these plans to verify their tumour coverage and to estimate the neutron dose. The goal of this study is to determine the sources of neutron dose to the patient and determine if it could be reduced by considering changes in treatment planing or beamline shielding. This chapter focuses on the geometry, beam planning, and primary and secondary dose to anatomical models in FLUKA. Section 5.1 describes estimated primary dose to a precision eye model. Here, geometry definitions, beam planning and primary dose results are presented for six tumour models. Section 5.2 focuses on the calculation of neutron doses to volumes in the eye model as well as a lower resolution full-body anatomic model.

5.1 Primary Dose to Eye Anatomy

Secondary neutron dose in proton therapy scales, for the most part, linearly with applied primary dose [32]. Non-linear effects include varying intra-fraction and inter-fraction beam conditions (centering, energy) as well as neutron dose from beam components upstream of the treatment head. For the purpose of this study, beam conditions are taken to be constant. As detailed in Chapter 4, beam centering and energy calibration is done prior to treatment and expected to remain constant throughout. Beamline components outside of the treatment room are well-shielded, but do con-

tribute a minor baseline neutron dose while the beam is active. Calculation of this effect is out of the scope of this work.

The remaining secondary neutron dose is generated within the treatment head and eye itself - both scaling linearly with primary dose. Thus neutron doses are quoted relative to primary dose and in the literature commonly stated as micro-Gray secondary per Gray primary ($\mu GyGy^{-1}$). Estimating this quantity first requires simulation of applied primary dose to a target. Section 4.1 describes the validation of primary dose within 2% of waterbox measurement. It is reasonable to extend this validation to tissues local to the eye where there is a high degree of uniformity in both chemical composition and density [71]. This section details the implementation of a precision anatomic eye model, tumour volume definition, estimation of dose, basic beam planning, and simulated relative primary dose.

5.1.1 Anatomic Eye Model

Section 2.2.6 gives a basic description of human eye anatomy; section 3.2.7 describes a vector-based CAD model to estimate this anatomy. The goal of calculating primary dose in this phantom is to normalize secondary dose estimates. We aim to only estimate primary dose given the rough 20% validation as in section 4.3.2. To achieve this, the main aims of this model are accurately represent tumour volume depth and width.

The standard in the literature is to normalize secondary doses to primary dose in water [32]. However, the inclusion of realistic anatomic volumes representing sensitive organs allows for further insight into secondary dose effects on the eye including dose generated within tissue. The VIPMAN model, discussed in 3.2.7 has a $4mm$ resolution owing to the limit number of voxels in a FLUKA simulation. Small organs of the eye, such as the macula or optic disk, are sub-pixel in size at this resolution. Thus, there are several benefits to exploration of dose in a separate eye phantom. Here, the smaller volume covered allows for a much lower resolution, given FLUKA voxel constraints, of $0.2mm$.

For use in a FLUKA simluation, the following transformations must be applied to the vector CAD model of section 3.2.7:

1. **Rotation** - For simplicity, all models are rotated by 35° gaze angle in the vertical and horizontal direction (relative to incoming proton beam) to move

sensitive organs out of the primary beam path. This rotation is clinically feasible giving anatomic limits [101].

2. **Volume Simplification** - Non-relevant volumes including iris and ciliary body are redefined as vitreous (similar chemically and in density) for model simplification. These structures are not considered OAR and prove difficult in the voxelization process.

3. **Voxelization** - CAD vector structures are voxelized via iterative ray tracing at $0.2mm$ resolution in the x,y and z directions

4. **Surrounding Tissue** - A simple flat-plane model of surrounding tissue is added for scatter purposes. The eye volume is padded with tissue such that the entirety of the beam stops in tissue. No eye-lid is modeled for simplicity as it irradiation is typically avoided in the treatment plan (taped out of the beam field) or included within treatment margins.

5. **Tumour Volume** - Addition of tumour volume to the bottom of the eye described in section 5.1.2.

6. **Translation** - The entire volume is translated such that the beam is centered on the tumour mass.

Figure 5.1 shows the voxelized eye model before and after transformation. Note that all eye orientations (35° x-y rotation) and tumour positions (bottom of the eye) are taken to be the same for simplicity and inter-plan comparison.

5.1.2 Tumour Volume Definition

With the goal of studying secondary neutron dose for varying treatment configurations (col. width, modulation, etc.) we define six tumour volumes and plans for treatment. As described in section 2.2.6, uveal melanoma have a 'mushroom' shape normally originating in the choroid layer of the eye. The two main metrics determining disease tier or staging are apical height (H_a) and basal width (W_b). We choose H_a and W_b in six combinations such that there are two each of tiers I,II and III:

These choices of tumour sizes were not made to all be clinically realistic. While the actual volumes are within the tumour tier definitions, H_a and W_b are correlated. Tumour 'C' at $9mm$ for example, would be defined as a tier III tumour, but $2mm$ basal

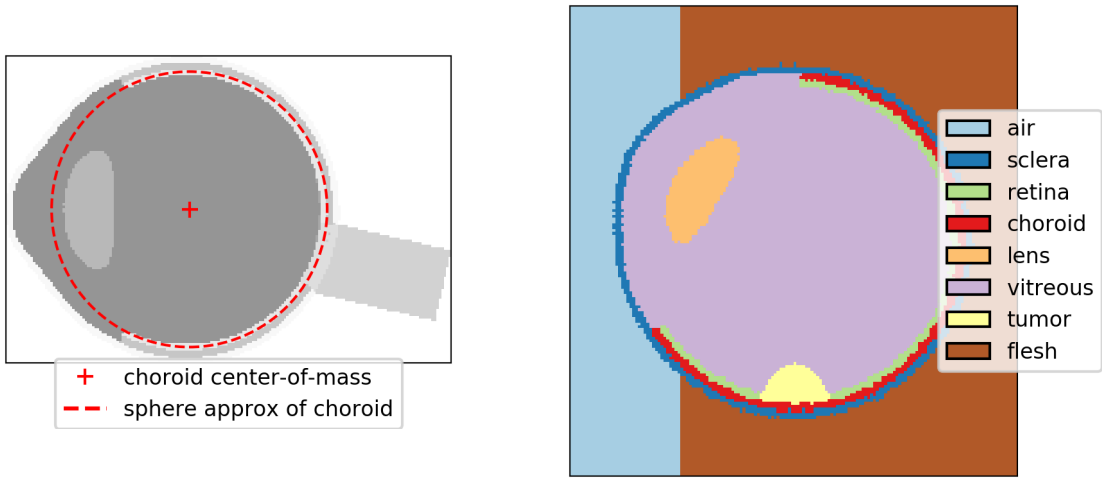

Figure 5.1: (left) Mid-plane slice of the original CAD model eye after voxelization. Shown in red is the choroid center-of-mass and circle approximating choroidal shape for use in tumour definition. (right) Mid-plane slice of transformed voxel eye model including tumour and surrounding tissue (right). Note that the optic nerve has been rotated out of the plane.

ID	Tier	Apical Height (mm)	Basal Width (mm)	Clinically Realistic
A	I	3.0	5.3	Yes
B	II	6.0	3.6	No
C	III	9.0	2.0	No
D	I	3.0	12.0	Yes
E	II	6.0	11.3	Yes
F	III	9.0	9.9	Yes

Table 5.1: Table of tumour volume definitions with anatomical characteristics.

width combined with $9mm$ height would be atypical of a real tumour. We select these sizes more to demonstrate the effect of different collimator and modulation width on neutron organ doses.

All tumours are positioned at the bottom of the eye. Tumour shape is defined by the intersection of a sphere (approximating the choroid layer) with an ellipsoid centered outside the eye. The desired apical height (H_a^{target},W_b^{target}) is achieved by way of iterative optimization with the following steps:

1. Start with an initial guess ellipsoid of with semi-major R_a and semi-minor R_b axes equal to the choroid sphere radius (R_c), centered at a distance $d = R_c$ from the center of the choroid

2. Calculate the two intersection points of the two shapes $(x_1, y_1), (x_2, y_2)$

3. Calculate the basal width $W_b = x_2 - x_1$ and apical height $H_a = R_c + R_a - d$

4. Calculate square-sum objective function:

$$O(d, R_a, R_b) = \sqrt{(H_a^{target} - H_a)^2 + (W_b^{target} - W_b)^2} \tag{5.1}$$

5. Repeat this process using a least squares minimization until achieving tumour dimensions withing one pixel ($0.2mm$) of desired targets

Figures 5.2 and 5.3 show the six tumour volumes optimized for H_a and W_b of Table 5.1. Overlaid with the voxel slices in green is the CTV delineating the tumour volume. In yellow is the CTV which includes the $1.5mm$ distal/proximal and $2mm$ lateral margins. This margin is calculated by extending the tumour volume by these margins in each direction, then taking the convex hull (outer exterior) of the external

points to find the shortest path which maintains these margins. Lastly, in red is the predicted beam plateau region to cover the calculated CTV.

The widths of Table 5.1 were selected to produce CTV's which would be exactly covered, including variation in tumour depth, by modulation widths of $8mm$ (Figure 5.2) and $14mm$ (Figure 5.3). These widths were chosen because they are representative of typical modulations widths used in treatment and also the exact schematics of the modulator wheels were available. Heights of Table 5.1 were selected to produce CTV's which would be covered by beams with collimators of $7mm$, $10mm$ and $12.5mm$ (maximum treatment field size is $25mm$diameter). The method of choice of volume sizes and accuracy of these selections will be discussed in the next section.

5.1.3 Beam Planning

There are three facets of treatment planning which must be emulated in this study - dose, patient/eye positioning, and beam shaping. The goal of this section is to select volumes and beam characteristics that give insight into secondary neutron dose scaling. Thus we seek to, when possible, select plans which vary only single parameters at a time (range, modulation width, collimator size). This comes at the expense of plan realism. Simulation of exact patient plans is out of the scope of this study (no eye CT data is available). Although, we do ultimately select plan parameters which are typical of real patient plans.

We follow a simplified method of beam planning:

1. Position the eye such that beam axis is coincident with the center of the CTV
2. Select a modulation width which covers the widest axial portion of the CTV
3. Select a collimator which produces a field wide enough to cover the CTV
4. Select a range shifter setting which centers the SOBP on the axial center of the CTV
5. Take the $2mm^3$ average dose at the center of the SOBP as the reference dose

Patient/eye position was covered in Section 5.1.2 by careful selection of tumour volumes. In reality, gaze angle would not be the same for each of these cases - but we seek to keep gaze angle a constant parameter for comparison purposes. This angle

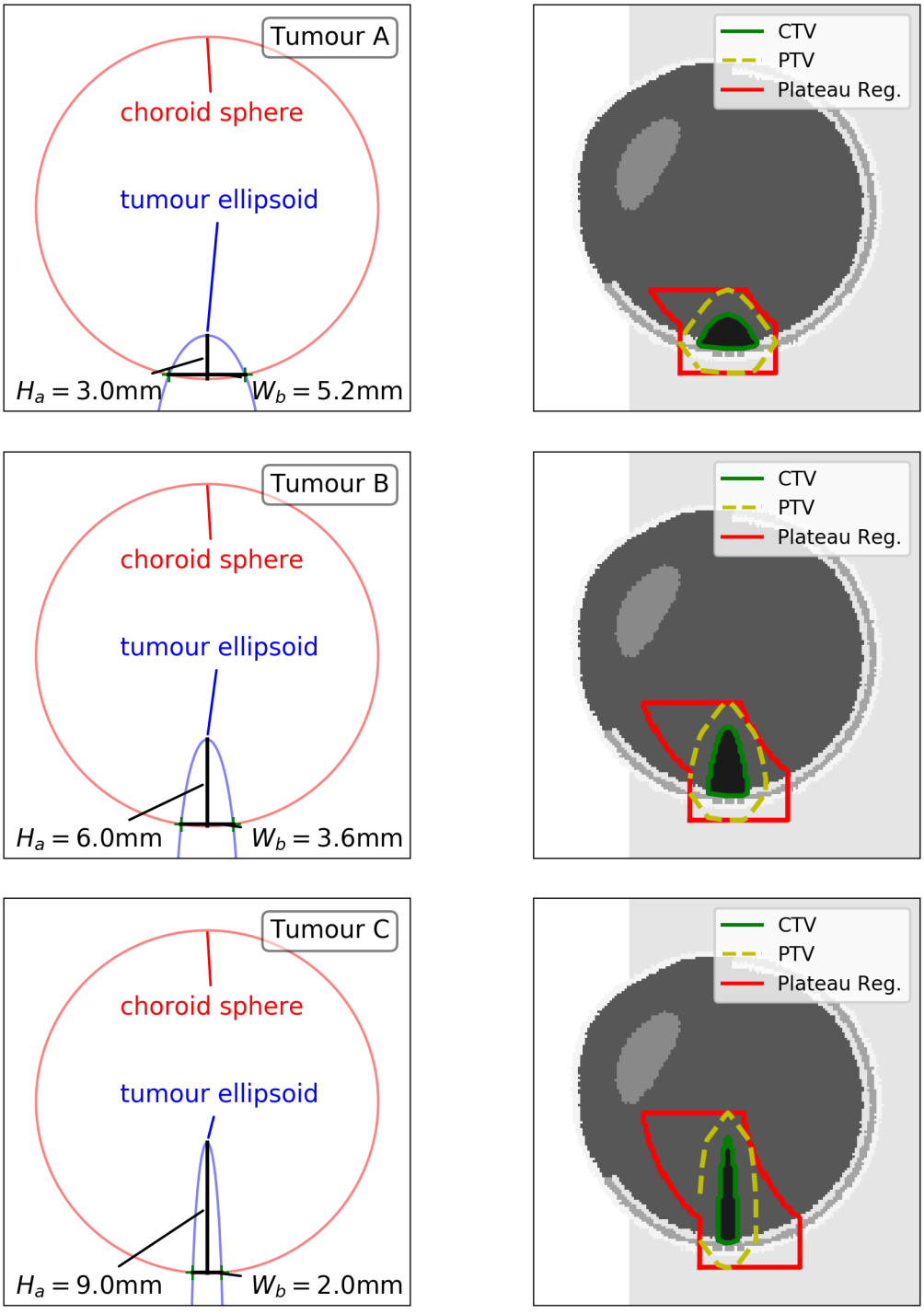

Figure 5.2: Tumour volume definition diagrams (left) and slice of voxelized phantom with CTV, PTV and beam plateau boundaries (right) for $8mm$ modulation with tier I,II, and III tumours (upper,middle,bottom).

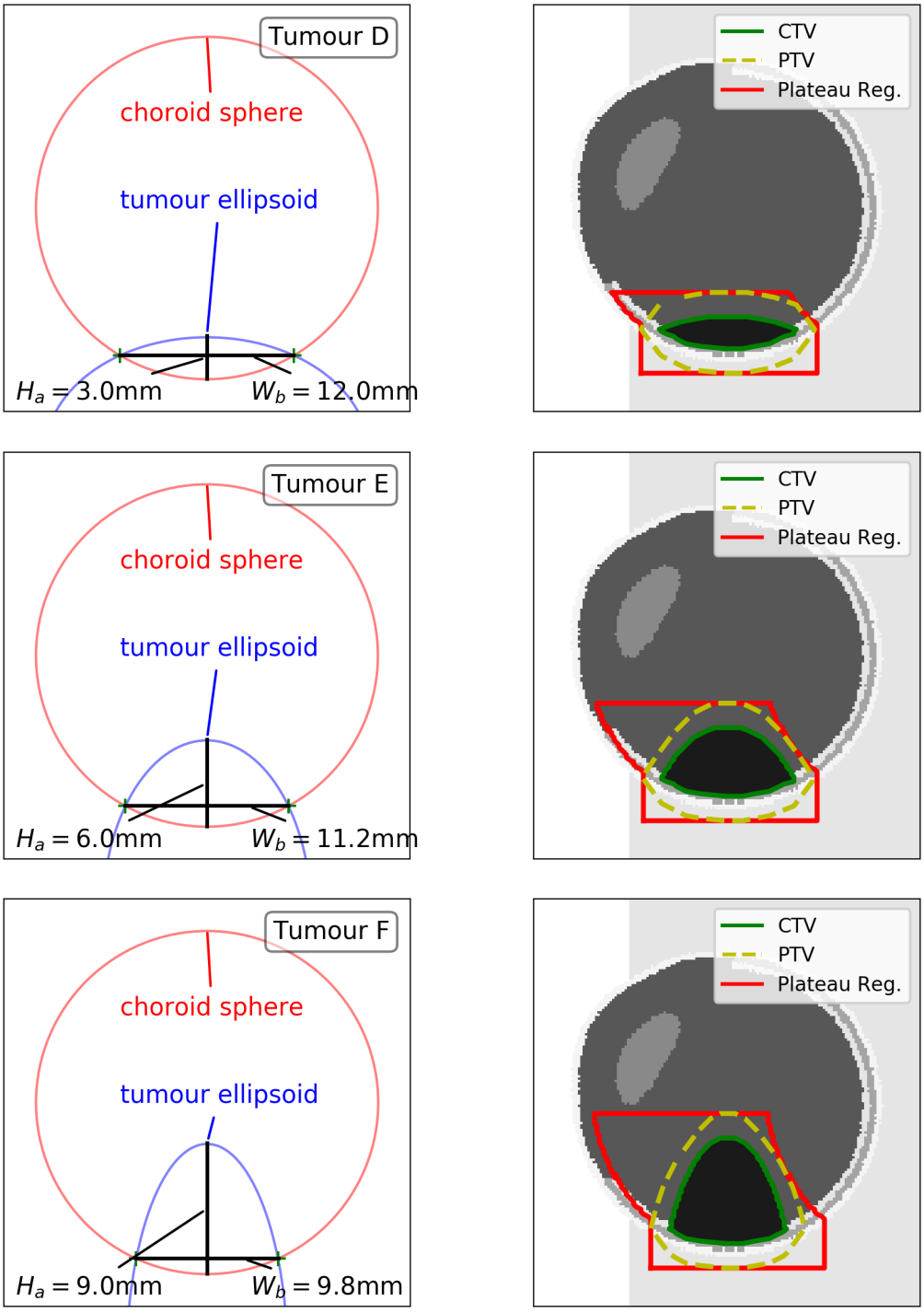

Figure 5.3: Tumour volume definition diagrams (left) and slice of voxelized phantom with CTV, PTV and beam plateau boundaries (right) for $14mm$ modulation with tier I,II, and III tumours (upper,middle,bottom).

was chosen to best avoid impinging on OAR's with the primary beam (discussed in Section 5.1.4).

Beam shaping is controlled by three components of the DDS: the modulator wheel defines the modulation (axial) width; the range shifter defines depth; and the patient collimator defines lateral width. Choice of these parameters is largely informed by tumour volume definitions of the previous section. Target volumes described in Table 5.1 were specifically chosen and oriented to require consistent circular collimators ($7mm$, $10mm$ and $12.5mm$) and modulators ($8mm$ and $14mm$). All that remains is to calculate the required range shift to position the SOBP dose plateau over the CTV. The general procedure for selecting the range shift is as follows:

1. Determine modulator wheel plateau range (R_{95}) experimentally as in Section 4.1.5
2. Using the calculated CTV of Section 5.1.2, determine the maximum required tissue depth for the plateau (R_{max}^{targ}) using standard ray-tracing
3. Calculate the required shift in tissue $\Delta R_{water} = R_{max}^{targ} - R_{95}$
4. Divide the shift by the PMMA range conversion factor (W_{eq}) as calculated in Figure 4.7: $t_{PMMA} = \Delta R_{water}/W_{eq}$
5. Calculate range shifter setting for t_{PMMA} from Equation 3.1

Table 5.2 shows the maximum depths and calculated range shifts for each of the target volumes. Initial modulation ranges were calculated using interpolations on experimental waterbox data as validated in Chapter 4. As designed, the resulting tumour geometries span the target modulation range ($8mm$, $14mm$) and collimator diameters ($7mm$, $10mm$, $12.5mm$) within $0.1mm$.

Note the target maximum range, R_{max}^{targ}, is the maximum beam range to cover the CTV. For the most part, Table 5.2 values are intuitive - increasing with tumour volume extent. However, R_{max}^{targ} is a function of both tumour volume extent and tissue surface variation. Due to surface variation between volumes D and E, it coincidentally occurs that both require the same R_{max}^{targ}.

Also notable in this planning process is the use of the 95% distal point (R_{95}) for range definition. Normally modulation width (m_{98}) is defined by the 98%-90% proximal/distal points as this is the most stable measurement of width. However; for the purpose ensuring tumour volume coverage, this study uses the 95% point for

planning. In clinical planning, no exact volumes or CT scans are available, so the standard modulation width and range are used.

ID	Mod. Width (mm)	R_{95} (mm)	R_{max}^{targ} (mm)	t_{PMMA} (mm)	RS Value	Col. Diameter (mm)
A	8	33.7	12.1	18.8	1670	7.0
B	8	33.7	13.1	17.9	1584	9.9
C	8	33.7	14.1	17.1	1497	12.4
D	14	34.4	15.5	16.5	1437	7.0
E	14	34.4	15.5	16.5	1437	10.0
F	14	34.4	16.1	15.9	1385	12.4

Table 5.2: Table of calculated tumour depths, range shifts and collimator sizes required to position SOBP over the CTV.

With the calculation of range shift complete, all parameters are determined for the six plans to be used in neutron dose simulation.

5.1.4 Primary Dose Estimation

For the purpose of planning, prior to MC simulation, we employ an interpolation procedure to approximate SOBP depth-dose characteristics. This method utilizes simulated water-box data to approximate depth-dose distributions for a given thickness of plastic modulator.

Central-axis dose distributions D are approximated with a 2D interpolation function on t (modulation thickness) and x water depth: $D(t, x)$. Thus given a modulator (steps T_i) and range shift (R) the SOBP dose distribution $SOBP_{T,R}$ can be approximated as:

$$SOBP_{T,R}(x) \approx \sum_i D(T_i + R, x) \tag{5.2}$$

The main advantage to this method is speed and range accuracy. Along the central beam axis dose can be calculated with a set a function calls - almost instantaneously. A comparable dose distribution simulated using MC would take 400 core-hours to reduce dose uncertainty to below 2% (see Section 4.2.1). The main disadvantage is loss of accuracy for large range shifts (due to perturbing of proton energy distribution upstream of the modulator) and decreased accuracy at shallow depths (due to lack of waterbox data shallower than 3mm owing to the plexiglass window). The

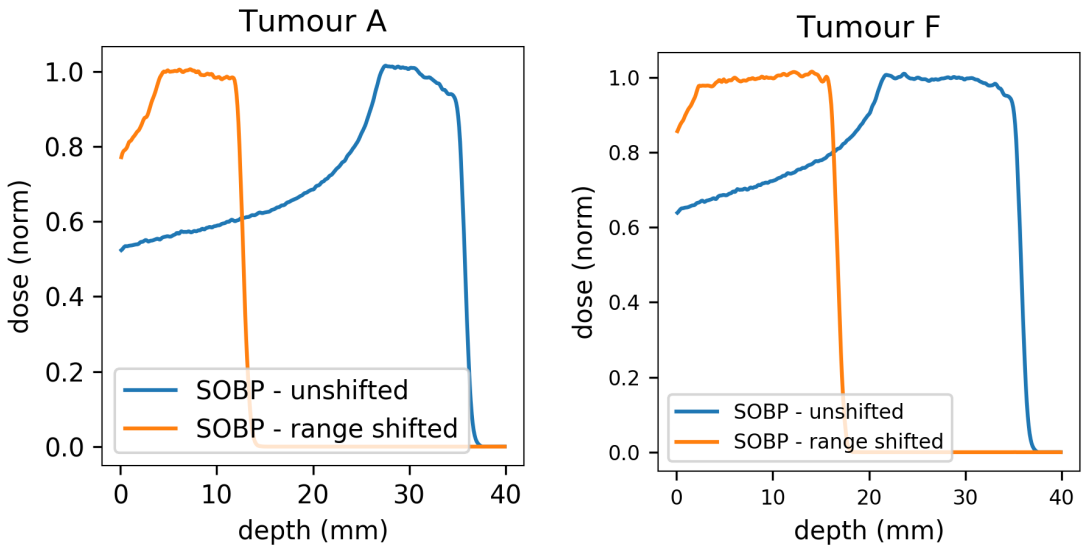

Figure 5.4: Interpolated depth-dose distributions for plans A (left) and F (right). Shown are both the unshifted and range-shifted distributions. Notable is the change in plateau slope due to energy-smearing in the range-shifter upstream of the modulator wheel.

method is used extensively in Chapter 7 for modulator wheel design and details of its implementation and validation can be found there.

Figure 5.4 shows beam-axis depth dose distribution for plans A (left) and F (right). In the unshifted distributions a notable decreasing slope is present as discussed in Section 4.1.5. Range shifting has the effect of increasing this slope. The change in slope is roughly proportional to the magnitude of the shift. This is result of the range-shifter being upstream of the modulator - perturbing beam energies before reaching the modulator which was designed to produce a flat SOBP from a $70MeV$ beam. This effect is accounted for in treatment planning.

A flat SOBP is ideal in planning using the aforementioned method. This slope change has the effect of degrading dose uniformity over the target region. This effect is accounted for in real treatment planning by setting a tolerance on SOBP slope [7]. Thus we do not expect a flat dose distribution in simulated primary dose.

To produce an estimated 3D dose distribution, we may approximate off-axis dose as exactly the central axis dose. This is valid as the beam profile is roughly flat over $5cm$, even at depth, provided the penumbral regions are avoided (see Sections 4.1.6 and 4.2.6). We take the central-axis dose and extend it from the surface of the anatomy (ignoring the small range variation due to air).

Figure 5.5 shows exactly this - the interpolated central-axis dose extended over the lateral width of the collimator for each plan. Isodose lines overlaid with these plots show coincidence of 100% isodose region with the center of the tumour target for plans B,C,D and E. Plans A and F suffer from significant SOBP plateau degradation as shown in Figure 5.4. Notable here is the coincidence of 95% isodose lines with CTV boundaries when comparing to Figures 5.2 and 5.3. This is expected, as the interpolation method is very accurate in reproducing SOBP range.

These 3D dose estimates are a tool that comes for free with no additional computation. This is useful in estimating beam/OAR coincidence and selecting gaze angle. Indeed the 35° gaze angle was chosen by examining cumulative dose volume histograms (CDVH) generated using these dose distributions. The angle selection was done in an ad-hoc fashion: examining a discreet set of angles and selecting a 'best' one in terms of OAR avoidance. This was in no way a true optimization process on gaze angle. Although, this tool could be extended to be used for such purposes - it is beyond the scope of this work.

Figure 5.6 shows sample CDVH's used in the angle selection process. Note that a certain volume of sclera, retina and choroid is necessarily irradiated as the tumour resides in the choroid layer of the eye. Significant OAR's include optic nerve and lens. The primary beam avoids the lens completely while the optic nerve experiences a maximum of ∼10% impingement by the beam in the case of Tumour F. This is a tradeoff as there did not exist a gaze angle which satisfied the plan constraints (same position, collimator, modulation) and did not impinge on the optic nerve is some way. It should be noted that these distributions are quite 'sharp' - this is expected as the interpolation method of dose calculation does not take beam penumbra into account.

5.1.5 Primary Dose to Eye Anatomy

Simulation Methods and Uncertainties

Simulation methods for waterbox validation are discussed at length in Section 4.2 with uncertainties discussed in Section 4.2.1. The main difference for eye model simulations is that dose is read-out in a 3D volume with $0.2mm^3$ bins to match the voxel resolution of the phantom. This is identical to the waterbox readout but in three dimensions. With this, uncertainties at the bin level are kept below 2% when 10^8 primaries are simulated, which was done for this part of the project.

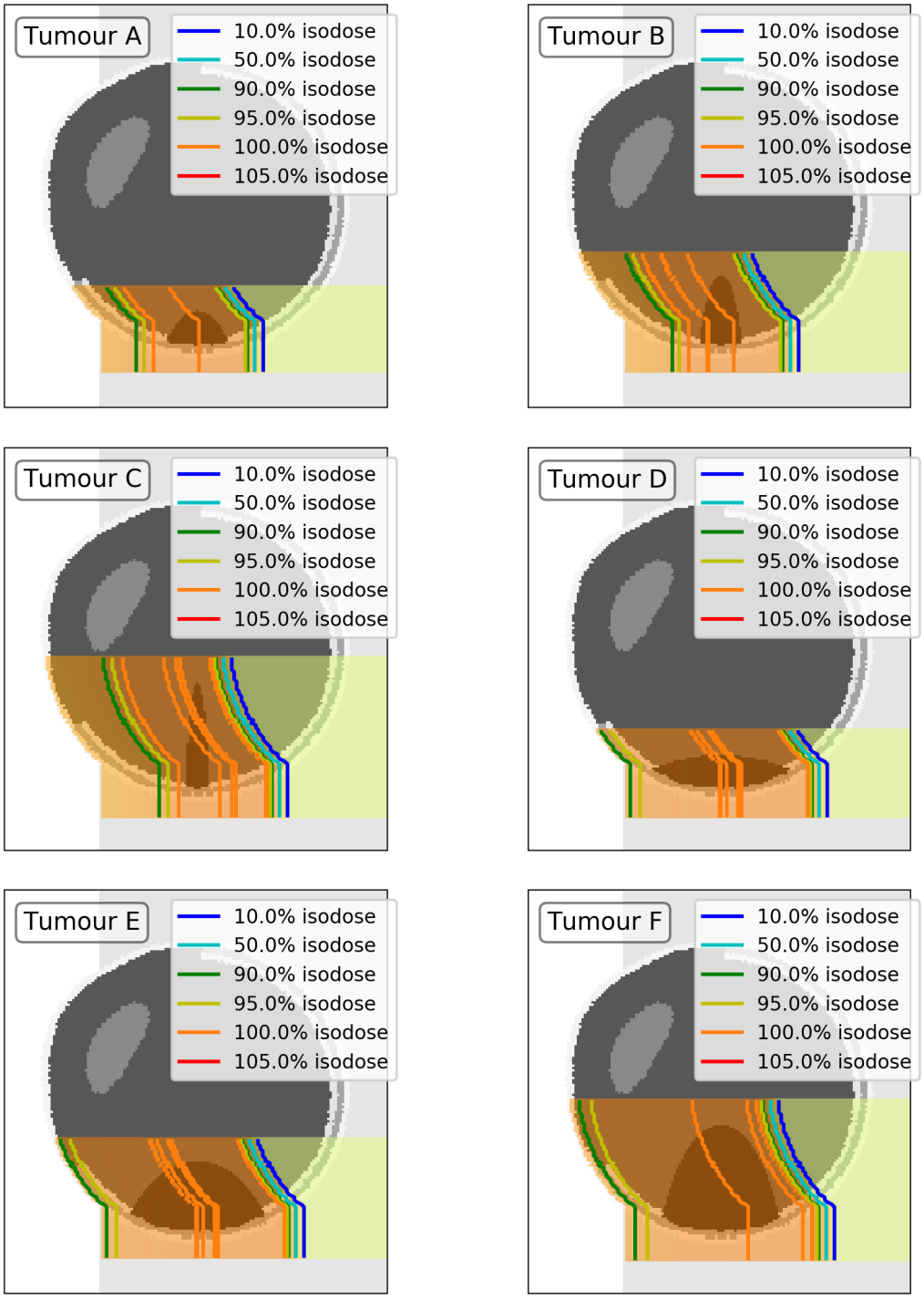

Figure 5.5: 2D interpolated dose distribution for plans A-F on the central slice in the x-z plane with overlaid isodose lines. Offset in 100% isodose lines is due to shifted-SOBP slope degradation.

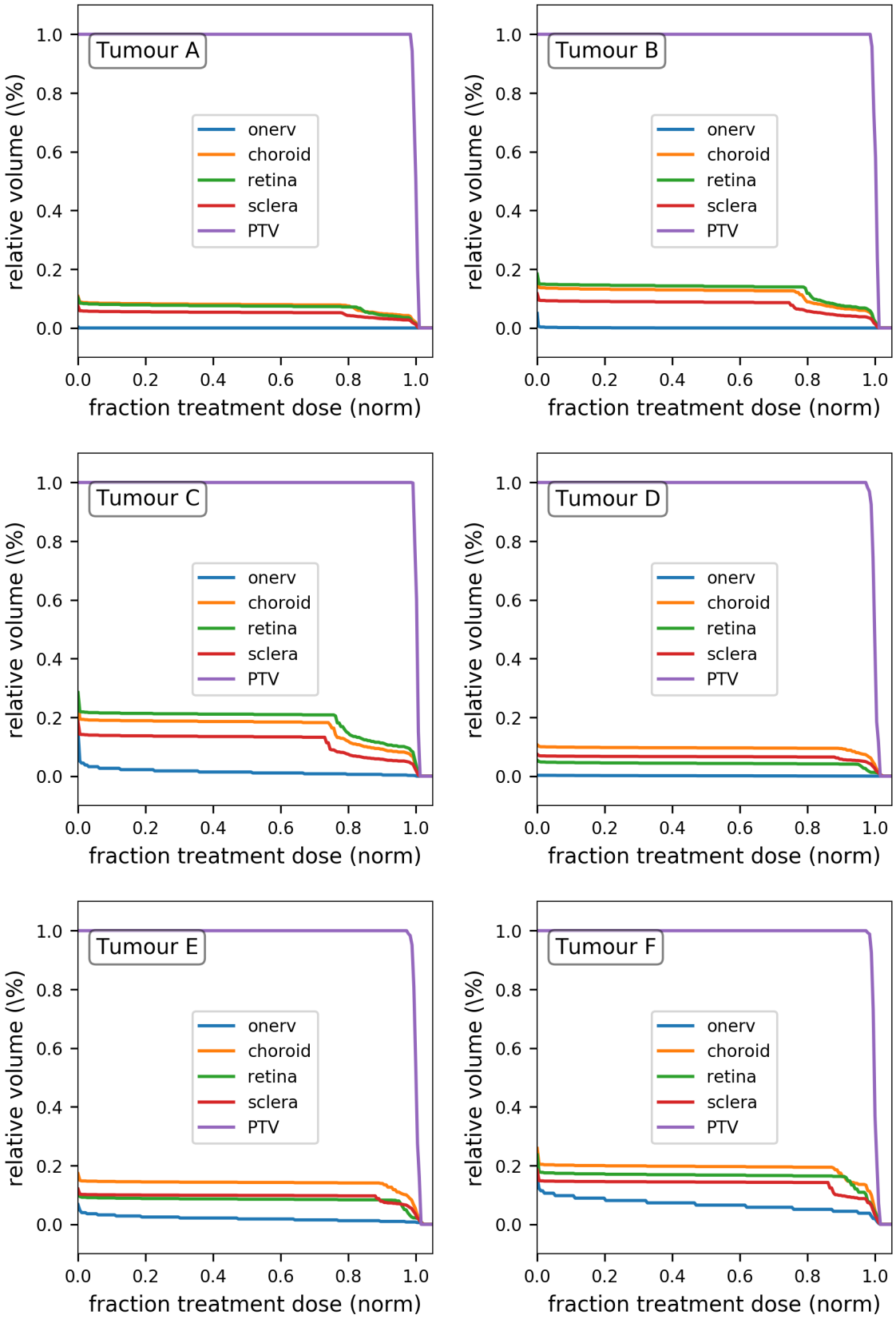

Figure 5.6: Cumulative dose histograms for interpolated 3D dose approximation. Shown are relevant volumes and total target coverage for each plan.

Simulated 3D Dose

Figure 5.7 shows isodose lines for MC simulated dose overlaid on central axis slice. Here we see that all plans successfully position the dose plateau over the tumour target. This indicates that range and modulation width estimates from the interpolated method are accurate. Plans A-C position the 95% isodose region over the center of the tumour target. Additionally, the MC isodose lines extend beyond the predicted dose in the lateral direction. No modeling of the beam penumbra was done and excess dose in the lateral direction is consistent with $2mm$ penumbral size of section 4.1.6.

Comparing Figure 5.7 to Figure 5.5, the dose interpolant method fails to simulate dose accurately at shallow depths. Plans D-F should have isodose lines extending to within $1mm$ of the surface. However, 95% isodose lines $3mm$ deeper in tissue than predicted using the interpolated dose method. This is not surprising as the interpolated depth-dose curves were built using waterbox data which does not account for any buildup at the surface of the $3mm$ box window. The curved surface of the eye also contributes to this discrepancy due to the varying proton range. Figure 5.8 shows central depth-dose profiles for interpolated and MC simulated dose. Here the discrepancy can be clearly at 0-$3mm$ depth. The $8mm$ modulated plans (A-C) avoid this issue due to tumour depth, but the plateau regions for plans (D-F) are substantially degraded. In terms of treatment viability, degradation of the plateau is a known issue and is compensated for in dose prescription

Figure 5.9 shows cumulative DVH's for MC simulated dose. Overall the DVH's match well to the predicted results of Figure 5.6. In all cases the tumour target DVH line is less steep and sharp than in the interpolated dose DVH's. This is expected since the interpolated method extends central-axis dose in the lateral direction. In the more realistic MC data, dose varies in the lateral direction, producing a worse coverage metric for the tumour target. Additionally plans C-F have degraded plateau regions, as shown in Figure 5.8, resulting in a larger shoulder in the tumour target DVHs. Lastly, $\sim$5% of the lens is exposed to penumbral primary dose in plan F. This effect was not accounted for in 2D interpolation. Overall, most plans effectively avoid organs at risk and produce expected coverage for the target volume.

Dose Normalization Factors

With confidence that the selected plans accurately position dose over the tumour target region, we may close this section by recording the mean dose to the tumour

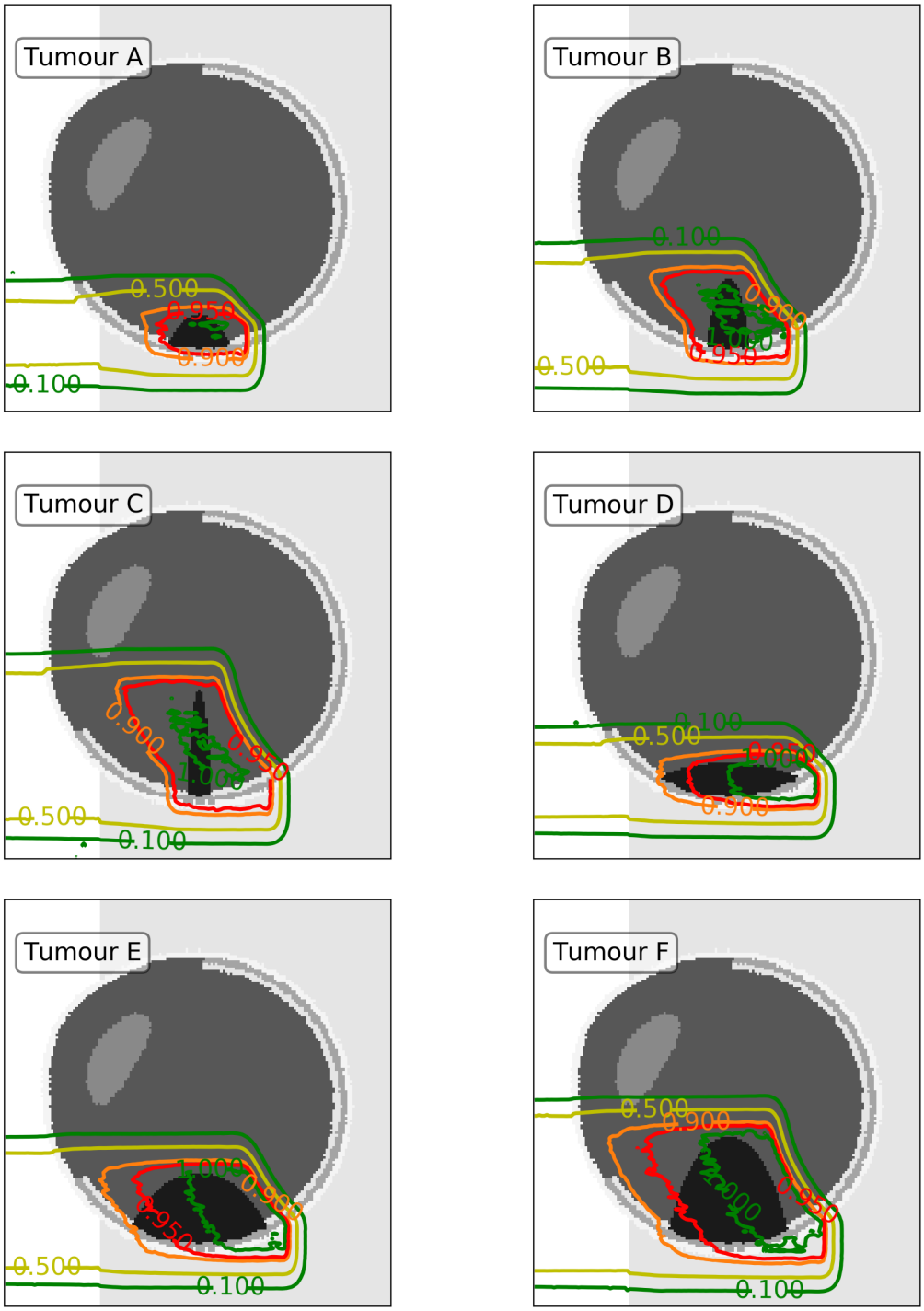

Figure 5.7: MC simulated isodose lines overlaid on anatomic eye central slice (X-Z plain.

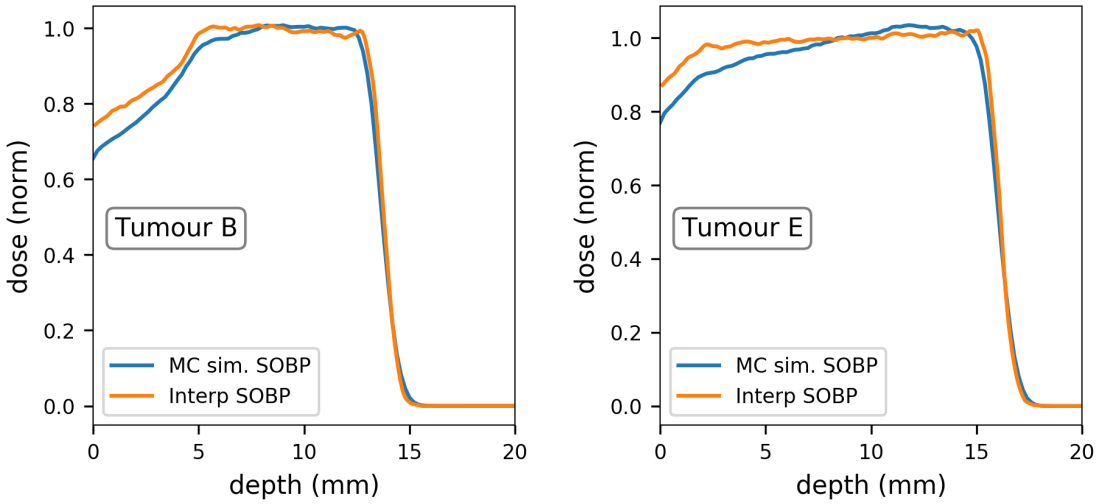

Figure 5.8: Central-axis SOBP dose distribution as calculated by the interpolation method (orange) and from MC simulation (blue) for Tumours B (left) and C (right). Notable is the decreased accuracy of the interpolation method near the surface ($< 3mm$).

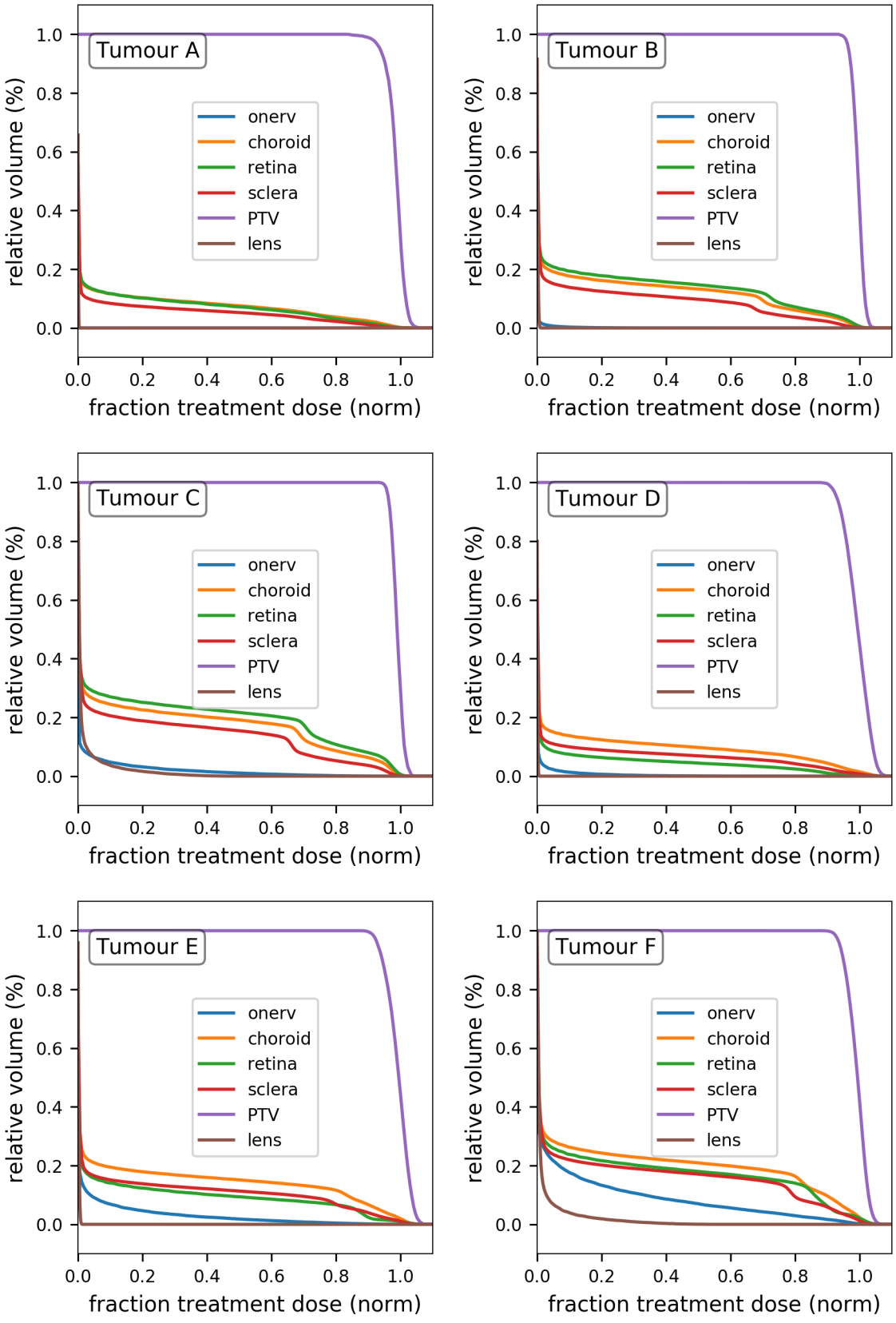

Figure 5.9: Cumulative dose volume histograms for MC simulated 3D dose.

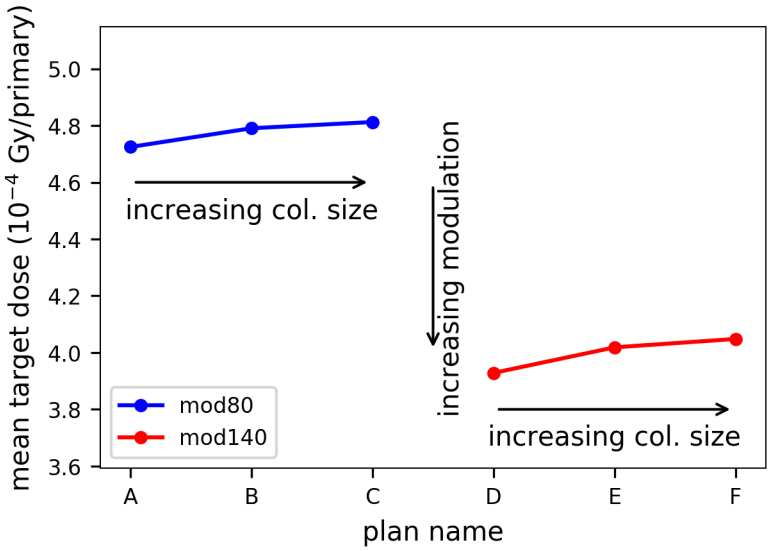

plan name	dose per primary ($10^{-4}Gy$)
A	4.72
B	4.79
C	4.81
D	3.93
E	4.02
F	4.05

Figure 5.10: Mean dose-per-primary at the center of each tumour target for plans A-F. (left) Doses are plotted showing increasing collimator size with plan name. (right) Values are tabulated for each plan All doses have a maximum 2% uncertainty associated with MC simulation statistics.

target for each plan.

Figure 5.10 shows the primary dose to $2mm^3$ located at the center of each target. Also tabulated here are the numerical values for dose normalization. Here we see a trend of increasing dose with collimator opening size and decreasing dose with modulation width, as expected. While the output factors cannot be directly compared, dose increases by $\sim$2% as collimators increase from 7-12.5mm which is consistent with output factors of Figure 4.30.

5.2 Secondary Dose to Anatomy

With primary dose per plan well understood, secondary neutron dose to anatomical models can now be simulated and compared to reported doses from other treatment centers. In this section, simulation methods, uncertainties, sources of secondary neutrons, and dose to anatomical phantoms is covered.

5.2.1 Simulation Methods and Uncertainties

Neutron interaction cross sections in tissue are $10^3 - 10^4$ lower than those of protons. In addition, the fluence of neutrons reaching the patient is lowered further by the production cross section in the beamline, shielding, $1/r^2$ fluence-distance dropoff, and proton beam loss in the DDS (shown in Figure 4.37). As a result, simulating neutron dose deposition in tissue requires far more computational resources than needed to compute primary dose.

Figure 5.11 shows the relative error as a function of primary protons on absorbed to VIPMAN organ volumes. As expected, increasing the number of primaries decreases the relative statistical error as reported by FLUKA. The exception here is volumes scoring zero absorbed dose are reported as 100% error - the case for the treated lens, optic nerve at lower than 10^8 primaries. In general, uncertainty in absorbed dose decreases as volume size increases. This is due to larger volumes (eg. brain, heart) experience higher neutron fluence, and therefore more events resulting in dose deposition. Additionally, organ doses further from the treatment site exhibit increased uncertainty (treated vs untreated eye).

At the highest number of primaries run, $5 \cdot 10^9$, the uncertainty in absorbed dose to the optic nerve is 80%. A reduction in uncertainty to 10%, would require increasing the number of primaries by approximately 60 times. Already, as discussed in 4.2.1, this run required 20,000 core-hours to complete. Increasing this by a factor of 60, would be computationally intractable with the resources available. Hence, it is not possible to rely on simulating each neutron dose-deposition event for the purpose of this work.

However, despite this limitation, the spectral fluence of neutrons can be estimated for a given volume without fully simulating the rare neutron interactions. This is achieved by recording the energy of every neutron traversing the volume (as a USRTRACK readout as described in 3.1.3). This results in increasing the recorded data by roughly a factor of the neutron interaction cross section. From this spectrum, the ambient equivalent dose can be calculated at an acceptable uncertainty without drastically increasing the simulated primaries. This is the same method performed in § 4.4 - where ambient equivalent dose was validated within an accuracy of 20%. Figure 5.12 shows the uncertainty in ambient dose equivalent as a function of primary particles. Here the maximum uncertainty on the optic nerve is reduced to $\sim$10%.

Improving efficiency in dose readout as above allows for studies of estimated equiv-

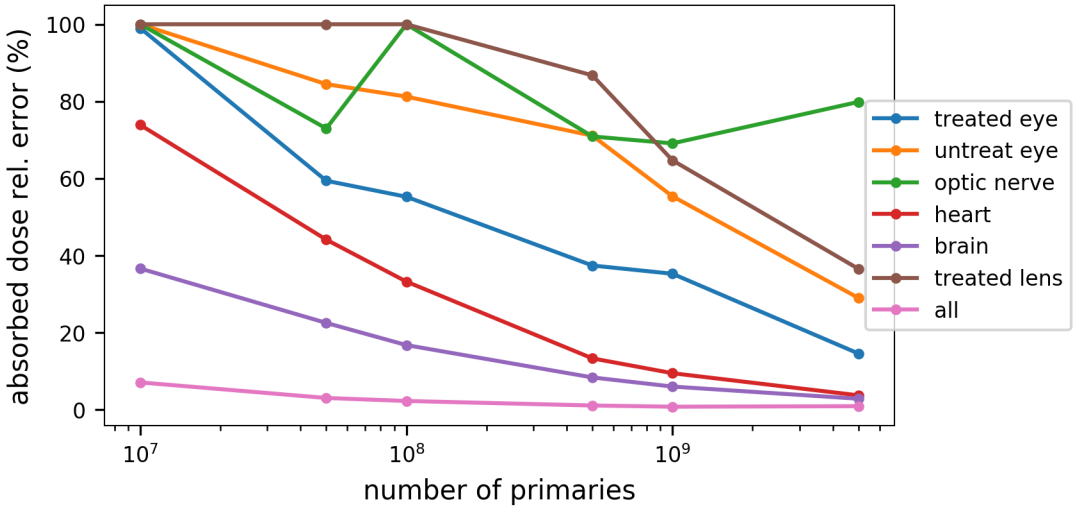

Figure 5.11: FLUKA simulated neutron absorbed dose uncertainty to VIPMAN as a function of number of primaries run.

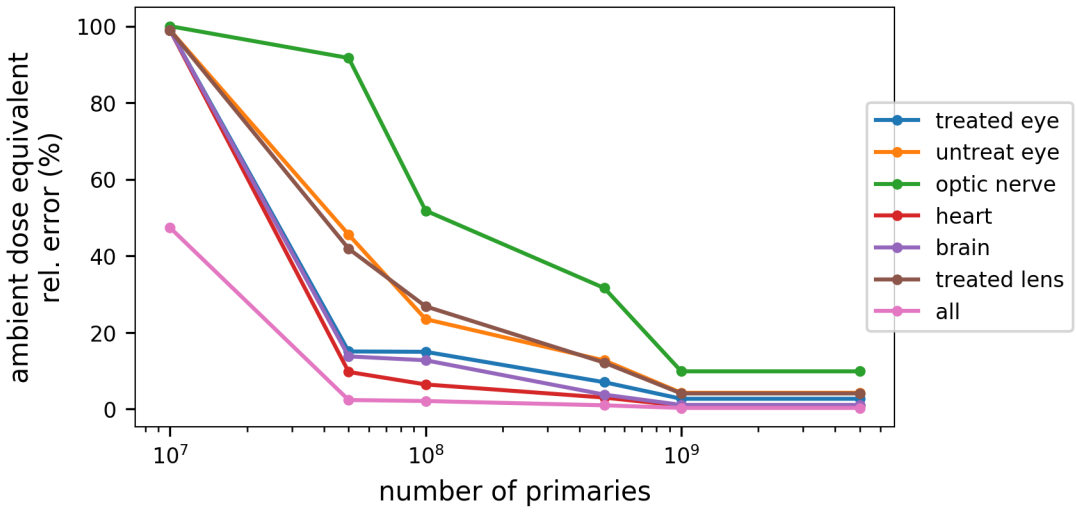

Figure 5.12: FLUKA simulated neutron equivalent dose uncertainty to VIPMAN organs as a function of number of primaries run.

alent dose to organ volumes of the VIPMAN phantom (§ 3.2.7) as well as finer organs of the eye using the anatomic eye model (§ 3.2.7). Additionally, we may partition the neutron dose by region in which the neutrons were produced.

5.2.2 Neutron Sources

Neutron secondary dose primarily results from neutrons generated in the DDS beam shaping components - collimators, modulator wheel, range shifter, scatterer[102, 103, 104]. Thus the resulting dose is a complicated function of the geometry of the DDS and shielding. Additionally, neutrons generated within tissue itself will also contribute to secondary dose; thus, the treatment field size and shape is plays an important role. This complicates inter-comparison between different passive scatter proton therapy facilities with reported out-of-field variations differing by orders of magnitude[105, 106, 107, 108]. Despite this, for the purpose of shielding design and planning, it is useful to understand the relative impact of neutron sources.

One approach to simulating neutron dose from each component would be to simulate the primary beam alone with each component and record the resulting dose. This however, would ignore effects from shielding and scattering which is particularly problematic when considering the scatterer is one of the largest sources of neutrons. Also, this approach would require neutron simulation runs for each component of interest - substantially increasing computational requirements. Instead, a particle tagging approach is taken. Upon neutron generation by the primary beam, a FLUKA custom user routine is called which attaches an integer, representing the region number, to the particle data. Upon scoring of the neutron fluence at the target, the region integer is read and the fluence is selectively applied in scoring. The result is a readout of neutron fluence corresponding to each region of origin for each target volume.

Figure 5.13 shows neutron particle fluence along the DDS for four different regions of origination. Shown are neutrons generated in the range shifter, modulator, collimator and VIPMAN tissue for 10^8 primary particles. These are the components that vary between patient treatments. Not shown are 'other' or constant sources including the scatterer and upstream collimation devices of the DDS. Note that these are particle fluences with no energy information and are summed in the vertical direction. In all of these plots, the forward-peaked nature of the neutron trajectories and origination point can be seen. Also visible is the attenuation due to shielding. This indicates that the FLUKA tagging routine is accurately recording the neutron

origination points.

Figure 5.14 depicts the summed neutron fluence at the position of the VIPMAN phantom. Shown are simulated fluences for the plans defined in § 5.1.2. Included here are 'other' sources - the dominant contribution coming from the scatterer at about an order of magnitude higher than the patient collimator.

Most neutrons reaching the phantom (located at $150cm$ axial) originate in the scatterer despite it being $\sim 150cm$ upstream of the isocenter. This is consistent with Figures 4.37 and 4.38 as between 40-80% of the beam is stopped by the primary collimator upstream of the range shifter. The next largest contribution is from the patient collimator where there is no neutron shielding due to space and beam-shaping restrictions. The range shifter and modulator follow, seeing less of the beam current than the scatterer and being shielded a the secondary collimator. Here there is a noticeable difference in modulator contributions between the $8mm$ plans (A-C) and the $14mm$ plans (D-F). This is expected as the average thickness of the $14mm$ wheel is $1.2mm$ (26%) thicker than the $8mm$. More interaction between the beam and PMMA modulator results in higher neutron fluence. Lastly, neutron production in tissue increases with collimator opening size (from A to C or from D to F). This is due to increasing field size or irradiated volume in the eye.

While it's useful to understand the number of particles produced, dose to the patient is strongly dependent on both the number and energy of the neutrons as discussed in § 2.1.4. Figure 5.15 shows typical energy spectra of dose-depositing neutrons reaching the phantom per source of origination. This spectrum is typical of neutrons undergoing (n,xp) in water[32]. Notable here is the decreasing neutron energy as the source approaches the VIPMAN phantom. The highest energy neutrons are produced in the scatterer, then range shifter, modulator, collimator and finally tissue. This is because primary proton energies are reduced as the beam traverses the DDS.

Convolving the energy fluence with the AMB74 dose-equivalent conversion factor [65, 99] gives ambient equivalent dose. This quantity, summed over all phantom regions (total body), is plotted across the test plans in Figure 5.16. Here the scatterer (other) and range shifter are responsible for the majority of total body exposure. This differs from the neutron fluences of Figure 5.14. The patient collimator produces more neutrons, but the higher energy neutrons produced in the range shifter (see Figure 5.15) result in higher equivalent dose to the body. To get a better picture of secondary dose distribution we break down equivalent dose contributions by source in Figures

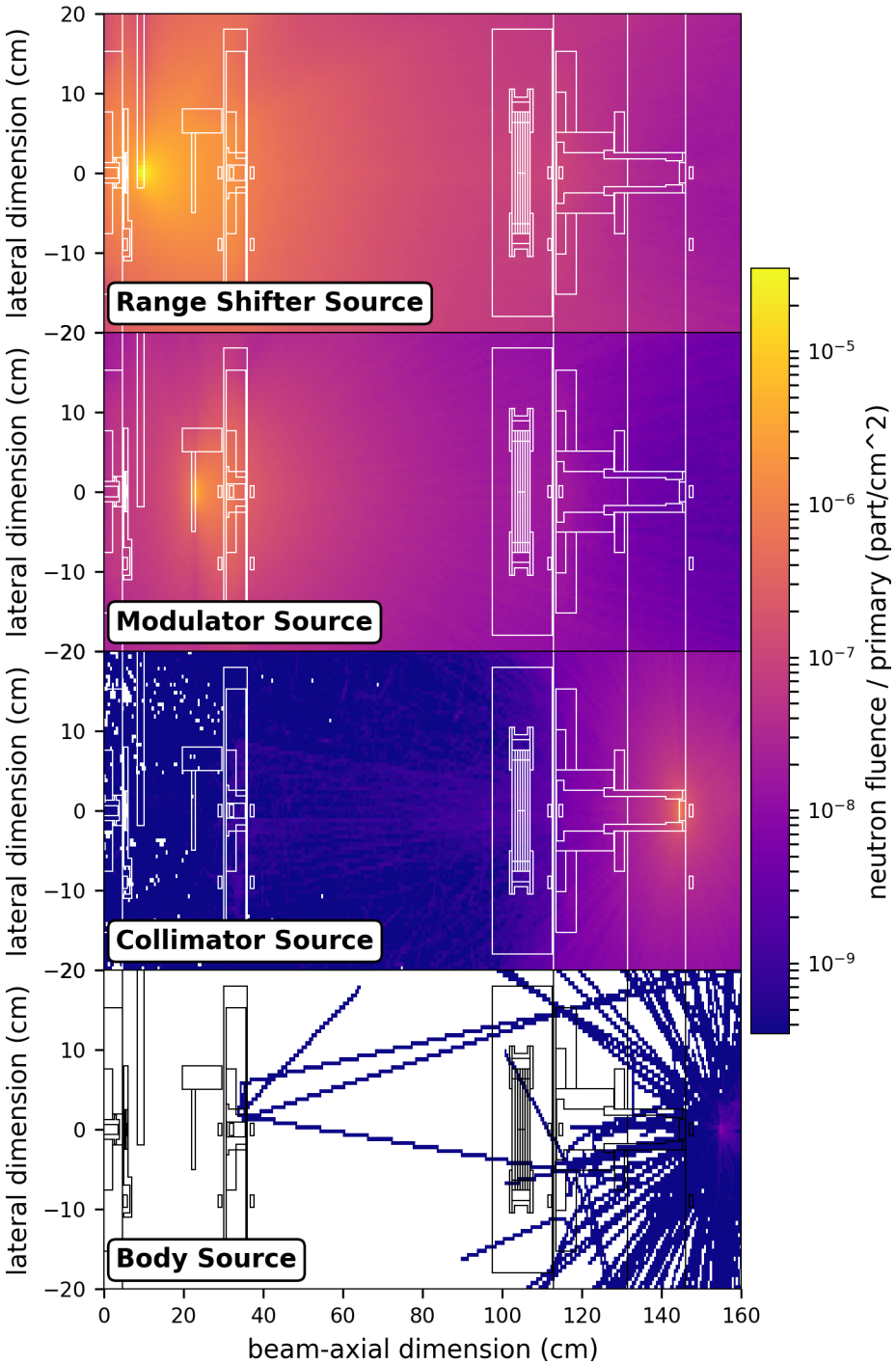

Figure 5.13: Neutron particle fluence per primary plotted along the DDS beamline in the lateral and axial directions. Fluence for 10^8 primary particles is summed in the vertical direction and displayed for range shifter, modulator, collimator and body sources. DDS outline is shown in white (top three) and black (bottom).

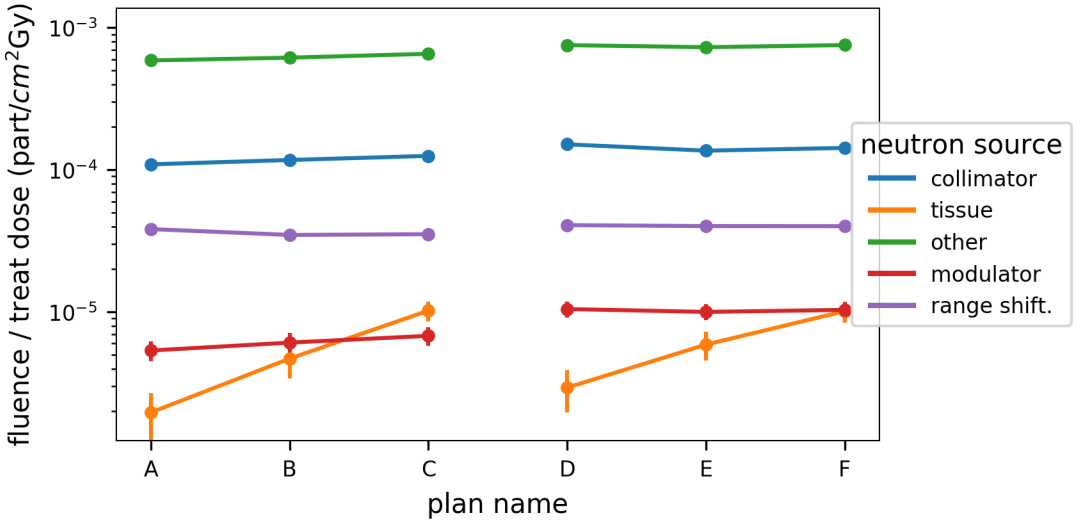

Figure 5.14: Neutron particle fluence measured at phantom position produced by beamline components and VIPMAN phantom 'tissue' for test plans. $8mm$ and $14mm$ modulated plans are shown on the left and right of the plot respectively.

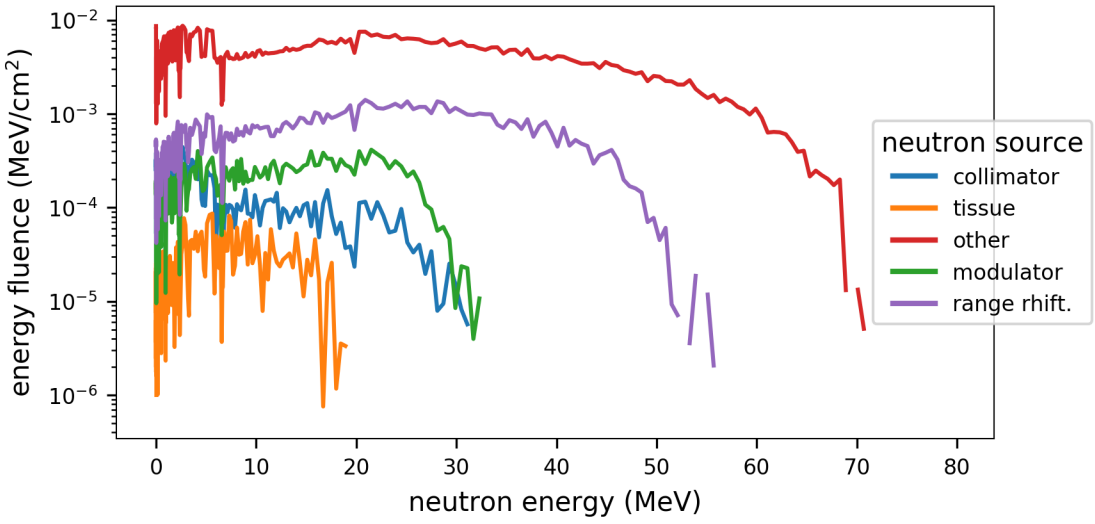

Figure 5.15: Energy spectra of neutrons reaching the VIPMAN volume. Note that energy bins are pre-set by FLUKA.

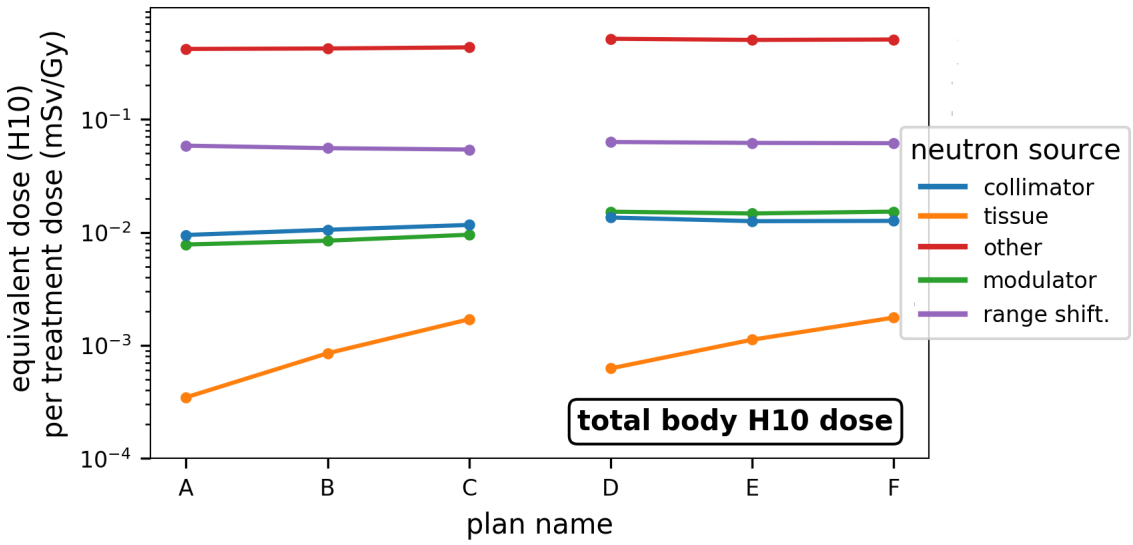

Figure 5.16: Total body equivalent dose (H10) per primary treatment Gy for test plans owing to various beamline components.

5.17-5.21. These plots show the volume-averaged equivalent dose to various organ volumes resulting from different neutron sources.

Figure 5.17 shows the equivalent dose generated by 'other' sources which can not be varied in patient treatment (primarily scatterer, 1st and 2nd collimators). Notable here is that the treated eye experiences the highest average dose due to this source. These are neutrons which are forward peaked and traverse the entire DDS. Since the primary beam must traverse this path unhindered, no shielding may be placed here to reduce the neutron dose to the eye. The increasing nature of this dose with collimator opening size (A to C, D to F) supports this idea. The wider collimator opening reduces shielding from scatterer-produced neutrons. The brain and lungs are much better shielded due by the ring of polyethylene surrounding both the primary and secondary collimators. While a reduction in dose to the body bulk could be achieved by increasing this shielding, dose to the eyes could not be reduced in this way.

Figure 5.18 shows the next largest contributor to equivalent dose - the patient collimator. This is consistent with other measurements indicating the patient collimator plays a significant role in secondary dose [109]. Due to the proximity to the phantom head, the eyes see the largest dose from this source. While planning could be altered to change the aperture shape to reduce this effect, the overall dose is up to two orders of magnitude smaller than scatterer dose. Since scatterer dose scales linearly with treatment time, it follows that the highest output factor treatment plan (most open aperture, smallest modulation) best reduces overall secondary dose to the body.

Figures 5.20 and 5.19 show equivalent doses resulting from the range shifter and modulator respectively. Although the uncertainties here are much larger than for other simulations, it can still be seen that the contributions are at the $10^{-7} mSv/Gy/cc$ level - two orders of magnitude lower than scatterer dose. This indicates optimizing range shifter or modulator for secondary dose is much less effective than simply lowering the overall treatment time to reduce scatterer dose.

Lastly Figure 5.21 shows tissue-generated neutron dose. All of these results have a characteristic increasing dose contribution as the aperture opening and modulation (see Figure 5.10). Thus secondary dose from neutrons generated in the body increase with field size at the $10^{-6} - 10^{-8} mSv/Gy/cc$ level (depending on organ distance from treatment site). Again, optimizing on field size to reduce this effect would not be as effective as reducing secondary dose by decreasing treatment time.

Overall, the largest source of secondary neutron equivalent dose to the phantom

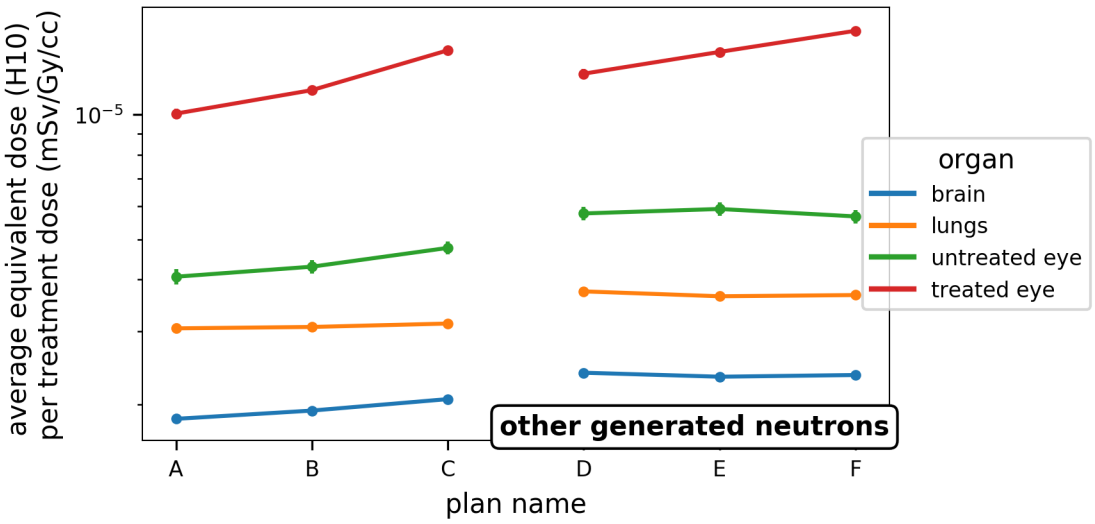

Figure 5.17: Average equivalent dose generated by 'other' sources to various organ volumes. Note these neutrons are primary generated by the scatterer.

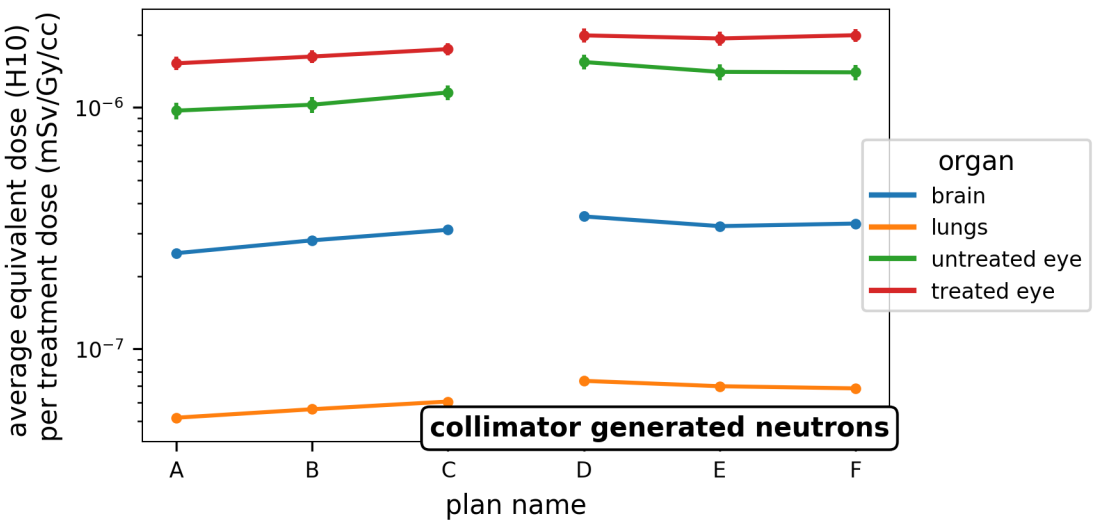

Figure 5.18: Average equivalent dose generated by the patient collimator to various organ volumes.

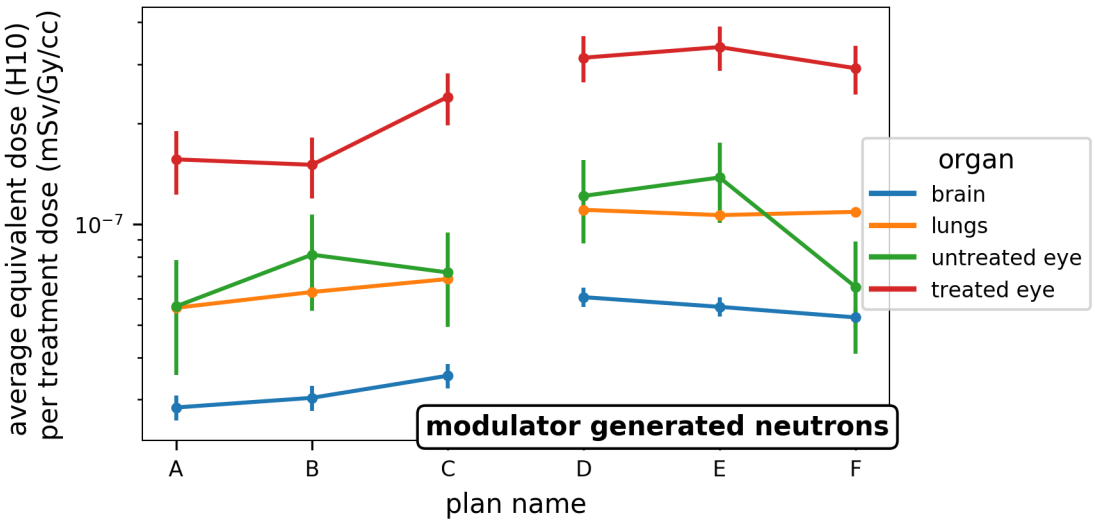

Figure 5.19: Average equivalent dose generated by the modulator wheel to various organ volumes.

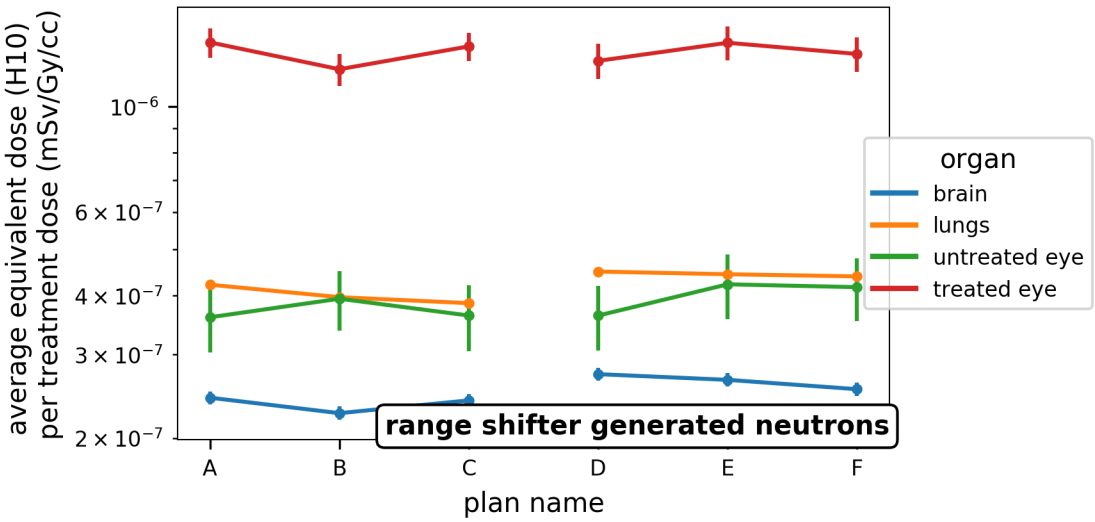

Figure 5.20: Average equivalent dose generated the range shifter to various organ volumes.

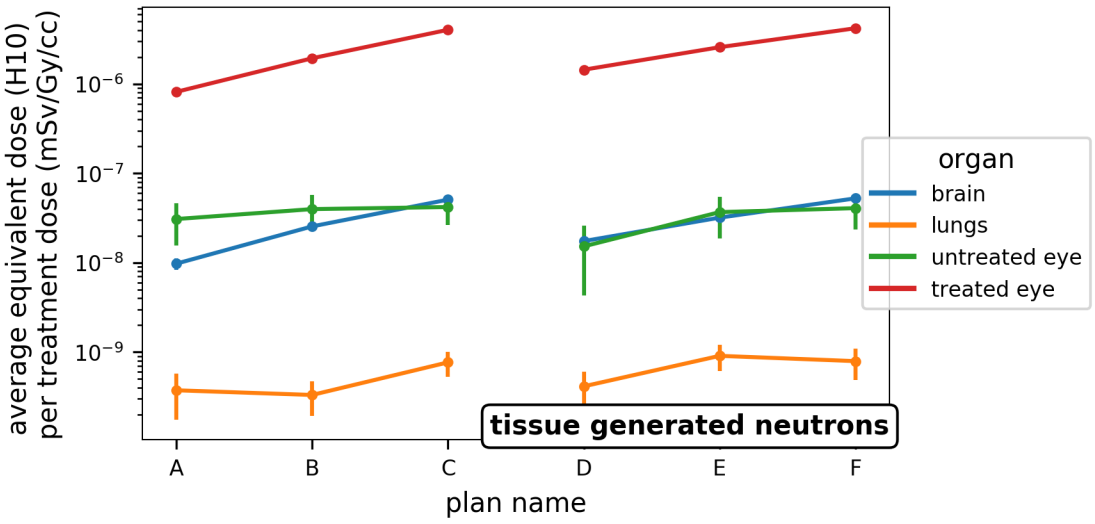

Figure 5.21: Dose equivalent to various VIPMAN organ volumes for test plans from neutrons generated in the VIPMAN tissue volume.

volume is the scatterer. This dose is orders of magnitude larger than those produced by patient and plan specific sources discussed above. Thus overall reduction in secondary neutron dose is best achieved via optimizing for reduced treatment time (highest output factor) and improving shielding around the DDS beam shaping components.

5.2.3 Neutron Dose to VIPMAN Model

Having a good understanding of the sources of secondary neutron dose, we present the simulated absolute equivalent dose to VIPMAN organs resulting from the test treatment plans. While these values are strongly dependent on the VIPMAN model size [104] and proton DDS geometry, we still may compare our results to those published by other treatment centers for the purpose of showing confidence in patient safety. All quoted values are scaled by the primary dose normalization factors calculated in § 5.1.5. Equivalent dose is calculated by multiplying the absorbed dose by an energy-dependent weighting factor (W_R) as suggested by ICRP37 [110].

Tables 5.3-5.8 show the absorbed and neutron equivalent dose to various organ volumes of the VIPMAN phantom. Notable here is the relatively large uncertainty compared to the ambient dose-equivalent values of § 5.2.2. Specifically, small organs such as the eyes, testes, and thyroid have a high associated statistical uncertainty in the equivalent dose as neutron dose-deposition events rarely occur in the small volume (see §5.2.1). Absorbed dose must be used in these calculations such that tissue density is taken into account. Weighting factors are fairly consistent across organ volumes - indicating incident neutron spectra are consistent between volumes. The main exception to this is the eyes, having the highest weighting factors, which are in a direct line with high-energy neutrons produced in the scatterer (see Figure 5.15).

In all plans, it can be seen that the phantom experiences a full-body dose bath ranging from $2 \cdot 10^2 - 1.5 \cdot 10^1 \mu SvGy^{-1}$. As a general trend, organs of the upper body, further from the treatment field, experience lower equivalent doses. The exception for some plans being the untreated eye equivalent dose which is unreliable due to relatively high statistical uncertainty. Overall for the purpose of inter-comparison of these plans, the ambient dose equivalent calculations are more reliable. TRIUMF employs ambient dose equivalent simulations for the purpose of radiation safety.

On average, dose due to neutrons originating in the treatment head are on the

order of 10^{-7} of treatment dose ($\sim 1\,\mu$Gy). This is within a factor of two from simulations of Orsay [111], but one order of magnitude lower than those of the Paul Scherrer Institute (PSI) [112]. For the former study, it is difficult to make objective comparisons since it is a double-scatterer experiment with a wall for shielding of the range-shifter and modulators. The lower magnitude compared to the second study is likely due to the simulation of only a pristine beam for secondary calculation. Additionally, the latter had a much higher neutron dose due to out-of-room beam interactions. Neutron doses to the brain and treated eye largely are due to secondary production in tissue. Here brain dose is at the 10^{-6} level, consistent with similar simulations and measurements [113]. Lastly, neutron contributions to dose in the treated eye are at the $\sim 2-5\%$ level and strongly dependent on the position and volume of tissue irradiated. Secondary absorbed dose increases with both the depth and size of the target volume. Overall, simulation of neutron absorbed doses are comparable to other centres' results. Uncertainties are largely dominated by organ size in the simulated phantom.

5.3 Summary

An anatomic eye CAD model was successfully converted into FLUKA format and used to design six different tumour models for the purpose of studying secondary neutron dose. Six plans, making use of two modulators and three collimators, were devised. A simplified optimization was performed to a fixed gaze angle, shared between the plans, to best avoid OAR's. FLUKA simulated primary dose was shown to be well-centered on all of the target volumes. Dose uniformity was found to be compromised for the larger modulation plans. Dose normalization factors were calculated for the plans to be used in normalization of neutron simulations.

Having validated beamline ambient equivalent neutron dose to within 20% in § 4.4, this quantity was studied for the six plans. Neutron contributions from major DDS components were separated by use of particle tagging. It was found that the largest source of both neutron fluence and resulting equivalent dose at the VIPMAN phantom was the scatterer. This component produced an order of magnitude larger equivalent dose than the range shifter, modulator or collimator. Thus the best method to reduce patient secondary dose is in the increase of beam output factor to avoid overall time of treatment.

Lastly, absorbed dose was simulated in the VIPMAN organ volumes. It was

Organ	Absorbed Dose ($\mu Gy\, Gy^{-1}$)	Weighting Factor (W_R)	Equivalent Dose ($\mu Sv\, Gy^{-1}$)	Stat. Uncert. (%)
Treated Eye	10.00	10.8	110	14.5
Brain	6.10	9.4	57.0	2.8
Heart	4.00	9.2	37.0	3.7
Esophagus	3.70	9.1	34.0	12.1
Liver	3.69	9.1	33.4	1.8
Testes	3.40	9.3	32.0	13.3
Lungs	3.38	9.4	31.6	2.7
Small Intestine	3.20	9.2	29.5	2.3
Large Intestine	2.80	9.1	26.0	4.3
Spleen	2.70	9.0	24.0	5.9
Thyroid	2.60	9.5	25.0	15.4
Untreated Eye	2.40	10.9	27.0	29.0
Pancreas	2.40	9.2	22.0	9.1
Kidney	2.10	9.1	19.0	5.4

Table 5.3: Absorbed dose, equivalent dose and energy dependent radiation weighting factors for plan A.

Organ	Absorbed Dose ($\mu Gy\, Gy^{-1}$)	Weighting Factor (W_R)	Equivalent Dose ($\mu Sv\, Gy^{-1}$)	Stat. Uncert. (%)
Treated Eye	10.0	9.8	100	14.3
Brain	6.20	10.0	61.0	2.7
Esophagus	4.20	9.5	39.0	13.3
Heart	4.10	9.9	41.0	3.7
Liver	3.80	8.7	33.3	1.7
Lungs	3.42	9.2	31.6	2.6
Large Intestine	3.10	9.5	29.0	4.3
Small Intestine	3.06	9.4	28.8	2.2
Thyroid	3.10	8.2	25.0	21.2
Pancreas	2.80	9.8	27.0	9.3
Spleen	2.80	9.9	28.0	5.8
Testes	2.70	8.8	24.0	13.3
Untreated Eye	2.50	6.8	17.0	27.0
Kidney	2.40	9.0	21.0	5.5

Table 5.4: Absorbed dose, equivalent dose and energy dependent radiation weighting factors for plan B.

Organ	Absorbed Dose ($\mu Gy\, Gy^{-1}$)	Weighting Factor (W_R)	Equivalent Dose ($\mu Sv\, Gy^{-1}$)	Stat. Uncert. (%)
Treated Eye	18.0	11.3	200	13.4
Brain	6.40	9.7	61.0	2.6
Untreated Eye	4.40	107	4.80	21.6
Heart	3.90	9.3	37.0	3.7
Liver	3.82	9.1	34.6	1.7
Lungs	3.44	9.4	32.2	2.6
Pancreas	3.20	8.9	28.0	8.4
Thyroid	3.20	9.6	30.0	14.0
Small Intestine	3.04	92.0	2.79	2.2
Esophagus	3.00	9.0	27.0	14.2
Large Intestine	3.00	91.0	2.70	4.4
Spleen	2.70	8.9	24.0	5.9
Testes	2.50	9.6	24.0	17.3
Kidney	1.96	9.1	17.9	5.0

Table 5.5: Absorbed dose, equivalent dose and energy dependent radiation weighting factors for plan C.

Organ	Absorbed Dose ($\mu Gy\, Gy^{-1}$)	Weighting Factor (W_R)	Equivalent Dose ($\mu Sv\, Gy^{-1}$)	Stat. Uncert. (%)
Treated Eye	13.0	10.9	140	15.1
Brain	7.40	9.6	71.0	2.6
Untreated Eye	5.00	10.9	54.0	20.5
Heart	4.80	9.3	45.0	3.9
Liver	4.50	9.1	41.0	1.8
Lungs	4.10	9.4	39.0	2.5
Testes	3.90	9.4	36.0	15.1
Small Intestine	3.71	9.1	33.9	2.3
Large Intestine	3.70	9.0	33.0	4.5
Thyroid	3.60	9.8	35.0	19.8
Spleen	3.30	8.8	29.0	6.3
Pancreas	3.20	9.2	30.0	9.2
Esophagus	3.10	9.1	28.0	12.6
Kidney	2.70	9.1	25.0	5.3

Table 5.6: Absorbed dose, equivalent dose and energy dependent radiation weighting factors for plan D.

Organ	Absorbed Dose ($\mu Gy\, Gy^{-1}$)	Weighting Factor (W_R)	Equivalent Dose ($\mu Sv\, Gy^{-1}$)	Stat. Uncert. (%)
Treated Eye	17.0	11.0	190	13.8
Brain	7.40	9.6	70.0	2.6
Untreated Eye	4.60	10.9	50.0	20.3
Heart	4.60	9.3	43.0	3.8
Liver	4.43	9.1	40.3	1.7
Lungs	3.95	9.4	37.0	2.5
Testes	3.90	9.5	37.0	12.8
Thyroid	3.90	9.6	37.0	17.6
Small Intestine	3.74	9.2	34.2	2.3
Large Intestine	3.50	9.1	32.0	4.5
Pancreas	3.50	9.2	32.0	8.9
Spleen	3.20	8.9	28.0	6.0
Esophagus	3.00	9.0	27.0	12.1
Kidney	2.60	9.2	24.0	5.6

Table 5.7: Absorbed dose, equivalent dose and energy dependent radiation weighting factors for plan E.

Organ	Absorbed Dose ($\mu Gy\, Gy^{-1}$)	Weighting Factor (W_R)	Equivalent Dose ($\mu Sv\, Gy^{-1}$)	Stat. Uncert. (%)
Treated Eye	13.0	11.2	150	13.5
Brain	7.50	9.5	72.0	2.6
Liver	4.55	9.1	41.5	1.8
Heart	4.50	9.3	42.0	3.6
Lungs	4.20	9.4	40.0	2.5
Small Intestine	3.86	9.2	35.3	2.3
Pancreas	3.90	9.2	35.0	8.9
Testes	3.60	9.4	34.0	16.1
Untreated Eye	3.40	11.0	38.0	22.3
Large Intestine	3.30	9.1	30.0	4.2
Spleen	3.30	8.9	29.0	6.6
Thyroid	3.20	9.5	31.0	15.0
Esophagus	3.00	9.0	27.0	11.6
Kidney	2.30	9.2	21.0	5.6

Table 5.8: Absorbed dose, equivalent dose and energy dependent radiation weighting factors for plan F.

found that calculated equivalent doses in the phantom were within the range of those reported by similar proton therapy facilities.

Chapter 6

3D Printed Plastics for Beam Modulation in Proton Therapy

6.1 Introduction

The following chapter covers the study of two 3D-printing methods and materials for use in proton beam modulation. It was published in Physics in Medicine and Biology[114], with some material removed for brevity including beam profiles, mechanical measurements and CT profiles. This additional data is included at the end of this chapter for completeness.

6.2 3D Printed Plastics for Beam Modulation in Proton Therapy

C. Lindsay, J. Kumlin, A. Jirasek, R. Lee, D.M. Martinez, P. Schaffer, C. Hoehr

Abstract: Two 3D printing methods, fused filament fabrication (FFF) and PolyJet^{TM} (PJ) were investigated for suitability in clinical proton therapy (PT) energy modulation. Measurements of printing precision, printed density, and mean stopping power are presented. FFF is found to be accurate to $0.1mm$, to contain a void fraction of 13% due to air pockets, and to have a mean stopping power dependent on geometry. PJ was found to print accurate to $0.05mm$, with a material density and mean stopping power consistent with solid poly(methyl methacrylate) (PMMA). Both FFF and PJ were found to print significant, sporadic defects associated with sharp edges on the order of $0.2mm$. Site standard PT modulator wheels were printed using both methods. Measured depth-dose profiles with a $74MeV$ beam show poor agreement between PMMA and printed FFF wheels. PJ printed wheel depth-dose agreed with PMMA within 1% of treatment dose except for a distal falloff discrepancy of $0.5mm$.

6.2.1 Introduction

Proton therapy (PT) has proven dosimetrically advantageous over standard photon radiation therapy treatments in sites such as the eye and paediatric central nervous system [115]. This is owing to the sharp, energy dependent nature of the proton depth dose distribution known as the Bragg peak (BP). Too sharp to be clinically useful, proton treatments require a delivery system which supplies an energy-modulated beam to a target volume to create a spread out Bragg peak (SOBP) in depth. Two methods are employed in beam delivery – active scanning and passive scattering. In the former, a tunable energy accelerator delivers sequential energy beams which apply dose to the target in depth layers. In the latter, material is placed directly into a monoenergetic beam (typically a spinning plastic wheel of variable thickness) to modulate energy[116](Paganetti, 2011, §5.2). Due to its early development and mechanical simplicity, the vast majority of treatments to date have been administered with a passive system [117].

Passive systems are well suited to single-field, uniform dose plans such as those employed in treating ocular tumours at the TRIUMF $520MeV$ cyclotron. Here, an azimuthally stepped wheel of poly(methyl methacrylate) (PMMA), known as a modulator wheel, rotates through the beam during delivery. Each step in the wheel produces a corresponding BP dose distribution. The step thicknesses and widths are chosen to produce a uniform plateau of dose to the target volume. A set of pre-made wheels define the size of the uniform plateau of dose delivered to the target volume. PMMA makes an excellent energy-degrading material as it is precisely machinable, consistent in density, radiation hard, minimally scattering and has a rapid decay profile. While all clinical requirements are met by this system, the prepared set of wheels do not account for patient specific geometries and the machining process is costly in time, financial resources and expertise. The burgeoning technology of 3D printing has the potential to alleviate these issues.

3D printing, or additive manufacturing, is the process of manufacturing 3D solid objects from a digital model. Originally developed in 1984, the process of building an object up in layers allows many more geometric possibilities over standard subtractive techniques such as computer numerical control (CNC) milling. Dropping vastly in price since its inception, 3D printing is now seeing widespread use in aerospace, automotive, architectural prototyping. This technology has also started to appear in medicine with successes including PT range compensation [9] and patient-specific

phantom dosimetry [10].

With the availability of medical-grade materials printing to accuracies at the sub-millimetre level, proton beam modulation using printed plastic becomes feasible. Studies into printing consistency, plastic density, geometric precision, and radiation effects are necessary. This work takes the first step, reproducing modulator wheels for the TRIUMF PT delivery system using two of the most common printing methods – fused filament fabrication (FFF) [118] and PolyJet^{TM} (PJ) [119]. The extreme sensitivity in proton range to beam degraders makes range modulation an excellent test of print precision. In addition to this, the measured properties of the printed materials are widely valuable in the manufacture of more common beam-degrading components in charged particle therapy such as PT range compensation or electron therapy bolus.

6.2.2 Materials and Methods

TRIUMF Accelerator and Proton Therapy Facility

The TRIUMF cyclotron, located on campus of the University of British Columbia, accelerates H^- ions to a peak of $520 MeV$ with a maximum current of $220\,\mu$A. The multi-user simultaneous extraction machine services three beamlines, including beamline 2C1 – a 65-$110 MeV$, 10 nA line to the PT facility. Here, an average of ten patients per year [120] receive PT in the treatment of ocular tumours with an extracted beam of $74 MeV$ at 6 nA.

The dose delivery system (DDS) is a standard passive scattering setup: lead scatterer, PMMA range shifter and modulator wheel [8], two brass collimators with polyethylene secondary shielding, monitoring chambers, and a tumour-specific brass nozzle collimator. Dose calibration is performed in the centre of a SOBP produced by a $23 mm$ PMMA modulator wheel which was designed for the original treatment energy of $70 MeV$[121]. DDS ion chamber output is calibrated to a national laboratory standard electrometer/ion chamber pair on a per-treatment basis. Relative geometric dose verification is performed in a waterbox using a BPW34 PIN photo-diode.

3D Printers

Two methods of 3D printing were tested for reproducibility, printed density, printing precision, surface defects and consistency of density. Both printers were also tested in the reproduction of the PT facility's 23mm PMMA wheel. In detail, the two printing methods are:

Fused Filament Fabrication (FFF) printers are based on the heating and layering of thermoplastics. Above a characteristic glass transition temperature, semi-molten thermoplastics can be extruded and precisely deposited into layers. A printer's extrusion head is fed a coil of thermoplastic; its nozzle heats the plastic and rasters it in layers. The plastic hardens promptly, building the 3D structure in layers to match the supplied design.

PolyJet^{TM} (PJ) printers lay successive layers of photo-polymer resin in the same manner as standard ink-jet printers. When exposed to UV light, photopolymers cure to form a solid. PJ printers semi-cure the photo-polymer while printing, then perform a full cure after a set thickness is laid. A removable support structure is printed when required.

Print Method	FFF	PJ
Manufacturer	StrataSys Inc.	StrataSys Inc.
Model	uPrint SE plus	Objet30 Pro
Layer Thickness	0.25mm	0.016mm
Lateral Precision	0.9mm[1]	0.1mm
Material	ABSPlus	VeroWhitePlus
	[122]	[123]
Density	1.07 g/cm^3	1.17-1.18 g/cm^3
Filament Diameter	1.75mm	N/A

Test Objects

Three identical cubes (length: 21.7mm) and two disks (height: 10mm, 2.07mm; radius: 14cm) were printed using both the FFF and PJ methods. Object dimensions

[1]Manufacturer quotes the minimum recommended material thickness in the lateral direction to avoid print errors.

were chosen corresponding to TRIUMF PMMA wheel design thicknesses. Disks were manufactured such that the print layers lay in the circular plane of the cylinder. Support structure and base were removed mechanically. Care was taken to evaluate each object in the 'print' direction (vertical, in which successive layers are deposited) as well as 'lateral' directions (plane of the printer base) as defects might differ.

Visual inspection and caliper measurements were performed to check machine printing precision. Each object was CT scanned (model: GE Lightspeed RT16) with one lateral direction aligned with the CT slice axis such that one print and lateral dimension were imaged at high resolution. Wheel surface defects were measured using a laser profilometer sensitive to the micron level(model: Nanovea ST400). Gamma spectroscopy was used to gauge activation of the two materials – using an N-type co-axial HPGe gamma spectrometer from Canberra ($0.5mm$ beryllium window, calibrated to a 20 mL ^{152}Eu source).

Water depth-dose profile measurements were done for each disk thickness to estimate water-equivalent thickness (t_w). The shift in the 90% distal falloff (ΔR_{90}) of the blocked beam in water is taken as the water equivalent thickness (t_w). When blocked by a material of density ρ, the thickness t is related to the mean stopping power $\bar{S}$ as [57]:

$$t_w = \Delta R_{90} = t\frac{\rho}{\rho_w}\frac{\bar{S}}{\bar{S}_w} \tag{6.1}$$

where subscript w denotes water and mean stopping power is defined as:

$$\bar{S} = \frac{\int_t S(E(x))dx}{\int_t dx} \tag{6.2}$$

Measuring ΔR_{90}, combining equations (1) and (2), and the water equivalence for PMMA [57], facilitates the calculation of $\bar{S}/\bar{S}_{PMMA}$ and a direct comparison of material mean stopping powers over the therapeutic range.

Stepped Wheels

Two reproductions of the TRIUMF PMMA wheel, close up photo shown in Figure 6.1, were produced for each printing method. Original PMMA wheel dimensions were $14cm$ in diameter with 20 steps ranging from $2.07mm$ to $21.7mm$ thickness. Under the assumption of similar stopping power to PMMA at therapeutic energy ranges, the wheel dimension in the beam direction was scaled according to printed material

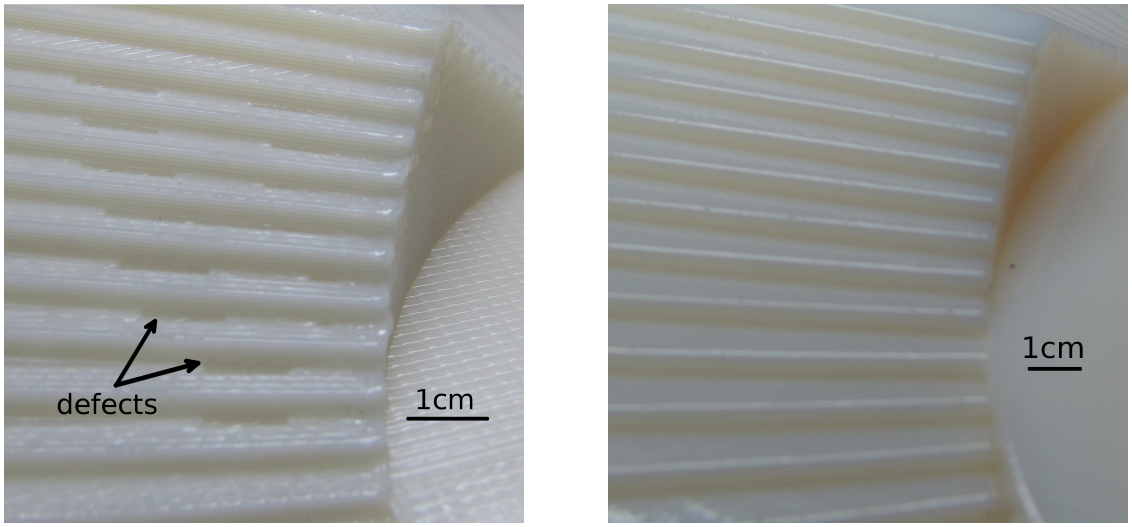

Figure 6.1:]
Photos of the FFF wheel (left) and PJ wheel (right). Notable are the consistent, significant surface defects in the FFF print.

density. Laser profilometer scans were done to ensure step height accuracy as well as to assess surface defects.

The SOBP distribution in water of two wheels of each of PJ and FFF were measured under clinical conditions. Measurements were each repeated three times per wheel for a total of twelve SOBP measurements. These data were assessed to determine the capability of each printer to reproduce an object given identical inputs (intra-print consistency). The average distribution was taken as the result. Lateral profile measurements of each wheel at $1cm$ depth were also performed.

6.2.3 Results and Discussion

Table 6.1: Standard deviation on caliper measurement (σ), average absolute print error ($|\bar{\epsilon}|$) and print error range (ϵ_{min},ϵ_{max}) for the FFF and PJ test objects.

		Print Direction			Lateral Direction		
	(mm)	σ	$\lvert\bar{\epsilon}\rvert$	ϵ_{min},ϵ_{max}	σ	$\lvert\bar{\epsilon}\rvert$	ϵ_{min},ϵ_{max}
FFF	$2mm$ Disk	0.05	0.3	(0.2,0.3)	0.1	0.3	(-0.4,-0.1)
	$10mm$ Disk	0.06	0.3	(0.2,0.4)	0.2	0.1	(-0.3,0.1)
	$20mm$ Cube	0.02	0.2	(0.08,0.3)	0.1	0.07	(-0.05,0.2)
PJ	$2mm$ Disk	0.01	0.001	(0.001,0.001)	0.04	0.04	(-0.09,0.0)
	$10mm$ Disk	0.01	0.005	(0.0,0.01)	0.03	0.07	(-0.1,-0.03)
	$20mm$ Cube	0.01	0.05	(-0.02,0.04)	0.06	0.02	(-0.04,0.2)

Printing Precision

Visual Inspection:

Test cubes were found to have visible defects associated with edges of the prints. Both the FFF and PJ cubes had inconsistent defects on the order of $0.1mm$ at the corners which were not associated with the print or lateral directions. Figure 6.1 (left) shows the rough finish of the FFF wheel stepped surface. Here, significant visible defects in a portion of the step pattern occur in the form of millimetre sized grooves. This pattern is regular and consistent between the two FFF wheel prints. Digital inspection of the STL file showed no such defects. This suggests the cause was

either a systematic error in printing due to the stepped geometry edges, or an error in reading the STL in the printing software. Figure 6.1 (right) shows the smooth, glossy finish of the PJ wheel. The wheel has no visible defects on the surface.

Caliper Measurements:

The measurements in the lateral direction for the FFF prints, shown in Table 6.1, are consistent with a resolution of $\sim 0.2mm$. PJ shows improved precision for all shapes at a resolution of $\sim 0.1mm$; however, defects in the cube prints indicate poor inter-print consistency associated with sharp corners.

In the print direction FFF print errors worsen. All prints were larger than design – indicating the layer thickness ($0.254mm$) is a limiting factor. It appears the FFF printer algorithm does not account for absolute precision in this direction – consistently opting for an over-print. This could prove problematic for beam modulation when the beam axis is oriented along the print direction. The PJ measurements are drastically improved over the FFF, with a thickness to the level of caliper accuracy ($0.01mm$). This is consistent with the manufacturer's quoted layer thickness of $0.016mm$ when cube corner defects are excluded.

Laser Profilometer:

Profilometer measurements of the cube surfaces, depicted in Figure 6.2 (left), show channels of depth $\sim 150\,\mu$m on the FFF surface in a grid pattern consistent with the raster method of printing. Considering the print algorithm, it is reasonable to assume similar defects in the interior – resulting in an overall reduction in density. The PJ print exhibits sporadic defects at the level of $20\,\mu$m. Scans of the bottom of the print indicate defects on the order of $30\,\mu$m due to the backing/supports required to print.

Printed Density

Caliper and Scale:

The FFF printer, using ABSPlus material, was found to print objects of an average density of $0.93\,\mathrm{g/cm^3}$– consistent between shapes within limits of measurement (shown in Table 6.2). Solid ABS plastic varies slightly in density with median value of $1.07\,\mathrm{g/cm^3}$. Thus, air pockets intrinsic to the printing process effectively reduce the material density by $\sim 13\%$. PJ, printing VeroWhitePlus, was found to provide

Table 6.2: Table of printed densities (ρ) and stopping power ratio to PMMA ($\bar{S}$ / $\bar{S}_{PMMA}$) for test objects.

	FFF		PJ	
	ρ (g/cm^3)	$\bar{S}$ / $\bar{S}_{PMMA}$	ρ (g/cm^3)	$\bar{S}$ / $\bar{S}_{PMMA}$
$2mm$ Disk	0.93 ± 0.02	1.0 ± 0.1	1.188 ± 0.006	1.0± 0.1
$10mm$ Disk	0.932 ± 0.005	1.10 ± 0.07	1.184 ± 0.001	0.98± 0.03
$20mm$ Cube	0.94 ± 0.01	1.08 ± 0.04	1.186 ± 0.006	1.01± 0.01
Overall	0.93 ± 0.02	1.06 ± 0.05	1.186 ± 0.006	1.0 ± 0.02

a consistent density between shapes of $1.186\,\mathrm{g/cm^3}$. This is in the range of solid, acrylate plastics such as PMMA.

CT Scan:

CT slices (thickness $0.4mm$) for a FFF cube print are shown in Figure 6.2 (upper). The print plane image (middle) show the regular grid pattern of the printing algorithm. The $4mm$ slice variation was found to be 2.3% of the average voxel value of 890 HU. The lateral plane (right) yields similar density values but shows a different density pattern in the print direction. The average magnitude of density variation is the same between directions, with the lateral direction presenting edge hotspots. High density internal hotspots and edge hotspots could be due to temperature variations or inherent in the geometry-dependent machine algorithm. Should the density variation depend strongly on geometry, then this print method would be clinically unacceptable.

CT data for a PJ cube print are shown in Figure 6.2 (lower). Here the $4mm$ slice variation is 0.3%, almost an order of magnitude more consistent than the FFF. Variations in density through the cube are consistent with CT machine noise, indicating a homogeneous medium within measurement capabilities. Again, density hotspots occur near the edges of the cube, consistent with the noted visible corner/edge defects. The PJ print algorithm relies on surface tension of the partially cured photopolymer. Edge hotspots could be due to freedom of flow of the material at the edge of the object, or compensation in the print algorithm for this effect.

Stopping Power

Table 6.2 shows stopping power ratios for the three test objects. Systematic errors for diode position and accelerator energy variation were included ($0.2mm$) leading to a t_w with $\sim 10\%$ and $\sim 1\%$ uncertainty for the $2mm$ and $10mm$ disks respectively. With the precision available, it is difficult to draw conclusions from the thin disk. Given the density results, it is expected that the FFF results (with material ABSplus) should be geometry dependent. This is affirmed here where the ABSPlus stopping powers are inconsistent between the disks and cubes. The PJ results (with material VeroWhitePlus) are consistent between shapes with a value consistent with solid PMMA. Despite the relative inaccuracy of these measurements, results of near-unity stopping power ratio ($\bar{S}/\bar{S}_{PMMA} \approx 1$), justify reproducing TRIUMF PMMA wheels

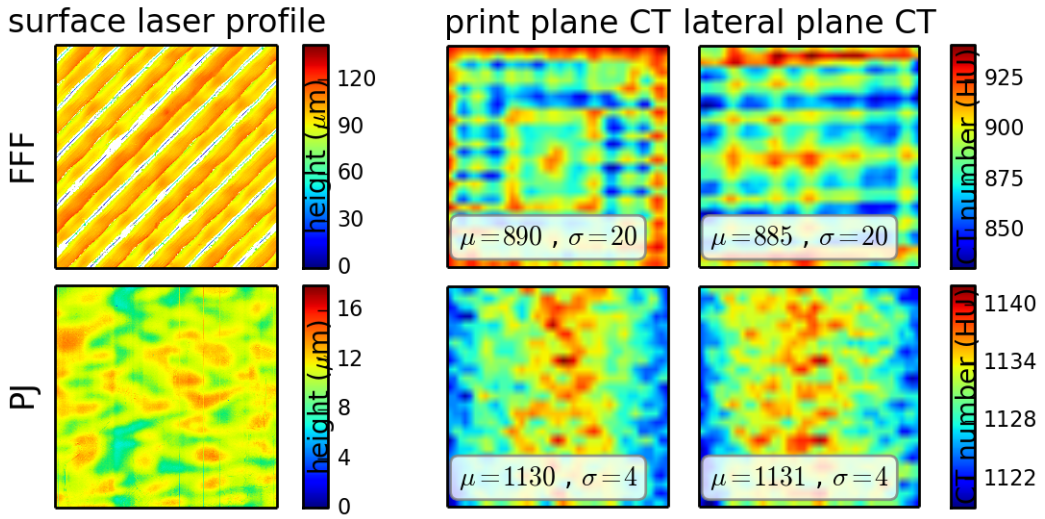

Figure 6.2: $5mm$ x $5mm$ laser profilometer surface scans (left) for the FFF (upper) and PJ (lower) test cubes – white is unreadable, color scale is relative to lowest measured point. CT slice ($0.4mm$ thickness) images perpendicular to the print direction (middle), and lateral direction (right) – μ is the mean; σ is the standard deviation.

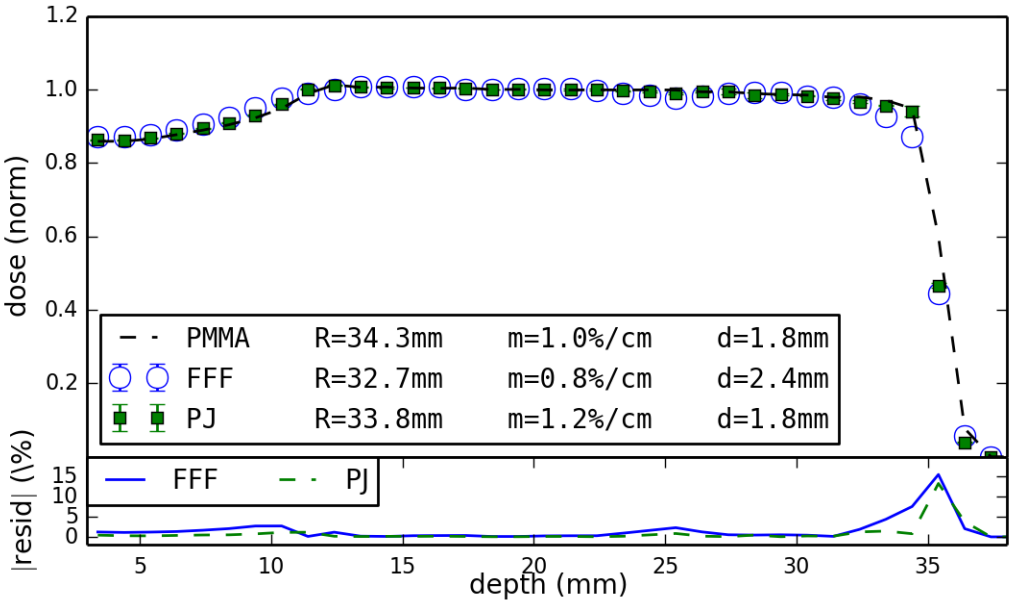

Figure 6.3: FFF and PJ printed wheel SOBP in water shown with target PMMA SOBP with 90% falloff range (R,$\pm 0.2mm$), plateau slope (m,± 0.2 %/cm) and 90%$-$10% distal penumbra width (d,$\pm 0.2mm$).

by simple density scaling.

Material Activation

Gamma spectroscopy was performed immediately after irradiation of a cube of each material to approximately 5 Gy. Initial scans indicated activation in both materials consistent with PMMA. Scans performed one week later showed no activity. The materials contain no detectable levels of long-lived activated components which make them suitable for practical, clinical use.

Stepped Wheel Dose Distribution

Measurement of the SOBP produced by density-scaled wheels are shown in Figure 6.3. Here, each curve is the combination of six measurements – three runs on two replica wheels. Standard deviation between measurements is very small (order 0.1%), indicating consistency between prints and beam stability during measurement.

Notable features of the FFF wheel contributing to its SOBP shape (Fig. 6.3) are the systematic $\sim 1mm$ surface defects, over-print of the thinnest layer (2.37 vs

2.07mm), interior density defects and slightly higher stopping power of the material. The resulting SOBP distal falloff (90%-10% region) is 0.6±0.3mm wider than the PMMA wheel. This is owing to air-pockets which produce unpredictable variations in modulation across the wheel. The plateau is consistent, with a dip in the centre corresponding to the visible surface defect. The incoming dose is slightly higher and transition into the plateau is not as sharp as the PMMA, owing to density/print precision. The discrepant plateau width and position produce a range discrepancy of ∼1.5mm, on the order of the distal planning margin of 2.5mm. Overall, the simple method of scaling by density is insufficient to reproduce the 23mmPMMA wheel depth-dose using this FFF printer.

The PJ SOBP, is consistent with the PMMA results to within 1% of treatment dose, except for the distal falloff region. Here the PJ print exhibits a decreased range of ∼0.5 mm. This discrepancy is small compared to measurement accuracy and distal planning margins. Additionally, the density value used to scale the PJ wheel dimensions included a 0.5% uncertainty (see Table 6.2) for both VeroWhite and PMMA, translating to a ∼0.2mm shift in range, which was not accounted for in this analysis. Plateau width, slope and distal penumbra are consistent between the two wheels. Overall, the simple method of scaling the PJ print to PMMA density results in a consistent SOBP distribution, with a range discrepancy on the order of experimental and scaling uncertainties.

Lateral measurements at 1cm depth were consistent within measurement sensitivity (0.2mm) between the PMMA, FFF and PJ wheels. Any defects in the wheels had no measurable effect on the lateral profile.

6.2.4 Conclusions

Two methods of 3D printing were successfully evaluated for use as beam energy modulating components in PT. It was found that the FFF solid print presented regular surface defects on the order of 150 μm, systematic macroscopic visible defects, 4mm slice density variation of 2.3% and wheel step height accuracy within 0.1mm. The PJ showed improved characteristics in all categories with no visible defects, density variation at 0.3%, and step heights accurate to 0.05mm. Printed densities were found to be 0.93 g/cm^{3}and 1.186 g/cm^{3}for the FFF and PJ prints respectively. This indicates that air pockets produce a 13% density reduction in the FFF print and no detectable density reduction in the PJ print. Mean stopping powers for 2, 10,

and 21mm thicknesses were found to be consistent with PMMA for PJ and geometry dependent for FFF. Density scaled 23mm wheels proved unacceptable for FFF and within 1% of treatment dose for PJ excepting a range discrepancy of 0.5mm.

Further studies into other 3D printing methods, such as stereolithography, and other machines are necessary to find the ideal system to implement clinically. Additionally, with the demonstrated sharp-edge defects, it may be beneficial to design stepless modulator wheels when considering 3D printing for this application. Successes in this work show that the PJ 3D printing technique is ready for use in proton therapy.

6.2.5 Acknowledgements

We would like to gratefully acknowledge primary funding for this work from the National Science and Engineering Research Council of Canada. Additionally, we thank Brian Hook of the TRIUMF Nuclear Medicine division for access to equipment and expertise in laser profilometry surface scanning.

6.3 Supplementary Data

The following figures were removed from the original publication for brevity.

Caliper Measurements

Figure 6.4 shows the error in printed dimensions for the test objects for both FFF and PJ methods. In the lateral direction, FFF has a large print variance owing to inconsistent wall thickness using this method. This effect is reduced for PJ, but still present as there is a limit stiffness possible and sag will occur due to gravity. In the print direction FFF consistently over-prints due to the relatively large layer thickness compared to PJ. The exquisitely small layer thickness of the PJ method shows in both the accuracy and low variation in the PJ print direction measurements.

CT Scan Uniformity

Figure 6.5 shows average CT profiles for the cube object for the FFF and PJ prints in both directions. Discussion is included in the §6.2.3.

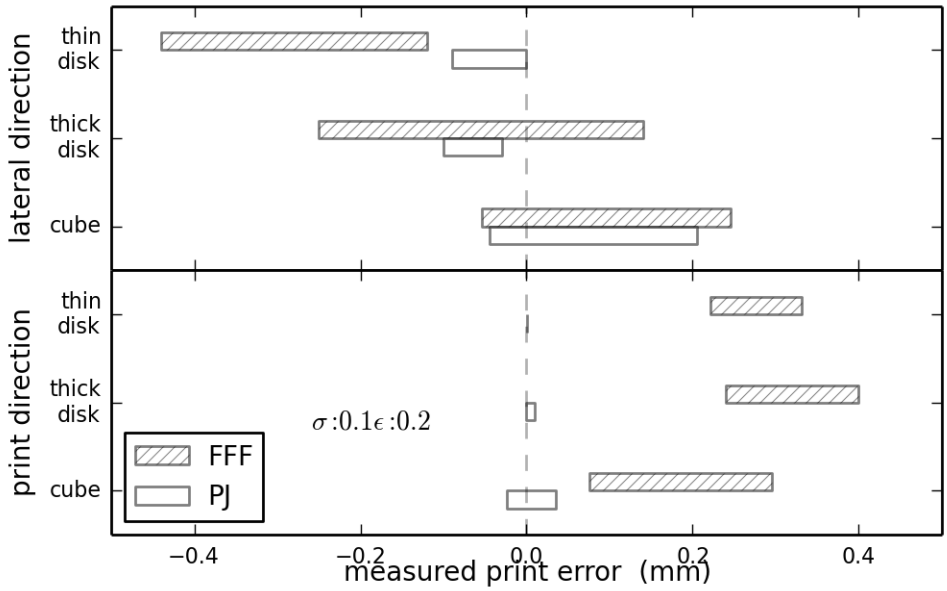

Figure 6.4: Test object dimensions (l) as measured using calipers expressed as a difference from design specifications ($l_{measured} - l_{design}$). Lateral direction shown above and print direction shown below.

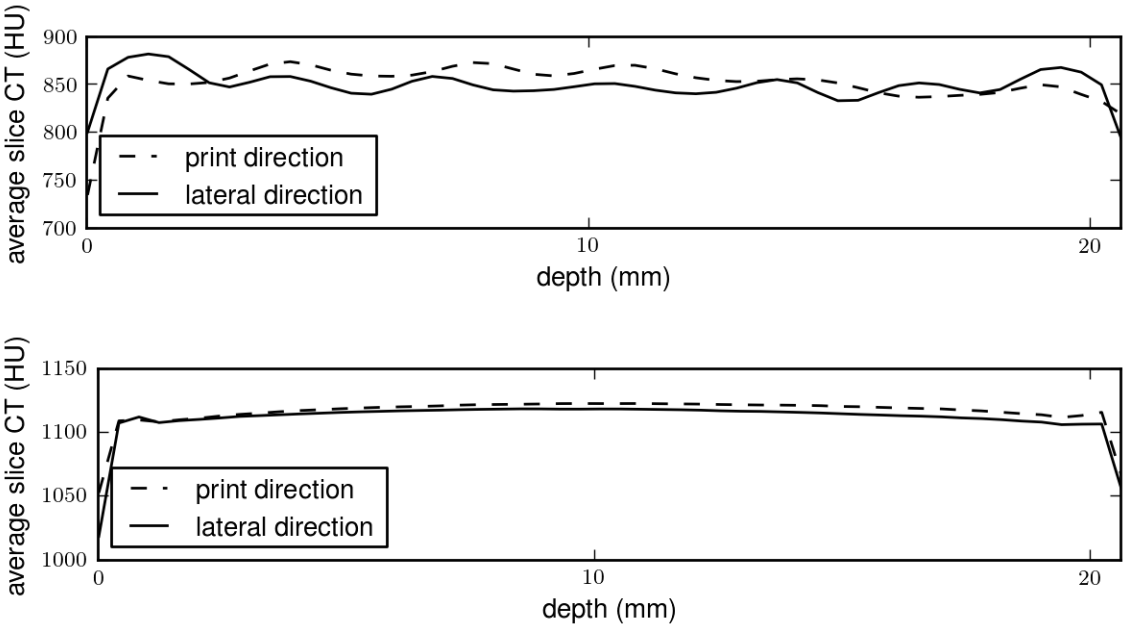

Figure 6.5: Average CT number by slice for both print and lateral directions for FFF (top) and PJ (bottom). μ is the mean; σ is the standard deviation.

Beam Profiles

Figure 6.6 shows lateral beam profiles in water at $1cm$ depth for the PMMA calibration wheel, PJ and FFF printed wheels. Within measurement precision ($0.5mm$ step size) there was no discernible difference in profile measurements.

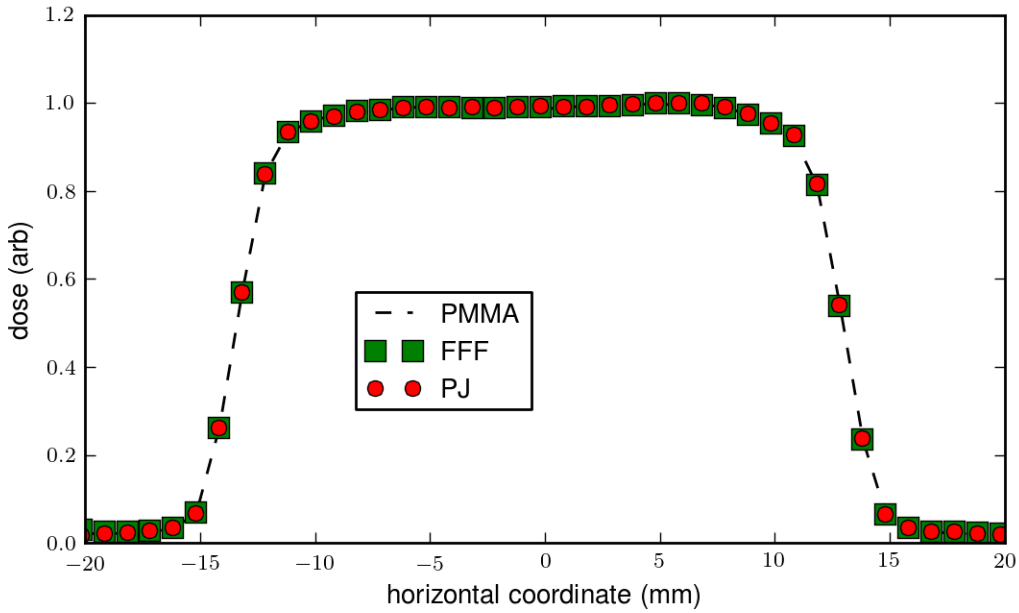

Figure 6.6: Horizontal dose profile measured at $1 cm$depth for the FFF,PJ and PMMA calibration wheels.

Chapter 7

Design and Application of 3D-printed Stepless Beam Modulators in Proton Therapy

7.1 Introduction

The following chapter covers optimization and production of stepless modulator wheels for use in proton therapy. Before this study, it was widely accepted that a limited stepped configuration produced the optimal dose distribution. This paper was published in Physics in Medicine and Biology[124] disproving this long-standing belief. Covered in this section is classic optimization for stepped wheels, a new optimization method for smooth modulation, manufacture of stepless wheels using PolyJet printing and comparison of measured results.

7.2 Design and Application of 3D-printed Stepless Beam Modulators in Proton Therapy

C. Lindsay, J. Kumlin, D. M. Martinez, A. Jirasek, C. Hoehr

7.2.1 Introduction

Monoenergetic protons produce a dose distribution which is too sharp to be useful in clinical proton therapy (PT). A polyenergetic beam is required to provide uniform dose to a tumour volume. In passive scatter PT, this is commonly accomplished by degrading a monoenergetic beam using a rotating plastic wheel of variable thickness known as a modulator wheel.

The design of stepped modulator wheels is a well developed topic (see Paganetti, 2011, §5.2). The general design strategy is to define the distal end of the spread out Bragg Peak (SOBP) by one heavily weighted Bragg Peak (BP) (in the thinnest wheel step). Successive steps are then added, optimizing the wheel angle share (weights), to produce a region of uniform dose. The difference in depth, or pull-back, between each BP is often constrained to be a fixed value as this works quite well and simplifies the optimization procedure [125].

While each design process may use different inputs depending on what is available (eg: measured BP data, analytic BP models with measured output factors), all classic methods of design can be generalized to the following:

Defining dose at depth x resulting from thickness t of beam degrader as $F(t_i, x)$, the number of steps n, and the wheel weight for step i as w_i the resulting SOBP of a stepped wheel is then:

$$D_{stepped}(x) = \sum_{i=1}^{n} F(t_i, x) \cdot w_i \tag{7.1}$$

An optimization aims to calculate the w_i such that the SOBP is flat in the plateau region. We take m points, denoted the 'mesh' points, in the SOBP plateau to optimize for flatness and define a target vector $\vec{t}$ of rank m. Setting the target $\vec{t}$ to $\vec{1}$ and writing equation 7.1 in matrix notation gives:

$$\vec{t} = \vec{1} = \mathbf{F}\vec{w} \tag{7.2}$$

In the simplest (and most commonly used) case, where the number of mesh points is equal to the number of steps ($m = n$), the optimization can be performed by inverting the square matrix $\mathbf{F}$ [116]:

$$\vec{w} = \mathbf{F}^{-1}\vec{1} \tag{7.3}$$

While this method is straightforward and fast, it restricts the accuracy of the resulting distribution since only a small number of mesh points are optimized. This limitation can be overcome by increasing the number of mesh points [8] and optimizing for the euclidean norm between the target and resultant:

$$\vec{w} = arg\,min_{\vec{x}\in\mathbb{R}^n}||\mathbf{F}\vec{x} - \vec{1}|| \tag{7.4}$$

where $\mathbf{F}$ is now rank $m \times n$.

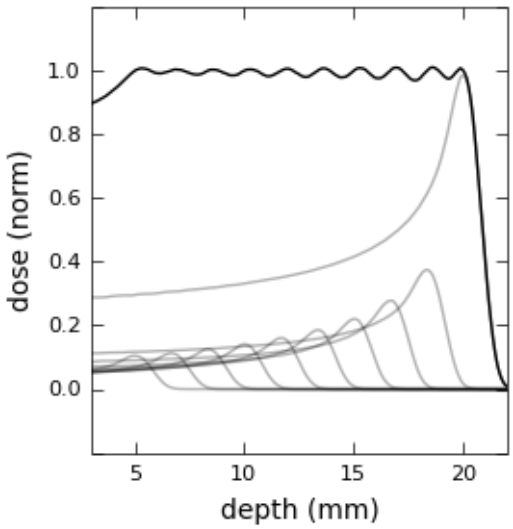

Figure 7.1: Koehler SOBP (N=10), falloff defined by deepest BP, poor uniformity.

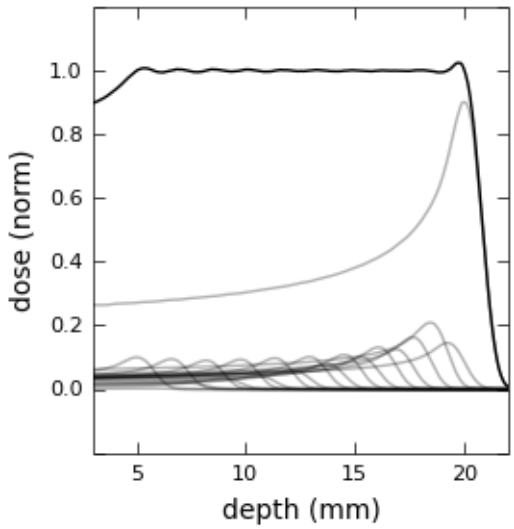

Figure 7.2: Koehler SOBP (N=20), improved uniformity, falloff influenced by second deepest BP.

Both the Koehler and Gardey method produce acceptable dose distributions; but, they are constrained by the limitation of fixed pull-back between peaks. This leads to a trade-off as described in [32], namely the uniformity improves with an increasing

number of steps used, as demonstrated comparing Figures 7.1 and 7.2. At the same time, the width of the distal penumbra increases as the number of steps exceeds a maximum limit. This is due to the influence of the second deepest BP on the total falloff of the SOBP, as shown in Figure 7.2.

Further investigations into increasing the number of peaks concluded that the limit of decreasing step size resulted in a *less* uniform distribution [126]. Here an optimization on a SOBP plateau mesh was driven by a square-sum-difference objective function. The optimization method was unconstrained, allowing for negative weights which were discarded. The space of solutions explored was that of equally spaced BPs. The conclusion was that in the many-step limit, the continuous solution was always worse than an optimal low number of steps. This result is accurate for the explored solution space of fixed pull-back between BPs.

A larger solution space may be explored by optimizing for a continuous (stepless) wheel distribution. Here the unconstrained, negative weight producing, optimization of Prieels may be replaced by a standard, constrained, gradient based approach. This work details the optimization procedure as well the simulated and measured results.

With the development of 3D printing and its early applications in radiotherapy, it becomes feasible to produce patient-specific modulator wheels for treatment of small fields (such as ocular tumors) in passive PT. Studies of the capabilities of high-end 3D printers indicate there can be significant defects associated with sharp corners [114]. Thus the use of 3D printing for proton beam modulation benefits greatly from a stepless design. In particular, this construction method applies to small-field passive scatter facilities due to the current limit of commercial 3D printer bed sizes. There is nothing particular in the optimization technique which limits it to eye-therapy energies. It is feasible, with an appropriate beam model, to apply the same technique to a higher energy beams for general PT. This is just as the Gardey method was first demonstrated and validated for eye therapy.

The printing of modulator wheels also enables the fast and inexpensive manufacturing of patient-specific wheels. Range compensation can be built into the wheels. This is of significance as the use of a static range-shifter perturbs the balance of the proton energy distribution which results in a sloped SOBP. Additionally, this stepless method lends itself well to wheels that optimize for proton radiobiological effectiveness (RBE). It is well understood that the RBE of protons varies significantly over a SOBP [127]. Designing a modulation scheme to compensate for this effect benefits greatly from the increased degrees of freedom available by using stepless design.

This work describes the design, printing and testing of stepless modulator wheels for use in proton eye therapy. The main objective is to produce stepless wheels which match or improve upon the SOBPs resulting from stepped designs.

7.2.2 Materials and Methods

Stepless Wheel Geometry and Definitions

The stepless wheel design follows closely that of the classic stepped designs. The interior portion, shown in Figure 7.3, supports the alignment and rotation of the wheel, while the exterior thickness profile degrades the beam.

Each wheel is designed to produce an SOBP of a certain range (D_{90}) and width (M_{98}). All wheels are designed to minimize target region variation ($\bar{\Delta}$) and distal margin (M_d). We adopt common definitions and symbols [32] where possible:

$\mathbf{D_{90}}$	depth of the distal 90% treatment dose point
$\mathbf{P_{98}}$	depth of the proximal 98% treatment dose point
$\mathbf{M_{98}}$	difference between P_{98} and D_{90}
$\mathbf{M_d}$	difference between distal 90% and distal 10% dose points
$\mathbf{X_T}$	depth region between P_{98} and D_{98}
$\mathbf{D_{ref}}$	dose at the centre of the target region
$\bar{\mathbf{\Delta}}$	average absolute dose difference from $\mathbf{D_{ref}}$ on $0.2mm$ mesh in target region
$\mathbf{\Delta_{max}}$	maximum absolute dose difference from $\mathbf{D_{ref}}$ in target region

The thickness profile, denoted $T(\theta)$, is defined by a collection of piecewise cubic functions, known as a cubic spline. These functions are constrained to pass through a series of *spline points* as shown in Figure 7.4. The wheel is symmetric in quarters with the profile defined on $[0,\pi/2]$.

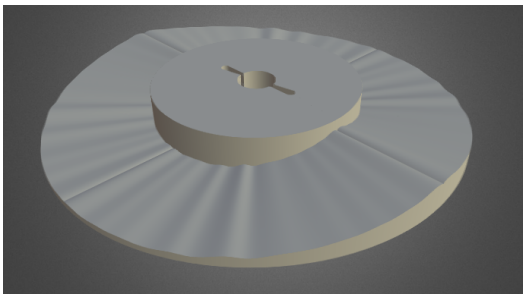

Figure 7.3: 3D rendering of stepless wheel geometry (modulation width $8mm$ at $70MeV$) showing interior support and exterior beam degrading elements.

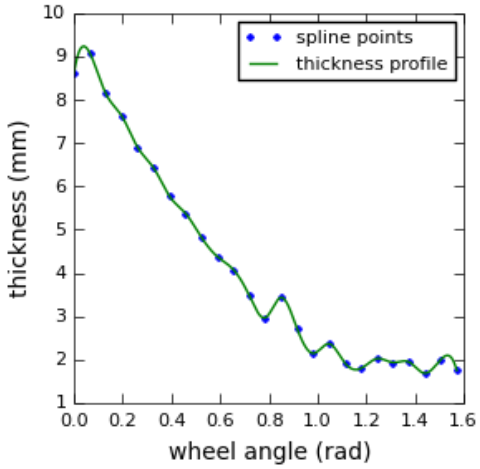

Figure 7.4: Thickness profile of stepless wheel designed for a modulation width of $8mm$ at $70MeV$.

Simulation and Dose Calculation

Proton depth-dose distributions were simulated using the FLUKA Monte Carlo (MC) transport package [[12] [65]]. The full PT treatment head and waterbox geometry were implemented. The hadron therapy (HADROTHE) default physics settings were used. This yielded a (peak normalized) agreement within 2% of axial depth-dose waterbox measurements using a BPW34 PIN diode.

A series of simulations were performed for a set of PMMA blocks (0.05-2.5cm) which replaced the modulator wheel in the standard geometry. A central beam axis depth dose curve was recorded for every thickness of beam degrader. Each simulation was run to the same number of primary particles, resulting in a variable statistical uncertainty (reported by FLUKA) depending on the thickness of the degrading block. Additionally, due to the number and energy spectrum of protons in water, the statistical uncertainty on dose increases with depth. The number of primaries, 10^9, was chosen to yield a maximum 1% statistical uncertainty for the thickest block at the D_{20} point.

The resulting set of depth dose curves were combined into a matrix. A 2D cubic-spline interpolation was then computed, giving a continuous function $F(t, x)$ on depth x and degrader thickness t. This function allows for rapid evaluation of dose for any

applicable depth and degrader thickness. The depth dose distribution of a stepped wheel is then calculated as in equation 7.1.

For a stepless wheel with thickness profile $T(\theta)$, over wheel angle θ, equation 7.1 becomes:

$$D_{stepless}(x) = \int_0^{2\pi} F(T(\theta), x)\, d\theta \tag{7.5}$$

The magnitude of dose calculated depends on the normalization of the weights and integral range. For simplicity, we may always normalize the maximum of the resulting distribution to unity. This is assumed for any given SOBP in this work.

A classically designed stepped wheel would typically have ∼10-20 steps, requiring as many dose evaluations as in equation 7.1. For a stepless wheel, the number of evaluations quickly increases with the desired accuracy in the integral of equation 7.5. To maintain a rapid dose calculation, a graphical processing unit (GPU) method was employed, as described below.

The dose interpolant function F was discretised into $0.2\mu m$ thick steps (the resolution of the 3D printer) and $0.2mm$ steps in depth d (the limit resolution of our waterbox measurements). This discreet t-d dose matrix was loaded onto a GPU using a python implementation of OpenCL [128], an open source library for GPU computation. Hardware-implemented interpolation and vector operations on this matrix allow for a ∼300 times speed increase in computing the integrals of equation 7.5 over a standard single CPU [[129], quadpack – adaptive Simpson quadrature method]. This method allows for rapid evaluation of the depth-dose distribution – enabling the inclusion of many more degrees of freedom than classical methods during optimization.

Thickness Optimization

The wheel thickness profile is defined by spline points described in Section 7.2.2 and shown in Figure 7.4. Each point has a position and thickness – both of these parameters may be considered as inputs to an optimization. However, to simplify the procedure and reduce coupling between parameters, we hold the positions of the points fixed. We choose N_{sp} such points to be uniformly distributed over one quarter of the wheel. At $N_{sp} = 30$, this amounts to $\sim 1mm$ spacing between points at the

center of the beam. The thickness profile $T(\theta)$ is then fully defined as the cubic spline interpolation between these points.

We partition the depth-dose profile into entrance, target and exit regions (X_{ent},X_{targ}, X_{exit}) defined by the desired range and width of the SOBP.

For the optimization we define vector objective function $F = \langle f_1, f_2, f_3 \rangle$ as follows:

target region standard deviation	$f_1(X) = \sigma(D(x)) \ \forall x \in X_{targ}$
entrance summed dose	$f_2(X) = \sum D(x) \ \forall x \in X_{ent}$
exit summed dose	$f_3(X) = \sum D(x) \ \forall x \in X_{exit}$

While a multi-objective optimization is necessary to map the full solution space, scalarization can be used to find an efficient solution if the objective function is monotonic [130]. The weighted sum method was employed producing the objective function:

$$O(X, W) = \sum_i w_i f_i(X) = w_1 \sigma(D(X_{targ})) + w_2 \sum D(X_{ent}) + w_3 \sum D(X_{exit}) \quad (7.6)$$

Noting that equation 7.6 (with $w_i \geq 0$) is monotonic increasing in f_i, an efficient solution is guaranteed [131]. We normalize the weights by the difference between the utopian (z^U) and approximate Nadir (z^N) objectives [132] available to the optimization:

$$w_i = \frac{1}{z_i^N - z_i^U} \quad (7.7)$$

This normalization factor represents the difference between the upper and lower bounds on the available efficient objective set. We only need to approximate these objectives in order to obtain useful weights:

- *Utopian* z^U: This is the ideal, potentially unavailable, objective vector. Intuitively this would represent a uniform target region, zero entrance / exit dose ($z = \langle 0, 0, 0 \rangle$). However, noting that all dose distributions are normalized to one, zero entrance dose is not available to the optimization. The entrance dose of an optimization can never be lower than that of a BP blocked by the thickest part of the wheel (t_{max}). With F, the dose interpolating function as in Section

7.2.2, the utopian objective is :

$$z^U = \langle 0, F(t_{max}, X_{ent}), 0 \rangle \tag{7.8}$$

- *Nadir* z^N: This is the upper bound on available efficient solutions. Given a solution with a perfectly uniform target region ($f_1 = 0$), the worst possible values for entrance and exit dose is when the SOBP is completely flat. For the situation where one of entrance or exit dose have been optimized, we reject any solutions where the target region contains a hotspot of more than 2% of D_{ref}. This gives an upper bound on our defined efficient solutions as:

$$z^N = \langle 0.02\, D_{ref}, N_{ent}, N_{ext} \rangle \tag{7.9}$$

where N_{ent}, N_{ext} are the number of dose sampling points for the entrance and exit regions respectively.

With equations 7.7,7.8,7.9, and adding additional weight parameters W_{ent}, W_{ext}, we get weights W:

$$W = \langle \frac{1}{0.02\, D_{ref}}, \frac{W_{ent}}{N_{ent}}, \frac{W_{ext}}{N_{ext}} \rangle \tag{7.10}$$

The edge-weight parameters allow for tuning of the entrance and exit dose importance in the optimization procedure. The value of these parameters determines the trade-off between uniformity, entrance dose and exit dose. The shape of the SOBP may then be tuned in this way by an informed decision maker (DM). Equations 7.6 and 7.10 define a scalar objective function which can be optimized using standard single-objective techniques.

The thicknesses of the spline points are optimized using a sequential least squares programming minimization method [scipy.optimize.minimize, method='SLSQP', [133] [129]]. The initial input thickness guesses were interpolated from a Koehler stepped solution. The stopping condition for the simulation was convergence in the objective function at the 10^{-8} level.

RBE Weighted Design

To demonstrate the ability of this method using a non-flat metric, we take a simple RBE model [134]:

$$RBE(D_p, \alpha_x, \beta_x, \alpha_p, \beta_p) = \frac{\sqrt{\alpha_x^2 + 4\beta_x D_p(\alpha_p + \beta_p D_p)} - \alpha_x}{2\beta_x D_p} \tag{7.11}$$

where α_x,β_x are cell kill parameters for a reference radiation, α_p,β_p are those for protons, and D_p is the proton fraction dose. We employ fit values as in Wilkins for V79 cell line – a linear fit to experimental data to determine α_p and a constant β_p for the linear energy transfer (LET), therapeutic regime.

LET, $L(x)$, is calculated at depth x as [55]:

$$L(x) = \frac{\int_0^\infty \phi_E(x) S^2(E) dE}{\int_0^\infty \phi_E(x) S(E) dE} \tag{7.12}$$

where $\phi_E(x)$ is the energy spectrum of the protons at depth x (sampled from FLUKA MC) and $S(E)$ is the proton stopping power. Bio-equivalent dose to V79 cell-kill is then evaluated through equation 7.11, taking dose and LET sampled from the MC as in Section 7.2.2.

Wheel Fabrication

Wheels were printed using a Stratasys Objet30 Pro PolyJet 3D-printer [135]. This printer was found to print reproducibly and with a resolution of $50\mu m \times 200\mu m$ and internal density variations on the order of 0.3% [114]. The wheels were printed with the flat portion against the base of the print bed, such that the precise dimension ($50\mu m$ resolution) was perpendicular to the proton beam face. Print time was approximately four hours.

Three wheels were printed – all designed for a beam energy of $70MeV$. The wheels were optimized to match the existing TRIUMF Gardey wheels according to the broken spline method of SOBP characterization [125] (§5.5). Two wheels were designed for plateau widths of 8 and $14mm$ with $W_{ent} = W_{ext} = 1$. The third wheel was optimized for a plateau width of $23mm$ with $W_{ent} = W_{ext} = 20$.

SOBP Measurements

The printed wheels were tested using the TRIUMF $500MeV$ cyclotron. This multi-user simultaneous extraction machine serves beamline 2C (BL2C) – a 65-$110MeV$,10 nA line to the PT facility. This facility is used in the treatment of ocular tumours with an extracted beam of $74MeV$ at 6 nA. The library of modulator wheels were designed, using a method developed at TRIUMF[8], for the original treatment energy of $70MeV$. The dose delivery system (DDS) is a standard passive scattering setup: lead scatterer, PMMA range shifter and modulator wheel[121].

SOBPs were measured in a waterbox using a BPW34 PIN diode mounted on a motorized stage with a positioning uncertainty estimated at $200\mu m$. Beam parameters were identical to original patient treatment conditions – 6 nA current at $70MeV$. The beam was collimated using a $25mm$ brass nozzle collimator.

7.2.3 Results and Discussion

Simulation

Koehler and Gardey stepped wheel SOBPs are shown in Figure 7.5. Both of these methods define the edges of the target region using singular BPs corresponding to the minimum and maximum wheel thicknesses. In Figure 7.5, the widest SOBP has defined peaks at depth $7mm$ and $30mm$. These edge points show the largest difference between the Koehler and Gardey methods. Typically, Koehler will give a more pronounced peak at the edges of the target region. This is owing to Gardey's use of more dose calculation points – allowing for smoothing close to the edges of the target region, where no BPs are available to Koehler. This is evident noting that the uniformity for Gardey is improved over Koehler in every case that was simulated. In both solutions, the size of the M_d is consistent within $50\mu m$. This is expected as both methods use the thinnest wheel step to completely define this falloff and include no metric in the optimization to improve this.

Figure 7.6 shows stepless wheel solutions for three edge-weighting values of 1, 20 and 100. In this method a Gardey solution is used as the initial guess for the optimization; however, there are no forced peaks at the edges of the target region. The choice of W here is purely demonstrative.

Given identical target design widths, increasing edge weight has three effects: decreased M_{98}, decreased M_d and decreased uniformity (see Table 7.2). Thus, in the

case of stepless modulation, uniformity and distal penumbra play against one another – similar to the trade-off described by Paganetti [32]. Indeed, in the $W = 100$ case, the SOBP exhibits a final and pronounced peak near the distal falloff.

Comparing the stepped and stepless methods (Table 7.1 and 7.2), simulated results indicate that the inclusion of exit dose in the optimization offers more control over the distal penumbra width. Increasing W beyond $\sim$20 gives an improved M_d. This is accomplished without worsening SOBP uniformity over a Gardey solution. This result is contrary to Prieels [126], which indicates that stepless solutions are worse than stepped solutions in both uniformity and distal penumbra width.

Prieels' approach involved iteratively adding more steps to the Koehler design method. They found that there was a low, optimal number of steps which always produced a more uniform SOBP than the 'large' step limit. This method does not allow for the direct optimization of smooth profiles. It assumes a stepped solution, always adding more steps of fixed pull-back. This removes many degrees of freedom which are available to the stepless approach described in this work.

Another problem with the approach of Prieels may have been the nature of the matrix inversion of equation 7.3. There is no constraint on negative weights in this approach. To mend this, any solution providing negative weights is discarded. Since the approach is iterative (each successive solution drives the next step calculation), this means many potential solutions are excluded from the process. The stepless gradient-based method ensures that all wheels are physical and proceeds from there.

Lastly, the stepless solution is multi-objective which allows for fine control and study of the trade-off between uniformity and distal falloff. The Prieels method did not address falloff outside of demanding a fixed final peak, leading to the conclusion that higher order stepped wheels would always tarnish the sharpness of the distal falloff.

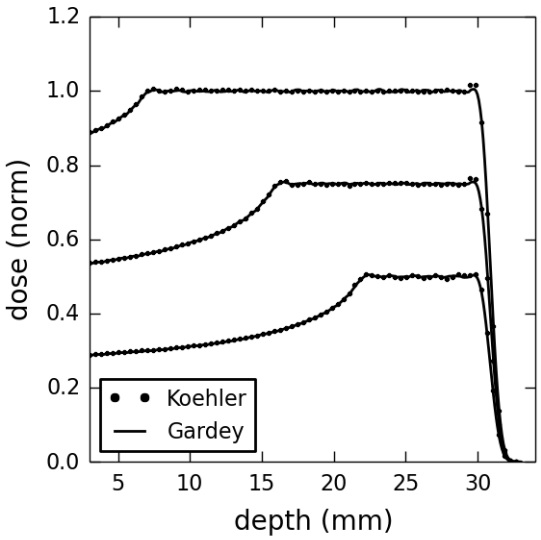

Figure 7.5: Simulated SOBPs using Koehler and Gardey methods for design widths of 8,14,23mm [$\mathbf{D_{ref}}$ normalized to 0.5,0.75,1 respectively].

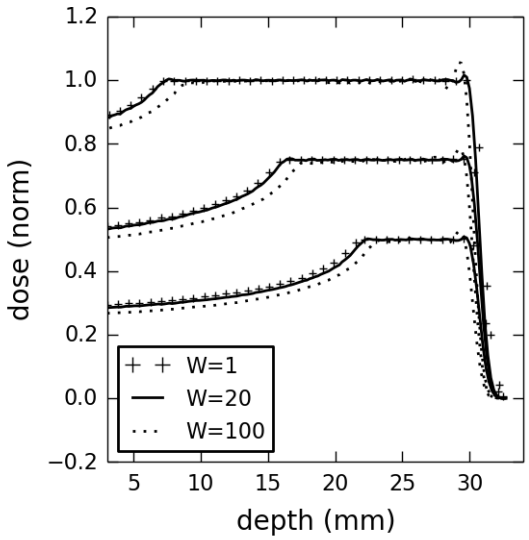

Figure 7.6: Simulated SOBPs using stepless method for design widths of 8, 14, 23mm [$\mathbf{D_{ref}}$ normalized to 0.5, 0.75, 1 respectively]. Shown are solutions for edge weight $W = 1, 20, 100$.

Table 7.1: Modulation width, distal margin and average uniformity for SOBPs from Figure 7.5.

Method	M_{98} (mm)	M_d (mm)	$\bar{\Delta}$ ($\%\mathbf{D_{ref}}$)
Koehler	8.7	1.24	0.94
	14.6	1.28	0.39
	23.7	1.28	0.25
Gardey	8.5	1.29	0.56
	14.5	1.27	0.22
	23.7	1.28	0.18

Table 7.2: Modulation width, distal margin and average uniformity for SOBPs from Figure 7.6.

Edge Weight	M_{98} (mm)	M_d (mm)	$\bar{\Delta}$ ($\%\mathbf{D_{ref}}$)
$W_e = 1$	8.98	1.38	0.28
	14.92	1.48	0.21
	23.98	1.4	0.15
$W_e = 20$	8.22	1.26	0.39
	14.31	1.27	0.27
	23.43	1.26	0.19
$W_e = 100$	6.92	1.17	1.19
	12.59	1.18	0.87
	21.38	1.16	0.68

Figure 7.7 shows MC simulated dose distributions for two wheels – one optimized for physical dose, the other optimized for Co-60 bio-equivalent dose (cell kill) as described in Section 7.2.2. Although this model is not well validated, it is useful to demonstrate non-flat dose shaping using the stepless method.

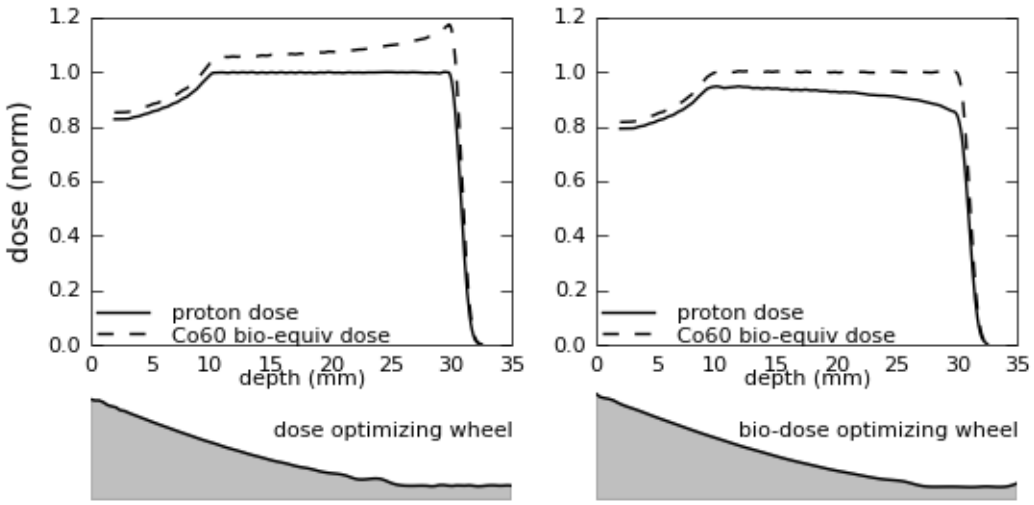

Figure 7.7: MC simulation showing proton and Co-60 bio-equivalent dose for two wheels – dose optimized (left) and bio-dose optimized (right). Shown below are wheel thickness profiles.

Figure 7.7 left shows the distinctive non-constant RBE effect occurring in the SOBP. Biological dose is ∼1.1 at the entrance and spikes near the proton range. Figure 7.7 right shows a wheel optimized to flatten this dose. Here the wheel produces a physical under-dosing to compensate for this effect. This optimization technique is well suited to optimize for non-flat dose when proton RBE is well understood.

Measurements

Figures 7.8 and 7.9 show measurements of the SOBPs by the Gardey method and our stepless method ($W = 1$). Here the stepless wheel was designed to match the range and width of the Gardey wheels. This was accomplished for both modulation widths within experimental measurement limits of $200\mu m$.

Notably, with $W = 1$, the stepless wheel SOBPs exhibit improved uniformity over the Gardey solution, but also M_d (see Table insert Figures 7.8,7.9) . This is consistent with the MC results listed in Tables 7.1 and 7.2. It should be noted that the simulated data does not match the measured data in the target region. This is not unexpected, since the original MC validation was only accurate within 2% over the target region initially. Use of measured data, or a simulation of greater accuracy, would improve the agreement between the MC and experimental measurements.

Figure 7.10 shows a stepless solution for $W = 20$. With the target region specifications identical to the other stepless designs, it is expected that M_{98} for $W = 20$ would be decreased, consistent with MC results. Here the stepless wheel improves both on $\bar{\Delta}$ and M_d over the Gardey solution. To rectify the range issue, it would be necessary to design the stepless wheel with an extended target region to compensate.

Comparing these distributions to one another is difficult under standard definitions. The Gardey solution exhibits a 'bowing' in the SOBP, where the dose reference point is higher than the proximal edge. The resulting target region is significantly skewed from the design with the distal 98% point at $P_{98} = 22.3 \pm 0.1mm$; whereas, the stepless design gives $P_{98} = 24.5 \pm 0.1mm$. This results in a 98%-98% width of $19.4mm$ and $21.5mm$ for the stepless and Gardey SOBPs respectively. For the same target region, the stepless result is more uniform, with a larger 98%-98% width than the Gardey SOBP.

Distal penumbra width for the stepless wheel was found to be $\sim 100\mu m$ less than that of the Gardey solution. With measurement uncertainty of $200\mu m$, this only indicates consistency between the two. More accurate measurement methods would be required to confirm simulated results. These measurements are evidence that the stepless design is capable of improving SOBP uniformity in all cases and of potentially improving the distal falloff over the Gardey solution. In addition, inclusion of exit dose in the optimization procedure would allow for control over the trade-off between $\bar{\Delta}$ and M_d.

7.2.4 Conclusions

A new method for the design of stepless beam modulators, which includes exit dose and variable pull-back, was successfully demonstrated. The stepless methods for design were implemented and compared against the stepped method for three target sizes. It was found that the stepless method can improve on SOBP uniformity while preserving or potentially improving distal penumbra width. Inclusion of exit dose in the optimization procedure was shown to give control over the trade-off between target uniformity and distal falloff size. Measurements of three 3D-printed modulator wheels showed success in matching to stepped SOBP distributions. All three measurements resulted in improved uniformity. Increasing the importance of exit dose resulted in

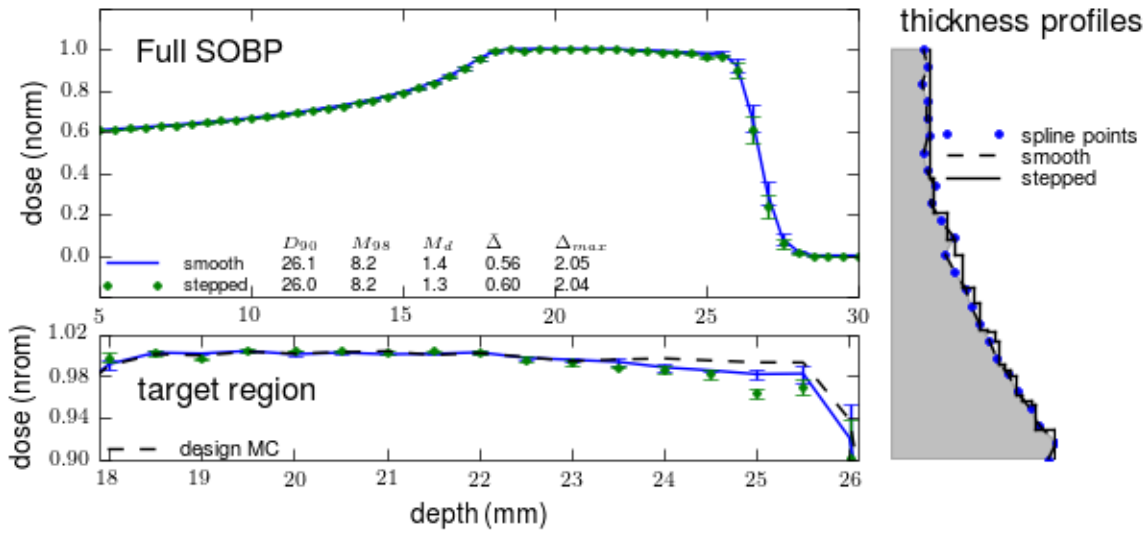

Figure 7.8: Measured SOBPs for a $8mm$ target region wheels (Gardey and $W = 1$). Shown is the full SOBP (upper), target region (lower) and wheel thickness profile (right).

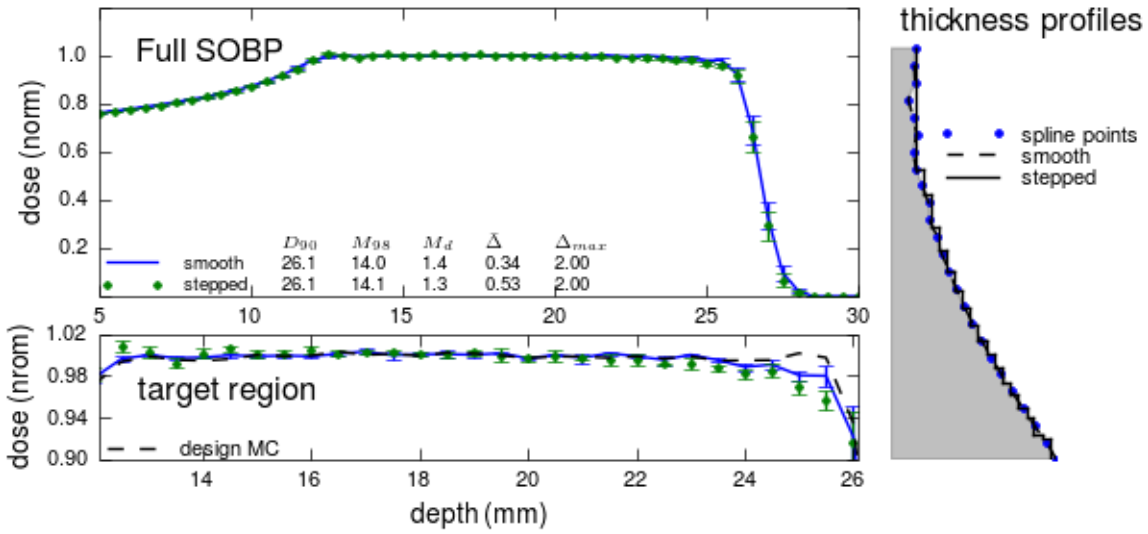

Figure 7.9: MC and measured SOBPs for a $14mm$ target region wheels (Gardey stepped and stepless $W = 1$). Shown is the full SOBP (upper), target region (lower) and wheel thickness profile (right).

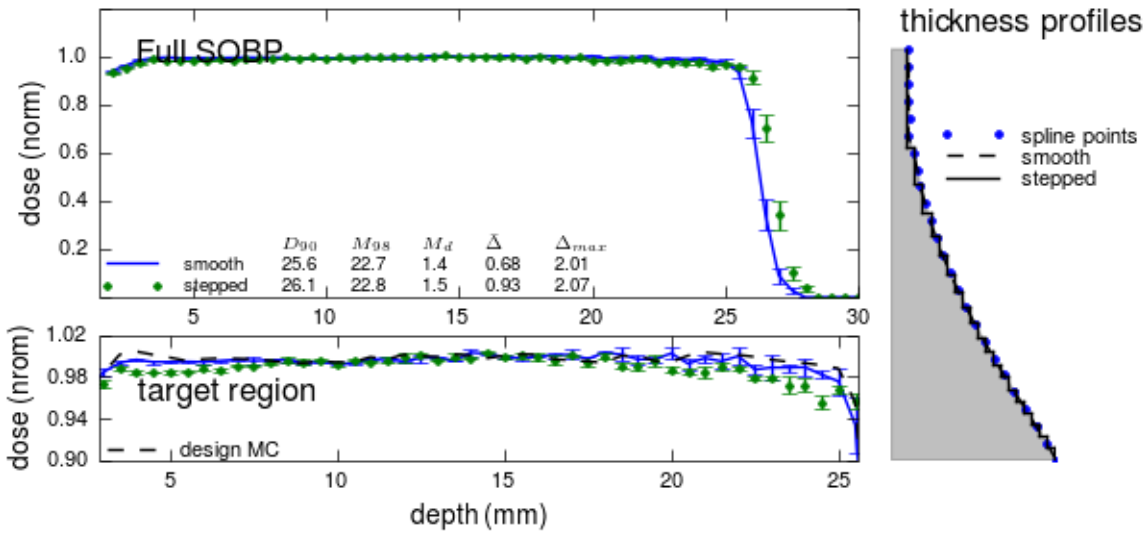

Figure 7.10: MC and measured SOBPs for a $23mm$ target region wheels (Gardey stepped and stepless $W = 20$). Shown is the full SOBP (upper), target region (lower) and wheel thickness profile (right).

improvement to distal falloff, but also reduction of range. Measurements accurate to better than $200\mu m$ are required to verify the effect of improved distal falloff. Also shown were simulations of modelled Co-60 biological equivalent dose and a wheel which was successfully optimized to flatten this effect.

These results show that this method is at least equivalent to the capabilities of the classic stepped designs. With this, it is feasible to design and 3D-print modulators during the clinical planning procedure. This would allow for a more finite control of modulation width, and potentially open the window to non-flat dose optimization.

Chapter 8

Activated Printed Eye Phantom

The following chapter concerns the study of a printed plastic eye phantom for use in PT PET dosimetry. The format of the chapter is that of a paper for the sake of consistency with the rest of the thesis. It was not published due to the negative result. Simulations in this chapter were based on the MC models and methods discussed in Chapters 3-5. The thesis author (C. Lindsay) and supervisor (C. Hoehr) were responsible for conception and supervision of this project. Lucite phantom data from 2012 was provided by C. Hoehr[22]. FLUKA simulations, phantom design/construction, and PET scan data was produced by two co-op summer students supervised by the thesis author. Their simulation data and models are presented in this chapter. Signal reconstruction, analysis and conclusions were produced by the thesis author (C. Lindsay).

8.1 Introduction

The dosimetric advantages in PT are largely owing to the sharpness of the dose distribution. The finite range of protons allows for reduced overall dose bath via single-field uniform-dose treatment and depth-based sparing. However, the position of the dose distribution in tissue is much more sensitive to depth and image uncertainties than for photon treatments[136]. The photon dose distribution is much less sensitive to small fluctuations in density than that of the proton. Changes in tumour depth resulting from anatomic or positioning differences from planning images may require costly re-planning much more frequently than for photon treatments[137]. Uncertainties in material proton ranges and interpretation of CT data play a significant role

in treatment planning uncertainty[88]. Confidence in accurate dose delivery requires attention to all of these details and more importantly - measurement and validation. Both validation of dose applied to the patient (*in vivo*) and of a treatment plan prior to treatment are valuable to ensure patient safety.

Protons traversing tissue at treatment energies have a chance to produce positron emitting isotopes as discussed in §2.1.4. The resulting back-to-back coincident gammas from the annihilating positron can be reconstructed into the original isotope distribution. Positron emission tomography has been studied widely as a tool for dosimetry in PT. In particular, plastic phantoms have been used to study offline signal strength and for MC modeling purposes[21, 138]. Clinical PET dosimetry has seen some success in qualitative range and field size validation[139]. Major difficulties include CT-based patient model and biological washout of the signal[140]. Improvements including MR-based patient models have been explored[141]. Feasibility studies were performed at TRIUMF in 2012[22]. Two phantoms and one patient were scanned for signal strength. Signal was present in both scans, but little positioning information could be extracted from the patient scan due to due to limited scanner resolution and low signal due to patient transport time. Also signal in the phantom could not be correlated to the applied dose due to a lack of simulated isotope production in the phantom. Despite the limited information from the patient scan, phantom studies showed promise in signal strength at a transit time of fifteen minutes.

With patient dose measurements infeasible, construction of an anatomic phantom could aid in understanding the accuracy of dose application. A phantom which resembled patient anatomy (emulating surface curvature) which could be positioned using the patient gaze angle would give a more comprehensive measure of positioning accuracy. Modern additive manufacturing techniques, specifically 3D printing as discussed at length in Chapter 6 and 7, allow for the construction of realistically shaped anatomic models. Additionally, PolyJet type machines offer variable density and flexibility in material prints[119]. A phantom could be constructed using these methods which more accurately reflects the density lung, bone or soft tissue - a very valuable feature when considering the sensitivity of PT accuracy to density differences. The TRIUMF PT system offers an opportunity to test the feasibility of printed materials for PET dosimetry. This study explores the feasibility of construction, planning, irradiation and scanning of an anatomical eye phantom for use in PT dosimetry.

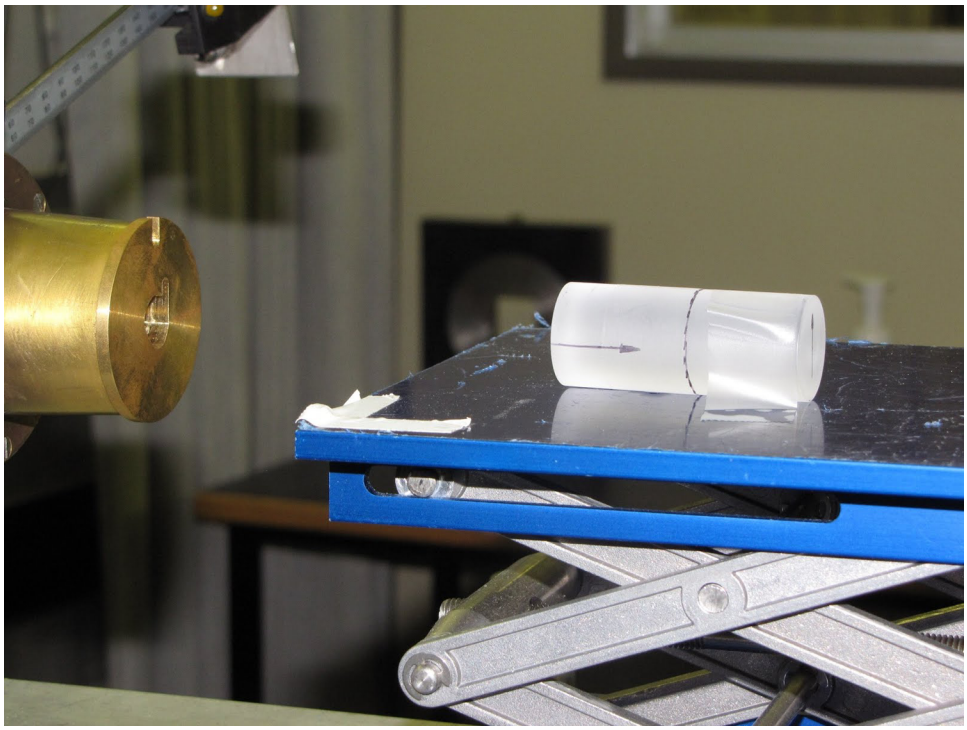

Figure 8.1: Lucite cylinder phantom positioned on adjustable stage in the front of patient collimator. Shown are markings used for isocentre positioning.

8.2 Materials and Methods

8.2.1 Lucite Cylinder Experiment

The first irradiation experiments were performed in 2012[22] at TRIUMF (see §2.3.1) to test the feasibility of measuring PET signal after proton therapy irradiation. For completeness we describe the parameters of the experiment here.

Lucite Cylinder Phantom

The target for irradiation was a $2cm$ diameter cylinder of Lucite (PMMA - $C_5H_8O_2$). The cylinder was positioned on an adjustable stage downstream of the patient collimator as shown in Figure 8.1. Markings on the cylinder were used to align to lasers coincident with the patient isocentre.

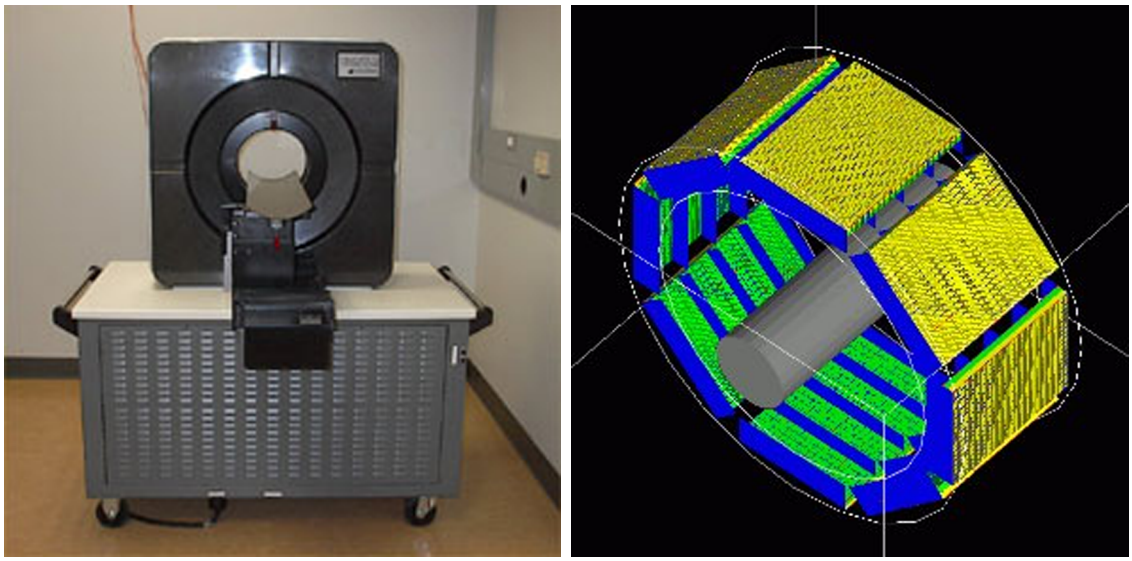

Figure 8.2: (left) Photo of μPET machine at UBC hospital radiology department. (right) Render of uPET geometry in GATE with cylindrical phantom.

Irradiation

The cylinder was irradiated with a $74MeV$ raw BP to a dose of $50Gy$. This dose is equivalent to the prescription for an entire treatment regimen which would normally be applied in four fractions. A $25mm$ (maximum opening) collimator was used to ensure the entire phantom face was irradiated. A Lucite beam stop was placed behind the phantom to absorb the unstopped beam going around the cylinder.

PET Scan

Upon completion of irradiation, the cylinder was immediately transported via a pneumatic underground transport line, typically used to transport PET radio tracers, from TRIUMF to the UBC hospital PET suite. Here the phantom was placed in a microPET focus 120 [142] PET scanner ($1.7mm$ resolution) - depicted in Figure 8.2-left. The estimated time from end of bombardment until beginning of PET scan was 12 minutes[22]. A standard filtered back projection (FBP) reconstruction was performed with $1.7mm$ slice thickness and counts per slice were recorded for comparison to the simulated scan.

FLUKA Simulation

The Lucite phantom was modelled in FLUKA, positioned at the patient isocenter, and a raw BP was simulated as discussed in detail in Chapter 4.2. Readout was performed by way of the RESNUCL readout card which allows for a custom FORTRAN routine to be run when an isotope is created via activation from the primary beam (see §3.1.3). This custom routine recorded the position and type of isotopes produced in the phantom region. Uncertainty on isotope production was taken as Poisson distributed. An equivalent to 2×10^{10} primaries were run - which reduced the statistical error to below 2% at the 10% distal point of the distribution.

PET Simulation and Reconstruction

The simulated isotope distributions for ^{11}C, ^{13}N and ^{15}O from FLUKA was loaded into a Python where 3D-rectilinear interpolation was used to produce a smooth distribution. These three distributions were then scaled (relative to one-another) according to their half-lives to simulate the 12 minute transport time to the scanner. Once scaled, the combined distributions were taken as PET decay probability distribution. This distribution was converted to a GATE[143] format, and run with a simulated microPET geometry (shown in Figure 8.2-right) provided by the UBC hospital PET group. Here the total counts was scaled to match the experimental number of counts in the 30 second original experiment. The open-source reconstruction software STIR[144] was used to reconstruct (FBP) the simulated detector counts output by the GATE program. Lastly the summed slices were compared to experimental data via total activity (area) normalization.

8.2.2 Plastic Eye Phantom Experiment

The second irradiation experiment was performed in 2016 to test the feasibility of using the activated PET signal for comprehensive targeting quality assurance.

3D printed Anatomic Eye Phantom

With the goal of performing a comprehensive patient positioning test, an anatomic eye model[69] was used to produce both a VOXEL model for MC simulation and a Standard Tessellation Language (STL) file for 3D printing. Figure 8.3 (top-left) shows the original open-source eye model including all major eye organs. This model

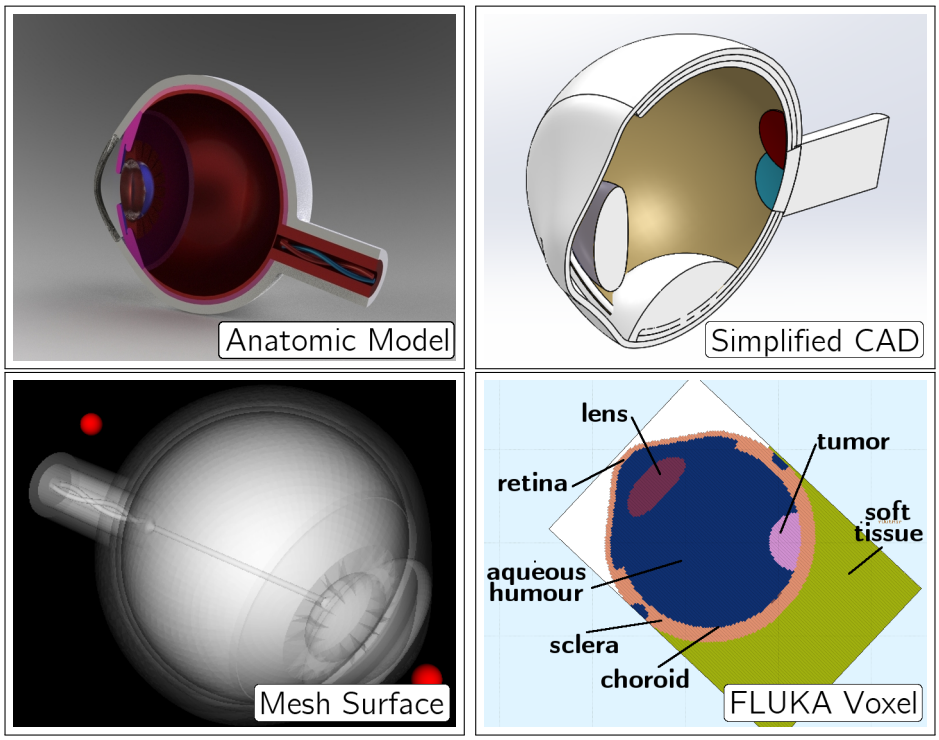

Figure 8.3: (top-left) Full anatomic eye CAD model. (top-right) Simplified CAD model removing complex organ geometries. (bottom-left) Mesh surface extraction. (bottom-right) Voxelized FLUKA geometry.

was simplified (Figure 8.3 top-right) using SOLIDWORKS CAD software, replacing complex structures such as the iris and cornea with vitreous material. Additionally a Tier III tumour target volume with basal width of $8mm$ and apical height of $4mm$ was inserted at the back of the eye. Tumour volume definition was performed as described in §5.1.2. For simplicity, volume was defined to require a 45° horizontal gaze angle and beam centred on the tumour volume.

Two further modifications were made to the eye model before exporting to printable STL format. Four mounting divots were added to the exterior of the eye to simplify eye positioning. Also a $2mm$ diameter hole was added along the central visual axis which extended through the entire volume. This hole allows for the passage of a laser - aiding in gaze angle selection. Lastly the model was scaled to a maximum diameter of $2.3cm$ such that it could be transported via rabbit-line to the UBC hospital for scanning. Figure 8.4 (left) shows the exterior of the final plastic model. This was exported to STL format and printed using VeroWhite[123] material on a Stratasis PolyJet machine[119]. Further details on the printing parameters, materials

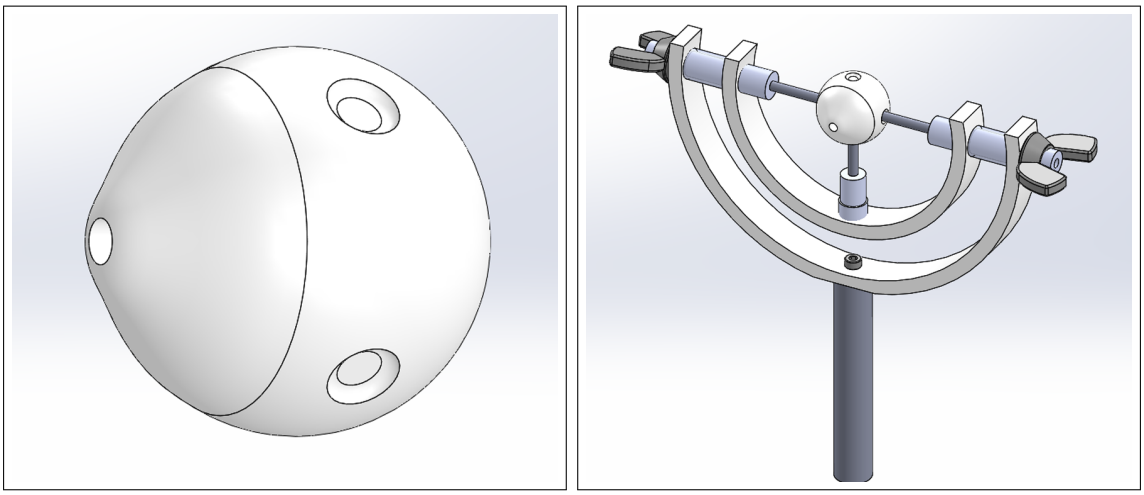

Figure 8.4: (left) Eye phantom CAD render showing support divots and positioning lazer opening. (right) Eye phantom affixed to adjustable 3D-printed gimbal.

and machine can be found in Chapter 6.

Positioning of the phantom was accomplished using a custom two-axis gimbal shown in Figure 8.4. The eye was mounted and tightened on the gimbal, which was mounted on an adjustable stage in the beamline. The isocenter lasers were used to center the eye in the beamline. The patient gaze-light was replaced by a mounted laser pointer and adjusted to the planned 45° gaze-angle. The gimbal was then rotated into the laser and fine-tuned such that the laser light appeared through the phantom opening. This ensured the phantom was both centred in the beamline and the gaze angle fairly represented the gaze of a patient. Figure 8.5-left shows the eye with gaze adjusted to match the laser. Figure 8.5-right shows the DDS field light on the phantom - indicating the positioning of the field.

Irradiation

The above tumour volume definition and positioning resulted in a $1.2cm$ diameter collimator with an $8mm$ modulation width (mod80), and a range setting of 770 ($0.97cm$). The eye was irradiated with a $8mm$ modulated beam to a dose of $50Gy$. As with the Lucite cylinder, this is equivalent to four times the normal fraction dose. This was done to get an improved signal in order to test feasibility. A Lucite beam stop was placed behind the phantom to absorb the unstopped beam.

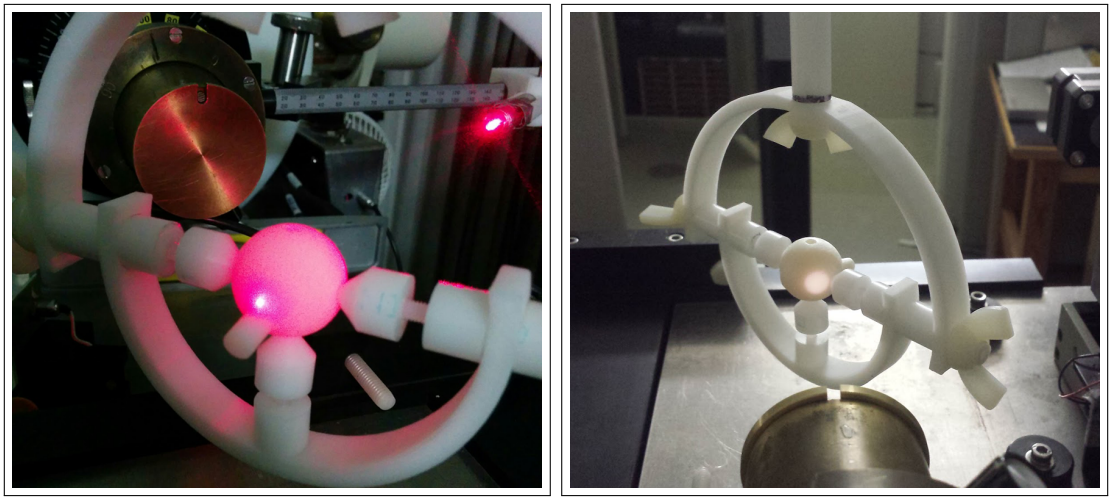

Figure 8.5: (left) Printed eye phantom affixed to positioning gimbal with gaze laser jig. (right) Printed eye phantom with beam collimator light shown for positioning.

PET Scan

Upon completion of irradiation, the eye was transported via rabbit-line from TRIUMF to the UBC hospital. In an identical fashion to the cylinder, the phantom was placed in a microPET focus 120 [142] PET scanner. The estimated time from end of bombardment until beginning of PET scan was 12 minutes and 20 seconds. A standard filtered back projection (FBP) reconstruction was performed with $1.7mm$ slice thickness and a 3D-volume was recorded to compare against simulation. Additionally a transmission-scan was performed (^{57}Co source, 122.1 keV photons) to produce a scanned volume ($1.2mm$ resolution) for the purpose of registering the scan with the simulated phantom volume.

FLUKA Simulation

The completed CAD model of the phantom was loaded into FreeCAD CAD software and a surface mesh was extracted (shown in Figure 8.3-bottom-left). This mesh loaded into Python where iterative ray-tracing produced a VOXEL volume which could be imported into FLUKA (shown in Figure 8.3 bottom-right). Further details on this process can be found in §5.1.1. As with the cylinder, an equivalent to 2×10^{10} primaries were run to produce the isotope and dose distributions to a achieve an uncertainty of 2% at the 10% distal edge of the isotope distribution.

PET Simulation and Reconstruction

Reconstruction for the eye phantom was identical to the case for the cylinder, except the eye transmission scan was used for the attenuation volume in the reconstruction and activity was scaled to the scan activity. With a reconstructed scan, the 3D eye volume must be reoriented to match the FLUKA simulation position. Here the placement of the eye phantom in the scanner is determined by registering the transmission scan against the known voxel volume used in FLUKA. This is accomplished by optimizing on azimuthal and polar angle rotation with the a square-sum difference objective function on the two voxel volumes.

Positioning Analysis

Once the experimental PET isotope scan is appropriately oriented with the FLUKA-GATE simulated scan, a comparison may be made between the two. Here a 3D

translational registration is performed by calculating the total square-sum difference between the two maximum-normalized PET distributions for various translations in the three dimensions. Lastly, an azimuthal and polar gaze angle comparison is done to determine the accuracy of angle positioning.

8.3 Results and Discussion

8.3.1 Lucite Cylinder

Figure 8.6 shows the experimental PET scan (top) and simulated FLUKA-GATE scan (bottom). Both the simulated and experimental images show the circular shape of the phantom with a reasonably uniform isotope distribution. This is as expected since the entire phantom face was irradiated ($25mm$ diameter field size). The simulated distribution appears to exhibit increased noise in the axial direction (right images) while the experimental scan appears more consistent over the volume (although this could be owing to the different colour schemes in plot display).

Figure 8.7 shows the summed axial PET signals and isotope distributions for both the experimental and simulated scans. Here isotope activity at end-of-bombardment (EOB) is shown for ^{11}C,^{13}N and ^{15}O (coloured stack). Also shown is the simulated PET activity (PET MC, black circles) as would be recorded including the travel and scan delay. The PET scan slices in (black solid line) are normalized to match the area of the simulated scan. This is equivalent to matching total number of annihilations in the scans. The most noticeable difference between the axial distributions is the shape toward the distal end. No ^{13}N signal remains in the PET scan corresponding to the BP, whereas the simulated scan exhibits a marked increase after the ^{11}C falloff. This may be due to MC package dependence in ^{13}N modelling[145] - investigation of which is beyond the scope of this work. Other than this difference, the agreement in axial-summed shape is excellent. This lends confidence in FLUKA's ability to simulated the ^{11}C distribution.

8.3.2 Anatomic Eye Phantom

Figure 8.8 shows the central-slice dose, ^{11}C, GATE and experimental PET scans. Examining first the dose - as in Chapter 5.1.5, the targeting was accurate in placing the 95% isodose (red) over the target region. The ^{11}C distribution, shown in the top-

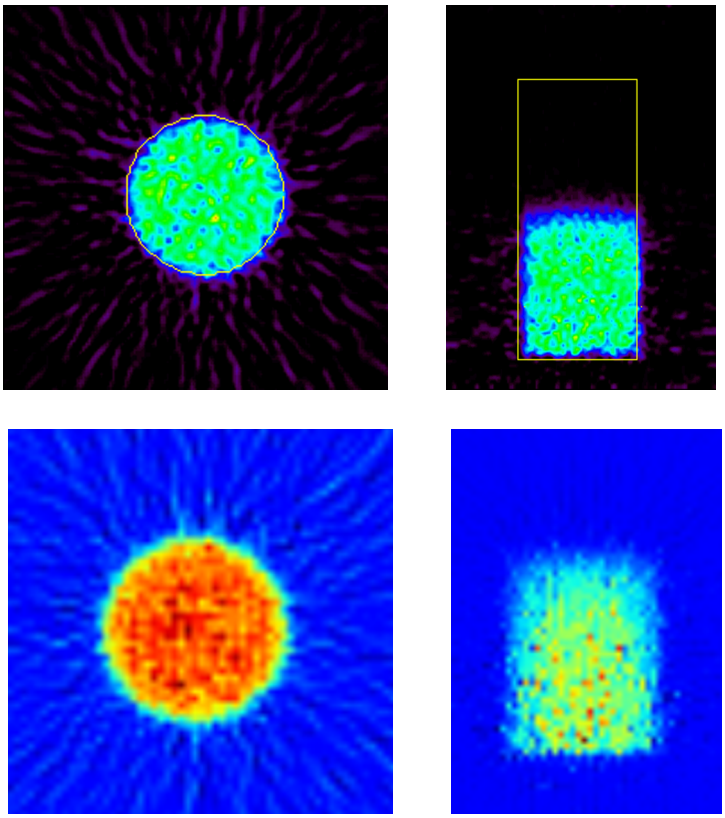

Figure 8.6: (top) Reconstructed MicroPET scan of activity from Lucite cylinder phantom. (bottom) GATE reconstruction of FLUKA simulated activity in Lucite cylinder phantom.

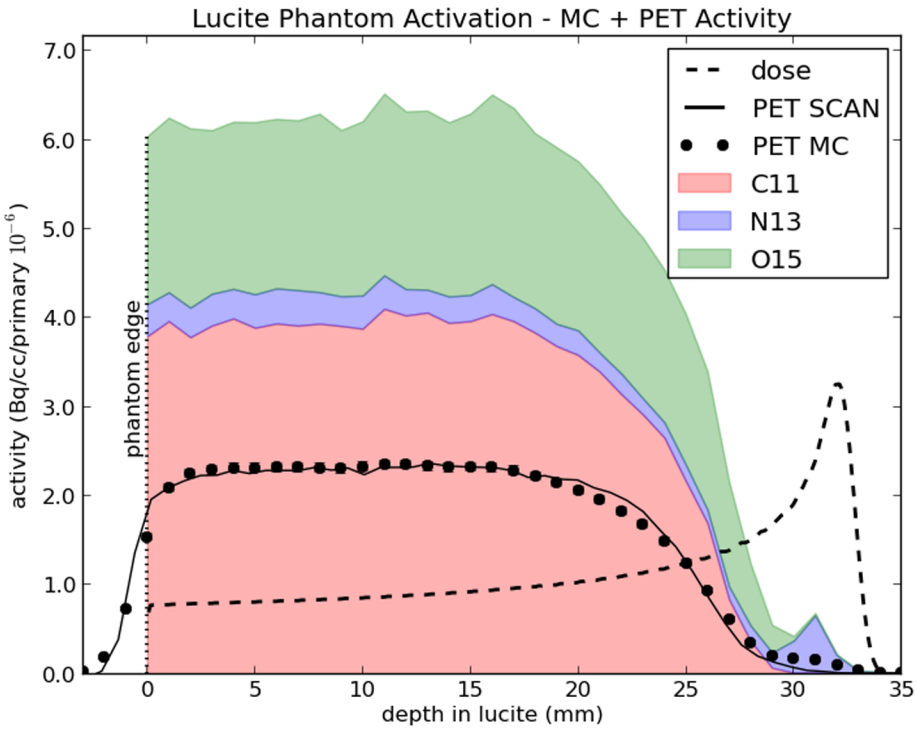

Figure 8.7: FLUKA simulated isotope activity summed by scan-slice in the beam direction. Shown is total activity per primary for C11,N13 and O15 at end of raw BP bombardment (coloured plots) and at time of scan (black circles). Shown also are reconstructed PET slices summed along the axial axis (solid black) and raw BP position (black dashed)

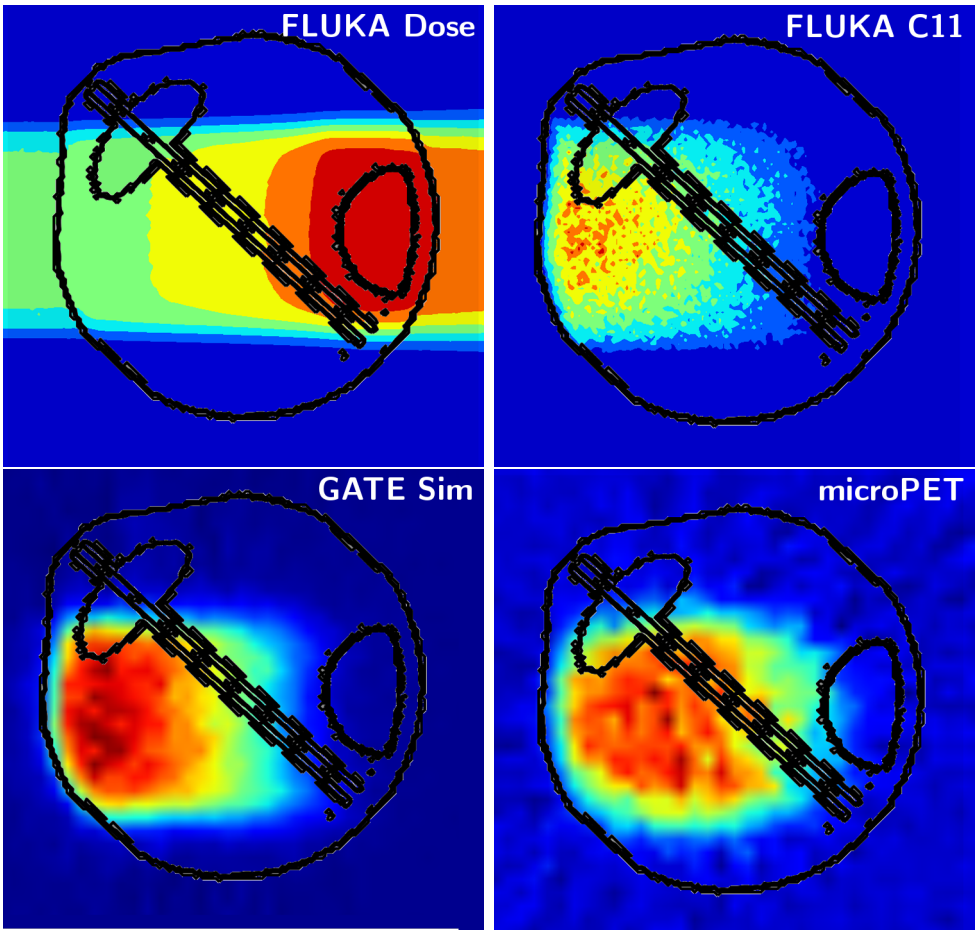

Figure 8.8: (top) FLUKA simulated primary dose (left) and C11 isotop distribution (right). (bottom) GATE simulated PET scan (left) and microPET experimental scan (right). Overlaid on all images is a boundary contour plot of the eye phantom (black lines).

right, exhibits a shallow maximum and decrease to zero activation around the dose peak. This indicates that this method would not be well-suited to shallow targets as very little ^{11}C (the most long-lived of isotopes at 20.3 minutes) would be present due to their production cross section. There is no appreciable ^{13}N or ^{15}O signal once the phantom had arrived at the scanner (as indicated by the Lucite sample) due to their shorter half lives.

Lastly, the microPET and GATE scans differ significantly. The microPET has a much higher degree of noise and is more spread out in depth than the reconstructed scan . A direct 3D difference is not useful due to overall normalization. Despite this, the bulk shape of the two PET distributions may be compared via position/rotation optimization.

Figure 8.9-top-left shows square-sum differences between measured and simulated PET distributions. This heatmap is for various polar (vertical) and azimuthal (horizontal) rotations about the center-of-mass for each distribution. Overlaid are one and two standard deviation ellipses for Gaussian fits to the data. The resulting fits show the optimized rotation angles to align the FLUKA and measured PET signals. Here the polar angle is well known, having a standard deviation of only 0.7°. However, the azimuthal angle is very poorly localized by this procedure with a 7.2° standard deviation. Taking this as uncertainty, a quoted measurement of azimuthal angle discrepancy would be on the order of 15% - too large to be reliable for assessment of gaze angle for quality assurance purposes. This error in localization is dominated by the registration process. The quality of the transmission scan was too low to accurately register to the FLUKA voxel structure. This limitation of the transmission scan could be overcome by including PET markers (sources) on the eye phantom for registration purposes. These markers would be visible in both the PET signal and transmission scan of the microPET scanner, but not in a human-sized clinical scanner.

Lastly, Figure 8.9 shows the 3D translational optimizations. Without an accurate rotational registration, these comparisons have little predictive power for positioning. This is because if misaligned rotationally, the PET scans differ in axial/lateral shape. This serves to 'smear' the position optimizations, resulting in large standard deviations of $\sim$6-8mm as shown in this Figure 8.9.

Two studies were performed as follow-ups to these experiments. The first was a study comparing isotope production in FLUKA[145] to another MC transport code GEANT4[146]. The main conclusion was that the two software packages were in good agreement except for ^{13}N production near the tail of the BP. The second study was an undergraduate thesis project[147] which involved MC simulations to reconstruct phantom position from activated isotope distributions. This concluded that there would be poor resolving power (worse than 2mm) on a simpler phantom at the level of dose applied for this experiment.

8.4 Conclusions

Two activation experiments were performed and simulated using FLUKA/GATE software. Full reconstruction pipelines were written and shown to have good qualitative agreement with measured PET signals. An anatomically accurate eye model was created along with beam-positioning system. The resulting PET signal was of suf-

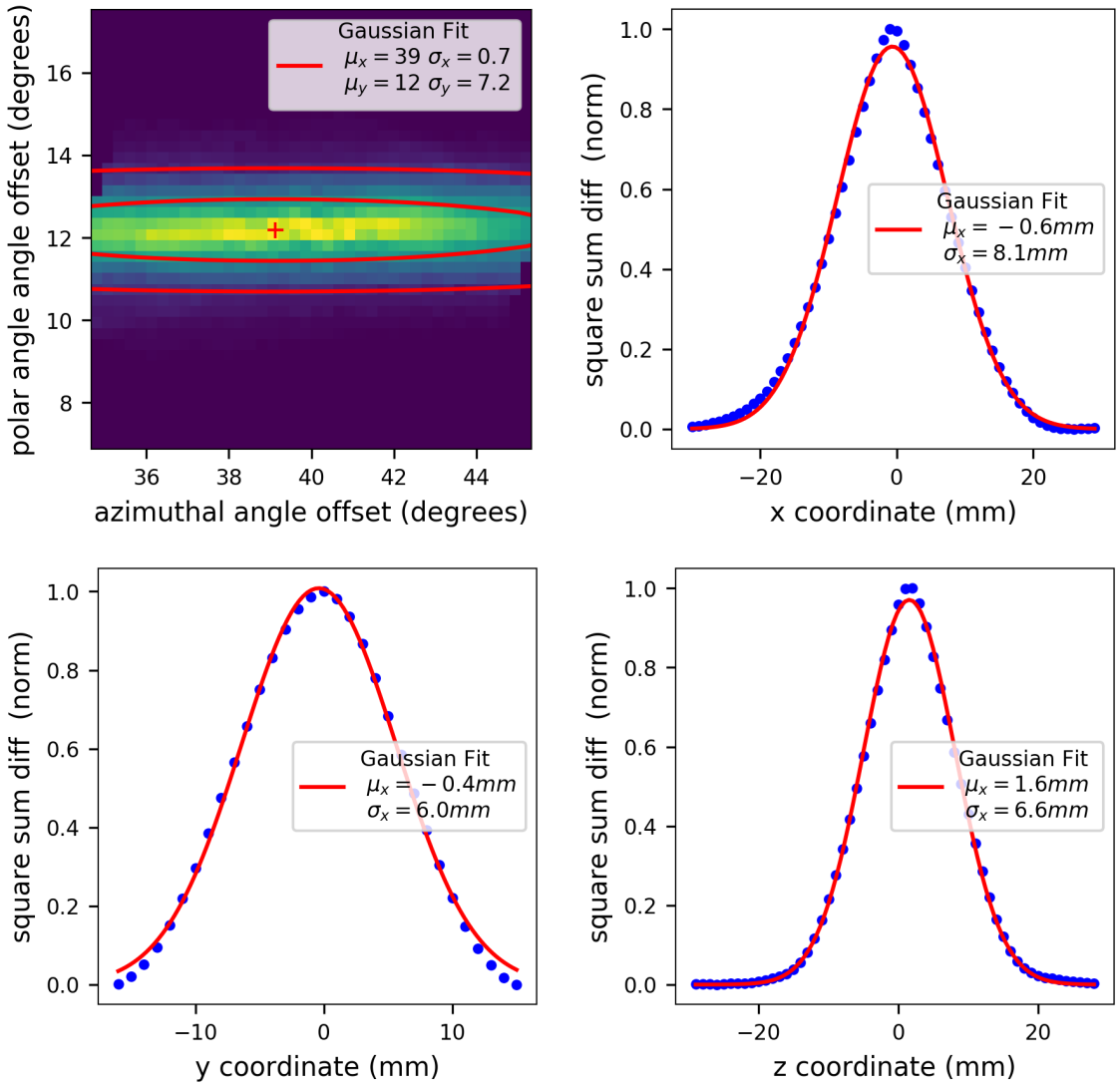

Figure 8.9: (top-left) Plot of optimization cost function (square-sum difference) comparing PET transmission scan volume against reference VOXEL structure. Translational square-sum differences between GATE simulated and microPET experimental PET scans for x,y,z coordinates (top-right,bottom-left,bottom-right). Shown also are Gaussian fits to determine offsets (red lines) along with mean and standard deviations.

ficient quality to extract positioning information; however, PET image registration failed due to the low quality PET transmission scan. With a lack of accurate volume registration, no statement could be made on the accuracy of beam positioning on the target volume.

Chapter 9

Summary and Conclusions

This dissertation has primarily focused on the simulation and validation of Monte Carlo simulations of the TRIUMF Proton Therapy Facility. From that work came studies into the use of 3D printing in fabricating modulator wheels and anatomic PET phantoms. The main goals of this research were to better understand: how dose was delivered by the TRIUMF accelerator; how secondary neutron dose was produced and the implications for patient safety; and how treatment delivery could be improved by way of better modulation or improved positioning via PET dosimetry. The end result of these years of study have far exceeded the original goals of simulating dose. This work has explored whole new optimization and fabrication techniques - challenging long-standing knowledge in the field.

9.1 Dissertation Summary

The most enabling and important portion of this work was development of accurate MC simulations of the dose delivery system. The FLUKA software package was implemented across a distributed computing network, running a detailed simulation of the beamline. The limits of the software were explored - developing custom routines for stepped and smooth modulator wheel geometries used in 4D simulations. Dose in water was simulated for a variety of beam configurations spanning the treatment regime. Detailed studies into range, output factors, beam profiles, calibrations and modulation schemes were exhaustively produced - all improving our understanding of dose delivery. MC primary doses were validated within 2% of treatment dose, with ranges accurate to within the limits of measurement by the equipment.

A detailed study of secondary neutron dose was conducted. For validation, neutron doses were measured transverse to the beamline using a BF3 detector. These measurements were validated within 20% in simulation - with the dominant uncertainty being in the calibration of the detector itself. For the purpose of patient safety, this was sufficient. Voxel based geometries were adapted to the FLUKA infrastructure, allowing for precise measurement of primary and secondary dose to anatomic models. Six tumour models were designed to span a range of modulation and collimator sizes. Primary dose normalization was simulated to normalize anatomic dose to these plans. It was found that the scatterer was the main source of neutrons by an order of magnitude. Anatomic doses indicated that the unshieldable opening of the beamline was the dominating factor in neutron dose. Hence, only improving treatment time (increasing output factor) was important in reducing secondary doses.

The third part of this work involved the use of the validated MC primary dose to study improving beam modulation. A new optimization technique, using a small number of points to define a cubic-spline surface, was developed. This optimization opened up a much larger surface space for modulator wheels than had been previously explored. Two 3D printing methods were studied for the fabrication of new modulator wheels. The PolyJet method was found to be extremely consistent in its print and suitable to the task of modulation. Three of TRIUMF‘s modulator wheels were printed and validated against the standard PMMA wheel. Printed smooth wheels were measure to produce improved dose uniformity and optimizing for distal falloff resulted in a potentially sharper distal edge. Turnaround on wheel design and printing was well under 24 hours - indicating that this method would be suitable for patient-custom beam modulator wheels.

Lastly the PolyJet printing method was used to fabricate an eye phantom adapted from anatomic CAD models. A treatment plan was developed along with a positioning system to mount the phantom in the beamline. FLUKA was used to produce a dose distribution and predict isotope production. PET scans yielded a strong PET signal, but the PET scanner produced a poor quality density scan. Upon attempting to register the density scan to the FLUKA generated output, it was found that the registration had a very high uncertainty. This made any positioning information in the PET signal useless. Future work on this project might include PET markers for phantom alignment or doping of the plastic structure with PET radio-metals to boost signal.

9.1.1 Outlook

Despite the closure of the TRIUMF PT facility, passive-scatter proton therapy continues to be a widely utilized treatment modality. With the in-tact DDS, TRIUMF still serves as an active site for research - many studies of which make use of the MC model described in this dissertation.

In collaboration with the BCCA Vancouver center, studies have been done into small plastic scintillator detector response[148]. These included calculations making use of FLUKA for dose evaluation and output factors. After this success, further studies into small-field dosimeters for use in radiotherapy continue.

Recently, extremely high dose-rate photon therapies have shown promise in improved differential cell-kill[149, 150, 151] . Initial patient trials using this modality have begun[152]. So-called 'flash' therapies are now being studied for use with protons[153, 154] . This modality requires an extremely high dose rate which is unsuitable for magnetically steered beams. TRIUMF is well situated for such research due to the high available beam current and pre-existing passive-scatter delivery system. A recent study[155] showed success using 3D printed modulator wheels printed with the PolyJet method - as explored in this thesis. Future research into FLASH therapy beam modulation will be conducted at TRIUMF using the FLUKA MC simulation and optimization techniques developed throughout this work.

Bibliography

[1] A Singh and A Topham. Incidence of uveal melanoma in the United States: 1973-1997. *Opthamology*, 110(5):956–61, 2003.

[2] Denniston AKO and Murray PI. *Oxford Handbook of Ophthalmology (OUP)*. 2009.

[3] Collaborative Ocular Melanoma Study Group. Assessment of metastatic disease status at death in 435 patients with large choroidal melanoma in the Collaborative Ocular Melanoma Study (COMS): COMS report no. 15. *Arch Ophthalmol.*, 119(5):670–6, 2001.

[4] Ilkka Puusaari, Jorma Heikkonen, and Tero Kivelä. Effect of Radiation Dose on Ocular Complications after Iodine Brachytherapy for Large Uveal Melanoma: Empirical Data and Simulation of Collimating Plaques. *Invest Ophthalmol Vis Sci.*, 45(10):3425–3434, 2004.

[5] E Tran, R Ma, K Paton, E Blackmore, and Pickles T. Outcomes of Proton Radiation Therapy for Peripapillary Choroidal Melanoma at the BC Cancer Agency. *Int J Radiat Oncol Biol Phys*, 85(5):1425–31, 2012.

[6] E.W. Blackmore, J. Vincent, S. Chavez, K. Gardey, G. Lam, U. Oelfke, T. Pickles, and K. Paton. Commissioning the TRIUMF Proton Therapy Facility. In *Proc. of the NIRS International Seminar on the Application of Heavy Ion Accelerators to Radiation Therapy of Cancer*, number 135, Chiba, 1994.

[7] E.W. Blackmore, K. Gardey, G. Lam, and U. Oelfke. Measurement of the Raw Bragg Peak at 70 MeV Under Different Operating Conditions. Technical Report 2, TRIUMF, March 1995.

[8] Kay-Uwe Gardey, Uwe Oelfke, and Gabriel KY Lam. Range modulation in proton therapy-an optimization technique for clinical and experimental applications. *Physics in medicine and biology*, 44(6):N81, 1999.

[9] Sang Gyu Ju, Min Kyu Kim, Chae-Seon Hong, Jin Sung Kim, Youngyih Han, Doo Ho Choi, Dongho Shin, and Se Byeong Lee. New Technique for Developing a Proton Range Compensator With Use of a 3-Dimensional Printer. *International Journal of Radiation Oncology* Biology* Physics*, 88(2):453–458, 2014.

[10] Eric D Ehler, Brett M Barney, Patrick D Higgins, and Kathryn E Dusenbery. Patient specific 3D printed phantom for IMRT quality assurance. *Physics in medicine and biology*, 59(19):5763, 2014.

[11] E.W. Blackmore. Neutron and Beta/Gamma Measurements for Proton Therapy. Technical Report 2, TRIUMF, May 1996.

[12] Alfredo Ferrari, Paola R Sala, Alberto Fasso, and Johannes Ranft. Fluka: A multi-particle transport code (program version 2005). CERN-2005-10 (2005), INFN/TC_05/11, SLAC-R-773, 2005.

[13] Susan Baldwin. Compute canada: advancing computational research. In *Journal of Physics: Conference Series*, volume 341, page 012001. IOP Publishing, 2012.

[14] Vladimir Feygelman, D Opp, K Javedan, AJ Saini, and G Zhang. Evaluation of a 3d diode array dosimeter for helical tomotherapy delivery qa. *Medical Dosimetry*, 35(4):324–329, 2010.

[15] Evan Maynard, Michelle Hilts, Emily Heath, and Andrew Jirasek. Evaluation of accuracy and precision in polymer gel dosimetry. *Medical physics*, 44(2):736–746, 2017.

[16] Eva Kasanda, Christine Burbadge, Vinzenz Bildstein, Josef Turko, Artemis Spyrou, Cornelia Höhr, and Dennis Mücher. Geant4 simulation of a range verification method using delayed γ spectroscopy of a 92mo marker. *Physics in Medicine & Biology*, 65(24):245047, 2020.

[17] Katia Parodi and Jerimy C Polf. In vivo range verification in particle therapy. *Medical physics*, 45(11):e1036–e1050, 2018.

[18] Wolfgang Enghardt, P Crespo, F Fiedler, R Hinz, K Parodi, J Pawelke, and Falk Poenisch. Charged hadron tumour therapy monitoring by means of pet. *Nuclear Instruments and Methods in Physics Research Section A: Accelerators, Spectrometers, Detectors and Associated Equipment*, 525(1-2):284–288, 2004.

[19] Teiji Nishio, Takashi Ogino, Kazuhiro Nomura, and Hiroshi Uchida. Dose-volume delivery guided proton therapy using beam on-line pet system. *Medical physics*, 33(11):4190–4197, 2006.

[20] Stefaan Vynckier, S Derreumaux, F Richard, A Bol, C Michel, and André Wambersie. Is it possible to verify directly a proton-treatment plan using positron emission tomography? *Radiotherapy and oncology*, 26(3):275–277, 1993.

[21] Katia Parodi, Harald Paganetti, Ethan Cascio, Jacob B Flanz, Ali A Bonab, Nathaniel M Alpert, Kevin Lohmann, and Thomas Bortfeld. Pet/ct imaging for treatment verification after proton therapy: a study with plastic phantoms and metallic implants. *Medical physics*, 34(2):419–435, 2007.

[22] C Hoehr, M Trinczek, F Li, K Dinelle, S Blinder, E Blackmore, W Kwa, R Lee, V Sossi, T Ruth, et al. Pet scanning of ocular melanomas after proton therapy. In *2012 IEEE Nuclear Science Symposium and Medical Imaging Conference Record (NSS/MIC)*, pages 3850–3853. IEEE, 2012.

[23] GB Goodman, GKY Lam, RW Harrison, M Bergstrom, WR Martin, and BD Pate. The use of positron emission tomography in pion radiotherapy. *International Journal of Radiation Oncology* Biology* Physics*, 12(10):1867–1871, 1986.

[24] John S Laughlin. Development of the technology of radiation therapy. *Radiographics*, 9(6):1245–1266, 1989.

[25] Eric J Hall, Amato J Giaccia, et al. *Radiobiology for the Radiologist*, volume 6. Lippincott Williams & Wilkins, 2006.

[26] Kenichiro Maeda, Hironobu Yasui, Taeko Matsuura, Tohru Yamamori, Motofumi Suzuki, Masaki Nagane, Jin-Min Nam, Osamu Inanami, and Hiroki Shirato. Evaluation of the relative biological effectiveness of spot-scanning proton irradiation in vitro. *Journal of Radiation Research*, 57(3):307–311, 2016.

[27] Xcom NIST. Photon cross sections database on the web page http://physics. nist. gov/physrefdata, 2008.

[28] Harold Elford Johns and John Robert Cunningham. *The physics of radiology*. Charles C. Thomas Springfield, IL, 1983.

[29] Martin J Berger. Estar, pstar, and astar: Computer programs for calculating stopping-power and range tables for electrons, protons, and helium ions. *Unknown*, 1992.

[30] Frank Herbert Attix. *Introduction to radiological physics and radiation dosimetry*. John Wiley & Sons, 2008.

[31] Lewis V Spencer. Theory of electron penetration. *Physical Review*, 98(6):1597, 1955.

[32] Harald Paganetti. *Proton therapy physics*. CRC Press, 2011.

[33] U Fano. Penetration of protons, alpha particles, and mesons. *Annual Review of Nuclear Science*, 13(1):1–66, 1963.

[34] T Landberg, J Chavaudra, J Dobbs, J-P Gerard, G Hanks, J-C Horiot, K-A Johansson, T Möller, J Purdy, N Suntharalingam, et al. Report 62. *Journal of the ICRU*, (1):NP–NP, 1999.

[35] JA Auxier. Radiation dosimetry. Technical report, Oak Ridge National Lab., Tenn., 1967.

[36] Syed M Qaim, Ferenc T Tárkányi, Pavel Obložinskỳ, Khunab Gul, Alex Hermanne, MG Mustafa, FM Nortier, Bernhard Scholten, Yuri N Shubin, Sándor Takács, et al. Charged-particle cross section database for medical radioisotope production. *Journal of Nuclear Science and Technology*, 39(sup2):1282–1285, 2002.

[37] Matthew T Studenski and Ying Xiao. Proton therapy dosimetry using positron emission tomography. *World journal of radiology*, 2(4):135, 2010.

[38] Arvind K Shukla and Utham Kumar. Positron emission tomography: An overview. *Journal of medical physics/Association of Medical Physicists of India*, 31(1):13, 2006.

[39] Robert R Wilson. Radiological use of fast protons. *Radiology*, 47(5):487–491, 1946.

[40] M Goitein and M Jermann. The relative costs of proton and x-ray radiation therapy. *Clinical Oncology*, 15(1):S37–S50, 2003.

[41] RN Kjellberg, WH Sweet, WM Preston, and AM Koehler. The bragg peak of a proton beam in intracranial therapy of tumors. *Transactions of the American Neurological Association (US)*, 87, 1962.

[42] William U Shipley, Joel E Tepper, George R Prout, Lynn J Verhey, Oscar A Mendiondo, Michael Goitein, Andreas M Koehler, and Herman D Suit. Proton radiation as boost therapy for localized prostatic carcinoma. *Jama*, 241(18):1912–1915, 1979.

[43] Evangelos S Gragoudas, Michael Goitein, Andreas M Koehler, Lynn Verhey, Joel Tepper, Herman D Suit, Robert Brockhurst, and Ian J Constable. Proton irradiation of small choroidal malignant melanomas. *American journal of ophthalmology*, 83(5):665–673, 1977.

[44] Hui Liu and Joe Y Chang. Proton therapy in clinical practice. *Chinese journal of cancer*, 30(5):315, 2011.

[45] Radhika Sreeraman and Daniel J Indelicato. Proton therapy for the treatment of children with cns malignancies. *CNS oncology*, 3(2):149–158, 2014.

[46] Barbara S Hawkins et al. The collaborative ocular melanoma study (coms) randomized trial of pre-enucleation radiation of large choroidal melanoma: Iv. ten-year mortality findings and prognostic factors. coms report number 24. *American journal of ophthalmology*, 138(6):936–951, 2004.

[47] FA Stewart, AV Akleyev, M Hauer-Jensen, JH Hendry, NJ Kleiman, TJ Macvittie, BM Aleman, AB Edgar, K Mabuchi, CR Muirhead, et al. Icrp publication 118: Icrp statement on tissue reactions and early and late effects of radiation in normal tissues and organs–threshold doses for tissue reactions in a radiation protection context. *Annals of the ICRP*, 41(1-2):1–322, 2012.

[48] M Tubiana. Repopulation in human tumors: A biological back-ground for fractionation in radiotherapy. *Acta oncologica*, 27(2):83–88, 1988.

[49] Leo E Gerweck and Sergey V Kozin. Relative biological effectiveness of proton beams in clinical therapy. *Radiotherapy and oncology*, 50(2):135–142, 1999.

[50] John Gueulette, Lothar Böhm, Jacobus P Slabbert, Blanche M De Coster, Gerald S Rutherfoord, Arnout Ruifrok, Michelle Octave-Prignot, Peter J Binns, A Nicholaas Schreuder, Julian E Symons, et al. Proton relative biological effectiveness (rbe) for survival in mice after thoracic irradiation with fractionated doses. *International Journal of Radiation Oncology* Biology* Physics*, 47(4):1051–1058, 2000.

[51] Harald Paganetti, Andrzej Niemierko, Marek Ancukiewicz, Leo E Gerweck, Michael Goitein, Jay S Loeffler, and Herman D Suit. Relative biological effectiveness (rbe) values for proton beam therapy. *International Journal of Radiation Oncology* Biology* Physics*, 53(2):407–421, 2002.

[52] Fada Guan, Changran Geng, Duo Ma, Lawrence Bronk, Matthew Kerr, Yuting Li, Drake Gates, Benjamin Kroger, Narayan Sahoo, Uwe Titt, et al. Rbe model-based biological dose optimization for proton radiobiology studies. *International journal of particle therapy*, 5(1):160–171, 2018.

[53] Harald Paganetti. Proton relative biological effectiveness–uncertainties and opportunities. *International journal of particle therapy*, 5(1):2–14, 2018.

[54] Jack Valentin. Relative biological effectiveness (rbe), quality factor (q), and radiation weighting factor (wr): Icrp publication 92. *Annals of the ICRP*, 33(4):1–121, 2003.

[55] Martin J Berger. *Penetration of Proton Beams Through Water: Depth-dose Distribution, Spectra and LET Distributions*. National Institute of Standards and Technology, 1993.

[56] William Henry Bragg and Richard Kleeman. Xxxix. on the α particles of radium, and their loss of range in passing through various atoms and molecules. *The London, Edinburgh, and Dublin Philosophical Magazine and Journal of Science*, 10(57):318–340, 1905.

[57] Rui Zhang and Wayne D Newhauser. Calculation of water equivalent thickness of materials of arbitrary density, elemental composition and thickness in proton beam irradiation. *Physics in medicine and biology*, 54(6):1383, 2009.

[58] Rui Zhang, Phillip J Taddei, Markus M Fitzek, and Wayne D Newhauser. Water equivalent thickness values of materials used in beams of protons, helium, carbon and iron ions. *Physics in Medicine & Biology*, 55(9):2481, 2010.

[59] Nora V Laver, Margaret E McLaughlin, and Jay S Duker. Ocular melanoma. *Archives of pathology & laboratory medicine*, 134(12):1778–1784, 2010.

[60] S Kaliki and CL Shields. Uveal melanoma: relatively rare but deadly cancer. *Eye*, 31(2):241–257, 2017.

[61] Ewart W Blackmore. Operation of the triumf (20-500 mev) proton irradiation facility. In *2000 IEEE Radiation Effects Data Workshop. Workshop Record. Held in conjunction with IEEE Nuclear and Space Radiation Effects Conference (Cat. No. 00TH8527)*, pages 1–5. IEEE, 2000.

[62] Shan Tong, Adam M Alessio, and Paul E Kinahan. Image reconstruction for pet/ct scanners: past achievements and future challenges. *Imaging in medicine*, 2(5):529, 2010.

[63] Vasilis Vlachoudis et al. Flair: a powerful but user friendly graphical interface for fluka. In *Proc. Int. Conf. on Mathematics, Computational Methods & Reactor Physics (M&C 2009), Saratoga Springs, New York*, volume 176, 2009.

[64] J. D. Hunter. Matplotlib: A 2d graphics environment. *Computing in Science & Engineering*, 9(3):90–95, 2007.

[65] M. Pelliccioni. Overview of fluence-to-effective dose and fluence-to-ambient dose equivalent conversion coefficients for high energy radiation calculated using the fluka code. *Radiation Protection Dosimetry*, 88(4):279–297, 2000.

[66] H Paganetti. Monte Carlo calculations for absolute dosimetry to determine machine outputs for proton therapy fields. *Phys Med Biol.*, 51(11):2801–2812, June 2006.

[67] Xu XG, Chao TC, and Bozkurt A. VIP-MAN: An Image-Based Whole-body Adult Male Model Constructed from Color Photographs of the Visible Human Project for Multi-Particle Monte Carlo Calculations. *Heath Phys*, 78(5):476–486, 2000.

[68] Michael J Ackerman. The visible human project. *Proceedings of the IEEE*, 86(3):504–511, 1998.

[69] Bobby Dyer. 3d cad human eye model. 2011.

[70] Freecad - open source cad. 2021.

[71] Brian Davies and Tim Morris. Physiological parameters in laboratory animals and humans. *Pharmaceutical research*, 10(7):1093–1095, 1993.

[72] E.W. Blackmore, K. Gardey, G. Lam, and U. Oelfke. Measurement of the Raw Bragg Peak at 70 MeV Under Different Operating Conditions. Technical Report 2, TRIUMF, March 1995.

[73] Ioannis Sechopoulos, David WO Rogers, Magdalena Bazalova-Carter, Wesley E Bolch, Emily C Heath, Michael F McNitt-Gray, Josep Sempau, and Jeffrey F Williamson. Records: improved reporting of monte carlo radiation transport studies: Report of the aapm research committee task group 268. *Medical Physics*, 2017.

[74] Giuseppe Battistoni, Julia Bauer, Till T. Boehlen, Francesco Cerutti, Mary P. W. Chin, Ricardo Dos Santos Augusto, Alfredo Ferrari, Pablo G. Ortega, Wioletta Kozowska, Giuseppe Magro, Andrea Mairani, Katia Parodi, Paola R. Sala, Philippe Schoofs, Thomas Tessonnier, and Vasilis Vlachoudis. The fluka code: An accurate simulation tool for particle therapy. *Frontiers in Oncology*, 6:116, 2016.

[75] M. Nozar. Fluka simulation studies of the solid target facility (stf) at bl2c4. Technical Report TRI-DN-11-10, TRIUMF, 2012.

[76] Bo Jung. Conversion coefficients for use in radiological protection against external radiation. *Acta Radiologica*, 40(4):465–466, 1999.

[77] American Association of Physicists in Medicine et al. Protocols for heavy charged particle beam dosimetry," a report of task group 20, radiation therapy committee, 1986.

[78] *Markus Chamber Model N23343 Datasheet.*

[79] Grant A McAuley, Anthony V Teran, Jerry D Slater, James M Slater, and Andrew J Wroe. Evaluation of the dosimetric properties of a diode detector for small field proton radiosurgery. *Journal of applied clinical medical physics*, 16(6):51–64, 2015.

[80] Siemens . BPW34S Datasheet. `https://datasheetspdf.com/pdf/124809/SiemensSemiconductorGroup/BPW34S/1`.

[81] M Pacilio, C De Angelis, S Onori, L Azario, A Fidanzio, R Miceli, A Piermattei, and A Kacperek. Characteristics of silicon and diamond detectors in a 60 mev proton beam. *Physics in Medicine & Biology*, 47(8):N107, 2002.

[82] Thomas Bortfeld. An analytical approximation of the bragg curve for therapeutic proton beams. *Medical physics*, 24(12):2024–2033, 1997.

[83] Benjamin M Clasie, Jacob B Flanz, and Hanne M Kooy. Interpolation of tabulated proton bragg peaks. *Physics in Medicine & Biology*, 57(21):N405, 2012.

[84] Dongxu Wang, T Rockwell Mackie, and Wolfgang A Tomé. Bragg peak prediction from quantitative proton computed tomography using different path estimates. *Physics in Medicine & Biology*, 56(3):587, 2011.

[85] Uwe Schneider, Peter Pemler, Jürgen Besserer, Matthias Dellert, Martin Moosburger, Jorrit de Boer, Eros Pedroni, and Terence Boehringer. The water equivalence of solid materials used for dosimetry with small proton beams. *Medical physics*, 29(12):2946–2951, 2002.

[86] Bernard Gottschalk. Comments on calculation of water equivalent thickness of materials of arbitrary density, elemental composition and thickness in proton beam irradiation. *Physics in Medicine & Biology*, 55(9):L29, 2010.

[87] JF Janny. Proton range-energy tables, 1 kev–10 gev, part 1. *Atomic Data Nucl. Data Tables*, 27:147–339, 1982.

[88] Harald Paganetti. Range uncertainties in proton therapy and the role of monte carlo simulations. *Physics in Medicine & Biology*, 57(11):R99, 2012.

[89] M Engelsman, H-M Lu, D Herrup, M Bussiere, and HM Kooy. Commissioning a passive-scattering proton therapy nozzle for accurate sobp delivery. *Medical physics*, 36(6Part1):2172–2180, 2009.

[90] Hanne M Kooy, Stanley J Rosenthal, Martijn Engelsman, Alejandro Mazal, Roelf L Slopsema, Harald Paganetti, and Jacob B Flanz. The prediction of output factors for spread-out proton bragg peak fields in clinical practice. *Physics in Medicine & Biology*, 50(24):5847, 2005.

[91] Hanne M Kooy, Matthew Schaefer, Skip Rosenthal, and Thomas Bortfeld. Monitor unit calculations for range-modulated spread-out bragg peak fields. *Physics in Medicine & Biology*, 48(17):2797, 2003.

[92] R Oozeer, A Mazal, JC Rosenwald, R Belshi, C Nauraye, R Ferrand, and S Biensan. A model for the lateral penumbra in water of a 200-mev proton beam devoted to clinical applications. *Medical physics*, 24(10):1599–1604, 1997.

[93] MM Urie, JM Sisterson, AM Koehler, M Goitein, and J Zoesman. Proton beam penumbra: Effects of separation between patient and beam modifying devices. *Medical physics*, 13(5):734–741, 1986.

[94] J. Hérault, N. Iborra, B. Serrano, and P. Chauvel. Monte carlo simulation of a protontherapy platform devoted to ocular melanoma. *Medical Physics*, 32(4):910–919, 2005.

[95] Wayne Newhauser, Nicholas Koch, Stephen Hummel, Matthias Ziegler, and Uwe Titt. Monte carlo simulations of a nozzle for the treatment of ocular tumours with high-energy proton beams. *Physics in Medicine & Biology*, 50(22):5229, 2005.

[96] L Stolarczyk, P Olko, T Cywicka-Jakiel, M Ptaszkiewicz, J Swakoń, B Dulny, T Horwacik, B Obryk, and MPR Waligorski. Assessment of undesirable dose to eye-melanoma patients after proton radiotherapy. *Radiation Measurements*, 45(10):1441–1444, 2010.

[97] I O Andersson and J Braun. A neutron rem counter. 1 1964.

[98] Triumf radiation protection group personal communication. 2014.

[99] ICRP. Conversion Coefficients for use in Radiological Protection against External Radiation. ICRP Publication 74. *Ann. ICRP*, 26(3-4), 1996.

[100] Triumf operations group personal communication. 2014.

[101] Han Woong Lim, Yumi Song, Ji Hong Kim, Yong Un Shin, Sun Jin Hwang, and Sukwoo Hong. Normal range of eye movement and its relationship to age. *Investigative Ophthalmology & Visual Science*, 58(8):747–747, 2017.

[102] Yuanshui Zheng, Wayne Newhauser, Jonas Fontenot, Phil Taddei, and Radhe Mohan. Monte carlo study of neutron dose equivalent during passive scattering proton therapy. *Physics in Medicine & Biology*, 52(15):4481, 2007.

[103] Shunsuke Yonai, Naruhiro Matsufuji, Tatsuaki Kanai, Yuki Matsui, Kaoru Matsushita, Haruo Yamashita, Masumi Numano, Takeji Sakae, Toshiyuki Terunuma, Teiji Nishio, et al. Measurement of neutron ambient dose equivalent in passive carbon-ion and proton radiotherapies. *Medical physics*, 35(11):4782–4792, 2008.

[104] Christina Zacharatou Jarlskog, Choonik Lee, Wesley E Bolch, X George Xu, and Harald Paganetti. Assessment of organ-specific neutron equivalent doses in proton therapy using computational whole-body age-dependent voxel phantoms. *Physics in Medicine and Biology*, 53(3):693–717, 2008.

[105] Andrew Wroe, Anatoly Rosenfeld, and Reinhard Schulte. Out-of-field dose equivalents delivered by proton therapy of prostate cancer. *Medical physics*, 34(9):3449–3456, 2007.

[106] X Yan, U Titt, AM Koehler, and WD Newhauser. Measurement of neutron dose equivalent to proton therapy patients outside of the proton radiation field. *Nuclear Instruments and Methods in Physics Research Section A: Accelerators, Spectrometers, Detectors and Associated Equipment*, 476(1-2):429–434, 2002.

[107] Ben Clasie, Andrew Wroe, Hanne Kooy, Nicolas Depauw, Jay Flanz, Harald Paganetti, and Anatoly Rosenfeld. Assessment of out-of-field absorbed dose and equivalent dose in proton fields. *Medical physics*, 37(1):311–321, 2010.

[108] MF Moyers, ER Benton, A Ghebremedhin, and G Coutrakon. Leakage and scatter radiation from a double scattering based proton beamline a. *Medical physics*, 35(1):128–144, 2008.

[109] Geraldine Mesoloras, George A Sandison, Robert D Stewart, Jonathan B Farr, and Wen C Hsi. Neutron scattered dose equivalent to a fetus from proton radiotherapy of the mother. *Medical physics*, 33(7Part1):2479–2490, 2006.

[110] ICRP-The International Commission on Radiological Protection. The 2007 recommendations of icrp, icrp publication 103, ann icrp 37 (2-4), 2007.

[111] J Farah, R Sayah, F Martinetti, L Donadille, V Lacoste, J Hérault, S Delacroix, C Nauraye, I Vabre, C Lee, et al. Secondary neutron doses in proton therapy treatments of ocular melanoma and craniopharyngioma. *Radiation protection dosimetry*, 161(1-4):363–367, 2014.

[112] Stefano Agosteo, Claudio Birattari, Marcello Caravaggio, Marco Silari, and Giampiero Tosi. Secondary neutron and photon dose in proton therapy. *Radiotherapy and Oncology*, 48(3):293 – 305, 1998.

[113] A Stankovskiy, S Kerhoas-Cavata, R Ferrand, C Nauraye, and L Demarzi. Monte carlo modelling of the treatment line of the proton therapy center in orsay. *Physics in Medicine & Biology*, 54(8):2377, 2009.

[114] C Lindsay, J Kumlin, A Jirasek, R Lee, DM Martinez, P Schaffer, and C Hoehr. 3d printed plastics for beam modulation in proton therapy. *Physics in Medicine & Biology*, 60(11):N231, 2015.

[115] Aaron M Allen, Pawlicki Todd, Lei Dong, Eugene Fourkal, Mark Buyyounouski, Keith Cengel, John Plastaras, Mary K Bucci, Torunn I Yock, Luisa Bonilla, et al. An evidence based review of proton beam therapy: the report of ASTRO's emerging technology committee. *Radiotherapy and Oncology*, 103(1):8–11, 2012.

[116] AM Koehler, RJ Schneider, and JM Sisterson. Range modulators for protons and heavy ions. *Nuclear Instruments and Methods*, 131(3):437–440, 1975.

[117] Particle Therapy Co-Operative Group. Patient statistics of particle therapy facilities worldwide, 2013.

[118] CJ Luis Pérez. Analysis of the surface roughness and dimensional accuracy capability of fused deposition modelling processes. *Int Jrn of Production Research*, 40(12):2865–2881, 2002.

[119] Rupinder Singh. Process capability study of polyjet printing for plastic components. *Journal of mechanical science and technology*, 25(4):1011–1015, 2011.

[120] Eric Tran, Roy Ma, Katherine Paton, Ewart Blackmore, and Tom Pickles. Outcomes of proton radiation therapy for peripapillary choroidal melanoma at

the bc cancer agency. *International Journal of Radiation Oncology* Biology* Physics*, 83(5):1425–1431, 2012.

[121] E.W. Blackmore, J. Vincent, S. Chavez, K. Gardey, G. Lam, U. Oelfke, T. Pickles, and K. Paton. Commissioning the TRIUMF Proton Therapy Facility. In *Proc. of the NIRS International Seminar on the Application of Heavy Ion Accelerators to Radiation Therapy of Cancer*, number 135, Chiba, 1994.

[122] Stratasys Inc. ABSPlus P430 Material Safety Data Sheet, 2013.

[123] Stratasys Inc. VeroWhitePlus RGD835 Material Safety Data Sheet, 2011.

[124] C Lindsay, J Kumlin, DM Martinez, A Jirasek, and C Hoehr. Design and application of 3d-printed stepless beam modulators in proton therapy. *Physics in Medicine & Biology*, 61(11):N276, 2016.

[125] B Gottschalk. Passive beam spreading in proton radiation therapy. *unpublished book*, 2004.

[126] D Prieels. A new technique for the optimization of a range modulator. *IBA Technical Note*, 88.17.52.003, 1997.

[127] Harald Paganetti. Relative biological effectiveness (rbe) values for proton beam therapy. variations as a function of biological endpoint, dose, and linear energy transfer. *Physics in medicine and biology*, 59(22):R419, 2014.

[128] John E. Stone, David Gohara, and Guochun Shi. Opencl: A parallel programming standard for heterogeneous computing systems. *IEEE Des. Test*, 12(3):66–73, May 2010.

[129] Eric Jones, Travis Oliphant, Pearu Peterson, et al. SciPy: Open source scientific tools for Python, 2001.

[130] R Timothy Marler and Jasbir S Arora. Survey of multi-objective optimization methods for engineering. *Structural and multidisciplinary optimization*, 26(6):369–395, 2004.

[131] Wolfram Stadler. *Fundamentals of multicriteria optimization*. Springer, 1988.

[132] Andrzej P Wierzbicki. *A methodological approach to comparing parametric characterizations of efficient solutions*. Springer, 1986.

[133] Dieter Kraft. A software package for sequential quadratic programming. Technical Report DFVLR-FB 88-28,, DLR German Aerospace Center, 1988.

[134] JJ Wilkens and U Oelfke. A phenomenological model for the relative biological effectiveness in therapeutic proton beams. *Physics in medicine and biology*, 49(13):2811, 2004.

[135] Stratasys Inc. Objet30 Pro Specifications. `http://www.stratasys.com/3d-printers/design-series/precision/~/media/AECD02CC265143198CD493D1664EEF55.ashx`, 2013.

[136] Shinichiro Mori, John Wolfgang, Hsiao-Ming Lu, Robert Schneider, Noah C Choi, and George TY Chen. Quantitative assessment of range fluctuations in charged particle lung irradiation. *International Journal of Radiation Oncology* Biology* Physics*, 70(1):253–261, 2008.

[137] Zhouguang Hui, Xiaodong Zhang, George Starkschall, Yupeng Li, Radhe Mohan, Ritsuko Komaki, James D Cox, and Joe Y Chang. Effects of interfractional motion and anatomic changes on proton therapy dose distribution in lung cancer. *International Journal of Radiation Oncology* Biology* Physics*, 72(5):1385–1395, 2008.

[138] AC Kraan, G Battistoni, Nicola Belcari, Niccolo' Camarlinghi, GAP Cirrone, G Cuttone, S Ferretti, A Ferrari, G Pirrone, F Romano, et al. Proton range monitoring with in-beam pet: Monte carlo activity predictions and comparison with cyclotron data. *Physica Medica*, 30(5):559–569, 2014.

[139] Antje-Christin Knopf, Katia Parodi, Harald Paganetti, Thomas Bortfeld, Juliane Daartz, Martijn Engelsman, Norbert Liebsch, and Helen Shih. Accuracy of proton beam range verification using post-treatment positron emission tomography/computed tomography as function of treatment site. *International Journal of Radiation Oncology* Biology* Physics*, 79(1):297–304, 2011.

[140] Katia Parodi, Harald Paganetti, Helen A Shih, Susan Michaud, Jay S Loeffler, Thomas F DeLaney, Norbert J Liebsch, John E Munzenrider, Alan J Fischman, Antje Knopf, et al. Patient study of in vivo verification of beam delivery and range, using positron emission tomography and computed tomography imaging after proton therapy. *International Journal of Radiation Oncology* Biology* Physics*, 68(3):920–934, 2007.

[141] Julia Bauer, Wenjing Chen, Sebastian Nischwitz, Jakob Liebl, Stefan Rieken, Thomas Welzel, Juergen Debus, and Katia Parodi. Improving the modelling of irradiation-induced brain activation for in vivo pet verification of proton therapy. *Radiotherapy and Oncology*, 128(1):101–108, 2018.

[142] Jin Su Kim, Jae Sung Lee, Ki Chun Im, Su Jin Kim, Seog-Young Kim, Dong Soo Lee, and Dae Hyuk Moon. Performance measurement of the micropet focus 120 scanner. *Journal of Nuclear Medicine*, 48(9):1527–1535, 2007.

[143] S Jan, G Santin, D Strul, et al. Gate (geant4 application for tomographic emission): a simulation toolkit for pet and spect. to appear in phys. *Med. Biol*, 2004.

[144] Kris Thielemans, Charalampos Tsoumpas, Sanida Mustafovic, Tobias Beisel, Pablo Aguiar, Nikolaos Dikaios, and Matthew W Jacobson. Stir: software for tomographic image reconstruction release 2. *Physics in Medicine & Biology*, 57(4):867, 2012.

[145] T Amin, A Infantino, C Lindsay, R Barlow, and C Hoehr. Modelling pet radionuclide production in tissue and external targets using geant4. In *Journal of Physics: Conference Series*, volume 874, page 012109. IOP Publishing, 2017.

[146] Sea Agostinelli, John Allison, K al Amako, John Apostolakis, H Araujo, P Arce, M Asai, D Axen, S Banerjee, G 2 Barrand, et al. Geant4a simulation toolkit. *Nuclear instruments and methods in physics research section A: Accelerators, Spectrometers, Detectors and Associated Equipment*, 506(3):250–303, 2003.

[147] Chelsea Dunning. In vivo dose verification in a lucite phantom after proton irradiation using pet imaging methods - ubc undergraduate dissertation. 2015.

[148] C Hoehr, C Lindsay, J Beaudry, C Penner, V Strgar, R Lee, and C Duzenli. Characterization of the exradin w1 plastic scintillation detector for small field applications in proton therapy. *Physics in Medicine & Biology*, 63(9):095016, 2018.

[149] Marie-Catherine Vozenin, Pauline De Fornel, Kristoffer Petersson, Vincent Favaudon, Maud Jaccard, Jean-François Germond, Benoit Petit, Marco Burki,

Gisèle Ferrand, David Patin, et al. The advantage of flash radiotherapy confirmed in mini-pig and cat-cancer patients. *Clinical Cancer Research*, 25(1):35–42, 2019.

[150] V Favaudon, C Fouillade, and MC Vozenin. Ultrahigh dose-rate," flash" irradiation minimizes the side-effects of radiotherapy. *Cancer radiotherapie: journal de la Societe francaise de radiotherapie oncologique*, 19(6-7):526–531, 2015.

[151] Vincent Favaudon, Laura Caplier, Virginie Monceau, Frédéric Pouzoulet, Mano Sayarath, Charles Fouillade, Marie-France Poupon, Isabel Brito, Philippe Hupé, Jean Bourhis, et al. Ultrahigh dose-rate flash irradiation increases the differential response between normal and tumor tissue in mice. *Science translational medicine*, 6(245):245ra93–245ra93, 2014.

[152] Jean Bourhis, Wendy Jeanneret Sozzi, Patrik Gonçalves Jorge, Olivier Gaide, Claude Bailat, Fréderic Duclos, David Patin, Mahmut Ozsahin, François Bochud, Jean-François Germond, et al. Treatment of a first patient with flash-radiotherapy. *Radiotherapy and oncology*, 139:18–22, 2019.

[153] Annalisa Patriarca, Charles Fouillade, Michel Auger, Frédéric Martin, Frédéric Pouzoulet, Catherine Nauraye, Sophie Heinrich, Vincent Favaudon, Samuel Meyroneinc, Rémi Dendale, et al. Experimental set-up for flash proton irradiation of small animals using a clinical system. *International Journal of Radiation Oncology* Biology* Physics*, 102(3):619–626, 2018.

[154] Elke Beyreuther, Michael Brand, Stefan Hans, Katalin Hideghéty, Leonhard Karsch, Elisabeth Leßmann, Michael Schürer, Emília Rita Szabó, and Jörg Pawelke. Feasibility of proton flash effect tested by zebrafish embryo irradiation. *Radiotherapy and Oncology*, 139:46–50, 2019.

[155] Georgios Kourkafas, Juergen Bundesmann, Timo Fanselow, Andrea Denker, Vincent Henrique Ehrhardt, Johannes Gollrad, Volker Budach, Andreas Weber, Norbert Kociok, Antonia M Joussen, et al. Flash proton irradiation setup with a modulator wheel for a single mouse eye. *Medical Physics*, 2021.